Title
Fluctuation analysis of nonequilibrium limit cycle oscillators : Application to hair cells

Author
Sheth, Janaki Kirit

Publication Date
2020

Peer reviewed|Thesis/dissertation

UNIVERSITY OF CALIFORNIA
Los Angeles

Fluctuation analysis of nonequilibrium limit cycle oscillators : Application to hair cells

A dissertation submitted in partial satisfaction
of the requirements for the degree
Doctor of Philosophy in Physics

by

Janaki Kirit Sheth

2020

ABSTRACT OF THE DISSERTATION

Fluctuation analysis of nonequilibrium limit cycle oscillators : Application to hair cells

by

Janaki Kirit Sheth
Doctor of Philosophy in Physics
University of California, Los Angeles, 2020
Professor Alexander Levine, Co-Chair
Professor Dolores Bozovic, Co-Chair

Mechanical detection of the auditory system displays exquisite sensitivity, with the inner ear capable of detecting pressure waves that result in Ångstrom-scale displacements. Detection in the inner ear is performed by mechanically sensitive hair cells, named for the bundles of stereocilia that protrude from their surfaces. The inner ear is also highly nonlinear in nature, exhibiting sharply tuned frequency selectivity and compression of dynamic range. Several experiments have consistently shown that the hair cells and their hair bundles are not just passive sensory detectors, rather underlying their exemplary behavior is an internal active mechanical process which is also adaptive in nature. Furthermore, this active process leads to an inherent mechanical instability manifested in the spontaneous limit cycle oscillations of the hair bundles. A number of theories based on nonlinear dynamics have described these active bundles using complex biophysical models as well as using a relatively simple two-dimensional mathematical model that exhibits a supercritical Hopf bifurcation. In this dissertation which is theoretical in nature, with the spontaneously oscillating inner ear hair bundle as our model biological system, we study the effects of stochasticity on nonlinear oscillators driven by internal active processes. First, we develop a framework for the general interpretation of such dynamical systems near a limit cycle. We demonstrate that in the presence of noise the phase of the limit cycle oscillator diffuses while fluctuations in

the directions locally orthogonal to the cycle display a Lorentzian power spectrum. Further we identify two mechanisms that underlie the complex frequency dependence of the diffusive dynamics. In the subsequent chapter, we detail how the effects of stochasticity maybe observed with respect to the change in shape and size of the mean limit cycle as well. In particular, we show that the noise-induced distortion of the limit cycle generically leads to its rounding through elimination of sharp features. Conversely, using a theoretical criterion one may identify limit cycle regions most susceptible to such distortion and obtain more meaningful parametric fits of dynamical models from experimental data. In the third chapter of this thesis we study fluctuation-dissipation relations in computationally-driven, nonequilibrium limit-cycle oscillators. A computational drive is loosely analogous to the adaptive internal activity that powers the spontaneous oscillations of the hair cells. It measures the current state of the system and modifies its power input accordingly. We observe that computationally-driven systems not only violate the equilibrium fluctuation-dissipation theorem (FDT) but also a generalized FDT. Thus in turn we propose that the breakdown of this generalized theorem may be used as a tool to broadly identify the presence and effect of such drives within biological systems. Lastly, by quantifying the computing ability of these drives we seek to derive a new generalized fluctuation-dissipation theorem which can be satisfied by complex computationally-driven biological systems such as the inner ear.

The dissertation of Janaki Kirit Sheth is approved.

Robijn Bruinsma

Tom Chou

Alexander Levine, Committee Co-Chair

Dolores Bozovic, Committee Co-Chair

University of California, Los Angeles

2020

Table of Contents

List of Figures

Acknowledgments

First of all I would like to thank my two advisors in the Physics department, Dolores Bozovic and Alex Levine for being great mentors. Without their advice, ideas and sometimes just their mere patience with me as I grew into the role of a theoretical physicist, this thesis would not have been possible. Thank you to my lab mates past and present for the many hours of fun, scientific or otherwise and for helping me navigate a new culture. Thanks Justin Faber, Jessica Lin, Nicholas Senofsky, Joey Marcinik, Liz Mills, Tracy Zhang, Yuki Quinones, Bas Meenderink and Rami Amro. I am also incredibly grateful for having found additional mentors in physics and other departments who through their scientific advice have helped shaped my graduate life path. Thank you Robijn Bruinsma, Tom Chou, Abeer Alwan, Jonathan Kao and William Speier; having studied under you and worked with you I have learned skills that complement my physics work and will undoubtedly prove useful in future endeavors. I would also like to acknowledge my family away from home - Chandler Schlupf, Niko Rombes, Alex Latshaw, Kelly Chang, Shyama Sathianathan, Mihir Laghate, Parthe Pandit, Shantanu Thakar, Pratik Chaudhari, Riccha Tripathi, Saakshita Prabhakar, Meera Ramaswamy, Gowri Kurup, Neeraj Ahuja, Shantanu Sinha, Abhimanyu Dhariwal, Nikunj Saunshi and Anvit Tawar for making these six years and this big transition in my life a wonderful affair. Also a huge shout out to the UCLA FEM magazine team who I have had the honor to work with and to the Socal hiking club with whom I have scaled many beloved peaks in the Socal area making mountaineering a sport I seek to take up more seriously. Lastly a heartfelt thank you to my parents, my extended family, Mark Harfouche (my newly - wedded husband) and his parents for being supportive and making India, America and Canada feel like home to us.

Curriculum Vitae

2010 – 2014	B.Tech. in Engineering Physics with minor in Electrical Engineering, Indian Institute of Technology, Bombay, India.
2014 – 2017	Teaching Assistant, Physics and Astronomy, UCLA.
2017 – 2019	Graduate Student Researcher, Physics and Astronomy, UCLA.
Summer 2019 – Spring 2020	Dissertation Year Fellowship, Graduate Division, UCLA.
Summer 2020	Internship at IBM Research.

Publications

[1] Janaki Sheth, Dolores Bozovic, and Alex Levine, "Violation of generalized fluctuation theorems in adaptively driven steady states: Applications to hair cell oscillations," (2020), arXiv: 2002.11854 .

[2] Janaki Sheth, Ariel Tankus, Michelle Tran, Nader Pouratian, Itzhak Fried, and William Speier, "Generalizing neural signal-to-text Brain-Computer Interfaces," arXiv: 1907.04265 .

[3] Janaki Sheth, Ariel Tankus, Michelle Tran, Nader Pouratian, Itzhak Fried, and William Speier, "Translating neural signals to text using a Brain-Computer Interface," (2019), Neurips workshop on Neuro+AI (2019) .

[4] Janaki Sheth, Ariel Tankus, Michelle Tran, Lindy Comstock, Itzhak Fried, and William Speier, "Identifying input features for development of real-time translation of neural signals to text," (2019), Proceedings of Interspeech (2019) .

[5] Janaki Sheth, Dolores Bozovic, and Alex Levine, "Noise-induced distortion of the mean limit cycle of nonlinear oscillators," Phys. Rev. **E99**, 062124 (2019), .

[6] Janaki Sheth, Sebastiaan Meenderink, Patricia Sheth, Dolores Bozovic, and Alex Levine, "Nonequilibrium limit-cycle oscillators: Fluctuations in hair bundle dynamics," Phys. Rev. **E97**, 062411 (2018), .

CHAPTER 1

Dynamics of the inner ear

1.1 Hearing

The vertebrate ear is a remarkable product of evolution. Its frequency response ranges from 20 - 20,000 Hz while at the same time allowing an untrained individual to distinguish between two tones differing in frequency by 0.5% [2]. Similarly, it can effortlessly parse 0-120 dB of sound-pressure level (SPL) - corresponding to a millionfold range in input amplitude - but is also sensitive to mechanical stimuli of picometer dimensions (as measured at the eardrum) [44]. This extraordinary performance is a result of the acoustical interplay of its three major components - the inner, middle, and if present, outer ear. The latter collects airborne sounds that are funneled through to the eardrum whose vibrations in turn are transmitted by the middle ear to the oval window, an elastic opening in the bony casing of the inner ear - an organ that transduces this mechanical energy into electrical signals suitable for neural analysis [26] Fig. 1.1(a). In humans, the inner ear plays a significant role in both our auditory and vestibular functions and is further comprised of multiple organs - the cochlea, utriculus, sacculus and three semicircular canals [1].

Amongst these, the cochlea is our primary auditory organ and owes its extraordinary success to the bevy of specialized sensory receptors called hair cells which are situated along the basilar membrane - one of the two elastic sheets that partitions the organ into three fluid-filled compartments [44]. The other is the Reissner's membrane (see Fig. 1.1(b)). There lie nearly 16,000 hair cells in each of our cochleae; from the surface of each cell protrudes a cluster of 20-300 cylindrical processes or stereocilia - collectively called the hair bundle. These cilia are arranged in rows of increasing height, and coupled to their neigh-

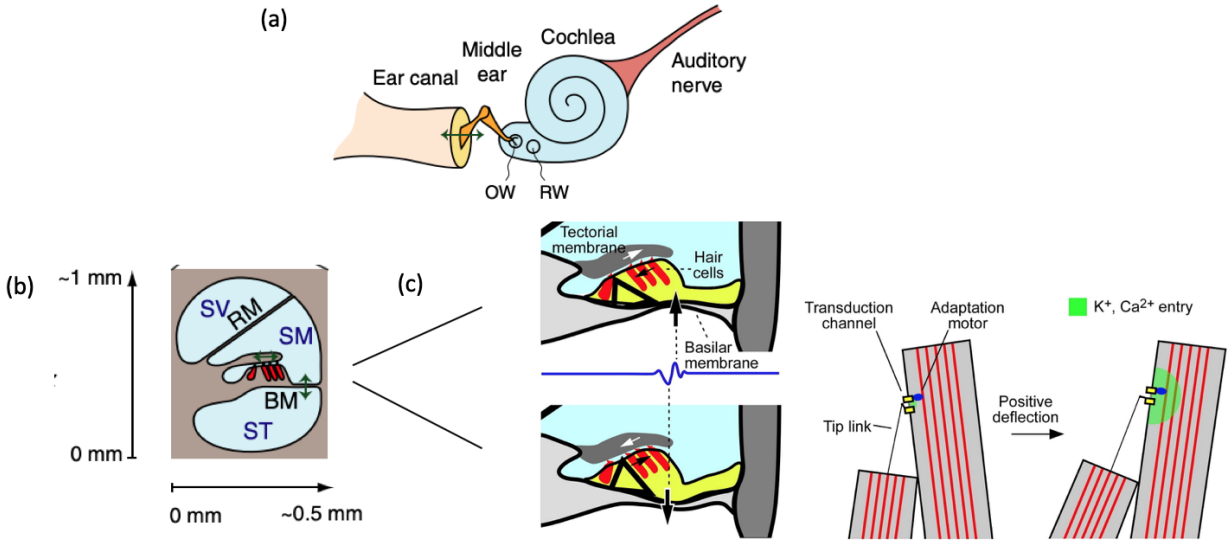

Figure 1.1: Structure of the ear and sound excitation in the human cochlea. (a) Sound propagating through air is funneled onto the eardrum by the external ear. The middle ear conveys the eardrums resulting vibration (arrow) to the cochlea, where it oscillates the elastic oval window (OW). Motion of the fluids inside this organ causes a second elastic opening, the round window (RW), to oscillate [44]. (b) A transverse section of the cochlea shows its two separating membranes: the basilar membrane (BM) and the Reissner's membrane (RM) which partition the organ into three compartments (scala vestibuli (SV), scala media (SM) and scala tympani (ST)) [29]. Also depicted are mechanotransductive hair cells in red atop the BM. (c) Simultaneous movement of BM and the tectorial membrane, deflect the hair bundles toward the taller stereocilia stretching some of their extracellular links and other components of transduction apparatus, causing ion channels to open which admits K^+ and Ca^{2+} into the somatic body [44].

bors via extracellular links. Furthermore, similar stereociliary hair bundles can be found in multiple other vertebrate auditory and vestibular organs and are often mechanically coupled using overlying structures such as the tectorial membrane in human cochleae, and otolithic membrane in the bullfrog sacculi [1].

In the cochlea, air-borne vibrations induced by an incoming sound causes a traveling wave along the basilar membrane. Its up-and-down motion combined with that of the tectorial membrane results in a back-and-forth movement of the hair bundles and consequently opens mechanosensitive ion channels that reside within each stereocilium (Fig. 1.1(c)). This leads to an inward ionic current of K^+ and Ca^{2+}, which depolarizes the hair cell membrane potential, and further triggers action potentials in connecting auditory nerve fibers through the release of the neurotransmitter glutamate. The entry of these ions through mechanotransduction channels is ensured by the unique configuration of the cells chemical environment, with their apical side bathed in endolymph, a K^+ rich solution and their basal side contacting perilymph, whose ionic composition is dominated by Na^+. The subsequent endocochlear potential difference provides the primary driving force for the inward current. Thus while the basilar membrane transfers mechanical energy, the Ressiner's membrane functions as the electrical isolator that sustains this endocochlear potential [44].

However there are several crucial subtleties associated with the former. Its mechanical properties vary continuously along the cochlear length, tuning each point on the membrane to a different frequency in its wide tonotopic range. Apart from frequency selectivity, the basilar membrane also exhibits exquisite compressive nonlinearity, that characterized by a one-third power law: while sounds as soft as those with an amplitude of 0.3 nm - smaller than surrounding thermal fluctuations - evoke in it mechanical vibrations, those six times larger only cause 10 nm displacements [45]. These impressive dynamic ranges in the presence of severe hydrodynamic drag-induced dissipation indicate that the inner ear is both active and highly nonlinear [18]. Such properties however are not restrictive to the membrane, they have also been extensively shown to be exhibited by the inner ear hair cells and hair bundles. In fact, interplay between the active motilities of the basilar membrane and its hair bundles

has been proposed to be one of the mechanisms underlying the remarkable sensitivity and robustness of the inner ear [29].

1.2 Bullfrog Sacculus

As is evident from the foregoing discussion, in order to understand the basic principles of mechanotransduction aka how incoming sound is eventually converted to neural signals, one must necessarily study the mechanics of hair cells and their stereocilia. However, due to sensitivity of the mammalian hair cells, experiments aimed at detailed probing of mechanical properties have utilized other epithelia. For example, much of our present knowledge of the bundle dynamics comes from auditory and vestibular systems of lower vertebrates such as chickens, turtles and frogs [58]. While significant differences do exist between species, fundamental similarities can be found such as in the active, non-linear nature of the inner ear manifested in its frequency selectivity, compressive nonlinearity and its ability to parse sounds with amplitudes smaller than the noise floor. In this manuscript, we will be mainly focusing on the bullfrog sacculus (Fig. 1.2(a)), which is an auditory/vestibular organ in the American Bullfrog (*Rana Catesbiana*) and is capable of detecting low frequency air-borne sounds and ground vibrations with a range spanning 50-130 Hz. Just as in the cochlea, from the saccular epithelial hair cells protrude hair bundles which are arranged in a quasi-hexagonal fashion and coupled to an overlaying tissue called the otolithic membrane (OM).

1.2.1 Saccular Hair Bundles

These bundles are typically $\sim$8 μm tall and $\sim$10 μm in diameter, comprising of approximately 60 actin fillament-filled stereocilia and a single microtubule-based kinocilium [44] (Fig. 1.2(b)). Structurally, each stereocilium tapers near its base i.e at its point of insertion to the cuticular plate, due to gradual decline in the number of constituent microfilaments from several hundreds to a few tens. In the presence of an external force the bundle essentially pivots about this flexible, compliant base [15]. Furthermore, these stereocilia are

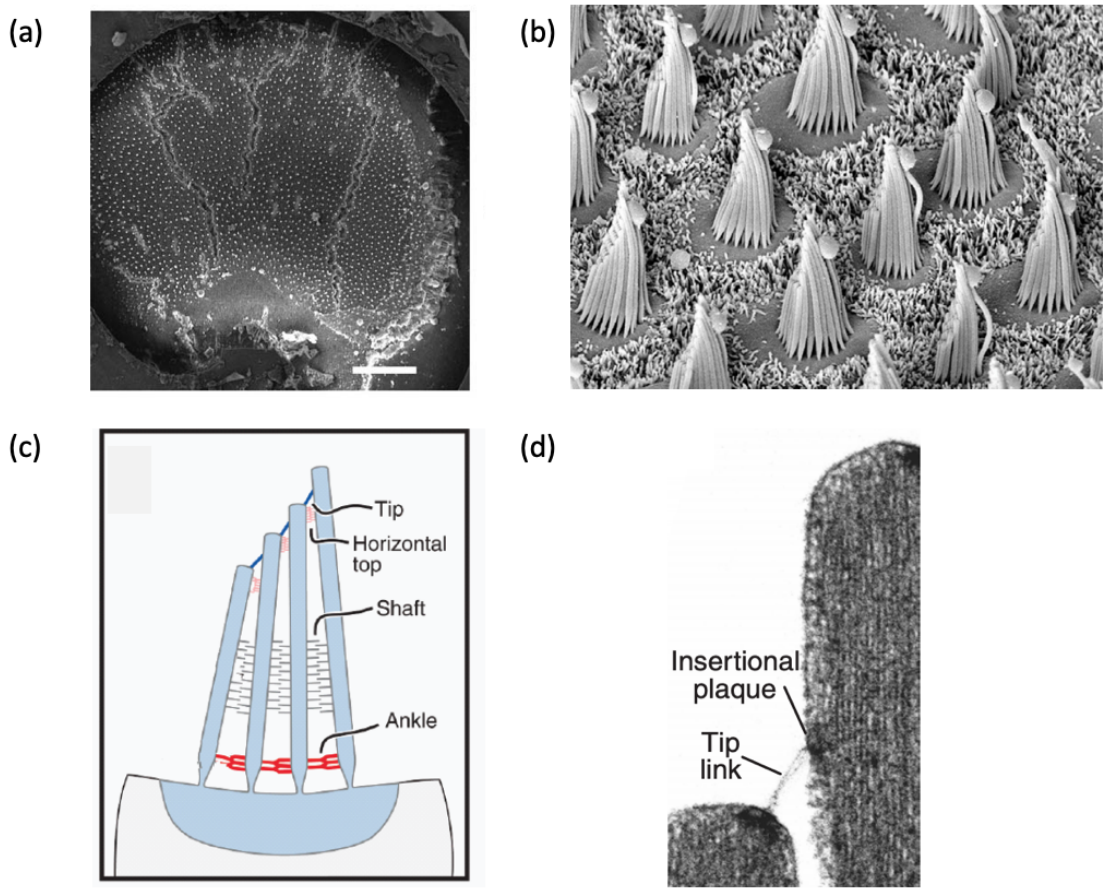

Figure 1.2: Morphology of the bullfrog sacculus

(a) Top-down SEM Image of the sacculus [55] (b) Zoomed in image depicts roughly a dozen protruding hair bundles from cellular surface [44] (c) Schematic diagram illustrating various links between neighbouring stereocilia (d) TEM image of a tip link connecting adjacent stereocilia. Insertional plaque at its upper end contains the Myosin-1c molecules that regulate tension in the gating spring.

intricately linked using proteinaceous connectors [58, 41] (Fig. 1.2(c),(d)).

Amongst these, the tip links are the most important connections for mechanotransduction. They are part of a crucial component of the hair bundle - its array of gating springs [41] - which senses deflection of the sensory organelle and conveys this information to the bundle's mechanically sensitive ion channels also known as its transduction channels. The opening (closing) of these channels is thus reliant upon the elongation (compression) of the associated gating spring. An excitatory (inhibitory) deflection of the bundle towards its kinocilium consequently leads to a depolarization (hyperpolarization) of the hair cell voltage whose resting potential otherwise is -60 mV. The resulting activation curve of bundle displacement vs. transduction current is well described by a Boltzmann function, with 15%-20% of the channels open at rest [1] (Fig. 1.3(a)).

One of the fascinating aspects of hair cell mechanotransduction is its reciprocity. While application of force to the gating spring regulates the opening and closing probabilities of its associated channel, at the same time, channel gating in turn affects tension in the spring. For example, opening of a channel relaxes the spring. This relaxation acts like an external force in the positive direction, causing the bundle to continue moving further [24]. Due to this phenomenon, often termed as gating compliance, while the hair bundle is Hookean in nature for large displacements in the positive and negative directions, over the range in which its channels can gate - about $\pm$ 20 nm centered at the cilium's resting position - the bundle's stiffness becomes zero or even negative [2] (Fig. 1.3(d)). Subsequently, the unrestrained hair bundle (one not coupled to an OM) cannot remain steady in this $\sim$50 nm region and is made to leap spontaneously in the positive and negative directions.

While this instability fostered by channel gating is a necessary ingredient for active hair bundle motility, it proves insufficient in the absence of an energy source that could potentially power this spontaneous motion. Furthermore, one may also inquire how does the cell respond to long static stimuli that are likely to saturate its afore stated narrow operating range. Previous studies have established that the stereociliary apparatus addresses these concerns using its molecular motors; these motors contain myosin-1c and scuttle up

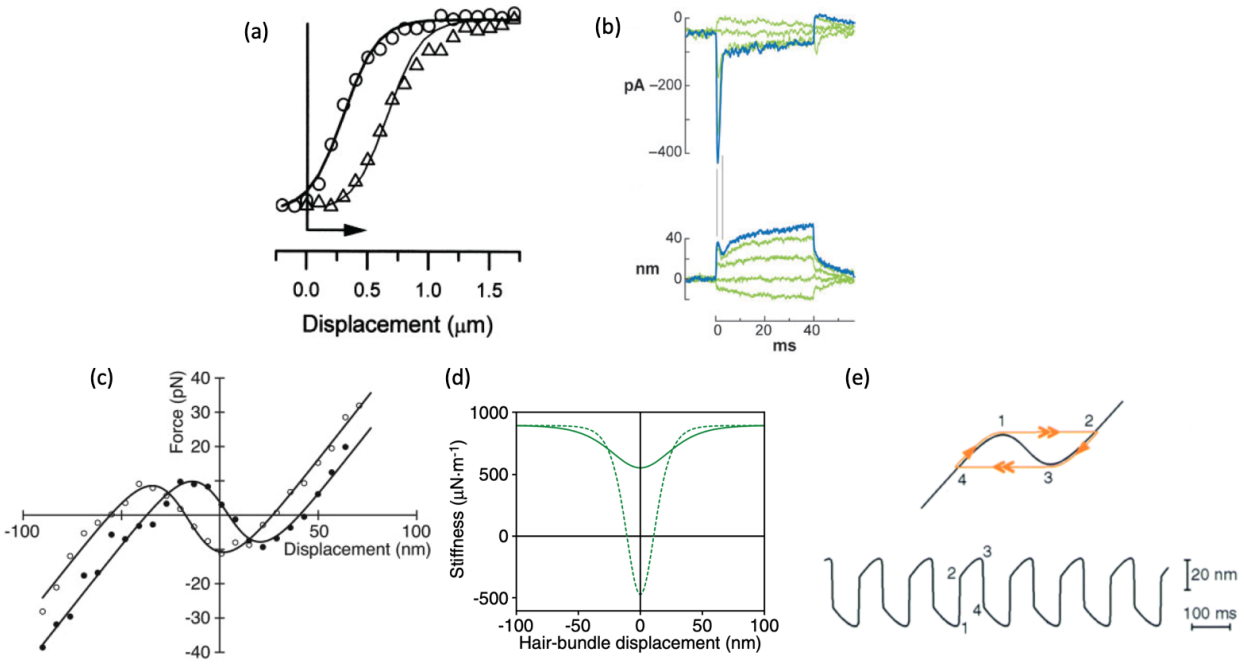

Figure 1.3: Adaptation, negative stiffness and resulting spontaneous oscillations

(a) Transduction current - bundle displacement curve of a saccular hair bundle. (Positive displacements to be considered excitatory.) [14] Note, the curve shifts along its displacement axis in presence a prolonged static positive stimulus. (b) Slow adaptation for a step deflection of 40 ms resulting in gradual decay of the inward current [58]. (c) Shifting of a bundle's displacement-force curve during oscillation with filled circles corresponding to the channel-opening state and open circles to -closing state [17]. (d) Gating compliance decreases bundle stiffness about its resting position. For large values of gating force, negative stiffness ensues (dotted curve) [44]. (e) Slow adaptation and negative stiffness work in concert to cause the bundle to oscillate spontaneously. The trace is from a model simulation [33].

and down actin filaments correspondingly increasing or decreasing tension in the conjugate gating springs [14].

Movement of the motors combined with the changing internal Ca^{2+} concentration, drives a unique form of mechanical adaptation that continually recentres the hair bundle's region of sensitivity and its operating range to the new position that it is held. Therefore for example, when the bundle is deflected towards its kinocilium, the incoming ionic current transiently peaks before decaying to its original resting level over time (Fig. 1.3(b)). This adaptive machinery comprises of two kinetic processes operating at different time-scales: first, a fast adaptation occurs within a millisecond or so; the second, slow adaptation has a time constant of roughly several tens of milliseconds [20]. While the exact mechanism underlying fast adaptation is still unknown, several theories have been proposed, all of which assume that the process is mediated by calcium inflow through the transduction channels [6, 10]. On the other hand, slow adaptation is relatively well understood and corresponds to a shift of the hair cells displacement-response curve in the direction of its external stimulus (Fig. 1.3(c)). For instance, excitatory bundle movements lead to Ca^{2+} influx which in turn causes motors to slip down the internal actin core, decreasing gating spring tension and closing ionic channels. The complement occurs for inhibitory deflections. The physiological utility of such motor climbing and slippage is clear: by slowly adapting to prolonged stimuli, the hair cells seek to remain sensitive to any new incoming stimulus [29].

The interplay between channel gating and the activity of myosin motors has been shown to lead to spontaneous limit cycle oscillations by the hair bundle, demonstrated *in vitro* in a number of species including the bullfrog sacculus [5, 33, 17] (Fig. 1.3(e)). Additionally, as one of the many mechanisms that plays a role in the organ's frequency selectivity and sensitivity, this active hair bundle motility has been unequivocally demonstrated to be highly spectrally tuned [1].

1.2.2 Saccular Hair Cell Somae

Another mechanism that tunes individual hair cells is electrical in nature: injection of a current pulse into the cell due to excitatory movements of the hair bundle causes a damped, sinusoidal oscillation of its membrane potential at a cell-specific resonant frequency. From a biophysical point of view this has primarily been attributed to the interplay between its voltage-activated Ca^{2+} channels and Ca^{2+}-sensitive K^{+} channels [22, 21]. However, multiple recent studies have documented additional basolateral ionic currents in the saccular hair cells and have also detected the occurrence of spontaneous self-sustained voltage oscillations [9, 25, 48].

Moreover, coupling between stereociliary motion and variations in the cellular potential is bidirectional. While the former clearly affects the latter due to ionic inflow, it has been shown that the membrane potential can modulate or fully suppress innate bundle oscillations, thus controlling its dynamic state in a process commonly referred to as reverse transduction [6, 3]. In particular, the authors of [34] through simultaneous electrophysiological and optical recordings show that such control is exerted by affecting the internal calcium concentration of the cilium, which in turn monitors the resting open probability of its mechanosensitive channels.

1.3 Active hair-bundle motility

The inner ear's active process underlies its mechanical amplification, frequency selectivity, compressive nonlinearity and spontaneous otoacoustic emissions. We have already detailed the first three, the last of these refers to the generation of sound in the receptor organ even in the absence of an external stimulus, and has been recorded in extremely quiet environments. The dynamical instability and self-sustained oscillations of its hair bundles and cells are postulated to power these emissions [2].

Active hair-bundle motility has also been shown to drive the inner ear's amplificatory process. For instance, external stimulation of an oscillating bundle's base by nanometer-scale

sinusoidal displacements often causes its tip to move by a still greater distance. Moreover, the average phase difference between the applied forcing and that of the oscillation exhibits zero-crossing at its characteristic natural frequency, with a phase lead (lag) for low (high) frequency signal. Both of these phenomena clearly delineate its non-linear active nature [31]. The same study further illustrates that during each cycle of stimulation the total external work done on the bundle was negative ($\sim$ -80 zJ); the hair cell in fact expends its own energy to amplify its mechanical response and sustain its movements.

1.4 Open questions

While many aspects of the mechanical and cellular processes behind the active hair motility have been established, many questions remain, and the study of the inner ear remains one of active pursuit. For example, while we understand that tuning is highly critical for optimal hearing, it is still unclear how the hair bundle's mechanical sensitivity is tuned. While, recent evidence suggests that efferent innervation may be a biological control parameter to achieve this [11] the details of how this neural activity may impact membrane potential and conversely the hair bundle are still unknown.

Moreover, as the inner ear is an active, non-linear organ, it also lends itself very well as a model system which can be probed using tools from the fields of non-linear dynamics and non-equilibrium statistical mechanics. Theoretical modeling work on the inner ear draws heavily from the former, while relations derived from the latter have proven useful in probing and delineating the active nature of the hair bundle organelle. Since in my work I will be using ideas from these fields to describe and understand the hair bundle and the hair cell, the forthcoming sections are intended to provide the necessary background.

1.5 Fluctuation-dissipation theorem and its generalizations

1.5.1 Violation of the fluctuation-dissipation theorem

A seminal study of the hair bundle's internal active nature analyses its violation of the fluctuation-dissipation theorem (FDT), a hallmark principle of equilibrium thermodynamics [27]. The theorem is given by the following equation,

$$\theta = \frac{\nu C(\nu)}{2k_B T \chi''(\nu)} \tag{1.1}$$

where one compares the correlation function (C) of a steady-state unperturbed stochastic observable to its linear response function (χ) when the system is perturbed by a small force. For systems in thermal equilibrium, $\theta = 1$. However, on evaluating this theorem with the hair bundle position as the observable of interest, Martin *et al.* in [32] show that the bundle is non-equilibrium in nature thus essentially eliminating the possibility that it can be a passive bi-stable system driven by noise (Fig. 1.4(a-d)). In fact, the root-mean-square of a free, passive hair bundle subjected to thermal Brownian motion is of the order of 3 nm, a value ten times larger than the threshold movement required for effective mechanotransduction. Some of the other sources of stochasticity that also modulate the unencumbered stereocilia and their autocorrelation functions are the frequency-dependent noise associated with motor attachment and detachment from the actin core [36], the clattering of ionic transduction channels and the shot noise due to ion transport. Overcoming these dissipative forces to parse sounds of low amplitude necessitates the presence of an internally active mechanism.

1.5.2 Generalized fluctuation-dissipation theorems

Several recent studies have explored whether such a universal fluctuation theorem also exists for non-equilibrium steady-state systems. In this work I will primarily dive into two such approaches. Prost *et al.* [42] explore a generalized fluctuation-dissipation theorem for a system exhibiting nonequilibrium fluctuations about a fixed point steady-state. Using their suggested change of variables a subsequent study [13] illustrates that an active hair bundle

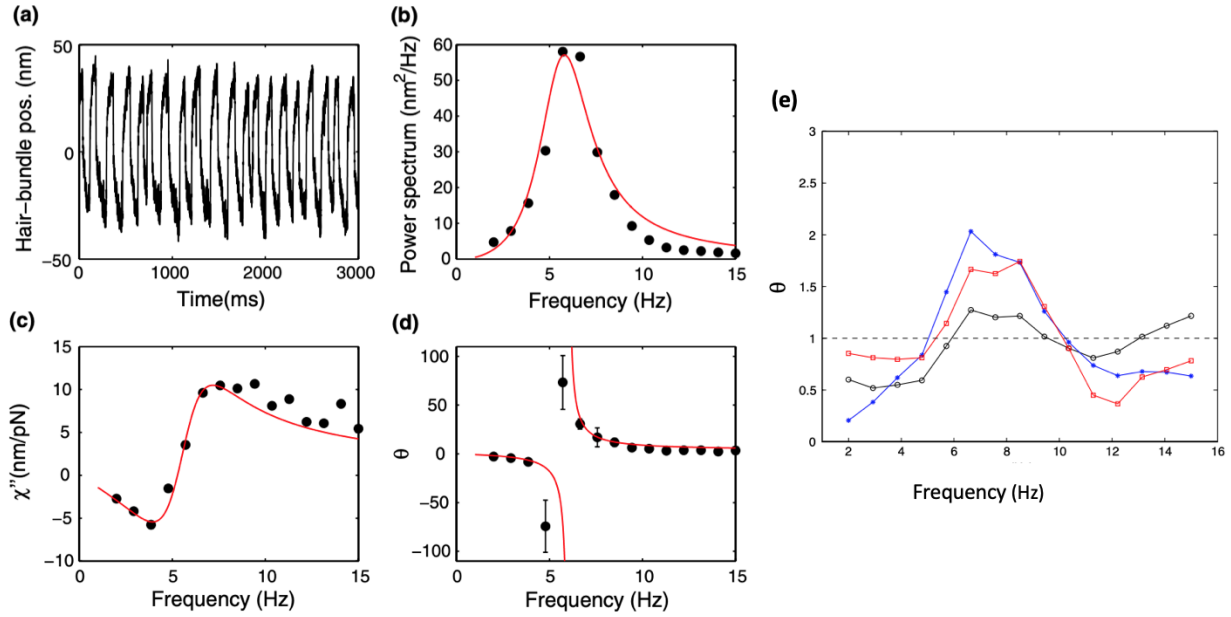

Figure 1.4: Violation of FDT by the hair bundle

. (a) Experimental trace of a spontaneously oscillating hair bundle. (b) Its highly tuned power spectrum (C(ν)). (c) Imaginary part of its linear response function ($\chi''(\nu)$). (d) Departure of θ from 1 illustrates the bundle's non-equilibrium behaviour. (e) The same ratio θ when applying the generalized GFDT of [13].

poised close to its point of criticality (*i.e.* in a region where its oscillation amplitude maybe deemed small enough to be approximated as a fixed point) in fact admits such a relation.

However, as the paper [36] suggests, the bundles might in fact lie deep in the oscillatory regime of their supercritical Hopf bifurcation. Here we point the reader to the next section on modelling where we will detail more thoroughly the Hopfian nature of the organelle. Since the previously stated generalized theorem is constrained to a fixed-point steady-state, in the presence of a limit cycle oscillator we study a different generalization, one proposed by Seifert *et al.* [50] : fluctuations of an observable relative to its local mean value behave like the corresponding response function. Thus subtracting away the mean non-equilibrium dynamics of the steady-state oscillator will potentially allow for $\theta = 1$ in Eq. 1.1.

1.5.3 Frenet frames

To facilitate this subtraction we propose a geometrical framework where we introduce the Frenet frame associated with the d-dimensional limit cycle of the oscillating hair bundle. For instance, let's consider a d-dimensional system of dynamical variables $\vec{X}(t) = \{x_1(t), \ldots, x_d(t)\}$, obeying the noise-free nonlinear system of differential equations

$$\dot{\vec{X}} = \vec{F}\left(\vec{X}\right), \tag{1.2}$$

where the dot denotes a time derivative. The function $\vec{F}$ depends on several parameters, whose values may be chosen to put the system in the limit-cycle regime. Thus, in the absence of noise, there exists a finite basin of attraction to a stable limit cycle solution of Eq. 1.2, with period T

$$\vec{X}_0(t) = \vec{X}_0(t+T), \tag{1.3}$$

and which is nowhere stationary in time.

To analyze the effects of noise on these dynamics, we linearize the system by introducing the Frenet frame associated with the d-dimensional curve defining the mean limit cycle, Eq. 1.3. That orthonormal frame consists of one tangent vector $\hat{t}(s)$, one normal vector $\hat{n}(s)$, and $(d-2)$ other mutually orthogonal vectors $\hat{b}_j(s)$, $j = 1, \ldots, (d-2)$. In subsequent

chapters, we analyse either a two-dimensional or a three-dimensional system. The 2-d frame comprises of $\{\hat{t}(s), \hat{n}(s)\}$, the 3-d frame also includes the binormal vector $\hat{b}(s)$. All d vectors of the Frenet frame may be parameterized by a single independent variable s, which denotes the arclength along the limit cycle, measured from an arbitrarily selected point on the cycle. One may alternatively define a phase angle $\phi = 2\pi s/\ell$, where ℓ is the arclength of the total limit cycle. We will use s and ϕ interchangeably in the following discussion.

Using the Frenet frame formalism, I have in my thesis work sought to understand the suitability and limitations of the Seifert-ian generalized fluctuation dissipation theorem [50, 53] as applied to the active, adaptive and nonlinear hair cell system. I shall elaborate upon our findings and conjectures in this regard in the forthcoming chapters.

1.6 Modelling the hair bundle and cell dynamics

Apart from experimental studies, theoretical work rooted in non-linear dynamics has significantly furthered our present-day understanding of the inner ear. As was discovered nearly two decades ago, the four defining characteristics of this auditory organ's striking active process emerge naturally if its mechanoelectrical transduction machinery operates on the verge of an instability - the supercritical Hopf bifurcation [8]. Physiological evidence supporting such a description has been obtained from nonmammalian tetrapod hair bundles [32, 2, 52] (Fig. 1.5(a)), the mammalian basilar membrane [47] (Fig. 1.5(b)) as well as hearing sensors of insects [54].

It is to be noted, that in this manuscript, we shall primarily interpret the Hopf dynamical system equations in context of the actively motile hair bundles. The normal form of this bifurcation can be written as :

$$\dot{z} = z\,(\mu - i\omega_0) + (b' + ib'')z|z|^2 + \eta_z(t) + f_z \tag{1.4}$$

where $z = x + iy$ denotes a complex variable, whose real part is mapped onto the bundle position and whose imaginary part does not have biological correlate but is a function of

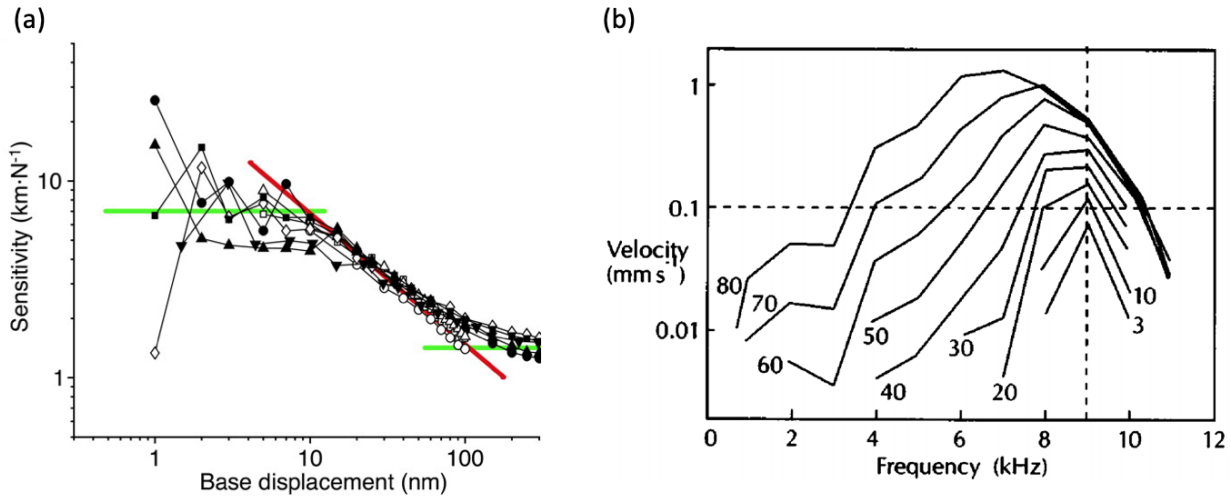

Figure 1.5: Characteristics of the ear's active process that suggest its proximity to the supercritical Hopf bifurcation

(a) Sensitivity curve of a hair bundle from the bullfrog sacculus enters a non-linear regime governed by a two-third power law for moderate amounts of stimulation [32]. (b) Laser velocimetric data from a living chinchillas cochlea displaying the root-mean-square velocity of one point on the basilar membrane as a function of driving frequency [40]. Each curve is evoked at a different level of stimulation, labelled in db SPL. Its compressively non-linear response has also been shown to follow the one-third law [47] and as is evident is highly frequency sensitive.

internal parameters such as motor adaptation, calcium dynamics, and ionic transport etc. For $\mu < 0$ the system has a single stable fixed point at $z = 0$ with an infinite basin of attraction, while for $\mu > 0$ it spontaneously oscillates leading to the emergence of a limit cycle attractor at $R_0 = \sqrt{\frac{\mu}{b'}}$. Herein $b' > 0$ ensures stability of this limit cycle about which the system traverses with an angular velocity of $\omega = \omega_0 + b'' R_0^2$. The hair bundle is proposed to be self-tuned at the bifurcation point i.e $\mu = 0$, since mathematical analysis indicates that a system posed near this criticality can exhibit a one-third power law, amplify small-magnitude stimuli and has a spectral response with sharp frequency selectivity [8].

However, the precise connection between these variables and the underlying hair bundle structures has been difficult to establish experimentally. As a consequence, a number of more complex models have been proposed, which are more directly based on the known biophysical processes operant within the organelle. These models explicitly include terms related to dynamics of the myosin motors, deflection of the stereocilia, and the electric potential across the cell membrane [30, 36, 46]. The experimental observations that variations in the membrane potential affect hair bundle motility and vice-versa have led to biophysical models that incorporate the non-linear dynamics of both the bundle and the cell as well as forward mechanoelectrical and reverse electromechanical transduction mechanisms. The analysis of these complex models reveals a rich phase diagram, containing distinct dynamical phases separated by both continuous and discontinuous bifurcations [36].

Interestingly, even the electrical resonance mechanism of the hair cell has been postulated to be poised near a Hopf bifurcation [40]. The full physiologically relevant mathematical model was initially proposed by Hudspeth and Lewis [22, 21], which latter studies have sought to map onto the Hopf normal form [35, 40]. One such model of a linear electrical resonator coupled bidirectionally to stochastic hair bundle oscillator was used in Ref. [19] to predict that higher quality voltage oscillations may enhance coherence of mechanical hair bundle oscillations.

1.7 Outline of the Dissertation

In this current work, we focus on the study of an inner ear hair bundle as an active, non-equilibrium limit cycle oscillator and using numerical simulations and analytics parse the effect of noise upon such a system. In chapter 2, we shed light on how well the two-dimensional Hopf mathematical model and a more biophysical three-dimensional model capture experimentally observed stochastically-driven fluctuations about the mean limit cycle curve. Next, in chapter 3, we probe the ability of noise to distort the oscillatory behavior of certain kinds of non-equilibrium systems and put forth a criterion that maybe used to identify limit cycle regions susceptible to such distortion thus enabling the readers to more meaningfully fit complex multi-parameter models to their data such as that obtained from the inner ear. Building upon our framework of chapter 2, in chapter 4 we explore how the computational nature of the actively motile hair bundle causes it to violate the fluctuation-dissipation theorem and some of its generalizations. Finally, chapter 5 describes future work of how one may instead instate a new generalized fluctuation-dissipation theorem which accords with such computation and thus may be satisfied by homoeostatically controlled biological systems such as the inner ear.

CHAPTER 2

Stochasticity in non-equilibrium limit cycle oscillators

2.1 Introduction

Analysis of the response of a nonlinear system to noise is typically performed by linearization about a stable fixed point, allowing one to write a system of linearized Langevin equations to describe the stochastic dynamics. Hair bundles exhibiting spontaneous oscillations, however, are described by a limit cycle rather than a fixed point. Thus in this chapter we explore a framework for the general interpretation of a stochastic dynamical system that lies near a stable limit cycle. We use this framework, comprising of the Frenet frame described in section 1.5.3, to not only detail the nature of fluctuations in such a system but also test for the robustness of the two-dimensional Hopf model and a three-dimensional biophysical model.

For example, for the noisy (henceforth "finite temperature") hair bundle oscillator, using its associated Frenet frame we can effectively "subtract" away the underlying average limit cycle of the stochastic bundle oscillations and thus easily linearize its fluctuations. We show that these fluctuations have a Lorentzian power spectrum in the $(d-1)$ directions that are orthogonal to the local tangent of the limit cycle. The local linear stability of the limit cycle forces these degrees of freedom to behave effectively like overdamped oscillators in a thermal bath. The fluctuations in the tangent direction, however, generate diffusive motion along the limit cycle. The first-order differential equation governing the limit cycle (Eq. 1.2) provides no restoring force to fluctuations that either advance or retard the motion of $\vec{X}$ in the tangent direction.

Additionally, we allow for the effective potential for the Lorentzian variables and the

effective diffusion constant of the arclength variable to themselves be time-dependent. There are two sources of this effect, which we call *mechanisms I and II*. Mechanism I is in effect when the linearized equations of motion about the Frenet frame have an effective coupling between the Lorentzian variables and the arclength variable. This coupling thus modifies diffusion of the tangential fluctuations in a frequency-dependent manner. Mechanism II occurs whenever the effective potential for the Lorentzian variables, the zero-temperature speed of the phase point about the noiseless limit cycle, or the effective diffusion constant of the arclength variable, are inherently arclength-dependent. So as the system transverses its limit cycle, this dependence makes the fluctuation spectrum vary in time. As they are arclength dependent, those variations generate extra structure in the power spectral density of the stochastic variables at discrete frequencies, determined by the zero-temperature period : $\nu_n = 2\pi n/T$, where n is an integer.

Additionally we use this framework to probe the generalizability of some of the previously detailed theoretical models, specifically the two-dimensional mathematical Hopf model and a more complex three-dimensional biophysical model. The latter comprises of the variables - hair bundle position, membrane potential and myosin motor activity. While these models have been shown to satisfactorily capture the mean dynamics of experimentally observed noisy spontaneous oscillations of hair bundles and cells [36, 19, 3], we shall also find them to describe well the fluctuation spectra in these data.

However, we note that the comparison between theory and the experimental measurements of hair bundle dynamics is fraught with a complexity. The more complex models include at least three dynamical variables. Although previous experiments have measured a number of physiological parameters, including stereociliary position, membrane potential, calcium concentration, and others [2, 29, 58], myosin motor activity during spontaneous oscillations is, so far, not directly observable. In essence, only lower-dimensional projections of the full dynamical systems, are experimentally accessible. In this chapter, we will thus study and compare a two-dimensional projection of the 3-d model, with the projection plane defined by the bundle position and the membrane potential.

Thus, the remainder of the chapter is organized as follows. In section 2.2, we introduce and analyze a two-dimensional model for a Hopf oscillator in the stably oscillating regime. In section 2.3, we apply our analysis to the three-dimensional biophysical model for hair bundle oscillations that explicitly includes the experimentally hidden variable of motor activity. In section 2.4, we turn to experimentally observed noisy spontaneous oscillations, exhibited by hair bundles of the amphibian sacculus. We find that predictions for the phase diffusion constant, based on *mechanism I* coupling of the simple supercritical Hopf system, are supported by the data. We also observe some features indicative of the proposed *mechanism II*. Finally, we conclude in section 3.4, where we review the relation between experiment and theory regarding the fluctuation spectrum of these limit cycle oscillators and propose new experiments.

2.2 Model I: Normal form for the supercritical Hopf bifurcation

We begin with the simplest two-dimensional approach to the hair cell dynamics, the supercritical Hopf oscillator in its normal form [56]. Its dynamical system can be described in terms of a single complex variable $z(t) = x(t) + iy(t)$ that obeys the (stochastic) differential equation

$$\dot{z} = z\,(\mu - i\omega) + bz|z|^2 + \eta_z(t). \tag{2.1}$$

One may identify the real part $x(t)$ with stereociliary displacement, and the imaginary part $y(t)$ with the bundle's internal active mechanism the details of which are irrelevant for the proceeding discussion. The zero-temperature dynamics of the model, *i.e.* when $\eta_z = 0$, are controlled by the values of the parameters $\{\mu, \omega, b\}$. We allow $b = b' + ib''$ to be a complex number whose real part is required to be positive ($b' > 0$) to ensure the stability of the limit cycle. When the (real) parameter $\mu < 0$, the system has a single stable fixed point at $z = 0$ with an infinite basin of attraction. For $\mu > 0$, this fixed point becomes unstable, and a circular limit cycle appears at radius $R_0 = \sqrt{\mu/b'}$. The zero temperature system traverses this limit cycle with a fixed angular velocity $\omega_0 = \omega + R_0^2 b''$.

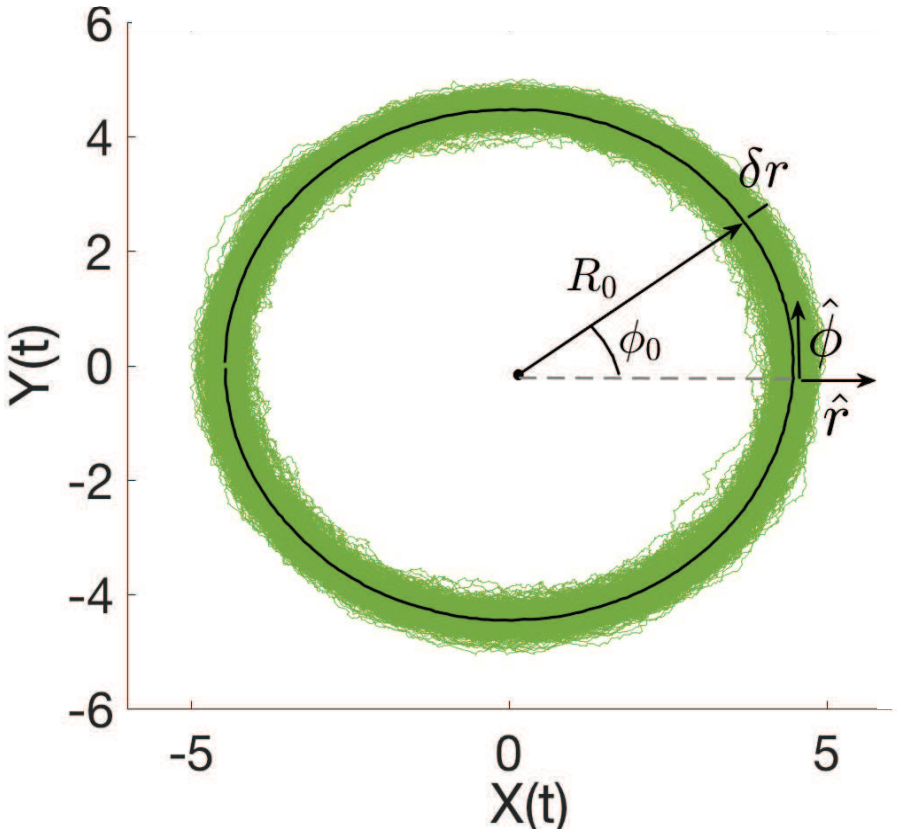

Figure 2.1: Numerical simulation of the stochastic Hopf oscillator: Calculations were performed based on Eq. 2.1. (a) The finite-temperature (green) trajectories and the mean (black) limit cycle. Also illustrated is the Frenet frame $\{\hat{r}, \hat{\phi}\}$ associated with the mean cycle. (b) A typical time series (black) of the stochastic dynamics of $x(t)$ and $y(t)$. The variables were low-pass filtered for further analysis (red dashed line).

We henceforth assume that the stochastic forces acting on this system are Gaussian random variables with zero mean and a frequency-independent second moment. The latter point is not essential for our analysis; one may consider the effect of colored Gaussian noise with the same formalism. In addition, we may assume that noise amplitudes along the orthogonal axes x, y are statistically independent, but potentially selected from different Gaussian distributions. Thus, we write

$$\langle \eta_i(t) \rangle = 0 \tag{2.2}$$

$$\langle \eta_i(t)\eta_j(t') \rangle = A_{ij}\delta(t-t') \tag{2.3}$$

with A_{ij} denoting elements of a diagonal matrix having two independent nonzero entries. The results obtained are consistent across several numerical values of A_{ij}. The range of values tested is further discussed in appendix A.

Recasting Eq. 2.1 in terms of polar coordinates

$$z(t) = r(t)e^{i\phi(t)}, \tag{2.4}$$

and then expanding about the zero-temperature limit cycle

$$r(t) = R_0 + \delta r(t) \tag{2.5}$$

$$\dot{\phi}(t) = \omega_0 + \delta\dot{\phi}(t) \tag{2.6}$$

we arrive at a local description of the fluctuations of the system in the limit cycle regime. On substituting for $r(t), \phi(t)$ in Eq. 2.1 and simplifying up to linear order, we derive

$$\delta\dot{r} = -2\mu\,\delta r + \eta_r \tag{2.7}$$

$$\delta\dot{\phi} = 2b''\sqrt{\frac{\mu}{b'}}\,\delta r + \eta_\phi. \tag{2.8}$$

We have introduced the projections of the stochastic force onto the local normal $\hat{r}$ and tangent $\hat{\phi}$ to the zero-temperature limit cycle, η_r and η_ϕ respectively. It should be noted that this $\{\hat{r}, \hat{\phi}\}$ frame is the Frenet frame for the circular limit cycle with $\hat{r} = \hat{n}$ and $\hat{\phi} = \hat{t}$.

From Eqs. 2.7, 2.8, we see that this two-dimensional system has one overdamped oscillator (Lorentzian) degree of freedom, corresponding to displacements of the system normal to

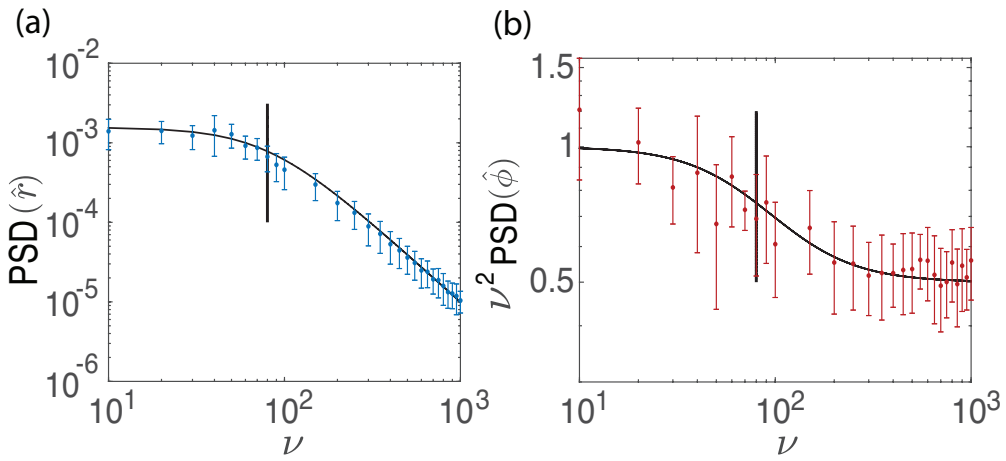

Figure 2.2: Fluctuation spectra of the Hopf oscillator

(a) Power spectral density of fluctuations in the radial variable (blue dots) as a function of frequency ν. Error bars denote standard deviations of the mean. The characteristic Lorentzian form has a corner frequency 2μ, marked by the vertical (black) line. (b) The frequency-dependent, effective phase diffusion constant, obtained from the product of the phase fluctuation power spectral density and ν^2. The spectrum exhibits a step, transition from a larger to a smaller diffusion constant, at the corner frequency of the radial fluctuations (vertical black line). The theoretical predictions - Eqs. 2.9, 2.10 - are indicated with superposed black lines.

the zero-temperature limit cycle ($\delta r\hat{n}$), and one diffusive arclength variable $s = R_0\phi$. In addition, we note that we should expect effects based on *mechanism I* to generate extra frequency dependence in the diffusion about the limit cycle, arising from the coupling of δr to the angular velocity variations $\delta\dot{\phi}$, seen in Eq. 2.8. Moreover, one observes that the non-zero parameter b'' controls the magnitude of this coupling, as it causes the fixed angular velocity of the system ω_0 to be dependent on the radius. We do not expect to observe effects of *mechanism II* in this system, since the curvature of the potential for δr is independent of ϕ, as is the coupling between that variable and $\delta\dot{\phi}$. Moreover, the mean velocity of the phase point of the zero-temperature dynamical system is independent of the arclength about the limit cycle.

If we make the further assumption that η_x and η_y are selected from the same ensemble, then the statistics of their projections onto $\hat{r}, \hat{\phi}$ are equal and independent of arclength. In that case, $A_{xx} = A_{yy} = A$, and we find the power spectral density for radial fluctuations to be a simple Lorentzian:

$$\langle |\delta r(\nu)|^2 \rangle = \frac{A}{4\mu^2 + \nu^2}. \tag{2.9}$$

However, the power spectrum of the phase fluctuations (our dimensionless arc length variable) is not simply diffusive, due to the mechanism I coupling between the normal and tangential fluctuations:

$$\langle |\delta\phi(\nu)|^2 \rangle = A\left[\frac{4b''^2\mu}{b'\nu^2\left(4\mu^2+\nu^2\right)} + \frac{b'}{\mu\nu^2}\right]. \tag{2.10}$$

The effective diffusion constant of the phase variable is larger at low frequencies $\nu < 2\mu$ than it is at higher ones. The *mechanism I* coupling, in essence, adds extra phase noise from the overdamped fluctuations of the radial variable. Since these radial fluctuations obey a Lorentzian power spectrum with a corner frequency of 2μ, the effect of this cross-coupling diminishes rapidly at frequencies higher than the corner frequency. This effectively decreases the phase diffusion at higher frequencies.

2.2.1 Fluctuations around a simulated Hopf limit cycle

We demonstrate these features of the fluctuation spectra using numerical simulations of the stochastic Hopf oscillator. The simulation details are standard and described in subsection 2.6.1. Fig. 4.2 illustrates the stochastic dynamics of the simulated supercritical Hopf dynamical system. The values of the Hopf parameters used to construct the same are: $\mu = 40$, $\omega_0 = 10$, $b' = 2$, $b'' = 2$. Panel 4.2(a) shows the mean orbit of the stochastic system in the phase space spanned by x, y (black line). The hair bundle phase space $\{-\pi, \pi\}$ is partitioned into nearly 200 bins. Trajectories in each bin are then averaged, resulting in the mean limit cycle. For all forthcoming figures in the chapter, similar methodology is applied to calculate the mean cycle.

Simulations provide us access to both this averaged curve and the zero-temperature one, but in experiments, we cannot access the latter. To better connect the simulations to the experimental observations shown later in this chapter, we study the behavior of these fluctuations about this averaged limit cycle. In this simple case, the average cycle is similar to the zero-temperature limit cycle. We return to this point in our summary. The green curves show a representative set of stochastic trajectories that meander about the mean limit cycle. The local Frenet frame for the average system, given by the unit vectors $\hat{r} = \hat{n}$ and $\hat{\phi} = \hat{t}$, is indicated in the figure. Panel 4.2(b) shows typical time series of the variables x, y after low-pass filtering. These were filtered at $400 \times 2\pi$ Hz; the Nyquist frequency was $500 \times 2\pi$ Hz.

We numerically compute the power spectral density (PSD) of the stochastic deviations of the simulated trajectories about the mean limit cycle of the supercritical Hopf oscillator (using code in A.1). The spectra of the fluctuations in the normal and tangential directions are shown in Figs. 2.2(a) and 2.2(b), respectively. In anticipation of the diffusive nature of the tangential or phase fluctuations, we plot the product of the tangential PSD and ν^2; note that this is the frequency-dependent phase diffusion constant. To obtain these results, we project the state of the system onto the local Frenet frame, corresponding to the point of the mean limit cycle closest to the phase space point of the system. The perturbation of this

state from the mean limit cycle, along the normal of the Frenet frame exhibits Lorenztian dynamics of an overdamped oscillator.

Fig. 2.2(b) is obtained from the drift-corrected difference between total arclengths traversed along the finite-temperature and the mean limit cycles. The arclength (s) is given by hair bundle displacement as projected along the tangent of the local Frenet frame nearest to the phase space point. The presence of noise $\{\eta_r, \eta_\phi\}$ causes the finite-temperature arclength to differ from the mean curve arclength. The difference is corrected for the underlying drift, and the resulting frequency spectrum is given by Eq. 2.10. The phase fluctuation $\delta\phi$ is equal to $2\pi(\delta s)/\ell$. Due to the coupling between the overdamped radial fluctuations and the phase velocity – see Eq. 2.8 – the phase diffusion constant crosses over from a higher value, at frequencies below the corner frequency of the radial Lorentzian PSD, to a lower one at higher frequencies; the crossover point of this step-like transition is marked by the vertical black line in both panels of Fig. 2.2. The phenomenon has a simple interpretation. Below the corner frequency, noise in the radial variable feeds back into the phase velocity fluctuations. Above the corner frequency, these radial fluctuations rapidly vanish, reducing the phase diffusion. There are no *mechanism II* effects, since the mean phase velocity, the phase diffusion constant, and the curvature of the effective potential in the radial direction are all phase independent.

2.3 Model II: Biophysical model

Hair bundle motility is more comprehensively described by higher-dimensional models that include multiple dynamical variables, aimed to accurately capture the biophysical processes operant within the hair cell. We focus here on a particular version of the model, which includes two observable physiological variables – hair bundle displacement $X(t)$ and the membrane potential of the hair cell $V_{ss}(t)$ – as well as an internal variable $X_a(t)$ associated with the position of the myosin motors along the actin filaments. For more details the reader is referred to Refs [19, 37]. This hair bundle model is defined by three nonlinear coupled

differential equations:

$$\lambda \dot{X} = -K_{gs}\left(X - X_a - DP_0\right) - K_{sp}X + \eta_x \tag{2.11}$$

$$\lambda_a \dot{X}_a = K_{gs}\left(X - X_a - DP_0\right) - \gamma F_{max}\left(1 - S_0\left[1 + \alpha\frac{V_{ss}}{V_0}\right]P_0\right) + \eta_{x_a} \tag{2.12}$$

$$\ddot{V}_{ss} = -\omega_v\left(\frac{\beta_0}{\omega_v C_m} + \frac{g_t P_0}{\omega_v C_m}\right)\dot{V}_{ss} - \omega_v^2\left(1 + \frac{g_t P_0}{\omega_v C_m}\right)\left(V_{ss} - V_0\right) - \frac{I_0\omega_v}{C_m}. \tag{2.13}$$

The model depends on sixteen physiological parameters, which are tabulated and described in subsection 2.6.1. The reader may follow code in A.5 to reproduce our model simulation.

We refer to this model as *three-dimensional* since it relates three biologically relevant variables. As normally discussed in the theory of dynamical systems, this model exists in a four-dimensional phase space, since the differential equation governing the membrane potential is second order in time. As a consequence, we can show only a three-dimensional projection of the system's four-dimensional limit cycle. We will see that the experimental data are confined to a two-dimensional projection of this three-dimensional limit cycle.

Models based on the first two equations, without the cellular membrane potential, have been extensively studied. This system contains an actively driven mechanical oscillator and is known to exhibit a dynamical phase portrait, exhibiting the so-called 'fish diagram' [36], with bifurcations separating quiescent, oscillatory, and bi-stable states of the hair bundle. These boundaries are controlled by both subcritical and supercritical Hopf bifurcations. The model employed here results from an extension of the two-dimensional model that includes the membrane potential (Eq. 2.13), described as an underdamped resonator with the same characteristic frequency as the bundle oscillator. The electrical oscillator is bi-directionally coupled to the active mechanical one. Oscillations of the hair bundle affect the membrane potential via the mechano-electrical transduction (MET) channel current $g_t P_0$, leading to forward coupling. Here, P_0 denotes the opening probability of mechanoelectrical transduction channels and its equation is given in 2.6.1. Variations of the membrane potential in turn modulate calcium influx, which affects the myosin motor activity; a dimensionless parameter α controls the strength of this reverse coupling [3].

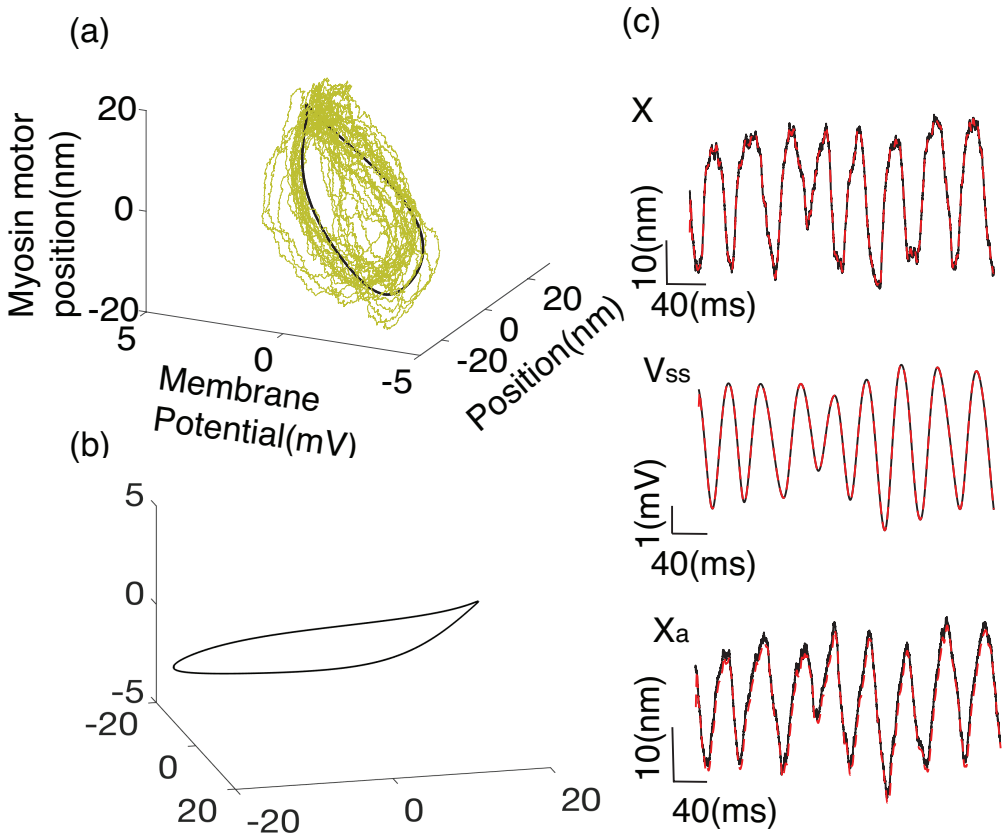

Figure 2.3: Numerical simulation of the three-dimensional hair bundle model Trajectories obtained by integrating Eqs. 2.11, 2.12, 2.13. Left panels (a) and (b) illustrate two different perspectives of the nonplanar zero-temperature limit cycle (black). The green curve in (a) shows a representative trajectory about this cycle. Right panel shows typical time series (black) of the stochastic dynamics of the three variables and their respective lowpass filtered curves (red dashed). Similar to the Hopf simulation, the cutoff for the filter was chosen at $400 \times 2\pi$ Hz. The system noise temperature was chosen to be $T_{eff} = \tau_{noise} T = 0.25T$. The constant τ_{noise} is indicative of the variance of the finite temperature hair bundle noise, and has value of 1 for a system obeying the fluctuation-dissipation theorem.

2.3.1 Fluctuations around a simulated three-dimensional zero-temperature limit cycle

We repeat our analysis of the fluctuations about the three-dimensional limit cycle. We introduce a third vector associated with the Frenet frame, the binormal vector defined by $\hat{b} = \hat{n} \times \hat{t}$. We may now similarly resolve stochastic deviations of the system depicted in Fig. 2.3, along this mutually orthogonal triad of vectors, associated with each phase point on the zero-temperature limit cycle (black curve).

In our simulations, the variance of the noise in the stochastic trajectory (green curve) is modulated by the constant – τ_{noise}. Since the experimental system may be subject to nonequilibrium noise sources, we consider the effect on the hair bundle dynamics of a variable noise amplitude unrelated to the system's thermodynamic temperature. In effect we modify all noise amplitudes so that they reflect fluctuations at an effective noise temperature $T_{eff} = \tau_{noise} T$. When $\tau_{noise} = 1$ the system obeys the fluctuation-dissipation theorem. Henceforth we refer to this specific value of $\tau_{noise} = 1$ as τ_0. In Fig. 2.3, the system noise temperature $T_{eff} = 0.25T$. The calculated three-dimensional zero-temperature limit cycle and the associated Frenet frames are shown in Fig. 2.4.

The deviations of the stochastic system from its nearest point on the zero-temperature limit cycle are resolved along the unit vectors $\hat{t}$, $\hat{n}$, and $\hat{b}$ of the local Frenet frame to obtain the power spectral densities of their fluctuations in Fig. 2.5 (code in A.6). We allude to the mean limit cycle case in later sections. Panels (b) and (c) show the (Lorentzian) relaxation of the degrees of freedom locally orthogonal to the limit cycle, in the normal (panel (b)) and binormal (panel (c)) directions. The fluctuations in these directions are those of overdamped oscillators. Panel (a) of this figure shows the frequency-dependent phase diffusion constant. Fig. 2.5(a) is obtained from the difference in total arclength of the zero and finite temperature oscillations, starting from an arbitrary phase point. The stochastic arclength variable is determined by the projection of the distance traversed by the noisy trajectory onto the unit vector $\hat{t}$ associated with the Frenet frames of the deterministic limit cycle. Arclength (s) and phase (ϕ) are interchangeable, and we depict fluctuations in the latter.

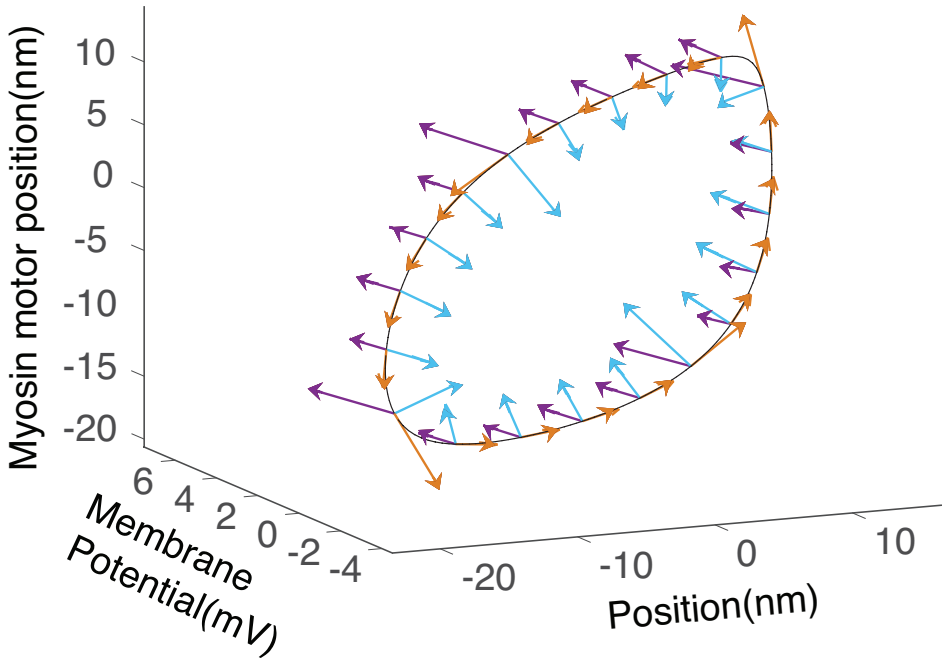

Figure 2.4: Rotating Frenet frame for the three-dimensional model

The zero-temperature limit cycle is indicated with the orange line. The local Frenet frame $\left(\hat{t}, \hat{n}, \hat{b}\right)$ is shown by the (orange, blue, purple) unit vectors respectively, with the frames at four of the phase angles magnified by an arbitrary value for clarity. Note that the limit cycle is nonplanar.

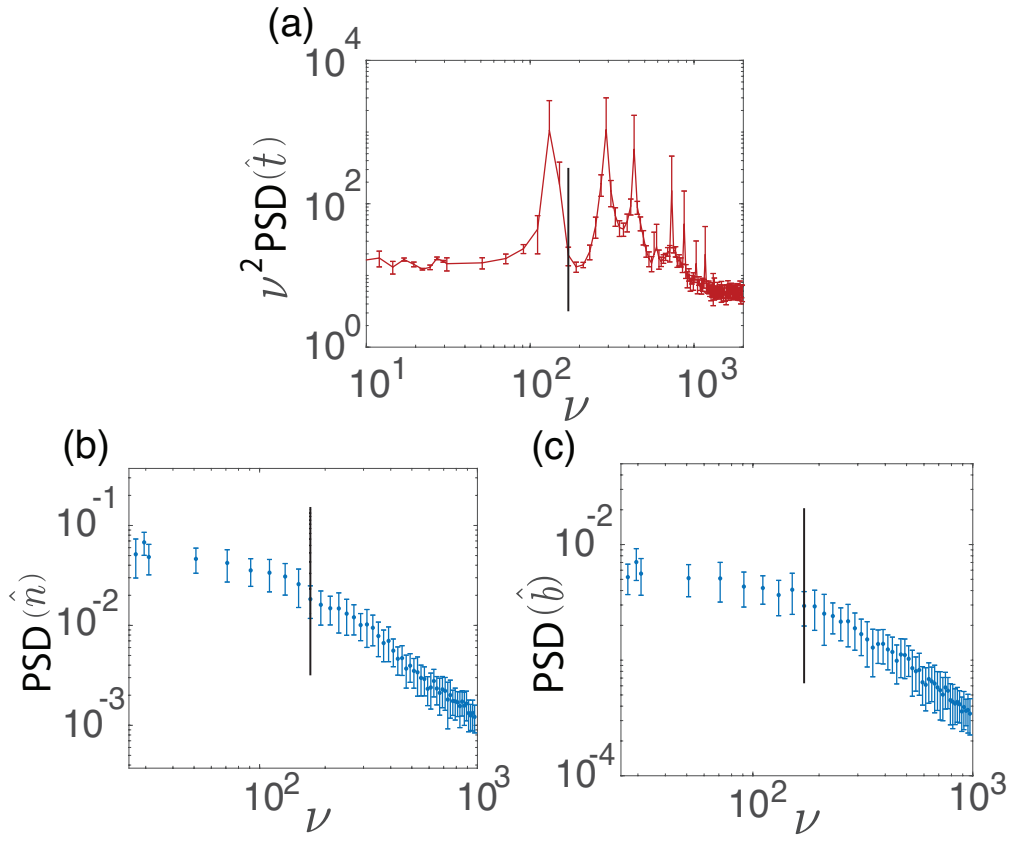

Figure 2.5: Fluctuation power spectra for the three-dimensional model

Fluctuations about the zero-temperature limit cycle were projected onto the co-moving Frenet frame. The stochastic data use noise amplitude given by temperature $\tau_{noise}T = 0.25T$. (a) The frequency-dependent diffusion constant. The spectrum shows peaks, as well as a crossover at the corner frequency (indicated by vertical black line), hinting to both mechanism I and II coupling. (b) The fluctuation power spectral density along $\hat{n}$. (c) The power spectral density of perturbations along $\hat{b}$. Both (b) and (c) exhibit Lorentzian spectra.

This model exhibits new temporal structure in the phase diffusion constant due to effects of *mechanism II*. Both the mean phase velocity and the phase diffusion constant depend on the phase angle. As a consequence, these quantities vary periodically in time as the system follows its limit cycle oscillations. This periodic variation of the phase diffusion constant introduces structure in the diffusion constant at frequencies corresponding to the inverse of the limit cycle period T, *i.e.,* at $\nu_n = 2\pi n/T$, where $n = 1, 2, \ldots$. These features are analogous to the Bragg peaks associated with the Fourier transform of the spatial density in a crystalline structure. Superimposed on these peaks is the *mechanism I* effect observed in the simpler Hopf model. There is a decrease in the effective diffusion constant for frequencies above the corner frequency of the two Lorentzian degrees of freedom for the same reasons as discussed earlier.

2.3.2 Lower dimensional projections

Realistic models of hair bundle dynamics include a number of variables describing the internal state of the hair cell, such as position of the myosin motors along the stereocilia (X_a), the forces they exert on the gating spring, internal calcium dynamics, and others [23]. Currently, most of these variables are not accessible experimentally. Typical recordings are limited to observations of hair bundle mechanics, its oscillation and response to an imposed drive. Recently, recordings of bundle mechanics were combined with electrophysiological recordings of the cell soma, in spontaneously oscillating and driven bundles [34]. This technique allows the simultaneous probing of two variables, the hair bundle position X and the cell membrane potential V_ss. However, even with regard to the simplified biophysical model, discussed in prior section, this still allows access to only two of the three variables, as X_a remains "hidden." The experimentally accessible system is thus a projection of the full dynamical system onto a lower-dimensional manifold.

In our system, we have experimental access (discussed in a subsequent section) to the two dimensional $\mathcal{E} = (X, V_\mathrm{ss})$ plane. To examine the implications of this projection using our numerical model, we start with the three-dimensional noisy limit cycle, and project it

onto the experimental manifold $\mathcal{E}$, as shown in Fig. 2.6. The full three-dimensional limit cycle is shown in light green, and the two-dimensional projection of the numerical simulation is shown in dark green. These curves have been simulated using noise amplitudes determined by Fluctuation-Dissipation theorem at room temperature. The figure also depicts the zero-temperature limit cycle for the three- and two-dimensional systems, in black and gray, respectively. From here on, to ensure consistent comparisons with experimental data, we shall analyze the simulated data in this two-dimensional projection.

2.3.3 Mean vs zero-temperature limit cycle in the biophysical model

The analysis of experimental data introduces another complexity, briefly alluded to in a prior section. The biological problem does not provide access to the noise-free system. While the two were nearly identical in the case of the supercritical Hopf oscillator, in a more complex system, the observable mean limit cycle may be different from the zero-temperature one. In fact, both the size and the shape of the limit cycle may change with the noise amplitude.

We illustrate the noise dependence of the shape of the mean limit cycle (dashed black) in the experimentally accessible manifold $\mathcal{E}$ depicted in the inset of Fig. 2.7. In panel (a), we represent the finite-temperature limit cycle using a density plot, where the regions get denser as the colors traverse from dark blue to light blue to yellow. This is indicative of the phase-dependent properties of the limit cycle. In the inset, we show the deterministic limit cycle (red) and the superposed mean limit cycle (dashed black), with finite noise in all three dynamical variables. As shown in the figure, the mean limit cycle distorts at finite temperature. The noise amplitudes were chosen to represent equilibrium fluctuations at room temperature, as determined by the fluctuation-dissipation theorem. We however note that this choice constitutes a simplification, particularly with respect to the variable reflecting myosin motor activity, where one might reasonably expect both colored noise and noise amplitudes unrelated to the dissipative terms in the equation of motion.

Furthermore, we observe that the zero-temperature limit cycle generally has sharper features – smaller radii of curvature – than the noisy one, as is evident, for example, in

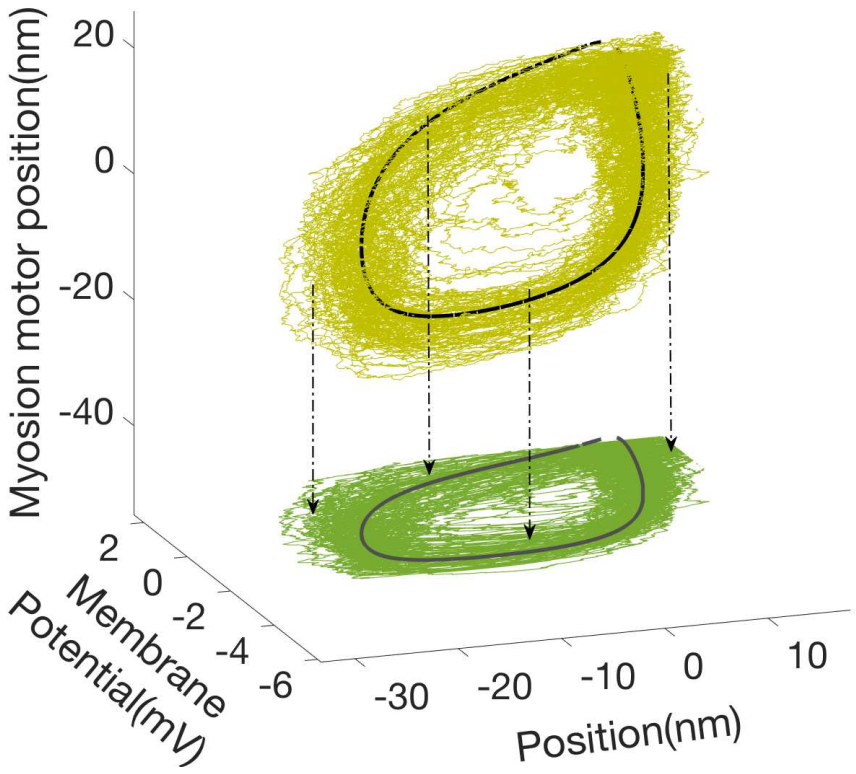

Figure 2.6: Projection onto the experimentally accessible plane

The three-dimensional system contains only two experimentally accessible variables, spanning the $\mathcal{E}$ manifold. Stochastic trajectories (light green curves) about the deterministic three-dimensional limit cycle (black line) are observed only by their projection onto the $\mathcal{E} = (X, V_{\text{ss}})$ plane. The projected trajectories (dark green) show fluctuations about a planar zero-temperature limit cycle (dark gray line). The inner two arrows denote the deterministic limit cycle projections, and the outer two point to the projected stochastic trajectory. To be compatible with experimental data, $\tau_{\text{noise}}/\tau_0 = 1$ for the given simulation, so $< \eta_x >^2$ is $2kT\lambda$ and $< \eta_{x_a} >^2$ is $2kT\lambda_a$.

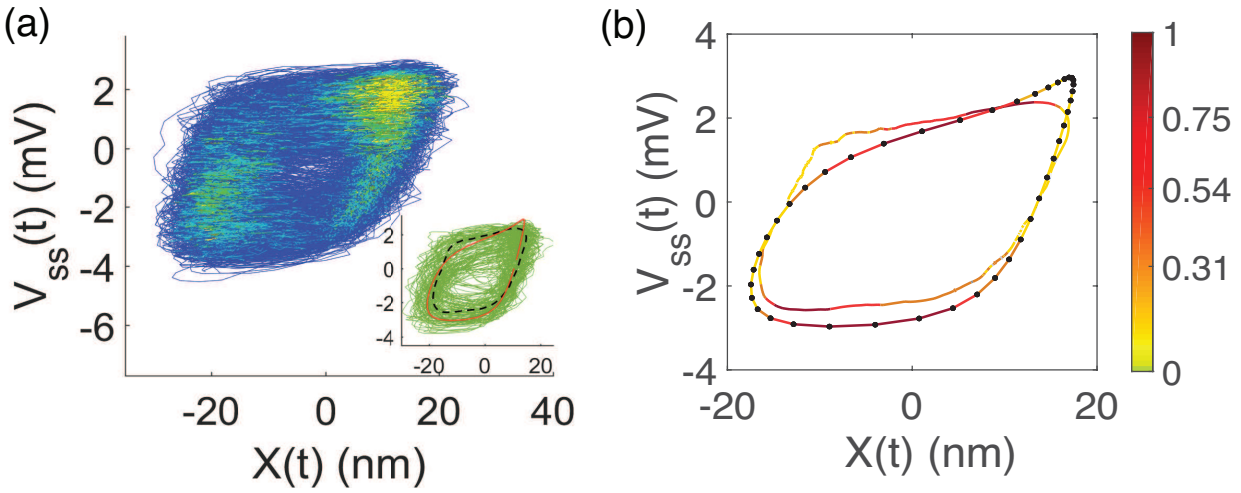

Figure 2.7: Effects of finite temperature

(a) A representative stochastic trajectory of length $t = 1060T$, where T is the mean period, is depicted using a density plot. The less dense regions are in dark blue. Yellow indicates those with the highest density. (Inset) The zero-temperature (red) and mean (dashed black) limit cycle, computed at finite-temperature $T_{eff} = \tau_0 T = T$, are superposed on the stochastic trajectory (green).(b) The mean two-dimensional limit cycle in the $\mathcal{E}$ manifold, for both the deterministic (connected dots) and stochastic (line) systems. The mean velocity of the phase point is denoted by a color map, where yellow (light gray)) color corresponds to lower and red (dark gray) to higher phase velocity. The velocities, as indicated on the color bar, are normalized to the maximum velocity of the hair bundle along its mean cycle, and are hence dimensionless.

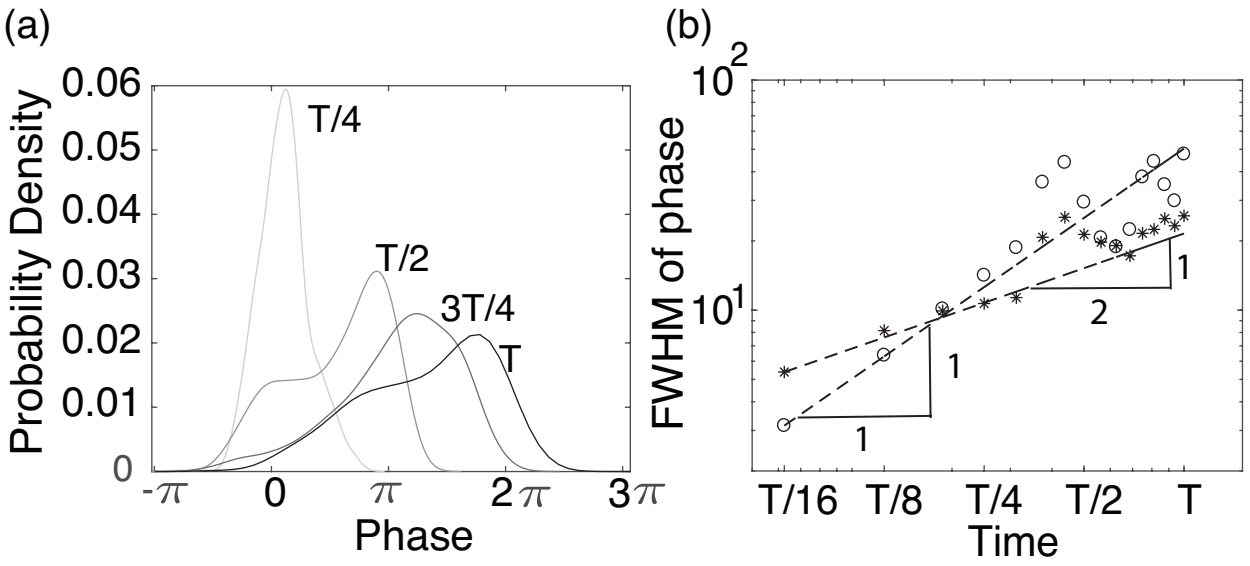

Figure 2.8: Phase diffusion along the limit cycle

(a) The time evolution of an ensemble of systems, synchronized at a fixed but arbitrary initial phase point. (b) The Full Width Half Maximum (FWHM) of the phase distribution is not simply proportional to $\sqrt{t}$. The points represent two data sets, evaluated at time delays of $(T/16, T/8 \ldots 15T/16, T)$, starting from two different initial phase points (shown as stars and open circles). We observe advective and diffusive spreading of the ensembles, as seen by the two slopes of 1/2 and 1.

the upper right corner of the inset in panel (a). This is also noticed in the upper right corner of the limit cycles in panel (b). We delve into the cause for this rounding of the zero-temperature limit cycle by noise in chapter 3. Additionally these sharp corners which lie in the denser regions of panel (a) coincide with the slowing down of the particle. Indeed, we see this from a plot of the mean velocity of the phase points on the limit cycle, illustrated as a heat map superposed on the zero-temperature limit cycle oscillation in panel (b) of Fig. 2.7, where cooler (yellower) colors denote slower speeds.

2.3.4 Phase diffusion and advection give rise to Bragg peaks

We explore the effects of phase diffusion in another way. At time $t = 0$, an ensemble of systems is poised at an arbitrary but fixed phase point on the limit cycle. Each system evolves in time under the action of the stochastic differential equations, Eqs.2.11,2.12,2.13, with noise variances of $2kT \times \tau_{\text{noise}}/\tau_0 = 2kT$. We compute the distribution of their phases (reported in terms of the total phase traversed about the limit cycle) at time delays corresponding to $T/4, T/2, 3T/4, T$, where T is the mean period of the stochastic limit cycle. As shown in panel (a) of Fig. 2.8, the distribution of phase points exhibits an asymmetric spreading. Due to the frequency dependence of the phase diffusion constant, we note that the spreading of the phase distribution is not simply proportional to $\sqrt{t}$, as can be seen in Fig. 2.8(b). This spreading is in fact also impacted by advection, as the ensemble of stochastic systems converge or diverge in the lower and higher velocity regions, respectively. The dominant effect that is observed depends upon the where in the oscillator does the system start and the sequence of regions that it encounters. For example, the open circle ensemble is dominated by advective spreading due to the local change in mean phase velocity along the limit cycle, while the star one is dominated by diffusive spreading. Moreover, we see that the distribution is not a simple Gaussian, as would be expected from a normal advection-diffusion equation. The variation of the mean phase velocity with phase accounts for most of this effect. Finally, we note that, after only one period $t = T$, the width of the phase distribution is comparable to the total phase around the limit cycle (2π). Hence, for this level of noise, the ensemble that was phase synchronized at $t = 0$ is (nonuniformly) distributed around the entire limit cycle after only one period.

A simple criterion can be developed to account for the emergence of phase coherent effects, such as the peaks arising from *mechanism II* effects. Questions regarding phase coherence can be recast into a statement about the ratio of the phase diffusion time $T^\star = \ell^2/D$ to the mean period T. Herein, ℓ refers to the total arclength, measured in units of limit cycle periods, over which the system is coherent. When $T^\star \gg T$, the period of phase coherence is equal to many limit cycle periods, and this phase coherence will result in the appearance of

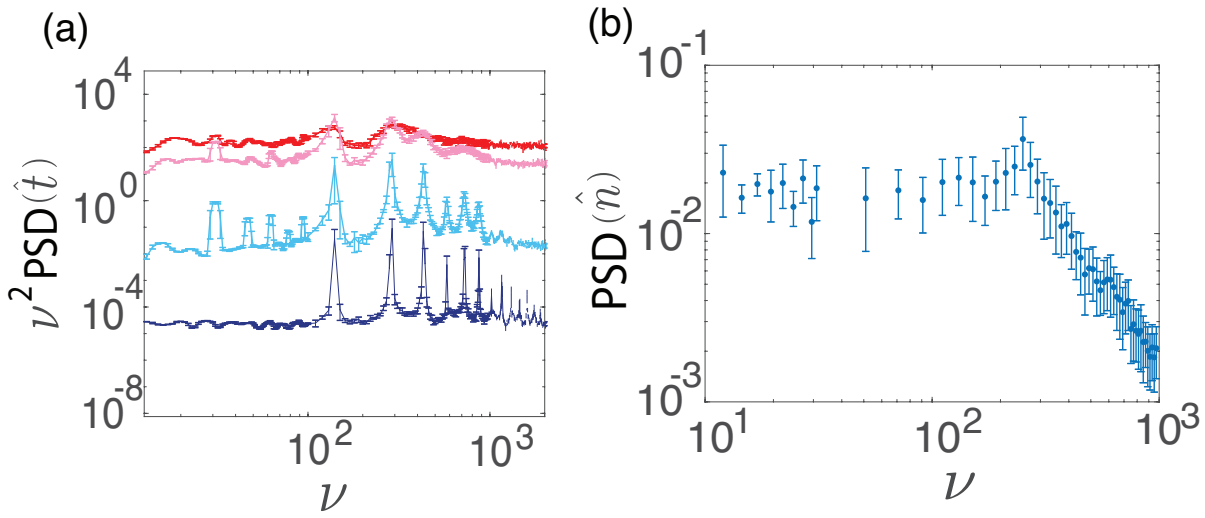

Figure 2.9: Fluctuation spectra of the projected system

(a) Frequency-dependent phase diffusion constant D_{s}, obtained at four different noise variances: $\tau_{\mathrm{noise}}/\tau_0 \times 2kT = 0.005kT, 0.05kT, 0.5kT, 2kT$ (blue (lowest), cyan (second from bottom), pink (second from top), red (topmost)). For $\tau_{\mathrm{noise}}/\tau_0 = 0.0025$, the system is nearly deterministic. Increasing noise amplitude broadens the Bragg peaks, as the system loses phase coherence over a time $T^\star \sim \ell^2/D$. The spectra have been shifted vertically for visibility by multiplying by $(10^{-4}, 10^{-2}, 1, 1)$. (b) In the two-dimensional projection comprising of X,V$_{ss}$, the orthogonal direction is $\hat{n}$. The power spectrum of fluctuations along this direction is Lorenztian.

peaks due to *mechanism II* effects. On the other hand, for sufficiently short phase coherence times $T^\star \ll T$, any periodic structure of the deterministic limit cycle oscillator is lost, and the peaks disappear from the fluctuation spectrum.

We observe this transition in our numerical simulations by adjusting the amplitudes of the noise, while holding the other parameters fixed. The results are shown in Fig. 2.9, where we produced numerical data based on the Eqs. 2.11, 2.12, 2.13 and projected the results onto $\mathcal{E}$. The resulting spectra of the phase diffusion constant, obtained at four different noise levels, are shown in the panel (a). The dark blue curve measures phase diffusion for an effective noise variance of $\tau_{\rm noise}/\tau_0 \times 2kT = 0.005kT$. In this nearly deterministic system, phase coherence, as defined above, is maintained for ~ 40 periods. As a consequence, we observe a full sequence of Bragg peaks. Upon increasing the noise variance to $\tau_{\rm noise}/\tau_0 \times 2kT = 0.05kT$ (light blue), we see that these peaks weaken and broaden. The phase coherence lasts for ~ 30 periods. Only the principal and second peak is observable at $\tau_{\rm noise}/\tau_0 \times 2kT = 0.5kT$ (light pink); these are barely visible at $\tau_{\rm noise}/\tau_0 \times 2kT = 2kT$ (red), as expected from the previous analysis. The time scales over which the system loses phase coherence are equal to ~ 5 and ~ 1 periods, respectively.

2.4 Experimental observations

To test the theoretical predictions from the prior sections, we compare them to experimental observations of hair bundle dynamics. Recordings were obtained from *in vitro* preparations of the bullfrog sacculus, following techniques described in earlier publications [43]. Biological preparations were mounted in chambers that allow optical access to hair bundles, while maintaining their active process [32, 31, 5]. Time traces of spontaneous hair bundle oscillations were obtained from twenty cells, exhibiting a broad range of limit cycle frequencies and amplitudes, as well as variation in the amplitude of the fluctuations about the mean limit cycle. Hair cells were pre-selected that exhibited only one mode of oscillation, hence a single peak in the spectral density; cells that showed more complex multi-mode oscillation were not considered in the current study. The experimental data depicted in Fig. 2.10, 2.12

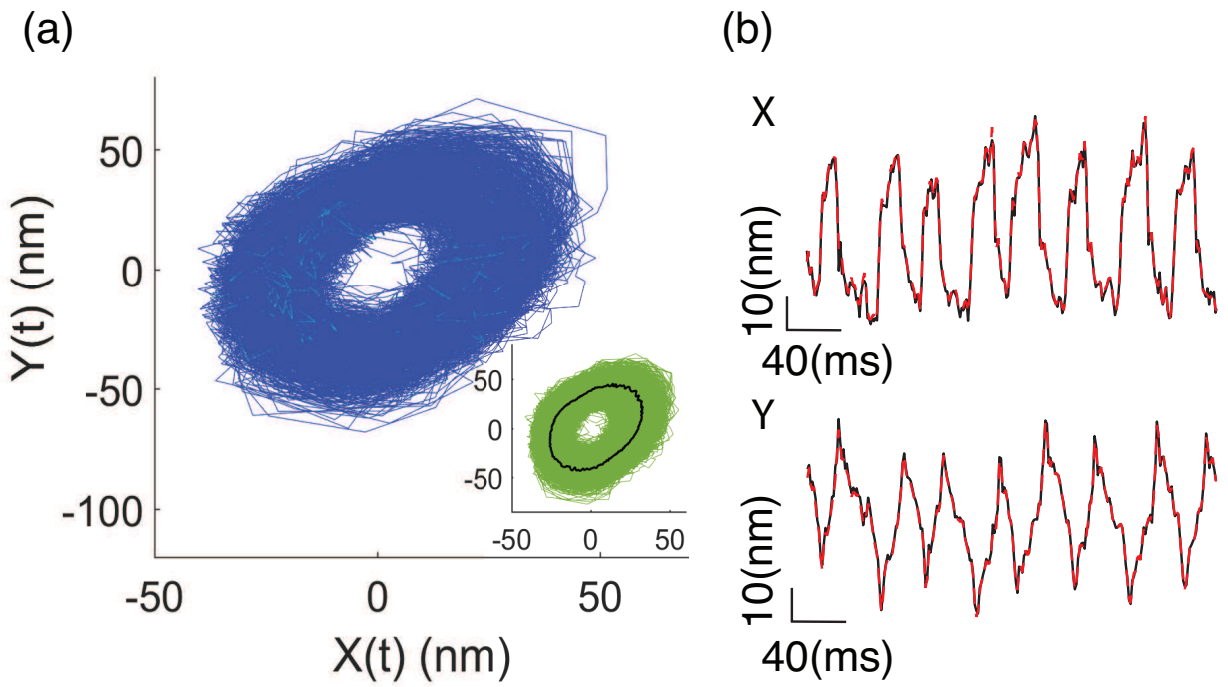

Figure 2.10: Experimental recordings of spontaneous bundle oscillations

(a) Density plot of a typical limit cycle trajectory (blue curve) of a saccular hair bundle in the phase space spanned by bundle position $X(t)$ and its Hilbert transform $Y(t)$. (Inset) Additionally, the superposed averaged limit cycle is shown in black. (b) Experimental recordings of hair bundle position $X(t)$ and its Hilbert transform $Y(t)$ (black curves); the data were corrected for slow drift innate in these biological preparations. The red dashed line show the low-pass filter time series used to construct the limit cycle.

were low-pass filtered at $400 \times 2\pi$ Hz (red-dashed); the Nyquist frequency was $500 \times 2\pi$ Hz.

2.4.1 Comparison to the supercritical Hopf system

The Hopf variables are related to each other by the Hilbert transform, which has previously been used to create the two-dimensional phase space for experimental data [49]. We follow that procedure, and in panel (b) of Fig. 2.10, show the time traces of the hair bundle position and its Hilbert transform. The panel (a) of Fig. 2.10 displays the density plot of the experimentally observed noisy limit cycle (blue). The superposed mean limit cycle (black)

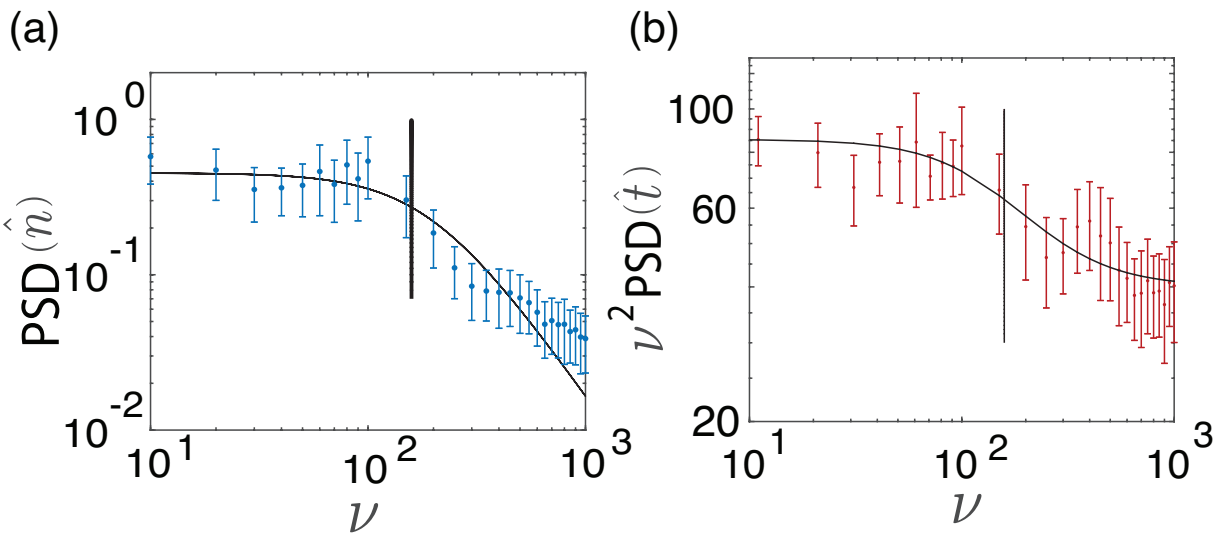

Figure 2.11: Experimental fluctuation spectra

(a) Power spectrum of fluctuations along the local normal to the mean limit cycle, showing a Lorentzian structure. The corner frequency is marked by the vertical black line. Error bars are given by the standard deviation of the mean in each frequency bin. (b) The observed phase diffusion constant showing the *mechanism I* crossover at the corner frequency found from the spectrum in part (a).

is shown in the inset. One observes the uniformity of phase space density which points to the lack of *mechanism II*. A hair bundle that exhibited more irregular oscillation is shown in Fig. 2.15 in subsection 2.6.2.

We next compared these limit cycle oscillations to those obtained from the normal-form equation for the Hopf system (Fig. 4.2). While there are geometric differences in the shape of the experimentally obtained mean limit cycle and that predicted by the Hopf normal form, the power spectra of perturbations, computed along the two directions of the Frenet frames using code in A.11, exhibit similar characteristics, as seen from a comparison of Fig. 2.2 and Fig. 2.11.

In Fig. 2.11, we observe the expected Lorentzian nature of the perturbations orthogonal to the curve (along $\hat{n}$) and the diffusive power spectrum for phase fluctuations. We find the predicted *mechanism I* effect in which the observed phase diffusion constant decreases from a

larger low-frequency value to a smaller high-frequency one. Moreover, the transition occurs at the corner frequency of the Lorentzian fluctuations, corresponding to fluctuations in the direction normal to the mean limit cycle. Hence, the fluctuations of the bundle about its mean limit cycle are in agreement with the prediction of the simple supercritical Hopf system. The study of small deviations supports the applicability of the Hopf oscillator description of hair bundle dynamics, even for the bundles situated deeply within the oscillatory regime.

2.4.2 Comparison to the biophysical model

For direct comparison to predictions based on the more detailed three-dimensional model of the hair cell, we combined measurements of hair bundle displacement with electrophysiological records of the membrane potential. Following techniques previously developed in the laboratory, we patch-clamped the hair cells, under two-compartment configuration, which maintains ionic conditions comparable to those found *in vivo*. These recording conditions maintain the innate bundle oscillations, while providing access to the electrical state of the cell. These measurements were made in current-clamp mode, yielding data on the time-varying membrane potential [34]. The time delay in the voltage recording, due to the pipette resistance and the hair cell capacitance was on the order of ∼1 - 2 ms. We neglect this in comparison to the bundle's time period ∼30 ms.

As mentioned above, there is to date no method of directly accessing internal myosin motor activity. Thus, we compare our experimental findings to the two-dimensional $\mathcal{E}$ plane, which constitutes a projection of the full three-dimensional limit cycle, shown in Fig. 2.6. We further note that fluctuations of this system will be studied as deviations from the mean limit cycle, as the "zero-temperature" limit cycle is not experimentally accessible.

In the inset of Fig. 2.12, we show a typical trajectory of the system in $\mathcal{E}$ spanned by the state variables $(V_{\rm ss}, X)$ (green curve). Superposed is the mean limit cycle indicated with a black line. In the density plot, similar to Fig. 2.7, we notice the non-uniformity of the phase space density, and anticipate the presence of *mechanism II*. Panel (b) shows sample traces of the recorded bundle position and somatic potential.

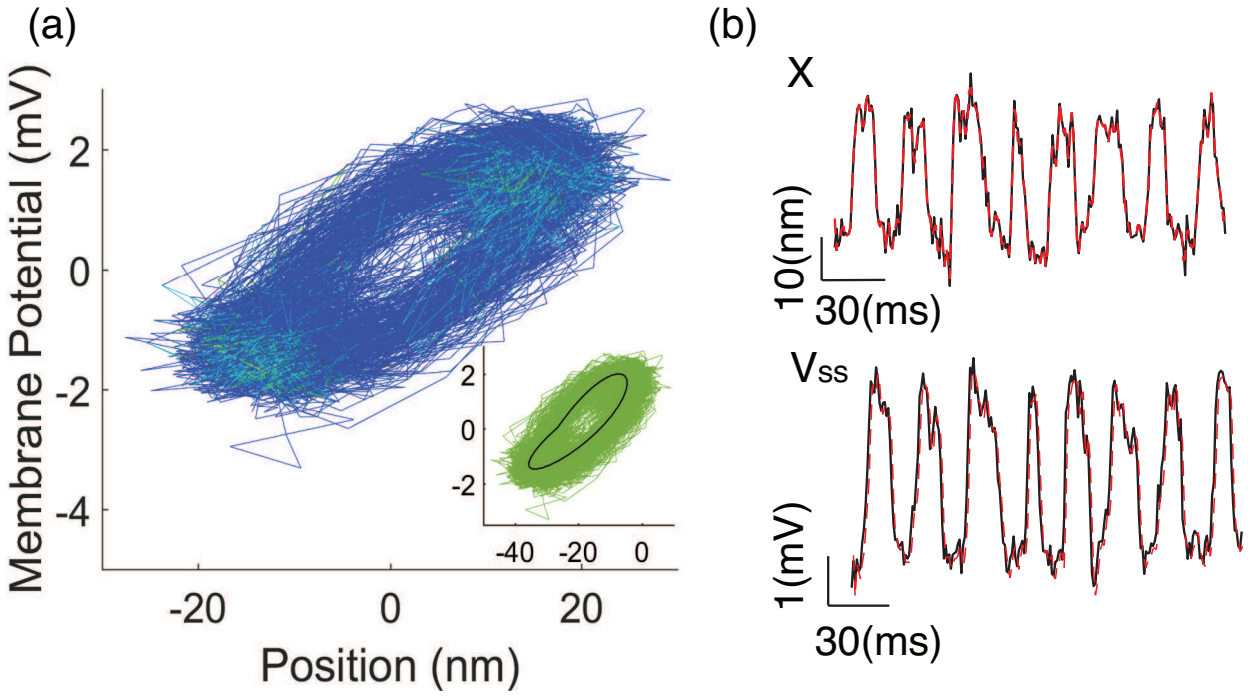

Figure 2.12: Experimental observations of bundle position and membrane potential (a) Density plot of limit cycle trajectory obtained from simultaneous experimental measurements of the bundle position and somatic potential (blue curve). The light blue regions are more densely populated than the dark blue ones. (Inset) The mean limit cycle is superposed as the black curve. (b) Bundle position $X(t)$ and membrane potential $V_{\text{ss}}(t)$ are shown in black. Their low-pass filtered versions are shown as red dashed lines. The resting potential of the hair cell is -67.5 mV, its capacitance is 13.5 pF and the holding current for the current clamp is -2.6 nA.

To explore fluctuation spectra in the experimental recordings, we introduce a Frenet frame associated with the averaged limit cycle and resolve the deviations of the stochastic system from that mean along the local normal and tangent vectors, as done previously. Note that in both Fig. 2.11 and Fig. 2.13, we study the system using the Frenet frame vectors $\{\hat{t}, \hat{n}\}$. However, these systems differ in the experimental variables that are accessed, as the latter includes an independent measurement of $V_{\rm ss}$.

In Fig. 2.13(a), we observe a Lorentzian power spectrum of the fluctuations along $\hat{n}$, consistent with predictions of the numerical model (2.9). We plot the frequency-dependent phase diffusion constant in Fig. 2.13(b), in red. The shapes of the spectra are comparable to those observed with the $\mathcal{E}$ projection of the theoretical three-dimensional model (Fig. 2.9), obtained at noise levels comparable to real systems (red curve). The figure includes a plot of the power spectrum of the total phase traversed along the mean limit cycle (blue), which exhibits distinct maxima at frequencies corresponding to the expected peaks of the phase coherent system, i.e., at the natural frequency and its harmonics. The superposition shows that the broad, barely distinct, peaks in the phase diffusion constant occur at frequencies corresponding to the first and second peaks. This correspondence suggests that the system remains phase coherent over times greater than one period of the limit cycle. We do not observe the *mechanism I* coupling as seen in Fig. 2.5, leading to an overall reduction of the phase diffusion constant at higher frequencies. We return to this point in the discussion.

We may also consider a number of limit cycle oscillators, all starting at an arbitrary but fixed phase point, to explore the phase advection and diffusion about the limit cycle. The results are shown in Fig. 2.14(a), with phase distributions displayed for times $t = T/4, T/2, 3T/4, T$. As can be seen from the figure, phase coherence persists for at least one limit cycle period, which supports our interpretation of the maxima in the phase diffusion constant at frequencies corresponding to the Bragg peaks.

We also examine the mean phase velocity around the limit cycle by collecting data from many cycles of the oscillation and binning the observed phase velocity by the phase. The result is shown in Fig. 2.14(b), where the mean phase speed is shown as a color map super-

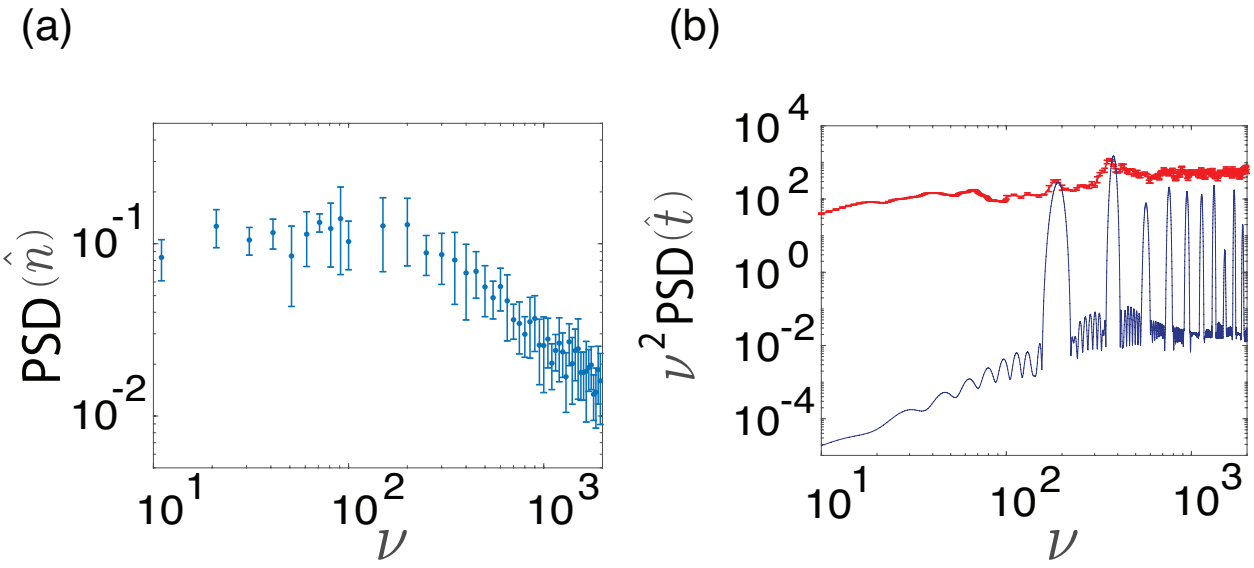

Figure 2.13: Experimental fluctuation spectra

(a) Power spectral density of fluctuations along the $\hat{n}$ direction. (b) Frequency-dependent phase diffusion constant (upper red) along with the Fourier transform of the arclength along the mean limit cycle (lower blue). The "Bragg peaks" of the mean limit cycle appear as less distinct features in the phase diffusion constant, at the natural frequency and its second harmonic, suggesting a *mechanism II* effect.

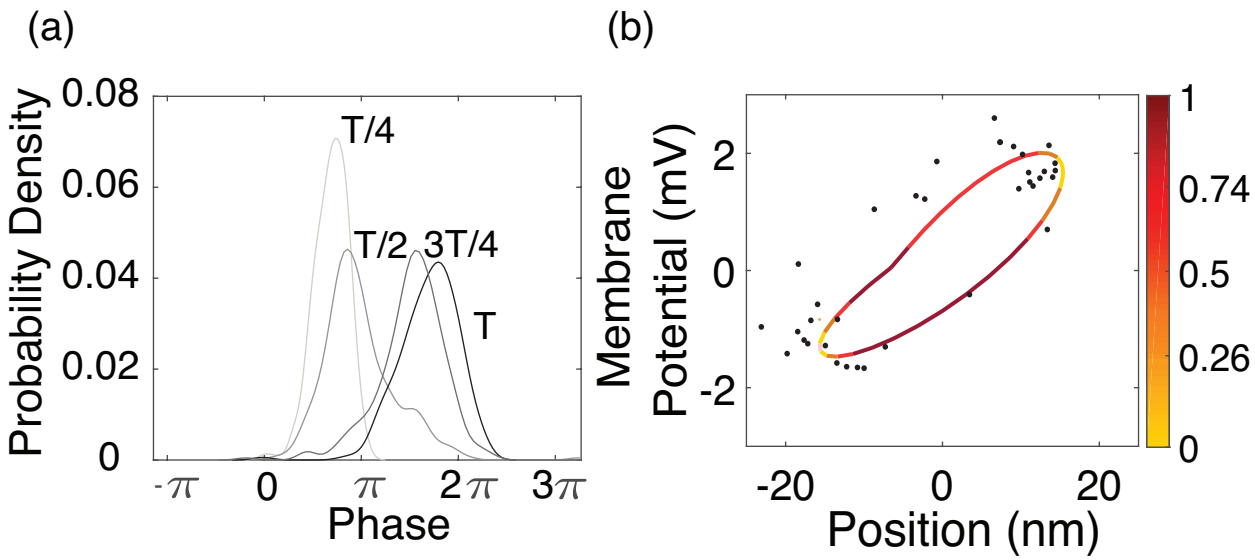

Figure 2.14: Measurements of phase diffusion

(a) The probability distributions of the phase, after time delays of $T/4, T/2, 3T/4$, and T, starting from phase synchronization at an arbitrary point. (b) The experimental mean limit cycle, with the mean phase velocity (normalized to the highest speed) shown as a color map. Redder (darker) colors indicate higher speeds. Data from one cycle of oscillation are shown as black dots. These panels are similar to Fig. 2.8(a) and Fig. 2.7(b) respectively.

posed on an averaged limit cycle, with redder colors representing higher phase speeds. The series of discrete points (black dots) shows the raw data from one typical trajectory around the limit cycle. This method was tested on six data sets obtained from three cells, each held at two different current-clamp values; similar results were obtained from all of the cells. Another example is presented in Fig. 2.19 in subsection 2.6.2.

2.5 Summary

In this chapter, we have proposed that the study of fluctuations of a stochastic limit cycle oscillator is facilitated by the use of a comoving Frenet frame associated with that limit cycle. This method allows one to resolve the observed fluctuations of a d-dimensional system in a natural moving reference frame, which yields a number of advantages. Fluctuations along the local tangent vector and the fluctuations along the $(d-1)$ directions orthogonal to that tangent are predicted to have a simple form, which can be understood in terms of the stability of the limit cycle itself. Namely, the $(d-1)$ orthogonal directions will behave as (potentially coupled) overdamped oscillators, leading to simple Lorentzian fluctuation power spectra. The phase degree of freedom is meanwhile necessarily diffusive due to lack of restorative forces in the tangential direction.

Further, we predict that there are two distinct ways in which fluctuations in a nonlinear, non-equilibrium system can couple, leading to more complex spectra. In *mechanism I*, we allow for coupling between the $(d-1)$ normal fluctuations and the phase fluctuation, leading to a crossover from higher to lower phase diffusion constant. The crossover occurs at the corner frequency of the Lorentzian fluctuation spectrum of the orthogonal degrees of freedom. In *mechanism II*, we find that the confining potential of the orthogonal fluctuations or the mean phase velocity can be phase-dependent. The phase diffusion constant can thus acquire more structure, including local maxima or "Bragg peaks" at frequencies corresponding to the mean period of the oscillator. We verified these ideas through numerical simulations based on both a simple model, the normal form supercritical Hopf model, and a more complex one, a three-dimensional model describing the specific biophysical processes of the hair cell of the

inner ear.

Applying this analysis to experimental data obtained from oscillating hair cells, we find that the supercritical Hopf model not only accurately predicts the mean limit cycle oscillatory behavior, but also describes well the fluctuation spectra normal to the limit cycle and the phase diffusion about it. In particular, we observe strong evidence for the predicted *mechanism I* coupling between the phase and normal fluctuations in the frequency dependence of the phase diffusion constant. Thus, the simplest supercritical Hopf model accurately accounts for both the mean dynamics, and the small fluctuations about that mean. One implication of this result is that the stochastic forces acting on the bundle appear to be adequately described by white noise. If there were just Brownian forces in the surrounding viscous fluid, this point would be unremarkable. However, the total noise in the system must include stochastic effects in various active elements, which may generate colored noise. Our results then constrain the frequency dependence of such stochastic forces acting on the Hopf model of the bundle.

The symmetry of the Hopf model precludes a *mechanism II* coupling here. We do not observe it in either the model (Fig. 2.2) or in the experimental data (Fig. 2.11). On the other hand, when we examine the more complete data sets, combining cell potential and bundle deflection, we do not observe (in Fig. 2.13) significant effects of *mechanism I* coupling between the normal and phase variables. Such a coupling is only weakly seen in the full 3d model (Fig. 2.5). When we project the full model onto the experimentally observable plane - see Fig. 2.9 - the evidence of the *mechanism I* coupling vanishes. The projection to the $\mathcal{E}$ plane appears to mask the frequency structure of the *mechanism I* coupling in the phase diffusion. Because of that projection, the tangent and normal vectors to the observable but projected limit cycle are superposition of the true Frenet frame vectors associated with the limit cycle of the full dynamical system. We speculate that this projection onto the experimental manifold $\mathcal{E}$ also masks the effect of the *mechanism I* coupling in the experimental data - see Fig. 2.13.

This analysis suggests new experiments that may be designed to probe the changes in the fluctuations and shape of the limit cycle in response to the variation of various model

parameters. The most pertinent would be an analysis of the change in the limit cycle in response to perturbations in myosin motor activity. Possible avenues include modulation of myosin activity through pharmacological manipulations, specifically, interference with its phosphorylation pathway, or modulations of the calcium concentration. Other experimental perturbations include variation of the temperature of the biological system, loading the bundle with an elastic element, and interference with the fluctuations of the membrane potential.

Finally, we note that there is growing interest in understanding the thermodynamics of nonequilibrium steady states. For example, there have been proposed generalization of the fluctuation-dissipation theorem [50] to nonequilibrium, but time-independent states. Considerations of out-of-equilibrium systems near a stationary fixed point have led to generalized fluctuation-dissipation theorems (GFDTs) [42, 13]. We will in the chapetrs 3 and 4 build on this previous body of work to analyse the obedience of such generalized theorems by hair bundles in their spontaneously oscillating regime.

2.6 Appendix

2.6.1 Simulation details

The stochastic simulations of Eq. 4.1 were carried out using the 4^{th}-order Runge-Kutta method for a duration of 60 s. The corresponding time steps were in the range of $10^{-4} \leftrightarrow 2 \times 10^{-3}$ s. The experimental data were obtained with time steps of 10^{-3} and 2×10^{-3} s.

Experimentally, the variance of the noise experienced by the hair bundle, normalized by the square of its drag coefficient ($\frac{2k_BT}{\lambda}$), is of the order of $3 \times 10^{-6} \frac{nm^2}{s}$, while amplitudes of spontaneous bundle oscillation typically vary from $10 - 50$ nm. The noise variances A_{ij} in the Hopf simulations were varied from $10^{-7} \leftrightarrow 0.4$, with bundle oscillation amplitude fixed at 1; consistent results were obtained over the full span of noise amplitudes. Fig. 4.2 employs the highest variance value in this range. The stochastic terms driving $\{x(t), y(t)\}$ were assumed to be uncorrelated. This assumption may be relaxed in future work.

Table 2.1: Model Parameters

Symbol	Values	Parameter
K_{gs}	750 μN·m^{-1}	gating spring constant
D	62.1 nm	gating compliance
K_{sp}	600 μN·m^{-1}	stereociliary pivot spring
γ	0.14	geometric coefficient
$F_{\max}$	500 pN	maximal force exerted by adaptation motors
P_0	0.63	probability of channel opening
α	0.8	Ca^{2+} feedback on motors
ω_v	$2\pi \times 20$ Hz	frequency of voltage oscillations, without the MET current
Q_v	30	quality factor in the absence of MET current
C_m	14 pF	capacitance of a hair cell
β_0	ω_v·C$_m$·Q$_v$$^{-1}$	damping coefficient in the absence of MET current
g_t	1.5 nS	conductance of transduction channels
V_0	-55 mV	resting potential of the cell
I_0	10 pA	leakage current
λ	2.8 μNs·m^{-1}	bundle drag coefficient
λ_a	10 μNs·m^{-1}	motors drag coefficient
k_B	1.38×10^{-23} m^2·kg·s^{-2}·K^{-1}	Boltzmann constant
T	300 K	Room temperature
N	50	Number of stereocilia
ΔG	10 k_BT	Intrinsic energy change on channel opening

These parameter values were obtained from references [36] and [37].

Eqs. 2.11, 2.12, and 2.13 were integrated using the Euler-mayurama method for a duration of 60 s using time steps of $5 \times 10^{-4} \leftrightarrow 10^{-3}$ s. The noise statistics of the bundle and myosin motors were assumed to follow white Gaussian ensembles with zero means and variances of $\{2k_BT\lambda, 2k_BT \times 1.5\lambda_a\}$, respectively [36]. Further, P_0, the opening probability of the channels is given by :

$$P_0 = \frac{1}{1 + Ae^{-(X-X_a)/\delta}} \tag{2.14}$$

$$A = e^{(\frac{[\Delta G + (K_{gs}D^2)/(2N)]}{k_BT})} \tag{2.15}$$

$$\delta = Nk_BT/(K_{gs}D) \tag{2.16}$$

The values of the parameters used in the simulations are given in Table 2.1. the reader may find the relevant codes attached in the "Code" chapter of this book. All simulations were performed in MATLAB (R2017a, the MathWorks, Natick, MA).

2.6.2 Experimental data

Significant cell-to-cell variation was observed in both the mean limit cycles exhibited by active hair bundles and in the fluctuations about those limit cycles. In the main text, we show a representative data set for a cell that showed relatively regular oscillations. A number of cells showed less regular limit cycles; we show here a data set representative of this type of cell. By irregularity we imply hair bundles exhibiting a broader peak in their position power spectra. In this case, rather than forming a ring, the trajectories about the limit cycle appear to fill a disk, as shown in Fig. 2.15.

Despite the more noisy limit cycle dynamics, one can extract the fluctuations along the local normal $\hat{n}$ and local tangent $\hat{t}$ to the averaged limit cycle. The power spectra of the fluctuations are shown in Fig. 2.16. The corresponding data set, is filtered with a cut-off at $225 \times 2\pi$ Hz; the Nyquist frequency is $250 \times 2\pi$ Hz. We note that the fluctuations in the normal direction (blue) are still well described by a simple Lorentzian (black) and obtain a corner frequency from this fit, which is denoted by the black vertical line. The phase diffusion constant shows, however, only a weak frequency dependence. The *mechanism I*

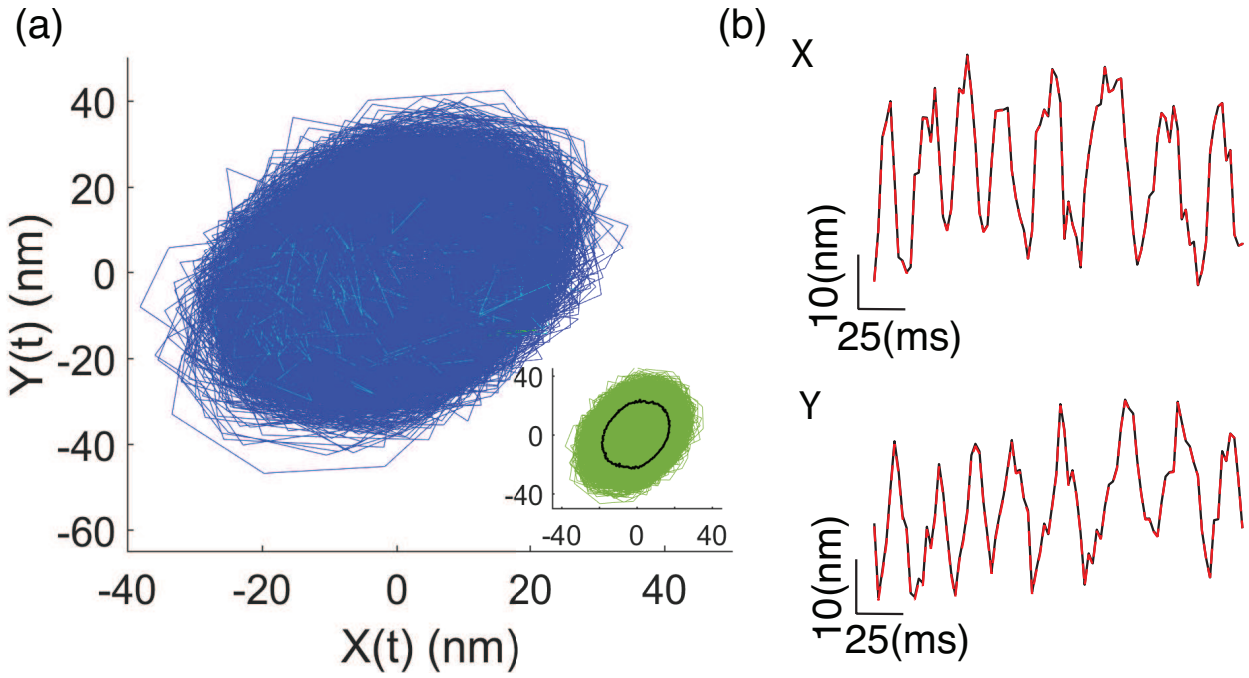

Figure 2.15: Experimental recording of an irregular oscillator

(a) Density plot of a typical trajectory and (in inset) a superposed averaged limit cycle (black) for a cell showing less well defined limit cycle dynamics. (b) Time series of the bundle position and velocity (obtained via a Hilbert transform) after low-pass filtering.

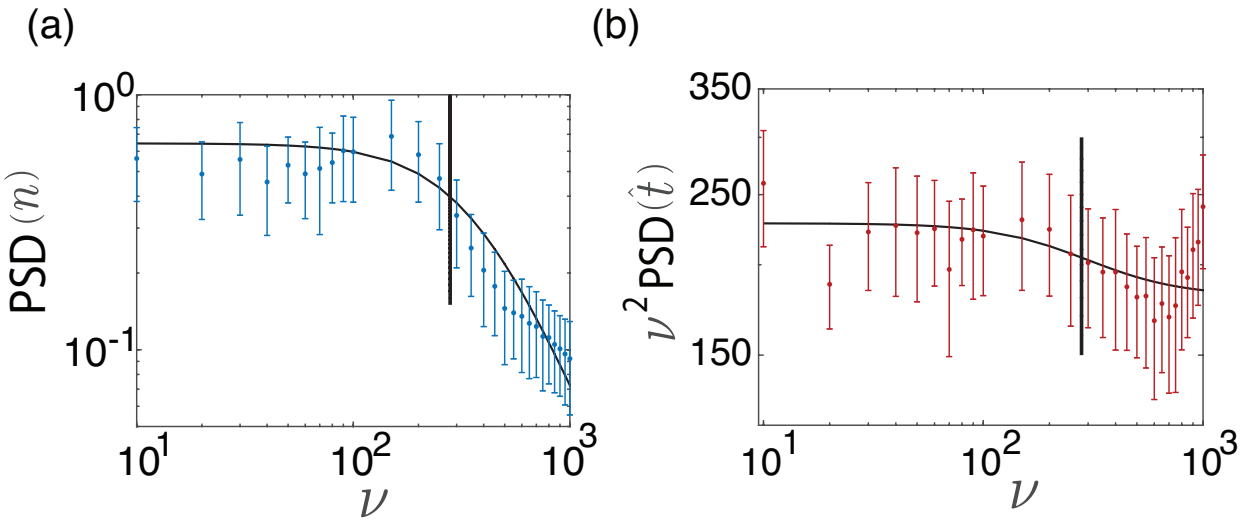

Figure 2.16: Fluctuation spectra of an irregular oscillator

(a) Power spectrum of the fluctuations in the normal direction (blue), along with a best fit Lorentzian (black). (b) Frequency-dependent phase diffusion constant. In both panels, the vertical (black) line indicates the corner frequency.

transition from a larger to a smaller diffusion constant at the corner frequency is, at best, suggested by these data.

We find similarly large cell-to-cell variations in the dynamics of hair cells when we obtain both bundle position and membrane potential. Another example of a bundle (green) described experimentally by its position and membrane potential is shown in the inset for Fig. 2.17, along with its averaged limit cycle (black). The respective density plot is also illustrated. Once again, we obtain similar power spectra for fluctuations in directions normal and tangent to this averaged limit cycle. The spectra are shown in Fig. 2.18. The phase diffusion dynamics obtained from the noisier cell were comparable to those shown in the main text - see Fig. 2.19.

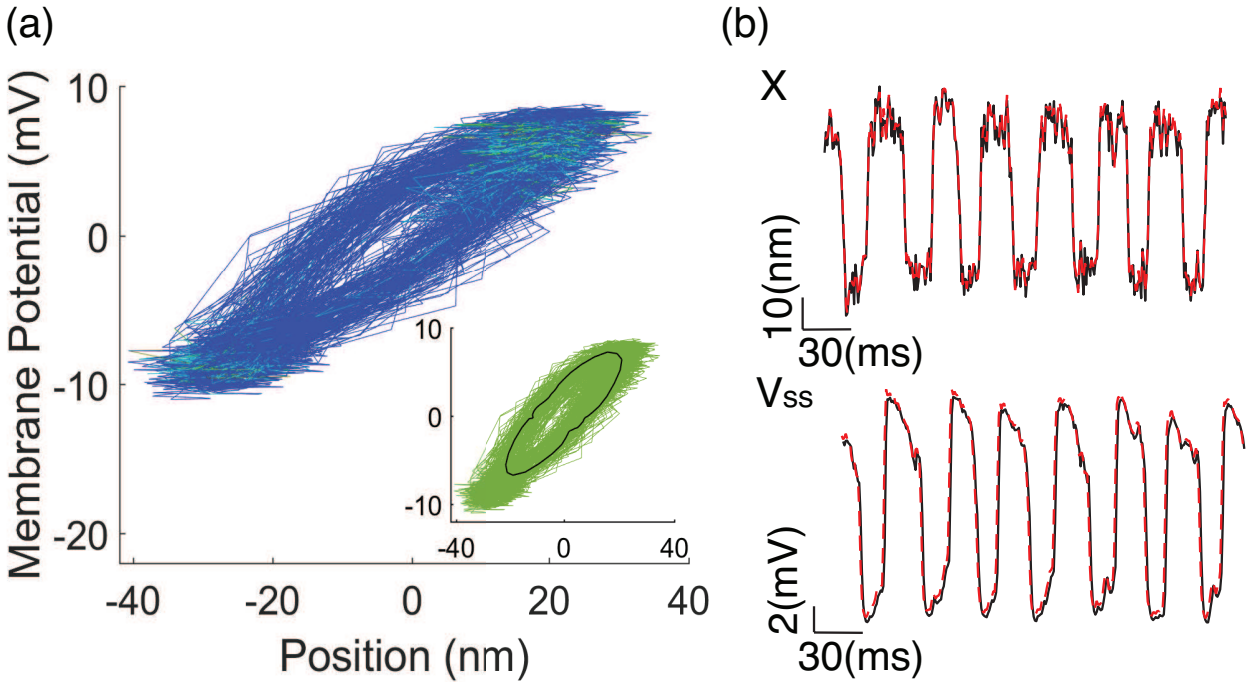

Figure 2.17: Experimental recordings of a noisy hair cell

(a) Density plot of the stochastic trajectory (blue) with (in inset) the superposed averaged limit cycle (black) in the space spanned by bundle deflection X and membrane potential V_{ss}. The dark blue regions are less populated than the light blue ones. (b) Time series of these dynamical variables, without (black) and with (red) low-pass filtering. The resting potential of the hair cell is -31 mV, its capacitance is 11 pF and the holding current -1.5 nA.

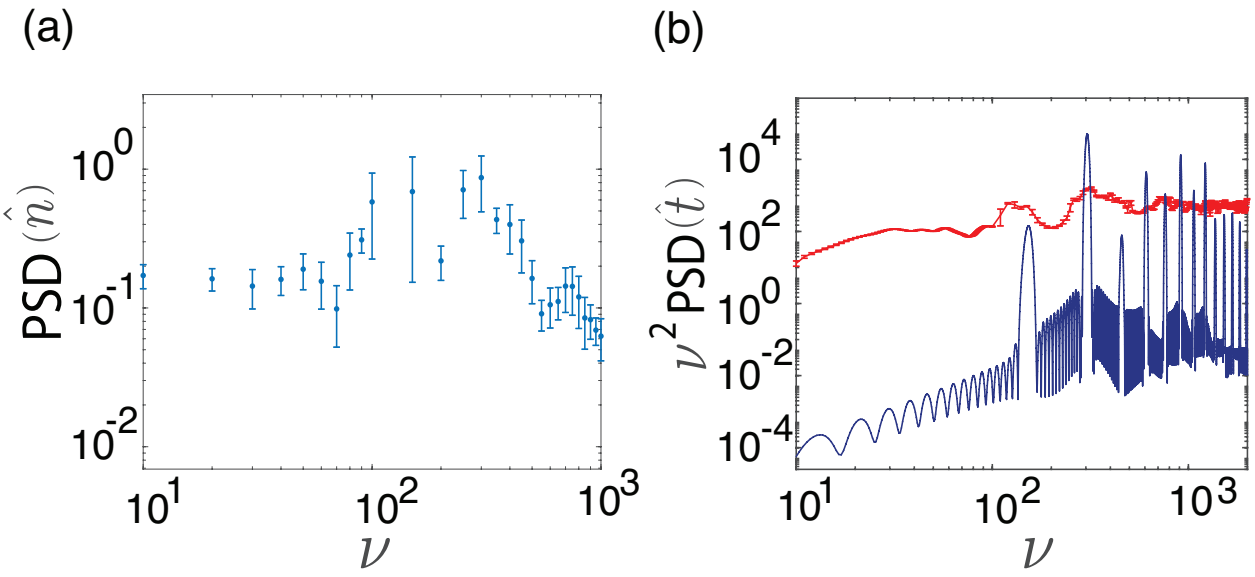

Figure 2.18: Experimental fluctuation spectra

(a) Power spectrum of fluctuations normal to the limit cycle. (b) Phase diffusion constant, exhibiting broad peaks at the natural frequency of the bundle and its second harmonic. The power spectrum (upper red) is qualitatively similar to that observed in simulations in Fig. 2.9(a) with noise variance of $2kT \times \tau_{\text{noise}}/\tau_0 = 2kT$. The power spectrum (lower dark blue) of the total phase traversed by the system along the average limit cycle is shown to locate the expected peaks.

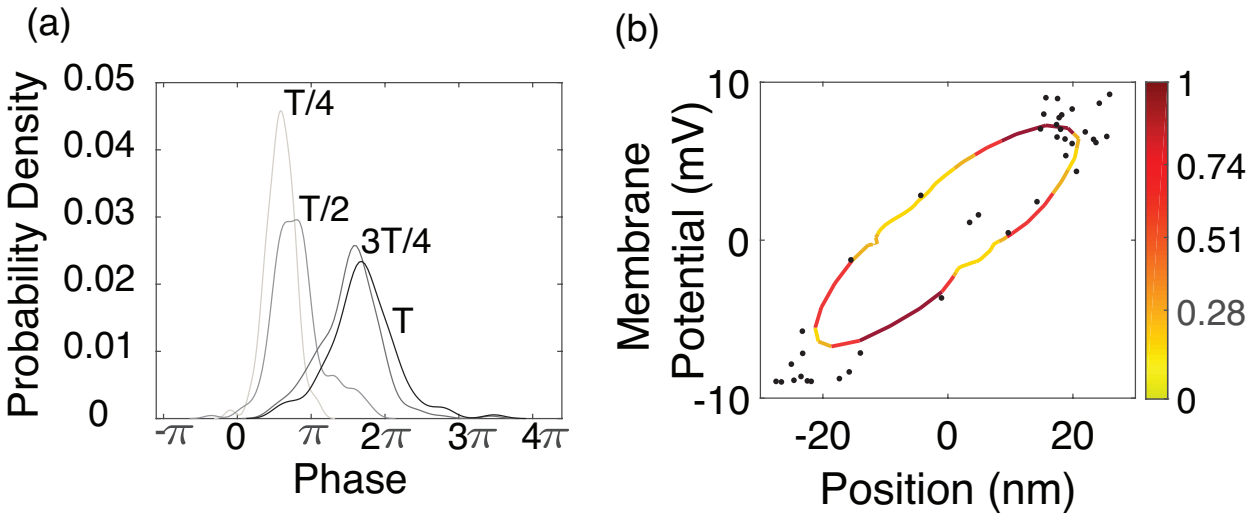

Figure 2.19: Phase diffusion for noisy hair cell

(a) The probability densities of initially phase synchronized ensembles, illustrating phase diffusion. As in the prior case, phase coherence persists over at least one limit cycle. (b) Mean limit cycle velocities shown as a color map on the mean limit cycle with (dimensionless) velocity increasing from colder (light yellow) to warmer (dark red) colors.

CHAPTER 3

Noise-induced distortion of the mean limit cycle

3.1 Introduction

There has been a growing interest in studying how noise affects the dynamics of limit cycle oscillators [38]. In this chapter we explore how the mean limit cycle of a stochastic system differs from the deterministic or *zero-temperature* limit cycle of the underlying dynamical system, for example in Fig. 2.7 as shown in the previous chapter. By doing so, we are able to glean whether noise leads to significant discrepancies between the experimentally accessible dynamics and deterministic theoretical models.

While the complex, more biologically relevant inner ear models allow for direct comparisons between numerical predictions and experimentally accessible observables, they also necessarily include a large number of fitting parameters and generally have higher dimensional limit cycles, as they account for more dynamical variables. For example, even the relatively sparse model of 2.3 that explicitly incorporates stereociliary position, myosin motor activity, and the somatic membrane potential [52] includes many more biologically relevant parameters than the simple two-dimensional models based on the Hopf bifurcation. But given that the experimental records are necessarily stochastic, and typically limited to only a fraction of the total set of dynamical variables in these complex models, the presence of many free parameters in a model raises questions regarding how to appropriately fit the data. There is an inherent trade off between constructing biologically realistic models and limiting the number of free parameters.

In this context we argue that the generic effect of noise on the limit cycles of dynamical systems is to smooth out the more sharp (high curvature) parts of the trajectory. We have

previously observed this effect, in the experimentally accessible manifold of the complex hair bundle biophysical model (see Fig. 2.7(b) and the inset of Fig. 2.7(a)). Introduction of stochastic fluctuations not only caused the trajectories to vary from cycle to cycle, but also changed the shape and size of the mean limit cycle. Reproducing the phenomenon again in Fig. 3.1 one can clearly notice the difference between the deterministic limit cycle (red) and the average (dashed black) of the hair bundle's stochastic trajectory (green), modeled using noise values corresponding to equilibrium fluctuations at room temperature [52].

This smoothing effect will necessarily impose an upper bound on the useful level of complexity of numerical models, as detailed features underlying the complex limit cycles in phase space become experimentally inaccessible. We explore the causes for the rounding of the zero-temperature limit cycle that makes unavailable to experimentalists the sharper features of the deterministic system. To investigate this question quantitatively, we focus on a generalization of the simple 2d Hopf oscillator, to which we introduce terms to add finer structure to the shape of the deterministic limit cycle. We observe how these fine details deform in the presence of stochastic forces and also demonstrate a methodology to determine from the model which of its features are most susceptible to experimental noise. By using this information, one should be able to more meaningfully decide on the suitability of various nonlinear models for interpreting one's data.

The remainder of this chapter is organized as follows. In section 3.2, we detail a two-dimensional regular Hopf oscillator in the stably oscillating regime. In section 3.3, we analyze the generalized version and illustrate the effects of stochasticity and of the internal active drive. Finally, we conclude in section 3.4, where we review the differences between the experimentally accessible trajectory and the theoretical model.

3.2 Regular Hopf oscillator

The supercritical Hopf oscillator is the lowest dimensional system ($d = 2$) that admits limit cycle oscillations. The normal form of this dynamical system can be described in terms of

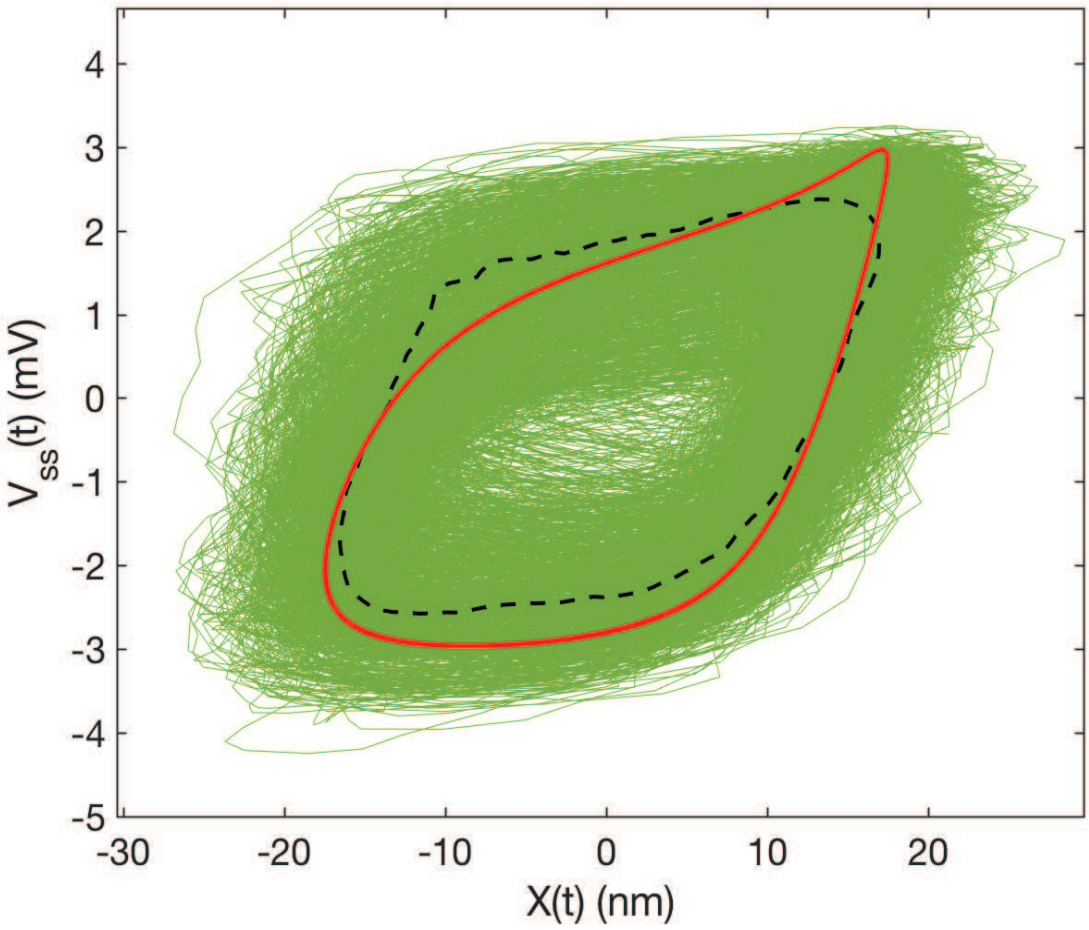

Figure 3.1: Stochastic trajectories of the hair bundle model

A representative stochastic trajectory (green) superimposed upon the deterministic (red) and mean (dashed black) limit cycles. The noise amplitude is by room temperature and the fluctuation-dissipation theorem $2k_BT\lambda$, with viscosity λ. This figure exemplifies the effect of noise that we study in this manuscript. For more details see Ref. [36].

the generalized position variable, $Z(t) = X(t) + iY(t)$, obeying the differential equation

$$\dot{Z} = Z\left(\mu - i\omega\right) + bZ|Z|^2 + \eta_Z \tag{3.1}$$

The dynamics of the deterministic system depend on the model parameters $\{\mu, \omega, b\}$. For $\mu > 0$, the stable solution is given by the limit cycle of radius $R_0 = \sqrt{\mu/b}$ and oscillation frequency ω. To fully specify the model, we introduce the stochastic force term η_α, where $\alpha = X, Y$ are the Cartesian coordinates. The complex noise amplitude discussed in Eq. 4.1 is related to these two noise terms by $\eta_Z = \eta_X + i\eta_Y$. Here and throughout this study, we assume that this noise is uncorrelated, Gaussian white noise with a vanishing mean and the second moment given by

$$\langle \eta_\alpha(t)\eta_\beta(0)\rangle = 2T\delta_{\alpha\beta}\delta(t), \tag{3.2}$$

where $\alpha = X, Y$. We introduce T as the amplitude of the white noise. We note, however, that in many systems, and in hair cells in particular, the noise may be nonthermal. This does not affect our results as long as those nonthermal noise sources are not strongly correlated in time. Even in that case, we expect that our qualitative results are not strongly dependent on the assumption of such frequency-independent noise amplitudes. However, our results do depend critically on the assumption that the noise amplitude not be too anisotropic. Strongly anisotropic noise could result in a new pattern of noise-induced deformations of the limit cycle distinct from those discussed here. Similarly, cross correlations between the noise in the x and y channels may result in unique stochastic behavior not accounted for here.

3.2.1 Scalar and vector potentials of the Hopf oscillator

We remind the reader that the trajectories of these nonlinear dynamical systems may be thought of as the classical motion of an overdamped particle in d dimensions, moving in response to a force field. For a two-dimensional system, the force field may be decomposed into the gradient of a scalar potential, which may be interpreted as the potential energy landscape for the system, and the curl of a vector potential. It is this latter nonconservative force that provides the drive allowing stable limit cycles to exist. The parameters $\{\mu, \omega, b\}$

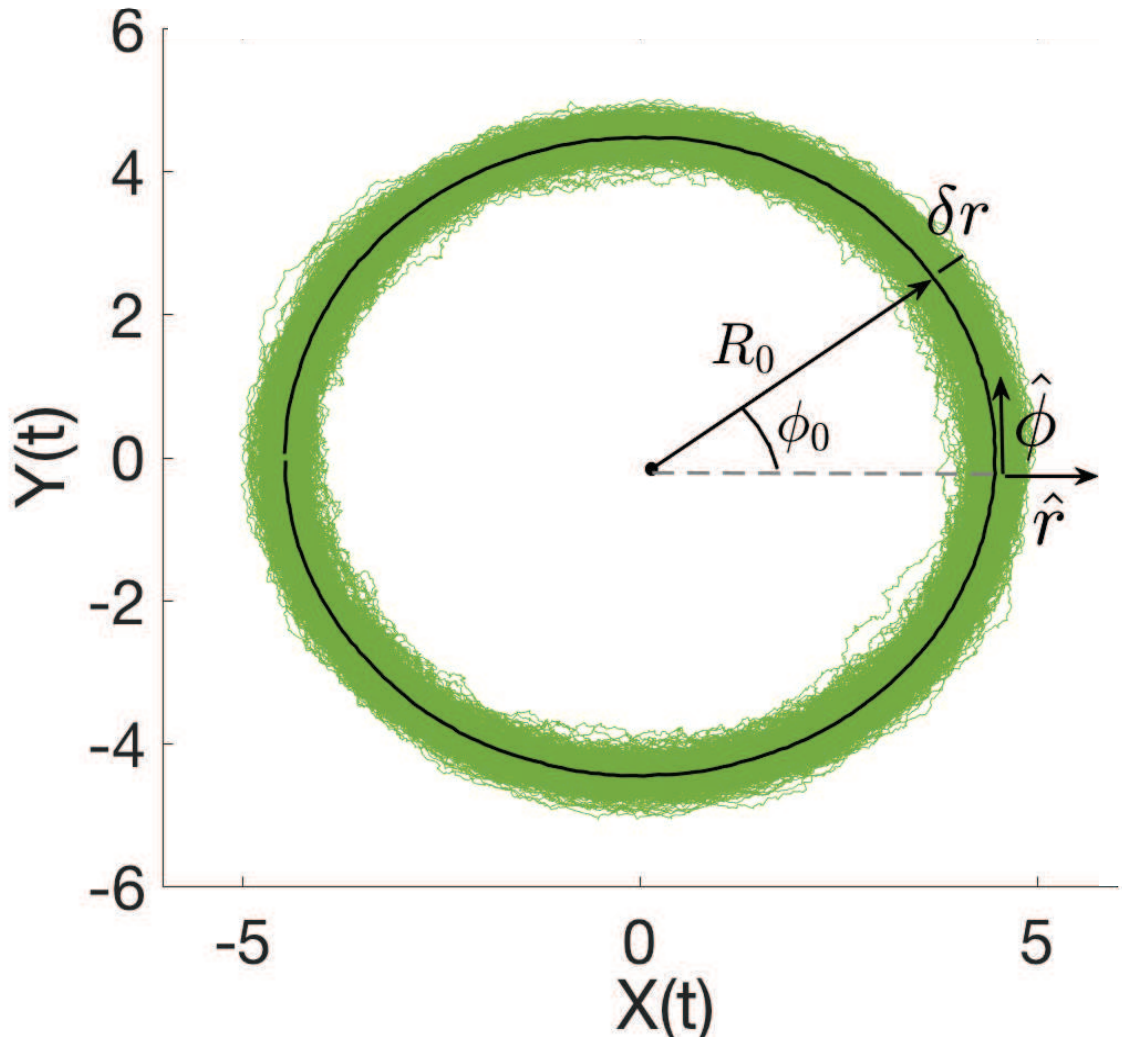

Figure 3.2: Numerical simulation of the stochastic Hopf oscillator

Calculations were performed using Eq. 4.1. (A) The finite-temperature (light blue) trajectories and the mean (red) limit cycle. (B) A typical time series (black) of the stochastic dynamics of $X(t)$ and $Y(t)$.

may be used to define the scalar (ϕ_s) and vector (ϕ_v) potentials of the system from which one may derive the conservative and nonconservative forces. Shortly we will introduce new features into the Hopf oscillator model by changing the landscape of effective potential.

The system of dynamical equations given by Eq. 4.1 can also be expressed in terms of a two-dimensional vector $\mathbf{X}(t) = X(t)\hat{x} + Y(t)\hat{y}$ obeying overdamped motion in a force field $\mathbf{f}(\mathbf{X})$:

$$\dot{\mathbf{X}} = \mathbf{f}(\mathbf{X}) \tag{3.3}$$

$$\mathbf{f}(\mathbf{X}) = \nabla\phi_s(\mathbf{X}) + \nabla \times \phi_v(\mathbf{X}) \tag{3.4}$$

The existence of such a decomposition of the generic vector field $\mathbf{f}$ is assured by Helmholtz's theorem. For the specific case of the Hopf system introduced in Eq. 4.1, the scalar and vector potentials may be simply computed:

$$\phi_s = -\frac{\mu(X^2+Y^2)}{2} + \frac{b(X^2+Y^2)^2}{4} \tag{3.5}$$

$$\phi_v = -\frac{\omega(X^2+Y^2)}{2}\hat{z}. \tag{3.6}$$

The scalar potential has one of two forms depending on the sign of μ. For negative values, the potential has a single minimum at the origin, and the deterministic dynamical system has a single fixed point. For positive μ, the origin is a local maximum of the scalar potential, and a new set of local minima appear on the circle of radius $R_0 = \sqrt{\mu/b}$ about that center. This form of the potential is the well-known "Wine bottle' shown in Fig. 3.3 . For finite values of the drive $\omega > 0$, we observe that the curl of the vector potential $\mathbf{f}_v = \nabla \times \phi_v$ is tangent to the circular ring. It drives the $\mathbf{X}$ variable anticlockwise along the limit cycle, defined by the circular ring of minima. The transition between the stable fixed point and the stable limit cycle of angular velocity ω occurs at $\mu = 0$ and is known as the supercritical Hopf bifurcation.

Turning to the motion of the stochastically driven system, we observe that, across a range of noise amplitudes, the trajectories remain constrained to the trough of the scalar potential at $R_0 = \sqrt{\mu/b}$ that stabilized the deterministic limit cycle. Because the scalar potential is

locally symmetric for positive and negative radial displacements from the limit cycle and since the vector potential has no radial component, the mean limit cycle of the stochastic system is identical to the deterministic one. Fig. 3.2 illustrates these stochastic dynamics.

In Fig. 3.2A, we show a representative trajectory (light blue) superposed upon the mean limit cycle (red). We plot in Fig. 3.2B typical $X(t), Y(t)$ traces, as might be obtained from hair cell data. Herein, $\mu = 80, b = 1, \omega = 200$, and the details of the simulation are described in Appendix A. The mean limit cycle for the finite-temperature system is computed by binning the phase space $\{-\pi, \pi\}$ into 200 bins and averaging over multiple trajectories. For this simple model of a Hopf oscillator, the average cycle is similar to the deterministic limit cycle, due to the high symmetry of the system. When the potential landscape of the system is more complex (i.e. exhibits lower symmetry), this correspondence between the mean and deterministic limit cycles no longer holds. We study the lower-symmetry, generalized Hopf system in the next section.

3.3 Generalized Hopf oscillator

3.3.1 Model and dynamical phase diagram

To explore the effects of noise on the mean limit cycle, we add symmetry-breaking terms to the Hopf oscillator by changing the scalar potential ϕ_s.

$$\phi_s = -\frac{\mu(X^2+Y^2)}{2} + \frac{b(X^2+Y^2)^2}{4} + \alpha cos(n\theta) e^{-(\sqrt{X^2+Y^2}-\sqrt{\frac{\mu}{b}})^2} \tag{3.7}$$

$$\phi_v = -\frac{\omega(X^2+Y^2)}{2}\hat{z} \tag{3.8}$$

The modulation introduces n local maxima (and an equal number of local minima) to the scalar potential that remove the azimuthal symmetry present in Eq. 4.4. By tuning the radial position of those extrema to the center of the circular trough of the Hopf potential, we force trajectories near the previous limit cycle to deform and can control that deformation by the strength of the perturbation α. Here, we consider the case of a four-fold potential landscape, $n = 4$, but we believe that none of the results shown below depend critically on

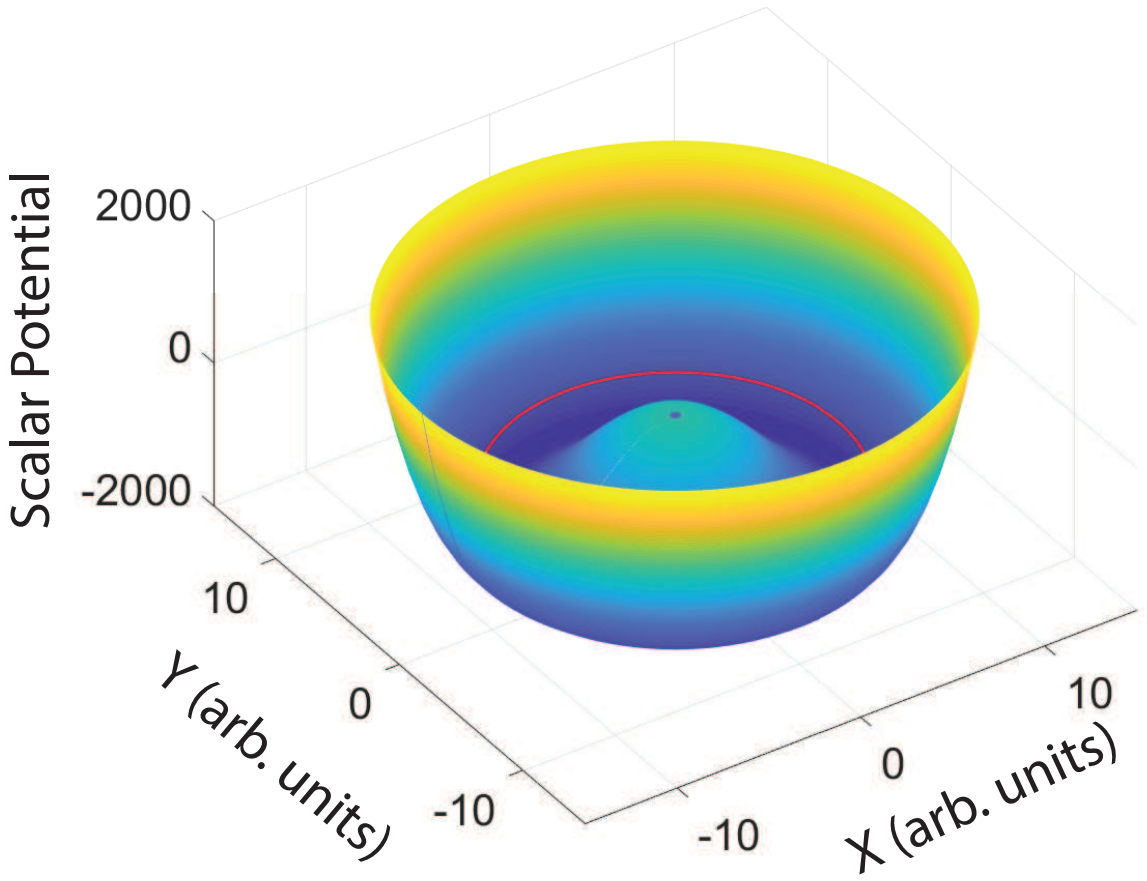

Figure 3.3: Hopf Scalar Potential

The deterministic limit cycle (red curve) lies in the minimum potential region of the Mexican hat potential described by Eq. 4.4. The color map runs from dark blue (low potential) to light yellow (high potential). The vector potential (not shown) is a constant azimuthal vector field which drives the limit cycle dynamics in a counterclockwise circular limit cycle of radius R_0. See text for details.

that choice.

Fig. 3.4 shows the modified scalar potential for $n = 4$, along with the deterministic limit cycle shown in yellow. It should be noted that there are pairs of degenerate paths about each of the local maxima. These minima also introduce new fixed points that remain stable for sufficiently small values of the vector potential. To find stable limit cycles we require that strength of the vector potential exceed

$$\omega^\star = nb\frac{\alpha}{\mu}. \tag{3.9}$$

Beyond this point, stable limit cycles exist, but their shape continues to change with increasing vector potential strength ω. We study these dynamics for various values of $\omega/\omega^\star$.

Introduction of the local minima renders the dynamical phase diagram more complex. In Fig. 3.5, we show this phase diagram under varying noise amplitude T and drive frequency ω. The top row of the phase diagram shows the full limit cycle, while the lower rows zoom in on one of the four equivalent local quadrants of the system. The $\omega = 0$ column shows the expected behavior of an equilibrium system with increasing levels of noise. For sufficiently small T, stochastic trajectories are confined to one of the four local minima (we show one such case in the figure). The trajectories deviate further from the minimum of the potential with increasing T, as one expects in the vicinity of a fixed point. Over sufficiently long times, one observes thermally activated hopping between these minima, so that the system diffuses around the ring set by the underlying circularly symmetric potential. Alternatively, the same behavior can be observed by increasing T at fixed length of the trajectories. The sequence (J, G, D, and A) in Fig. 3.5 demonstrates these effects.

In the case of small but finite ω, the drive biases the hops between local minima to favor those in the anticlockwise direction, along the force generated by the vector potential. However, if one chooses $\omega < \omega^\star$, the drive is not sufficient alone to drive transitions between local minima, and the deterministic system remains trapped within one of these wells of the scalar potential. In this study, we are primarily interested in the case where the deterministic system has a stable limit cycle, so we begin our studies where the vector potential is just strong enough to destabilize the local minima. A sequence of such minimally stable deterministic

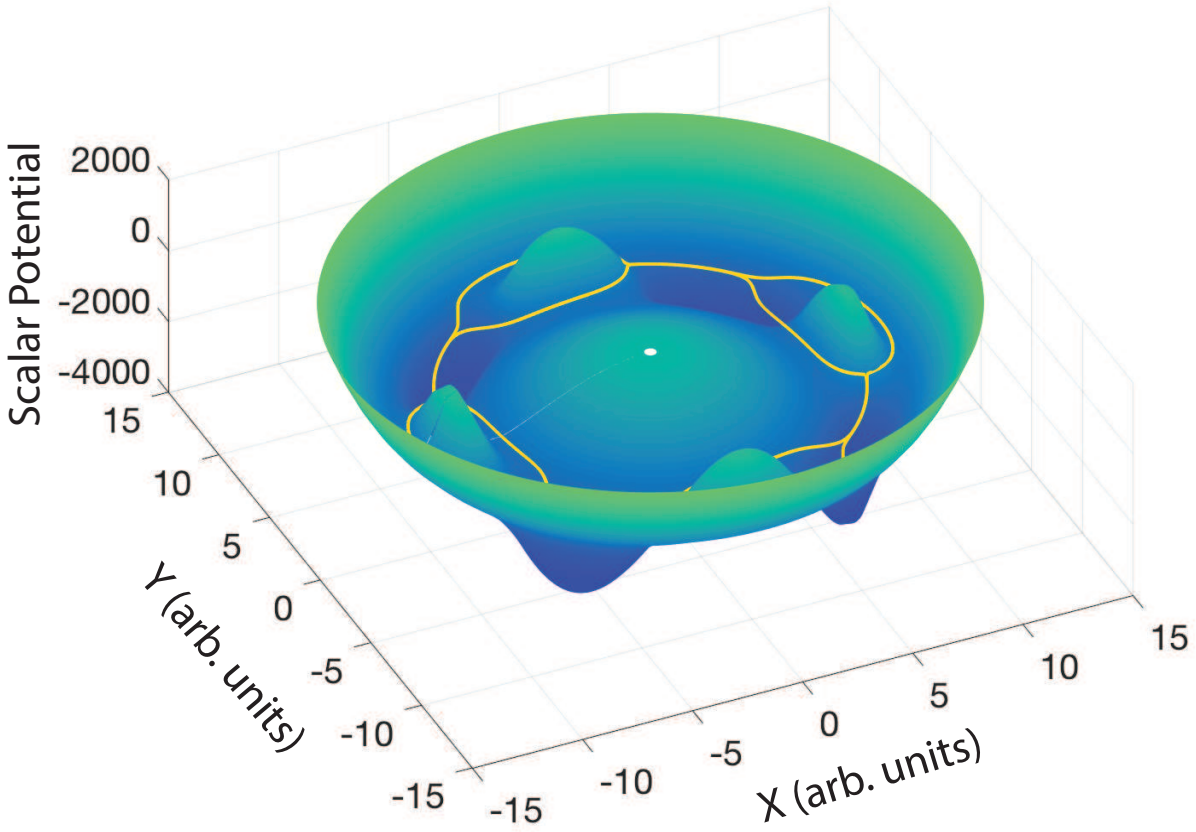

Figure 3.4: Scalar Potential map for generalized Hopf

3d plot of the scalar potential in Eq. 3.7, for $n = 4$ with the valleys seen in dark blue and hills in between them. The color map spans across dark blue (low potential) to light green (high potential). The deterministic limit cycle (yellow) for small vector potential skirts around the hills and pinches at the valleys.

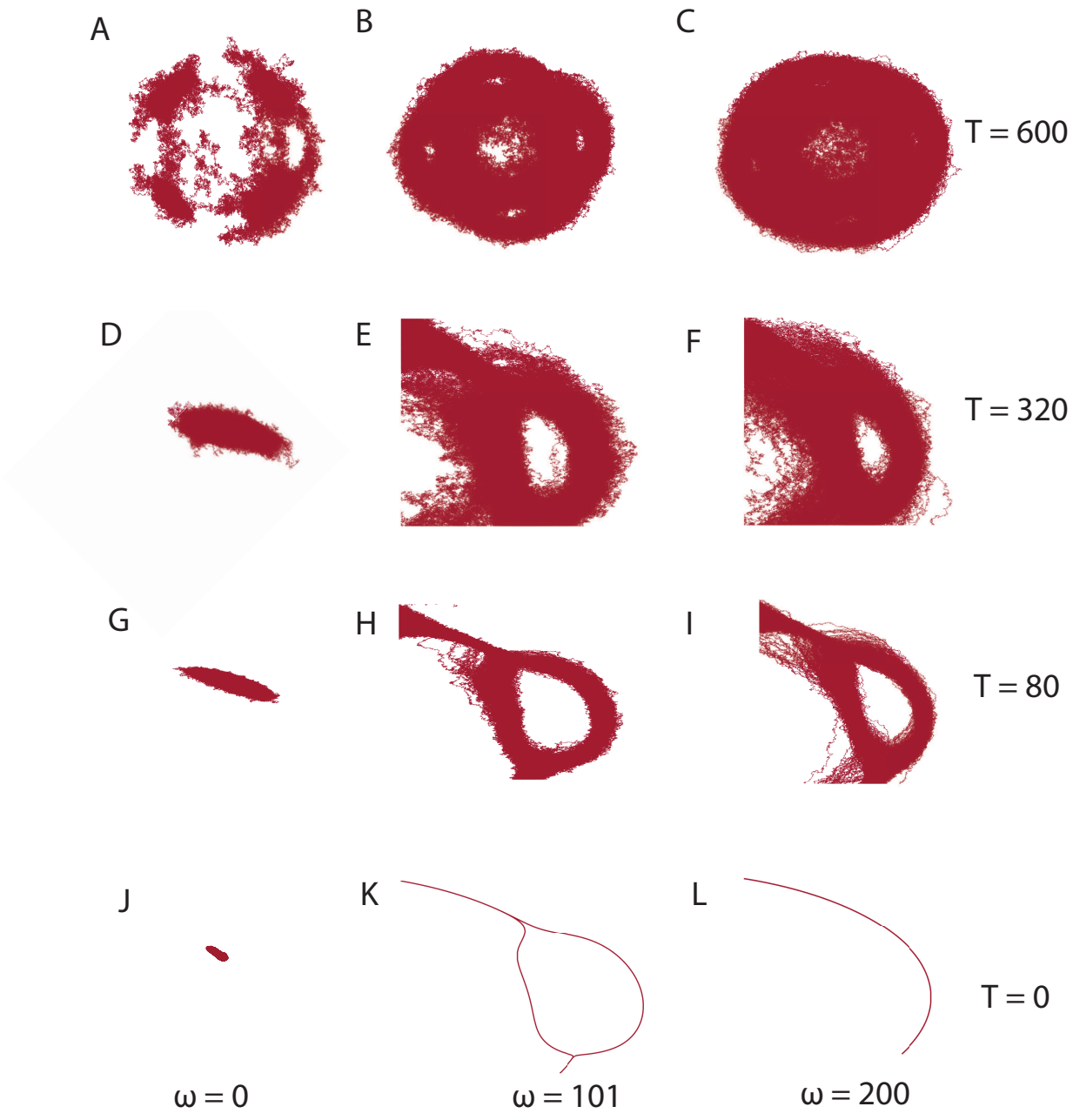

Figure 3.5: Stochastic trajectories with variation in temperature and ω

Quarter lobes of the trajectories obtained by solving Eq. 3.7 using ω values of $\{0, 101, 200\}$ and $\langle \eta_z^2 \rangle$ values of $\{0, 80, 320, 600\}$.

trajectories with increasing noise amplitude can be see in (K, H, E, B) of Fig. 3.5. We note that even small values of the noise amplitude are capable of allowing the dynamical system to explore both trajectories about the local potential maxima.

Finally, with a sufficiently strong vector potential (here $\omega = 200$), the deterministic system (and the system with sufficiently small noise amplitude) approaches the circular limit cycle of the standard Hopf oscillator with the circularly symmetric diving force overwhelming the symmetry-breaking scalar potential. This is shown in panel L of Fig. 3.5. Upon increasing the noise amplitude, as shown in the sequence (L, I, F, C) of Fig. 3.5, we observe both paths around the local maximum appearing once again. Since the limit of very large drive restores the circular symmetry, and since we aim to study the noise-induced loss of fine detail in more complex limit cycles, the large ω limit will not be considered further. In panels H and I, one observes a dispersion of trajectories around the point where the inner path about the local maximum reconnects with the outer path. This localized broadening is an example of noise-activated *corner cutting* in the generalized Hopf model that is the focus of this chapter.

3.3.2 Noise-induced *corner cutting*

We now explore in detail the noise-induced corner cutting at intermediate values of both noise amplitude and drive, consistent with panel H in the phase diagram. As expected, the deterministic oscillator occupies the low potential regions at nearly all phases of the oscillation (see Figs. 3.6(A),(B)). However, upon increasing the noise amplitude in the system, as shown in panels (C) and (D) of Fig. 3.6, the trajectories deviate from the $T = 0$ curve by cutting across the sharper (higher curvature) features of the deterministic path.

The net effect of these devations is that the mean shape of the limit cycle increasingly deforms with noise amplitude. In particular, the higher curvature features of the deterministic limit cycle, apparent where the inner path (smaller radius) around the local maximum converges with the outer path, are lost with increasing noise amplitude. We refer to this phenomenon as *corner cutting*, since the sharper corners of the deterministic limit cycle are smoothed out.

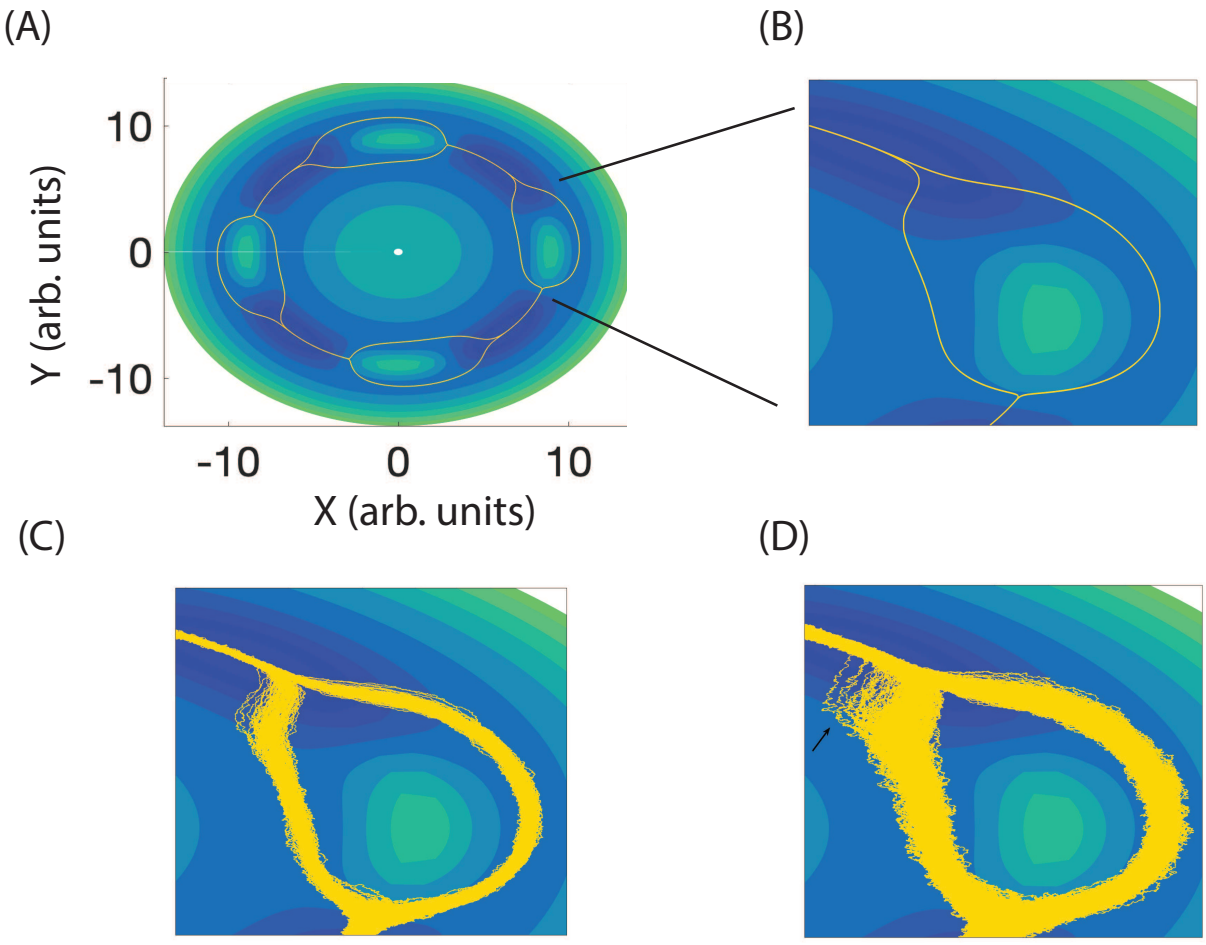

Figure 3.6: Examples of corner cutting

(A) The deterministic oscillator tracks the local minimum potential regions. (B) One lobe of the potential landscape. (C) Oscillator at $\langle \eta^2 \rangle = 10$. (D) Oscillator at $\langle \eta^2 \rangle = 30$. A (black) arrow points to an example of a corner cutting trajectory. These have been simulated using parameter values $\mu = 80, b = 1, \alpha = 2000, n = 4$, resulting in $\omega^\star = 100$ – see Eq. 3.9 – and $\omega = 101$.

The corner cutting observed in the generalized Hopf model resembles that observed in the hair cell oscillator model. One observes in Fig. 3.1 the noise-induced rounding of the high curvature corner in the upper right quadrant of the deterministic limit cycle. Comparing panels C and D of Fig. 3.1, we see that increasing noise amplitude increases both the frequency at which paths deviate from one that follows the local potential minimum and the degree of their deviations, indicating that this effect is indeed driven by stochastic processes.

The degree of corner cutting at different points along the deterministic trajectory, which exhibit the same scalar potential, are not equivalent. For example, we do not observe as much corner cutting at the point where the limit cycle diverges when approaching the local maxima as where these paths converge on the other side. This shows that phenomenon is not simply a feature of the local scalar potential, which is the same at both of these points.

In Fig. 3.7, we plot the drive force associated with the vector potential $\mathbf{f}_V$ along the mean limit cycle. The mean limit cycle is calculated in a similar manner as the regular Hopf oscillator, with an additional calculation at each phase to check for the presence of one or two maxima in the trajectory density. The peaks are considered distinct if they are radially separated from $R_{0=}\sqrt{\mu/b} = \sqrt{80}$ by a distance of 0.2 or more. We identify the corner-cutting paths as events that lie at a potential energy greater than $3T$ compared to the potential energy of the mean curve.

One immediately observes the distinction between the entry and exit points of the loop around the local potential maximum. Near the entry point, the vector potential force is tangent to the path of the limit cycle. Near the point where the inner path merges with the outer one, however, the drive force has a significant component normal to the mean path. The drive force plays a role in enhancing the thermally excited deviations from the mean limit cycle. Moreover, asymmetric deviations from the deterministic limit cycle resulting in deformation of the mean limit cycle from the deterministic one are strongest in regions where two conditions are met. First, there must be a significant component of the drive force normal to the deterministic limit cycle, and second, the confining potential about that limit cycle must be weak.

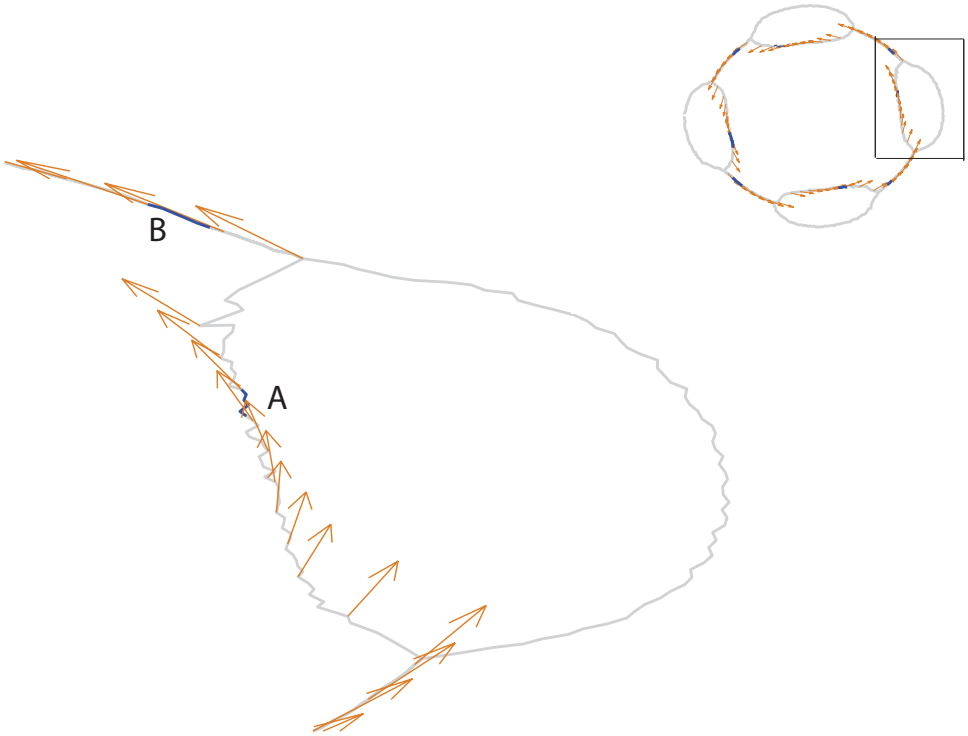

Figure 3.7: Direction of f_v

One of the lobes of the mean limit cycle (grey) of the $\langle \eta^2 \rangle = 30$ stochastic system, with the (blue) regions (A,B) corresponding to arc lengths amidst which the corner cutting trajectories deviate from the particle's average behavior. The direction of $\mathbf{f}_V$ is illustrated by (orange) arrows. This lobe corresponds to the marked lobe in the (upper right) inset.

In the lower panel of Fig. 3.8, we plot the potential energy versus distance, measured along the local normal to the mean limit cycle. Plots are obtained at various points (labeled A, B, C, D) along that limit cycle, indicated in the upper panel of the same figure. The potential in the normal cross section at A shows two minima, consistent with the two paths of the deterministic limit cycle at that point. Upon approaching the junction of those two paths at B and C, one sees these two local minima merge into a single broader minimum. This minimum then deepens, and the confining potential sharpens, as one moves alway from the local maximum (shown at D). It is clear that the combination of the weak (small curvature) confining potential and large normal component of the drive force at points near B make this area most susceptible to noise-induced trajectories escaping from the mean path. The asymmetry of those escapes, *i.e.*, their preference for moving to smaller radii, leads to an enhancement of the noise-induced distortion of the mean limit cycle near B.

Based on the above analysis we expect that the effect of noise on the mean limit cycle of the oscillator depends strongly on the arclength. In other words, different regions along the deterministic limit cycle deform differently with increasing noise amplitude so that the shape of the limit cycle itself changes with noise amplitude. To investigate this effect, we measure the normal distance between the deterministic limit cycle and the one measured at "high temperature", where $\langle \eta^2 \rangle = 2000$. In Fig. 3.9, we color the deterministic limit cycle using a heat map to represent this noise-induced deformation. In that figure, the cooler (yellower) colors depict smaller noise-induced distortions. The deformation is clearly nonuniform along the limit cycle (although still symmetric under rotations of the figure by $\pi/4$ due to the underlying symmetry of the $n = 4$ perturbation). The greatest deviations occurs at the region corresponding to (A-D) of Fig. 3.8, showing that the principal cause of these distortion "hot spots" are the corner-cutting trajectories where the two limit cycle arcs converge at the end of the local potential maxima.

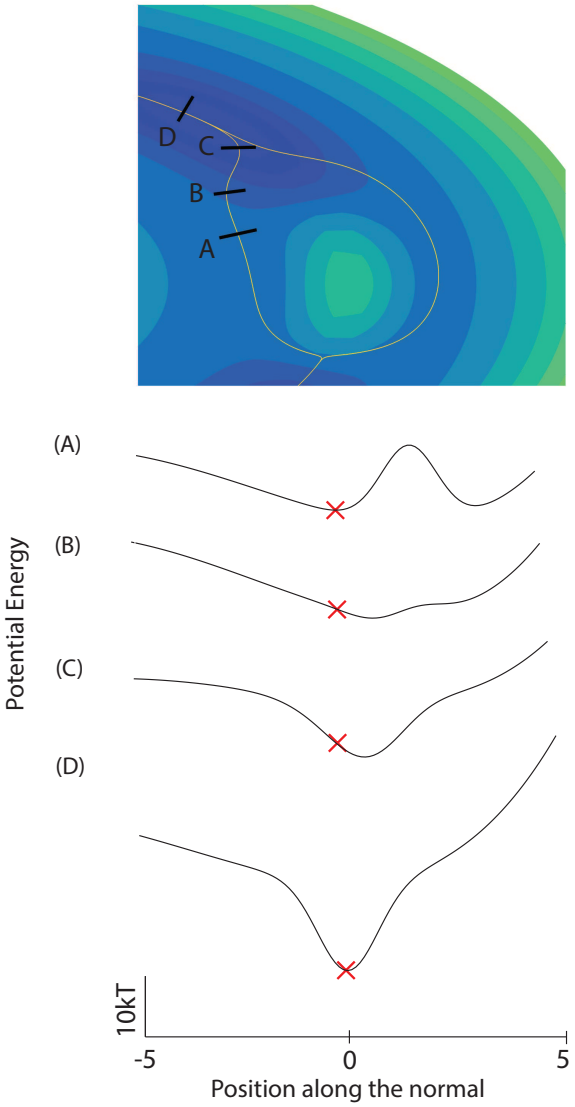

Figure 3.8: Confining potential

(A-D) Energy landscapes in the $\hat{n}$ direction to the zero-temperature limit cycle, corresponding to the A-B arclength in Fig. 3.7. The (red) cross is indicative of the noiseless particle position, with negative values pointing towards $(0, 0)$. These positions correspond to the (black) cuts along the (yellow) limit cycle atop.

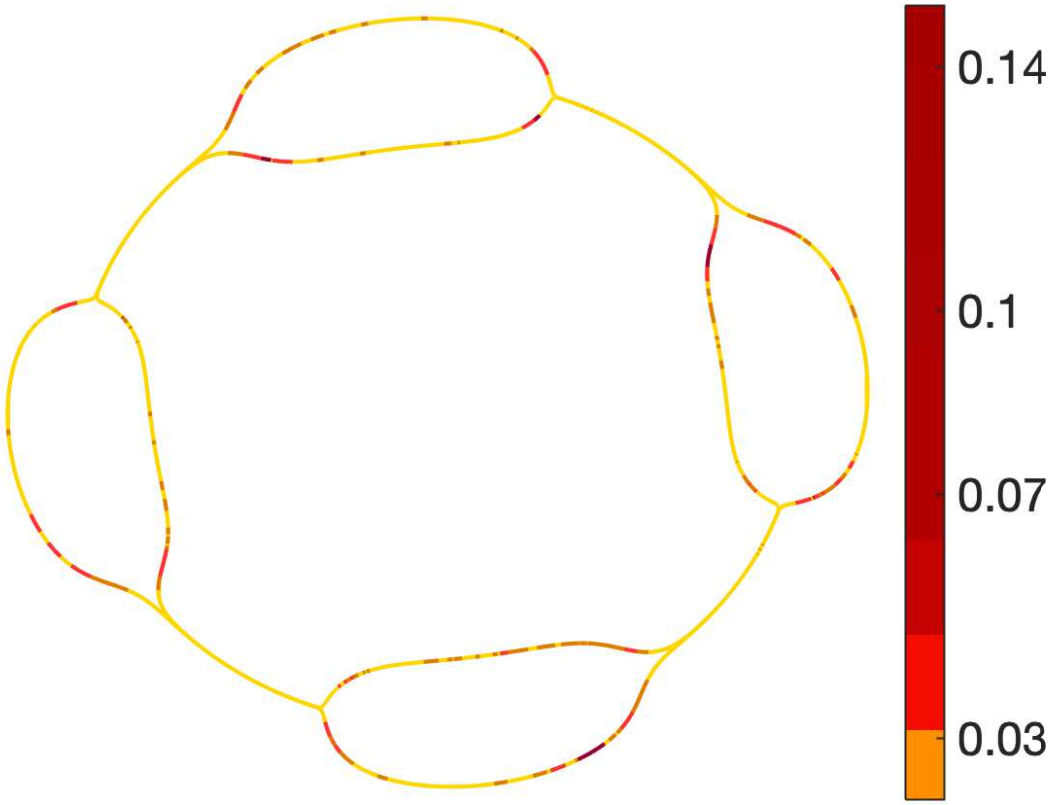

Figure 3.9: Nonuniform distortion of the limit cycle

The distance of the mean limit cycle at $\langle \eta^2 \rangle = 2000$ from the underlying noiseless curve shown as a color map. These values are normalized to the average value of the zero-temperature cycle, $\sqrt{\mu/b}$.

3.3.3 Predicting regions of noise-induced limit cycle distortion

To better understand the extent of distortion hotspots (*i.e.*, their length along the mean limit cycle), we analytically estimate the typical time interval for a stochastic trajectory to return to the mean limit cycle, assuming that it has already significantly deviated from it. Assuming a relatively constant angular velocity about the limit cycle, one can then estimate the limit cycle arclength required for the particle to return to the mean limit cycle after such a noise-induced deviation. In this way, we obtain a rough measure of the size of the regions of the limit cycle where one can expect significant noise-induced distortions. Identifying points on the limit cycle where trajectories are likely to diverge from the mean limit cycle and estimating the typical extent of distortion hotspots allows one to predict from the underlying deterministic equations which parts of the limit cycle are inherently more susceptible to noise.

To address this question, we consider a trajectory that starts at some fixed distance from the mean limit cycle. We choose this distance using the criterion that the system's deviation has increased its potential energy to $3T$ above the minimum (which occurs at or near the mean limit cycle in the limit of a weak drive). We treat the stochastic dynamics of the system in the plane perpendicular to the limit cycle, which we assume here to be one dimensional (higher dimensional generalizations are possible). For the analytic estimate, we consider the confining potential to be locally quadratic, an approximation warranted by the measured confining potential plotted along the local normal to the limit cycle in Fig. 3.8. We do not include a local nonzero normal component of the drive force, but the calculation can be readily generalized to include a roughly constant force term.

Using these simplifications, we compute the mean first passage time distribution for the system to return to the potential minimum. The details of the calculation are presented in Appendix 3.5.2. κ denotes the curvature of the confining potential, and its variation around the limit cycle is illustrated in Fig. 3.10. As explained in Appendix 3.5.2, we compute the integrated survival probability $N(t)$ of trajectories starting at a fixed normal distance from the mean limit cycle and vanishing upon their return to it. The negative time derivative

of this quantity is the probability distribution of the first return time. We plot the integral $N(t)$ as it is less susceptible to noise in the numerical data. Given a starting position x_0 in a harmonic potential with curvature κ, we find the integrated survival probability to be

$$N(t) = erf\left[\left(\frac{\kappa}{2k_{\mathrm{B}}T(1-e^{-2t\kappa B})}\right)^{1/2} x_0 e^{-t\kappa B}\right]. \tag{3.10}$$

Here B is the mobility of the overdamped system (which is set to 1 in our simulations, without loss of generality) and $k_{\mathrm{B}}T$ is a measure of the amplitude of the Gaussian white noise. In our simulations, k_{B} is normalized to 1.

We plot κ, the curvature of the confining potential in the direction normal to the limit cycle, of our generalized Hopf model as a color map superposed on the limit cycle in Fig 3.10. As expected, corner-cutting occurs where that potential is smaller than average. More significantly, we plot the decay of $N(t)$ predicted solely from that local curvature, for two representative parts of the limit cycle: (1) a region of small κ (upper left), where the distribution of the return times is broad, indicating that many trajectories deviate from the mean path over significant portions of the limit cycle, and (2) a region of high curvature (lower left), where trajectories that do deviate rapidly return to the mean path.

To test this analytic prediction for the return time distribution, we use stochastic numerical simulations to compute the distribution of return times for trajectories that start off the mean path, using the criterion discussed above. The histogram of those return times is plotted (yellow bars) in Fig. 3.11. The numerical data are taken from a region where the confining potential is weak so that such large excursions from the mean are relatively common, allowing us to obtain a larger data set of deviant trajectories. Superimposed on this plot is the integrated survival probability $N(t)$ computed from Eq. 3.10. There are no free fitting parameters.

We observe reasonably good agreement between the simple model and the numerical data. The largest discrepancies appear to be that the simple model overestimates the rapid return times and underestimates the return times that are of the order of $\sim 1/\omega$. We believe that this error results from our neglect of the vector potential force, which changes rather

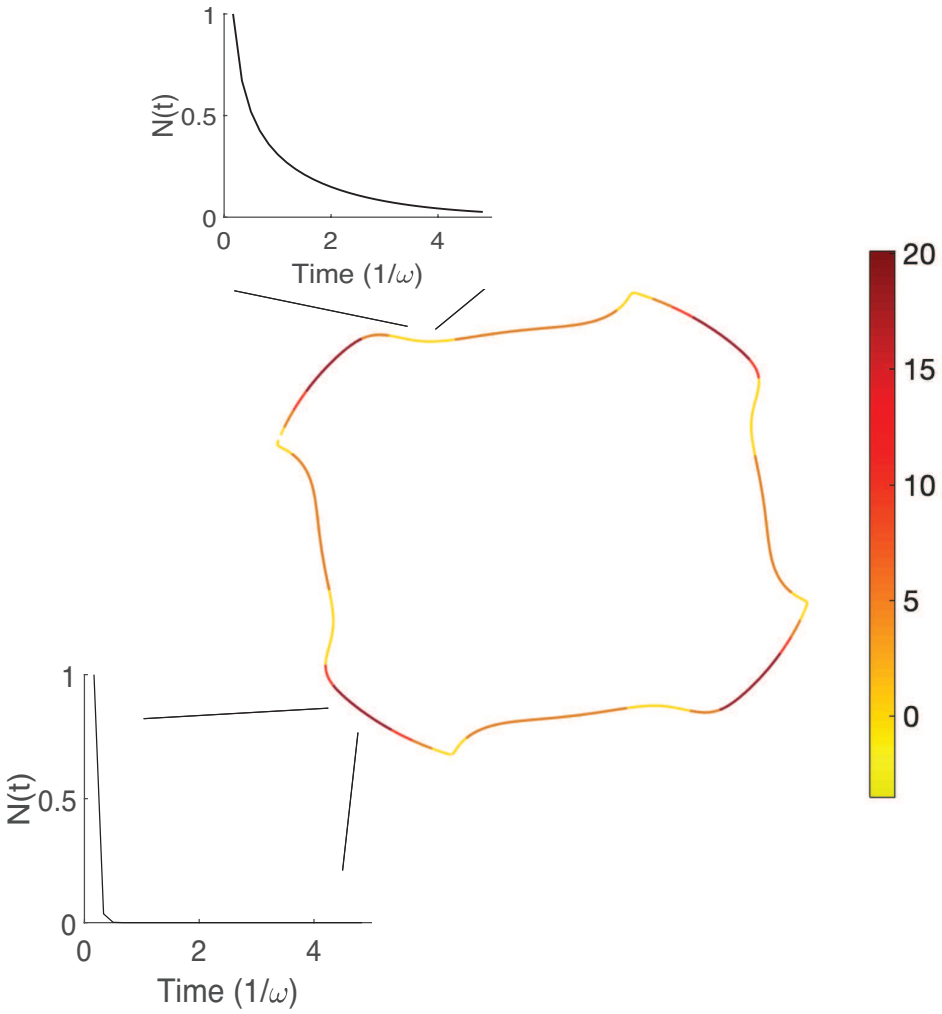

Figure 3.10: Curvature of the confining potential

The plot depicts κ values along the zero-temperature limit cycle. We depict the inner curve, since the asymmetry of the problem, renders it more susceptible to corner-cutting. Additional plots exhibiting Eq. 3.28, illustrate the time of decay for the total number of trajectories that have escaped the mean path of a system with noise variance $\langle \eta^2 \rangle = 30$. This points to a theoretical method of determining regions in the oscillatory system that are prone to distortion in the presence of noise, and hence less reliable when fitting parameters to experimental data.

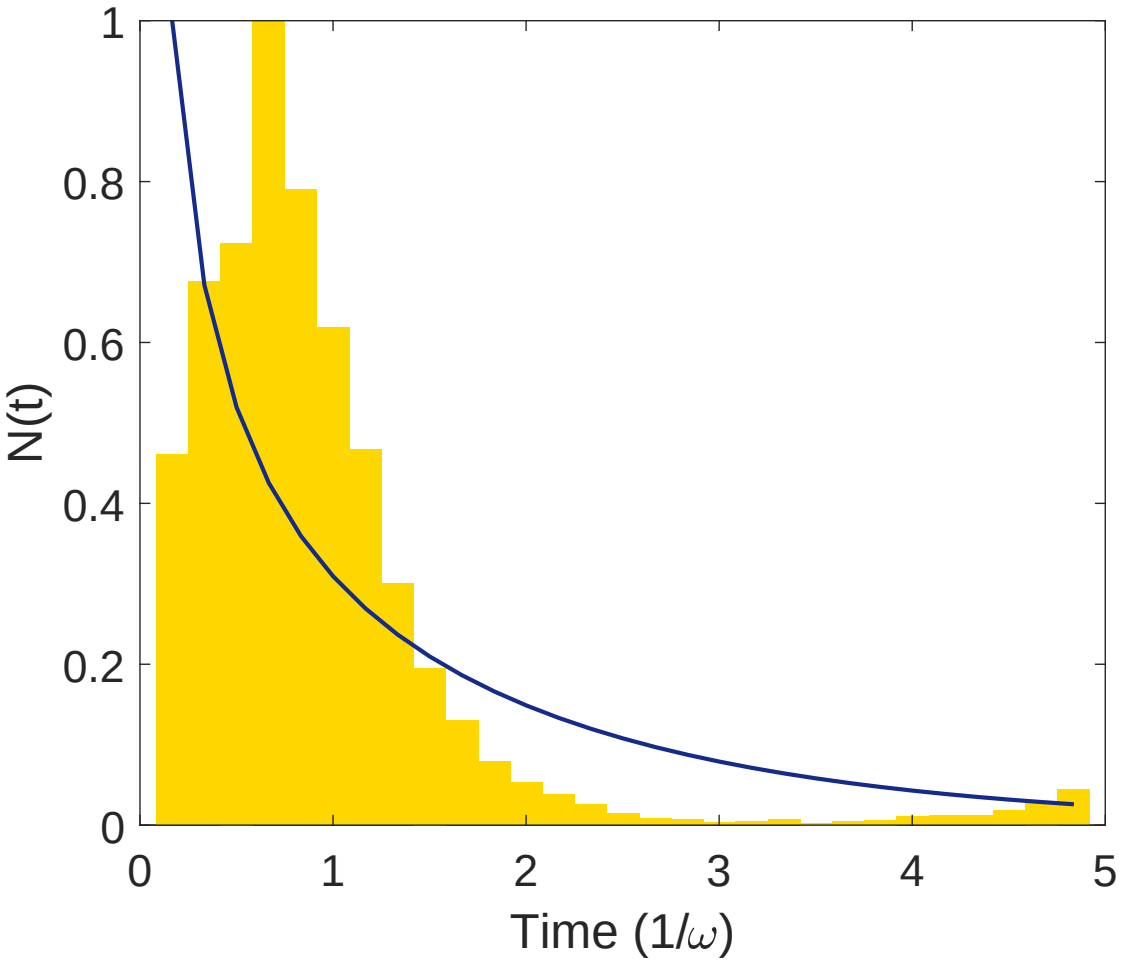

Figure 3.11: Return time distribution

The histogram represents the distribution of the stochastic trajectories that lie $3T$ above the minimum potential. We consider trajectories that leave the mean limit cycle in a region of small potential curvature ($\kappa = 0.6$) as shown in Fig. 3.8B. The overlaying plot is the theoretical prediction of Eq. 3.10.

rapidly in this portion of the limit cycle. As shown in Fig 3.7, trajectories leaving the limit cycle at this point experience initially the normal component of the driving force, and this normal component of the force decays rapidly as the system traverses the limit cycle. The result is that rapid returns are suppressed by the vector potential force, but this suppression of returns vanishes quickly as the particle continues on its trajectory. While the details are not captured by this simple quantitative estimate provided by Eq. 3.10, it has qualitative value in predicting regions of the limit cycle where large noise-induced deformations are likely to occur. We note (data not shown) that in regions of large κ, we observe few large excursions from the limit cycle and rapid returns when such excursions do occur.

3.4 Summary

We have shown that the fluctuations of a stochastic nonlinear oscillator can affect the size and distort the shape of its average limit cycle, as a function of noise amplitude. This effect appears to be dominated by particular parts of the limit cycle that combine two special features. First, the confining potential that stabilizes the deterministic limit cycle is broad, and second, the non-conservative driving force has a significant component normal to the local tangent of the limit cycle. These two criteria provide a way to determine quantitatively how susceptible the deterministic limit cycle is to noise-induced distortions. Since the criteria for large deformation occur near high curvature parts of the deterministic limit cycle, we refer to these distortions as *corner-cutting* events. We also provide a simple estimate of the duration of large, noise-induced excursions from the typical path of the nonlinear system and thereby provide a measure for the size of the noise-deformed regions of the limit cycle.

Using that estimate, one is able to predict which features of the limit cycle of a periodic, nonlinear, dynamical system are susceptible to noise and which are not. This leads to two observations. First, we believe that, in using noisy experimental data to fit parameters of complex nonlinear models, one must first determine which parts of the limit cycle of the dynamical system are least susceptible to that noise and weight the fits of the various model parameters accordingly. This is particularly true in systems where the details of the

noise sources are poorly understood and, as a consequence, the expected noise amplitude is unknown. Secondly, we predict that more noisy dynamical systems will generically have fewer high curvature features in their limit cycles due to corner cutting. This trend has not yet been confirmed to our knowledge.

Applying these findings to models of biological systems in general, and hair cells in particular, we suggest that increasing the complexity of dynamical models provides diminishing returns: more sophisticated models typically introduce new and finer features to their limit cycles, which we show will be smoothed by averaging over stochastic trajectories. For active systems exhibiting a limit cycle, increasing amount of averaging brings one arbitrarily closer to the mean limit cycle, not to the deterministic one. As mentioned earlier, Fig. 3.1 illustrates this averaging and the resulting disparity between the mean and noiseless limit cycles of a three-dimensional hair bundle model. The effect is analogous to that of the thermal expansion of crystals where a combination of thermal noise and a nonsymmetric potential lead to temperature-induced changes to the mean atomic spacing. Hence, if the presence of realistic noise amplitudes in the model leads to a significant distortion of the mean limit cycle, any finer features of the deterministic model will be inherently inaccessible to experiment.

Since we expect noisy limit cycle oscillators to not typically exhibit sharp features in their limit cycles regardless of the complexity of their underlying dynamical models, one may wish to investigate them more closely in noisy biological systems. Their presence should be atypical at least, and such features imply tight dynamical control through very large curvatures of the effective confining potential. That tight control may point to selection pressure on the relevant dynamical features of the biological limit cycle, although other interpretations would remain possible.

There are a number of extensions to this analysis that can be considered. First, one may examine the role of colored (frequency-dependent) noise in the system. Here, we expect that increasing the noise amplitude at low frequencies will produce larger scale distortions than those at high frequencies. The quantitative details of this effect have not been pursued yet.

Further, one may consider more complex issues, such as stochastic variations in the model parameters themselves. These will generally introduce multiplicative noise in the system and render the problem significantly more complex. We expect, however, that basic features explored here will still provide a rough set of guidelines for determining what parts of the limit cycle are susceptible to internal stochastic forces.

3.5 Appendix

3.5.1 Simulation details

The stochastic simulations of Eq. 4.1 were carried out using the 4^{th}-order Runge-Kutta method for a duration of 60 s, which corresponds to approximately 6500 limit cycles. The time steps used in the simulation were in the range of $10^{-4} \leftrightarrow 2 \times 10^{-3}$ s. The time steps for the simulations of Eqs. 3.7,3.8 were $6 \times 10^{-7} \leftrightarrow 3 \times 10^{-6}$. We did not observe any numerical instabilities of the solution during these runs.

We explored a large range in the amplitude of the noise variance $\langle \eta_Z^2 \rangle$, covering the range of $10^{-7} \leftrightarrow 0.4$ where the amplitude of the limit cycle oscillator oscillation amplitude was held to be $O(1)$. The stochastic terms driving the dynamical variables $\{X(t), Y(t)\}$ were always assumed to be uncorrelated.

3.5.2 First passage time distribution for a quadratic confining potential

To estimate the distribution of return times over which corner cutting trajectories come back to the mean limit cycle, we consider a simple Smoluchowski equation giving the time evolution of the probability distribution of the normal distance of a trajectory from the mean limit cycle. We make a number of simplifying assumptions. First, we assume that the effective potential for this one dimensional problem is fixed in time. In the actual system, this potential is time varying as the particle traverses it trajectory, but as long as the excursions from the mean limit cycle are sufficiently brief, this approximation should provide a reasonable estimate of the return probabilities. Secondly, we assume that the force associated with the vector potential may be ignored. We find that this non-potential force is typically subdominant; in principle, a time-independent approximation to this force could be included in the analysis explored below by adding a constant force, corresponding to a simple tilt of the potential landscape. Finally, the landscape of that confining potential is assumed to be locally quadratic, as illustrated by panels (C) and (D) in Fig. 3.8.

Given these approximations, we may write the Smoluchowski equation as

$$\frac{\partial P(x,t)}{\partial t} = D\frac{\partial^2 P(x,t)}{\partial x^2} + \kappa B\frac{\partial x P(x,t)}{\partial x} \tag{3.11}$$

where, $D = Bk_{\mathrm{B}}T$ is the effective diffusion constant and B the mobility. κ is curvature of the confining potential, which may be computed directly from the equations of motion and the curve associated with the mean limit cycle. Using this equation we will compute the probability that a trajectory, starting at a particular normal distance from the mean limit cycle, returns to that mean limit cycle for the first time after a time interval t. This is the well-known first passage time distribution.

We note that Eq. 3.11 has a simple time-independent solution corresponding to the equilibrium position distribution of a harmonic oscillator with spring constant κ:

$$P_{\mathrm{st}}(x,t) = \sqrt{\frac{\kappa}{2\pi k_{\mathrm{B}}T}}e^{-\frac{\kappa x^2}{2k_{\mathrm{B}}T}} \tag{3.12}$$

Writing the time-dependent probability distribution that evolves towards $P_{\mathrm{st}}(x)$ according to Eq. 3.11 as a product: $P(x,t) = P_{st}(x,t)^{1/2}g(x,t)$, we obtain a new evolution equation for $g(x,t)$:

$$\frac{\partial g(x,t)}{\partial t} - Bk_{\mathrm{B}}T\frac{\partial^2 g(x,t)}{\partial x^2} + \frac{B\kappa}{2}(\frac{\kappa}{2k_{\mathrm{B}}T} - 1)g(x,t) = 0. \tag{3.13}$$

We note that the $g \longrightarrow 1$ at long times in order to be consistent with Eq. 3.12.

Using separation of variables, $g(x,t) = f(t)h(x)$ and simple redefinition of the curvature $\frac{\kappa}{2k_{\mathrm{B}}T} = \beta$, we find that f and h obey the ordinary differential equations:

$$\frac{df}{dt} + \frac{f}{\tau} = 0 \tag{3.14}$$

$$\frac{d^2h}{dx^2} - \beta^2 x^2 h + (\beta + \frac{1}{\tau D})h = 0. \tag{3.15}$$

From Eq. 3.14 we see that $g(x,t)$ decays exponentially in time with decay rates τ^{-1} set by solutions of the Eq. 3.15. That equation may be reduced Hermite's differential equation via a rescaling of both the independent $y = \sqrt{\beta}x$ and dependent $h(y) = u(y)e^{-\frac{y^2}{2}}$ variables:

$$\frac{d^2u}{dy^2} - 2y\frac{du}{dy} + \frac{u}{\beta\tau D} = 0 \tag{3.16}$$

The eigenfunctions $H_n(y)$ of this differential operator

$$H_n(y) = (-)^n e^{y^2} \frac{\partial^n e^{-y^2}}{\partial y^n} \tag{3.17}$$

allow us to determine the discrete set of decay rates

$$\tau_n^{-1} = 2n\beta D. \tag{3.18}$$

Combining Eqs. 3.12,3.14,3.15 and,3.17, we write the solution to Eq. 3.11 (in terms of the scaled spatial variable y) as

$$P(y,t) = e^{-y^2} \sum_n c_n H_n(y) e^{-\frac{t}{\tau}}, \tag{3.19}$$

where the undetermined coefficients c_n are given by the initial condition: $P(y, t = 0)$. We take that initial condition to be a delta function $\delta(x - x_0)$, where x measures the normal displacement from the the mean limit cycle and x_0 is set by choosing the point where the potential energy of the system is $3k_BT$ above that of the mean limit cycle. From the orthonormality of the Hermite polynomials,

$$\int_{-\infty}^{\infty} dy e^{-y^2} H_n(y) H_m(y) = \delta_{mn} 2^m m! \sqrt{\pi}, \tag{3.20}$$

we obtain the undetermined constants in terms of $y_0\sqrt{\beta}x_0$:

$$c_n = \frac{H_n(y_0)}{2^n n! \sqrt{\pi}} \tag{3.21}$$

From these we have the conditional probability

$$P(y,t|y_0,t_0) = \sqrt{\frac{\kappa}{2\pi k_B T}} e^{-y^2} \sum_n \frac{H_n(y) H_n(y_0)}{n!} \left(\frac{e^{-t\kappa B}}{2}\right)^n \tag{3.22}$$

that a trajectory starting at y_0 at time zero reaches y at time t. Returning to the unscaled independent variable and using Mehler's approximation we write

$$P(x,t|x_0,t_0) = \left(\frac{\kappa}{2\pi k_B T(1 - e^{-2\kappa Bt})}\right)^{1/2} e^{-\frac{\kappa(x - x_0 e^{-t\kappa B})^2}{2k_B T(1-e^{-2\kappa Bt})}}. \tag{3.23}$$

In order to ensure we compute the first passage time to the origin, we must eliminate trajectories that pass through $x = 0$ on their way to (x, t). We do so in the usual way by

introducing an absorbing boundary condition at the origin. This is simply accomplished by subtracting the above result from an imagined solution:

$$\tilde{P}(x,t) = P(x,t) - P(-x,t). \tag{3.24}$$

Using this result, we compute the total probability remaining at time t:

$$N(t) = \int_0^\infty \tilde{P}(x,t)dx. \tag{3.25}$$

The resulting integral can be written as

$$N(t) = (\frac{\kappa}{2\pi k_{\rm B}T(1-e^{-2\kappa Bt})})^{1/2} \times \int_0^\infty dx \left\{ e^{-\frac{\kappa(x-x_0e^{-t\kappa B})^2}{2k_{\rm B}T(1-e^{-2\kappa Bt})}} - e^{-\frac{\kappa(x+x_0e^{-t\kappa B})^2}{2k_{\rm B}T(1-e^{-2\kappa Bt})}} \right\} \tag{3.26}$$

The remaining integral is easily performed to yield a solution written in terms of the error function:

$$N(t) = \frac{2}{\sqrt{\pi}} \int_0^{y_0} e^{-(y-y_0)^2} dy \tag{3.27}$$

$$= erf\left[\left(\frac{\kappa}{2k_{\rm B}T(1-e^{-2\kappa Bt})} \right)^{1/2} x_0 e^{-t\kappa B} \right]. \tag{3.28}$$

This result appears in the main text – see Eq. 3.10.

CHAPTER 4

Violation of generalized fluctuation-dissipation theorems in computationally driven steady states

4.1 Introduction

As the reader might have gleaned from the thesis introduction, specifically section 1.2.1, inner ear hair cells demonstrate a number of adaptation processes that are instrumental in maintaining the exquisite sensitivity of the hair bundle even under exogenous mechanical loading. Moreover, this force feedback mechanism of a hair cell – driven by its endogenous molecular motors, including Myosin 1c – both depends on and determines the state of its hair bundle. The mechanical feedback loop between the myosin motors and bundle displacements has other consequences as well. It allows for an unstable dynamical regime in which the sterocillium bundle responds to mechanical input like a spring with a negative spring constant [33]. In this regime, the bundle undergoes spontaneous oscillations even in the absence of incoming pressure waves due to the active feedback between motor activity and bundle displacement. Additionally, since that endogenous drive depends on deformation of the bundle *i.e.* on the state of our biological system, an internally-driven spontaneously oscillating hair cell provides a direct mechanical example of an adaptive control of a nonequilibrium steady state. We note that similar examples may be found in a number of biological systems, including cellular regulations [39] and bacterial chemo-sensing [28].

Biological systems are generally noisy, due to thermal fluctuations of their constituent elements. Consistently with this, hair cell oscillations encounter stochasticity from a number of sources such as the brownian motion of the surrounding fluid, stochasticity of the myosin

motor attachment and detachment and shot noise arising from ionic transport. As a result, the limit cycle oscillations of the hair cell bundle are innately noisy and thus provide a window on the basic nonequilibrium statistical mechanics of a noisy limit cycle oscillator. Further, as detailed earlier, they operate under feedback control where the drive maintaining the nonequilibrium steady state responds to the state of the system.

In this chapter, we use the Hopf theoretic description of the spontaneously oscillating hair bundle state as a model system to study fluctuation theorems associated with such noisy nonequilibrium systems. It is well known that fundamental equilibrium fluctuation theorems can fail in nonequilibrium steady states. In fact, the breakdown of the standard fluctuation dissipation theorem (FDT) [7] has been used as a way to characterize the nonequilibrium steady state of cytoskeletal networks [12]. For a more detailed take on the equilibrium fluctuation-dissipation theorem and its violation by the hair bundle, we refer the reader to section 1.5. More recently, there has been a new exploration of fluctuation theorems applicable to nonequilibrium steady states [50, 53, 51, 4, 57]. In this chapter, we will primarily concern ourselves with the generalized fluctuation-dissipation theorem (GFDT) as proposed by Seifert and Speck [53, 51] and apply it to a subclass of non-equilibrium steady-state systems – that comprising of stochastic, driven, limit cycle oscillators. Here we show that, as expected, the driven hair bundle violates the standard, equilibrium FDT, but does obey a generalized fluctuation dissipation theorem (GFDT). This agreement with the GFDT, however is predicated on the drive being non-computational. A computational drive is one which measures the system's current state and responds predictably by modifying its power input accordingly. This modulatory behavior is in fact loosely analogous to the myosin-motor based feedback mechanism in the inner ear hair bundles. We show that upon inclusion of this feature related to the homeostatic control of the hair bundle oscillations, we obtain new violations of the nonequilibrium GFDT. We propose that, just as the violation of the original FDT in biological systems is an important quantitative measure of nonequilibrium dynamics [16], the violation of the nonequilibrium generalization of the FDT, the GFDT, should be a useful quantitative indicator of active feedback or homeostatic control

in biological dynamical systems.

4.2 Stochastic Hopf oscillator model

The stochastic supercritical Hopf oscillator is two-dimensional in nature and can be described in terms of a complex variable $z(t) = x(t) + iy(t)$, which obeys the differential equation

$$\dot{z} = z\left(\mu + i\omega\right) - bz|z|^2 + \eta_z(t) + f_z(t), \tag{4.1}$$

where $f_z(t)$ is an external deterministic force acting on this overdamped system, and $\eta_z(t)$ is a stochastic force, described below. The dynamics of the deterministic and unforced system ($f_z = \eta_z = 0$) are controlled by the values of the model parameters $\{\mu, \omega, b = b' - ib'', (b', b'' > 0)\}$. The real parameter μ is the control parameter of the system. When $\mu < 0$, this term damps the oscillations, leaving the system with a single fixed point at $z = 0$, with an infinite basin of attraction. As this parameter becomes positive, there is positive energy input into the system, and the oscillator undergoes a supercritical Hopf bifurcation, resulting in a circular limit cycle of radius $R_0 = \sqrt{\mu/b'}$, which also has an infinite basin of attraction. The oscillator has an angular frequency given by $\omega_0 = \omega + R_0^2 b''$, where we assume that ω is real.

To specify the stochastic system, we include a Gaussian white noise force $\eta_z = \eta_x + i\eta_y$ with a zero mean:

$$\langle \eta_i(t) \rangle = 0, \tag{4.2}$$

$$\langle \eta_i(t)\eta_j(t') \rangle = A_{ij}\delta(t - t'), \tag{4.3}$$

with the symmetric and diagonal matrix$A_{ij}(A_{xy} = 0)$ allowing for the uncorrelated noise in the x and y channels to be drawn in principle from different Gaussian distributions. Finally, we include deterministic external perturbations via $f_z(t) = f_x(t) + if_y(t)$. Henceforth, for convenience we will be working in polar coordinates: $r = \sqrt{x^2 + y^2}$ and $\phi = \arctan(y/x)$ [**?**].

Trajectories derived from Eq. 4.1 are those of an overdamped particle moving in two dimensions in response to a force field $\mathbf{f}$, which can be decomposed into the gradient of

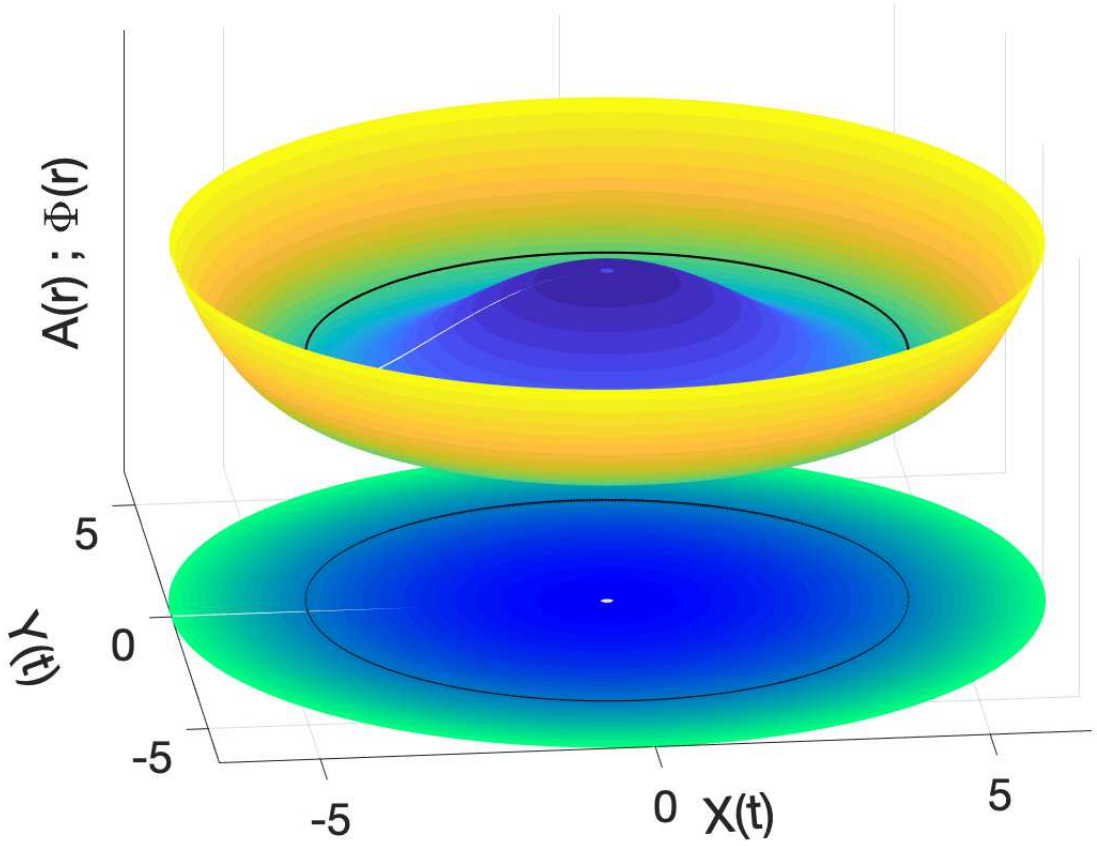

Figure 4.1: Scalar and Vector potential maps of the Hopf oscillator

The deterministic, unforced Hopf limit cycle (black curve) of radius R_0 sits in the azimuthally symmetric minimum potential region of $\Phi(\mathbf{r})$ as defined in Eq. 4.4 and is driven by the curl of $A(\mathbf{r})$ given in Eq. 4.5. The colormap for the three-dimensional $\Phi(\mathbf{r})$ runs from dark blue ($r = 0$) to yellow ($r = 7$). The magnitude of the vector potential $A(\mathbf{r})$ is shown as a colored disc which varies from dark blue ($r = 0$) to light green ($r = 7$).

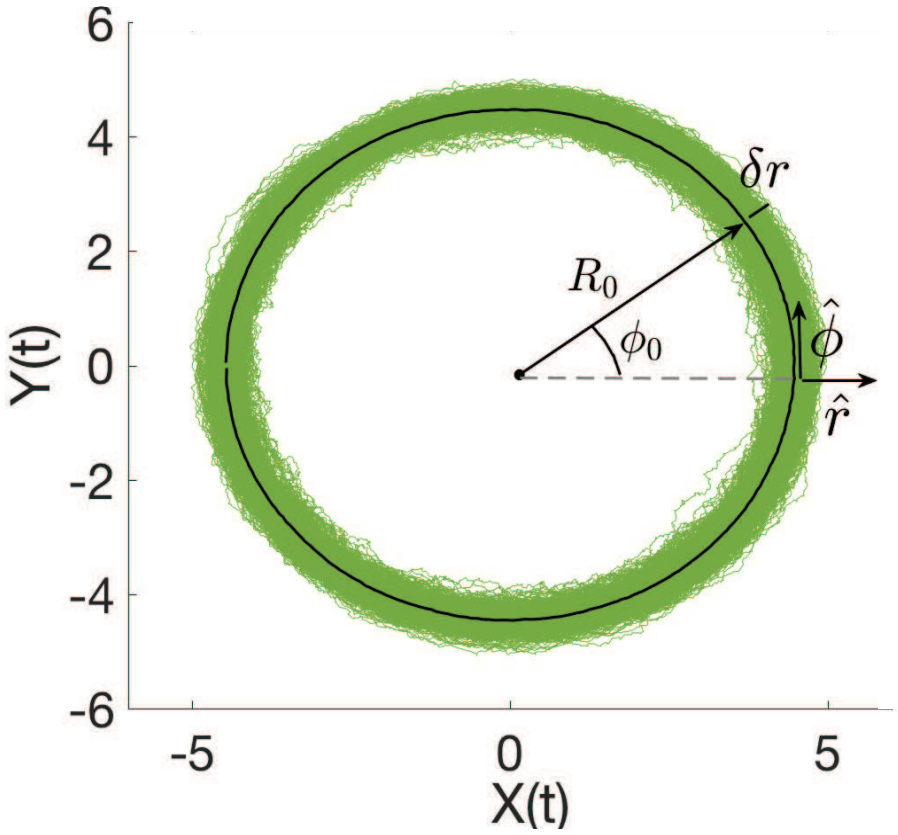

Figure 4.2: Typical stochastic trajectory of a noisy Hopf oscillator

Based on Eq. 4.1, the multiple trajectories are shown in green. The system's mean limit cycle is shown as the black circle, which has a particularly simple Frenet frame $\{\hat{r}, \hat{\phi}\}$ – these unit vectors denote the local normal and tangent to the curve, respectively.

an azithumally symmetric scalar potential energy $\Phi(r)$ and the curl of a vector potential $\mathbf{f} = \hat{z}A(r)$, where

$$\Phi(r) = -\frac{\mu}{2}r^2 + \frac{b'}{4}r^4, \tag{4.4}$$

$$A(r) = -\frac{\omega}{2}r^2 - \frac{b''}{4}r^4. \tag{4.5}$$

$\Phi(\mathbf{r})$ is the well-known "Wine Bottle" potential and is illustrated in Fig. 4.1 along with $A(\mathbf{r})$. Also shown is the particle's deterministic, limit cycle. The curl of its vector potential $\mathbf{f}_v = \nabla \times A(\mathbf{r})$, is a constant azimuthal force that drives the particle circularly along the minima of $\Phi(\mathbf{r})$. Its power input to the Hopf oscillator is,

$$P = \mathbf{f_v}.\dot{\phi} \tag{4.6}$$

$$= r(\omega + b''r^2)^2 \tag{4.7}$$

$$= (R_0 + \delta r)(\omega + b''R_0^2)^2 + 4b''R_0^2(\omega + b''R_0^2)\delta r \tag{4.8}$$

where, δr is the radial deviation of the particle about R_0 in the presence of external perturbing forces. The power input now has two components, the first of these is the power one traditionally expects for a stochastic particle undergoing centripetal motion. The second however is what we shall henceforth refer to as the power input due to a computational drive, meaning that the drive is now cognizant of the current state of the stochastic system (in this case, as determined by δr) and modifies its power accordingly. Lastly, for the plots in Fig. 4.1 we use: $\mu = 40$, $\omega = 10$, $b' = 2$ and $b'' = 2$.

When driven by white noise, the conservative system with $\omega = b'' = 0$ corresponds to the case of an overdamped particle in thermal equilibrium at some finite temperature. The vector potential, representing the action of the hair cell's endogenous molecular motors, does work on the overdamped system, generating the limit cycle oscillations, as shown in Fig. 4.2. We use the same parameter values as above. Other simulation details are described in Appendix 4.5.1.

The appearance of a force field produced by a vector potential does not alone generate a limit cycle or even a nonequilibrium steady state. The necessary and sufficient conditions

to create such a state with a time-independent force field is that: (1) the force field is proportional to the curl of a vector potential, and (2) the force does work on the particle that represents the state of the oscillator. A classic counterexample, where the second condition is not met, is provided by a charged particle in a magnetic field. In Appendix 4.5.2, we review this case, showing that a damped, charged particle in a two dimensional harmonic potential and in a uniformly applied magnetic field, aligned in the direction perpendicular to the plane of the charged particle's motion, obeys the standard FDT.

Generally, for hair cell models, one allows the b coefficient to be complex, as mentioned above. In this case, the azimuthal drive generates dynamics of the form: $\dot{\phi} = r^{-1}\nabla \times \mathbf{A} = \omega + b''r^2$. Note that the power input of the drive is now rendered *computational* in nature. In the dynamical systems literature, when the azimuthal coordinate is driven independently of the state of the system here given by r, *i.e.*, when $b'' = 0$, the system is said to experience isochronous driving. Conversely, computational driving where $b'' \neq 0$ is referred to as nonisochronous. For our purposes, the important feature of this model is that the computing ability of the drive forcing the steady-state limit cycle oscillations can be continuously varied through the one model parameter b''.

To study the fluctuations of the system about its limit cycle (when $\mu > 0$), we expand about the limit cycle

$$r(t) = R_0 + \delta r(t) \tag{4.9}$$

$$\dot{\phi}(t) = \omega_0 + \delta\dot{\phi}(t), \tag{4.10}$$

to find two coupled stochastic linear Langevin equations for the fluctuations of the radius δr and phase $\delta\phi$ of the oscillator

$$\delta\dot{r} = -2\mu\,\delta r + \eta_r + f_r, \tag{4.11}$$

$$\delta\dot{\phi} = 2b''\sqrt{\frac{\mu}{b'}}\,\delta r + \eta_\phi + f_\phi. \tag{4.12}$$

Here, the terms $\{\eta_r, \eta_\phi\}$ and $\{f_r, f_\phi\}$ are projections of the stochastic and perturbative forces respectively onto the local normal $\hat{r}$ and tangent $\hat{\phi}$. These unit vectors span the Frenet-Serret frame associated with the averaged limit cycle of the oscillator, being the local normal and

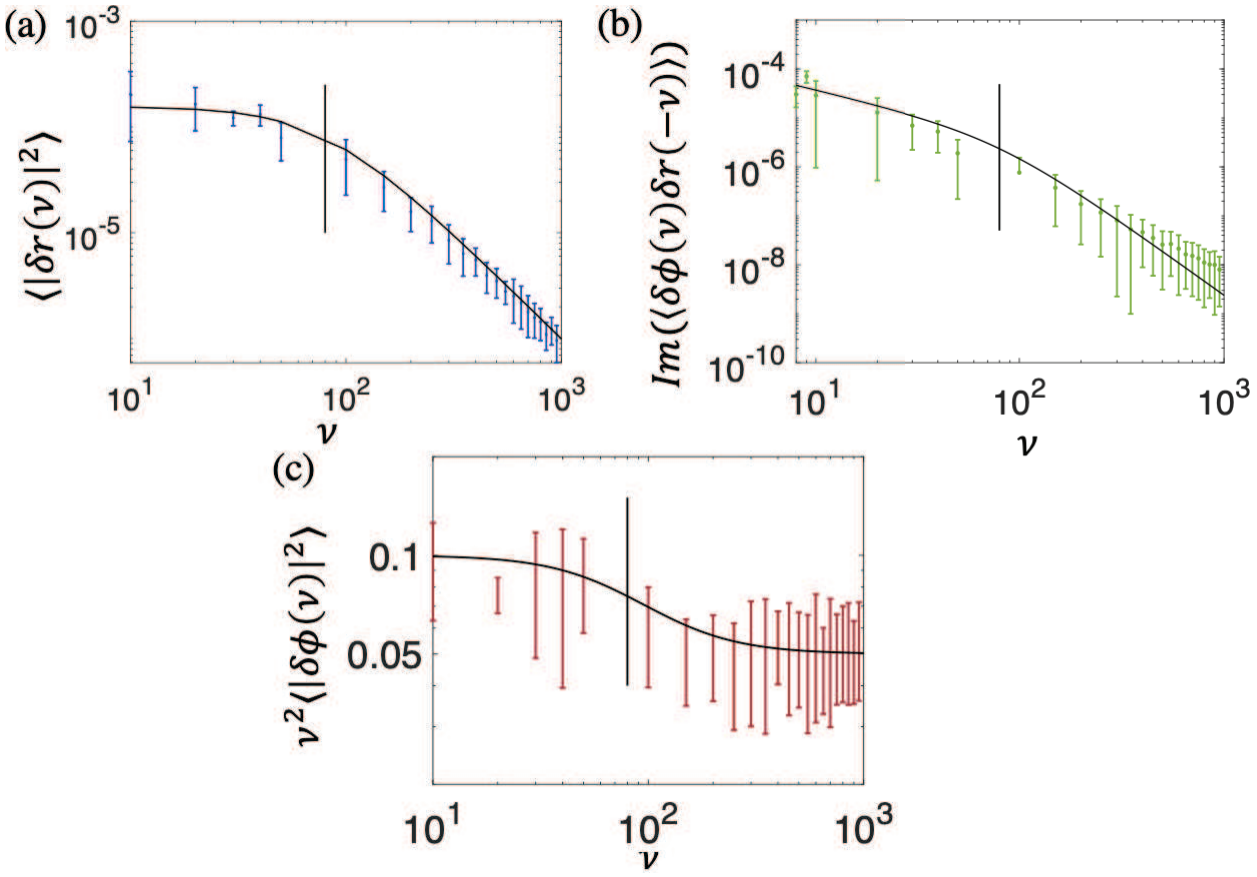

Figure 4.3: Correlation functions of the nonisochronous Hopf oscillator

Measured two-point correlations (colored points) of fluctuations $\delta r(\nu)$, $\delta\phi(\nu)$ of the simulated stochastic Hopf limit cycle oscillator are shown in the frequency domain along with their corresponding analytical calculations (black lines) – see Eq. 4.16. Error bars show the standard deviation of the mean. Panel (c) illustrates the frequency-dependent phase diffusion constant. The adaptive drive introduces δr, $\delta\phi$ cross-correlations (panel (b)) so that the radial fluctuations enhance phase diffusion for frequencies below the Lorentzian corner frequency of the radial fluctuations, indicated by the vertical (black) line in all the panels.

tangent directions, respectively (see Fig. 4.2). The details of this averaging are in Appendix 4.5.1.

The Frenet-Serret frame advances and simultaneously rotates along the mean curve at an angular velocity of ω_0. By working in this co-moving reference frame, we subtract away the mean non-equilibrium dynamics of the steady-state oscillator. Doing so allows us to recover a GFDT for the nonequilibrium system, as discussed by Seifert and coworkers [53]. Note that the use of the dimensionless phase angle ϕ instead of the arclength variable $s = R_0\phi$ requires the noise amplitudes $\eta_{r,\phi}$ to have different length dimensions. To account for this explicitly, we set second moments of the Gaussian force fluctuations in the frequency domain (given by ν) to be

$$\langle|\eta_r(\nu)|^2\rangle = 1 \tag{4.13}$$

$$\langle|\eta_\phi(\nu)|^2\rangle = R_0^{-2}, \tag{4.14}$$

which also has the effect of setting the effective noise temperature to $1/2$, since the mobilities in the Hopf equation have been set to unity. To account for this dimensional difference, it will be convenient in the following to define a symmetric "temperature matrix" by $T_{rr} = 1, T_{r\phi} = R_0^{-1}, T_{\phi\phi} = R_0^{-2}$. This choice of coordinates has no other consequences for our analysis.

To verify the GFDT in the co-moving frame, we first compute the correlation matrix in the frequency domain

$$\mathbf{C}(\nu) = \begin{bmatrix} \langle|\delta r(\nu)|^2\rangle & \langle\delta r(\nu)\delta\phi(-\nu)\rangle \\ \langle\delta\phi(\nu)\delta r(-\nu)\rangle & \langle|\delta\phi(\nu)|^2\rangle. \end{bmatrix} \tag{4.15}$$

Using Eqs. 4.11, 4.12 we obtain

$$\mathbf{C}(\nu) = \begin{bmatrix} \frac{1}{4\mu^2+\nu^2} & 0 \\ 0 & \frac{b'}{\mu\nu^2} \end{bmatrix} + 2b'' \begin{bmatrix} 0 & \frac{-i}{\nu(4\mu^2+\nu^2)} \\ \frac{i}{\nu(4\mu^2+\nu^2)} & \frac{2b''\mu}{b'\nu^2(4\mu^2+\nu^2)} \end{bmatrix} \tag{4.16}$$

The radial autocorrelations are those of an overdamped harmonic oscillator, as expected from the form of the scalar potential in Eq. 4.4, calculated near the circular limit cycle

$r = R_0$. Similarly, the autocorrelations of the phase angle $\sim \nu^{-2}$, as expected for phase diffusion. When the drive is non-computational or isochronous ($b'' = 0$), there is a simple, frequency-independent phase diffusion constant, and there are no cross correlations between the radial and phase fluctuations. A computational drive, however, introduces both a frequency-dependent phase diffusion constant (observed in hair-cell data [52] shown in chapter 2) and, more importantly, new correlations between the radial and phase fluctuations. Both of these effects arise because the internal drive changes its power input in response to the state of system, given by δr. All three correlation functions are shown in Fig. 4.3, where the solid (black) lines show the theoretical predictions, and the (colored) points the numerical results from our Brownian simulations. The error bars on the numerical data points represent the standard deviation of the mean.

A direct calculation of the response matrix

$$x_\alpha(\nu) = \chi_{\alpha\gamma}(\nu) f_\gamma(\nu) \tag{4.17}$$

gives

$$\chi(\nu) = \begin{bmatrix} \frac{1}{2\mu - i\nu} & 0 \\ -2b''\sqrt{\frac{\mu}{b'}}\frac{1}{(i\nu)(2\mu - i\nu)} & -\frac{1}{i\nu} \end{bmatrix}. \tag{4.18}$$

We define the deviation matrix from the GFDT as

$$\Delta_{\alpha\beta}(\nu) = \left[\chi_{\alpha\beta}(\nu) - \chi_{\beta\alpha}(-\nu)\right] T_{\beta\gamma} - 2i\nu C_{\alpha\gamma}(\nu), \tag{4.19}$$

and find that deviations from the GFDT (FDT in the co-moving frame associated with the deterministic limit cycle) appear only in the presence of an adaptive drive, reflected in $b'' \neq 0$:

$$\Delta(\nu) = 2b'' \begin{bmatrix} 0 & \frac{(-\nu + 2i\mu)}{(4\mu^2\nu + \nu^3)} \\ \frac{(\nu + 2i\mu)}{(4\mu^2\nu + \nu^3)} & \frac{-i4b''\mu}{b'\nu(4\mu^2 + \nu^2)} \end{bmatrix}. \tag{4.20}$$

Only the Lorentzian fluctuations of the radial δr variable obey the GFDT when the drive is computational. When $b'' \neq 0$, the feedback between the azimuthal driving force and the radial oscillations breaks the GFDT due to both new cross correlations $C_{r\phi}$ and a modified

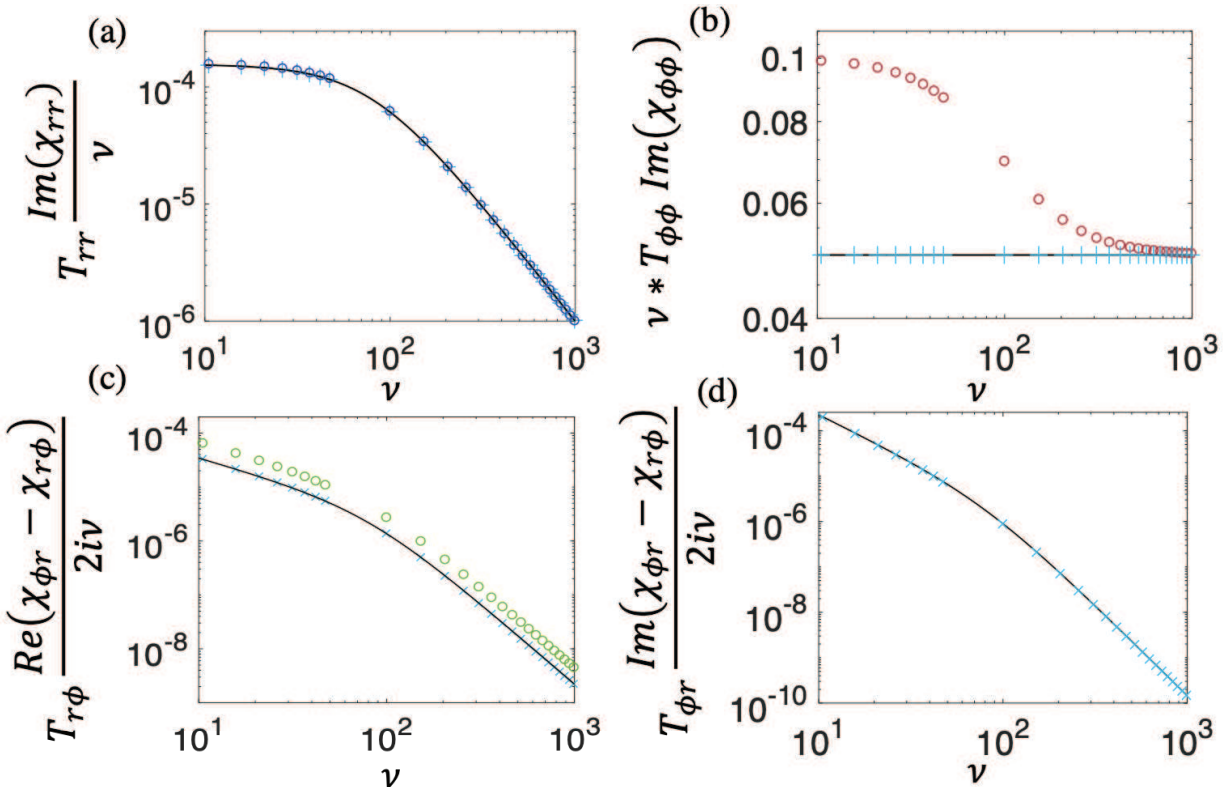

Figure 4.4: Breakdown of GFDT for the Hopf oscillator

We compare the measured two-point correlations of Fig. 4.3 (circles) with those inferred from numerical response function data via GFDT (light blue crosses). The latter agrees with the analytical calculations (black lines) of $[\chi_{\alpha\beta}(\nu) - \chi_{\beta\alpha}(-\nu)]\,\mathcal{T}_{\beta\gamma}$ using Eq. 4.18. While the GFDT predicted correlation function agrees with observations for the radial fluctuations (panel (a)), it differs from those for the phase diffusion (panel (b)). In the bottom panels, we show the real (panel (c)) and imaginary (panel (d)) parts of $\chi_{\phi r}(\nu) - \chi_{r\phi}(-\nu)$. The former is related to the cross-correlations of δr and $\delta\phi$. The GFDT prediction of these correlations also fails (blue crosses vs green circles).

phase diffusion $C_{\phi\phi}$. This breakdown of the GDFT to the best of our knowledge cannot be removed by an appropriate change of variables, as has been explored for nonequilibrium fluctuations about a fixed point [42].

In Fig. 4.4(a), we show the correspondence between the correlation data obtained from numerical simulations (dark blue circles) and that expected from the response function (light blue crosses) for the radial variable based on the GFDT. In Fig. 4.4(b), where we compare the frequency-dependent phase diffusion constant measured from the numerical data (red circles) and the GFDT-based prediction (blue crosses), we see the failure of the GFDT for the computationally driven system. Clear deviations are seen at low frequencies, as predicted by Eq. 4.20. When the drive is not computational ($b'' = 0$) – see Fig. 4.15 in appendix 4.5.3 – these deviations vanish. The GFDT is once again obeyed. We also show the real and imaginary parts of $\chi_{\phi r}(\nu) - \chi_{r\phi}(-\nu)$ in panels (c) and (d) respectively. The former predicts the cross-correlations of the radial and phase fluctuations via GFDT. Those predicted blue crosses illustrated in panel (c) also fail to agree with the simulation data (green circles). In all panels (a - d), we show our analytical calculations of $[\chi_{\alpha\beta}(\nu) - \chi_{\beta\alpha}(-\nu)]\,\mathcal{T}_{\beta\gamma}$ as obtained from Eq. 4.18 (black lines). These are in universal agreement with the GFDT-based correlation functions inferred from numerically simulated response function data (light blue crosses).

4.3 Three-state model with a computational drive

4.3.1 Model I

To better understand the role of a computational drive in breaking GFDT, it is helpful to examine the same phenomenon in a more simple, finite-state model. We analyze two such three-state systems. First, as shown in Fig. 4.5, we consider a system with three states labeled by $s = \{-1, 0, +1\}$ and having energies $\{\epsilon, 0, 0\}$. When calculating occupation probabilities, the Boltzmann constant k_B is assumed to be 1 without loss of generality. The system's discrete-time dynamics combine a drift velocity $v_{\text{drift}} = 0, 1, 2$ anticlockwise around the triangle of states – see Fig. 4.5 – and stochastic hopping. v_{drift} is the drive that

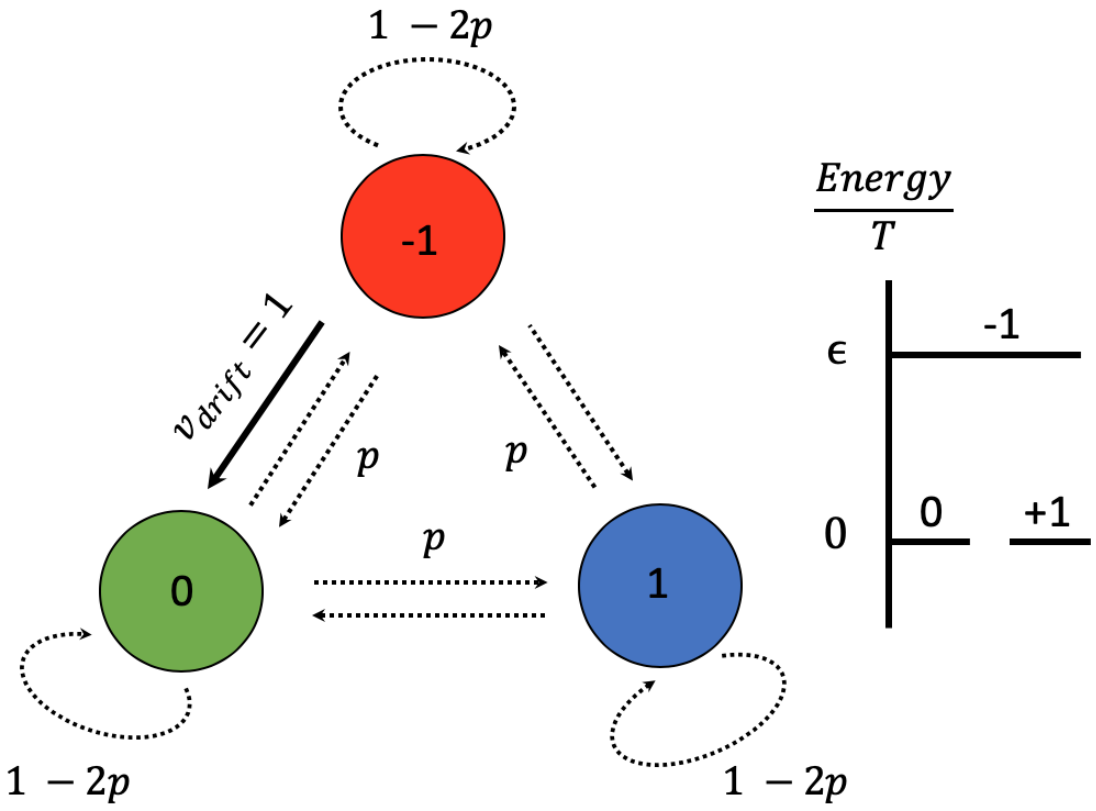

Figure 4.5: Schematic diagram of the three-state system

Its states $\{-1, 0, 1\}$ are denoted by red, green, and blue disks and have energies $\{\epsilon, 0, 0\}$ respectively. In the equilibrium steady state, $v_{\text{drift}} = 0$. Conversely, when $v_{drift} = 1$ or 2, the system has a non-zero internal drive. The resulting steady state probability current may be removed by working in a co-moving frame.

introduces probability current in the non-equilibrium steady-state system, thus explicitly breaking detailed balance. For example, the deterministic system (p = 0) with $v_{\text{drift}} = 1(2)$ generates uniform anticlockwise (clockwise) motion of state occupation around the triangle shown in Fig. 4.5. For $v_{\text{drift}} = 1$, the occupation probability distribution traverses from state m to n such that n lies circularly to the right of m in the set $\{-1, 0, 1\}$. When $v_{\text{drift}} = 2$, it traverses in the opposite direction. Meanwhile the hopping rate p, $0 \leq p \leq 0.5$, is unbiased when $\epsilon = 0$ and generates diffusion amongst the three states. Thus the stochastic system ($p > 0$) with no drift ($v_{\text{drift}} = 0$) obeys detailed balance and corresponds to an equilibrium system. The role of the constant drift is then to create a finite state analog of the stochastic non-computationally driven Hopf model ($\omega_0 \neq 0, b" = 0$). The power input of this drive when $v_{\text{drift}} = 1$, $m = -1$ and $n = 0$ is,

$$P = (1-2p)\epsilon_{-1} - p\epsilon_0 \tag{4.21}$$

$$= (1-2p)\ln\frac{1-2p}{p}. \tag{4.22}$$

We arrive at this value by falsely assuming that the system satisfies detailed balance and the difference in rates can in fact be attributed to the difference in energy levels of the states -1 and 0. This gives us $\epsilon_{-1} = \ln\frac{1-2p}{p}$ if $\epsilon_0 = 0$.

We will later incorporate a computational drive by allowing the value of v_{drift} to temporally depend upon the history of state occupation which allows us to study the finite-state analog of the computationally-driven Hopf oscillator ($\omega_0 = 0, b" \neq 0$).

We incorporate such computation by setting

$$v_{drift}(t_i) = \lfloor \sum_{j=1}^{\infty} r e^{\lambda(i-j)} \xi\left(t_{i-j}\right) \rfloor \mod 3, \tag{4.23}$$

where $\lfloor . \rfloor$ is the floor function returning the integer part of its argument. We have also introduced the function $\xi(t_{i-j})$, which takes the value $1, -1$ or 0 when the system is in state $1, -1$ or 0 respectively at time t_{i-j}. In turn $\xi(t_i)$ is defined using the indicator functions $\sigma_k(t_i)$ which are 1 (0) when the system is (is not) in state k at time t_i:

$$\xi\left(t_i\right) = (-1)^{\sigma_{-1}(t_i)}\left[1 - \sigma_0(t_i)\right]. \tag{4.24}$$

Finally we note that the computational drive depends on two constants r, which determines the responsiveness of the computation, and λ, which sets the memory time λ^{-1} for the drive.

We first perform numerical simulations of the symmetric model ($\epsilon = 0$) that obeys detailed balance ($v_{\text{drift}} = 0$). We tracked the stochastic trajectories ($p = 0.02$) of 40 realizations of the system over a total of 4×10^4 time steps for each of the realizations. For additional details of these simulations, we refer the reader to Appendix 4.5.1. Setting $\epsilon = 0$ resulted in the occupation probability of the three states being one third, as expected (not shown). From these trajectories, we also compute all two-point correlation functions

$$C_{nm}(\tau) = \frac{1}{2}\left[\langle \sigma_n(t_i + \tau)\sigma_m(t_i)\rangle + \langle \sigma_m(t_i + \tau)\sigma_n(t_i)\rangle\right]. \tag{4.25}$$

The average is taken over an ensemble of trajectories at time delay τ. Under the assumption of ergodicity, one may alternatively average over longer time series from one trajectory. Further, an experimentalist investigating the stochastic dynamics of a nonequilibrium steady state system might implicitly assume time reversal invariance. Therefore our definition of the correlation function was chosen to make it explicitly time reversal invariant when $n \neq m$. Clearly, if the driven system admits a non-vanishing probability current, this symmetry will not be valid. However, since we propose using the violation of fluctuation-dissipation theorems as a test for both an underlying limit cycle in general and a computationally driven one in particular, we will suppose *a priori* that the correlation data is analyzed assuming time-reversal invariance in the steady state.

To test the standard FDT, we numerically obtained the response of the occupation probability of state n, $p_n(t) = \langle \sigma_n(t)\rangle$, to a force conjugate to the occupation of state -1,

$$\delta p_n(t_i) = -\sum_{j=-\infty}^{i} \chi_{n,-1}(t_i - t_j)\delta\epsilon_{-1}(t_j), \tag{4.26}$$

by setting the energy of that state to $\epsilon_{-1} = 3$ for one time step and observing the subsequent stochastic evolution of the system. We confirmed that our perturbation was in the linear response regime by varying ϵ_{-1} – see appendix 4.5.4. In Fig. 4.6, we plot $\chi_{-1,-1}(\tau)$, $\chi_{0,-1}(\tau)$, and $\chi_{1,-1}(\tau)$ as solid red, green, and blue curves respectively. As expected, the transient

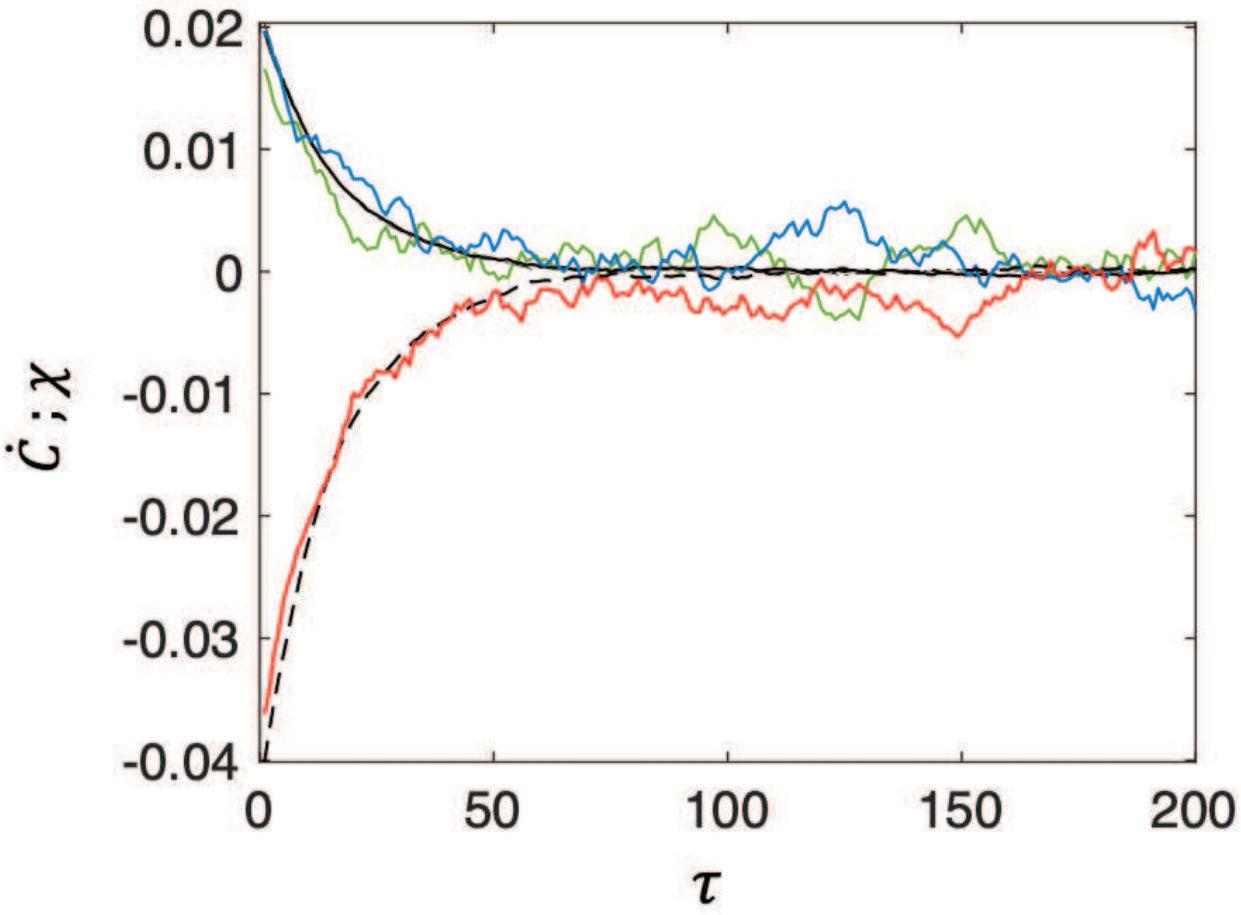

Figure 4.6: Test of FDT for the equilibrium system

By comparing $\dot{C}_{-1,-1}$ (black dashed line) and $\chi_{-1,-1}$ (red line), we check that the response of the system to a force driving it out of the -1 state matches the appropriate correlation function derivative. We also find the expected correspondence between $\dot{C}_{0,-1}$ (black solid line) and $\chi_{0,-1}$ (green line) as well as $\dot{C}_{1,-1}$ (black dashed-dot line) and $\chi_{1,-1}$ (blue line).

increase in the energy of the -1 state suppresses the occupation probability of that state and symmetrically increases the occupation probability of the other two states: $+1$ and 0. The system recovers its equilibrium probabilities exponentially with a decay rate of about 20 inverse time units.

The standard FDT requires that these response functions must be equal to the time derivative of the correlation functions $\dot{C}_{n,-1}(\tau)$ evaluated at time delay τ. We plot the numerically obtained time derivatives of the correlation functions $\dot{C}_{-1,-1}$, $\dot{C}_{0,-1}$ and $\dot{C}_{1,-1}$ as dashed black, solid black, and dashed-dot black lines respectively in Fig. 4.6. As expected, we find that the time derivatives of the correlation functions of state occupation agree with the responses of the occupation probability to a force conjugate to that variable. All the correlation functions in this figure were normalized such that $C_{n,m}(0) = \delta_{n,m}$. The response functions were multiplied by an empirical temperature, in this case 0.2. The remaining plots for this system are all normalized using this value.

We now consider the case of a constant drive, setting $v_{\text{drift}} = 1$. In Fig. 4.7(a), we demonstrate the violation of FDT by this system. The red curve is the numerically computed response function $\chi_{-1,-1}(\tau)$, and the dashed black curve is the derivative of the corresponding correlation function $\dot{C}_{-1,-1}(\tau)$, whose oscillatory nature can be attributed to the internal drive of the model. The standard FDT requires these to be equal. They are not, indicating breakdown of FDT. However, for this model we propose that one may obtain a valid GFDT similar to that of [53] by evaluating the correlation and response functions in a reference frame co-moving with velocity v_{drift}. To transform to the co-moving frame, we introduce new indicator functions,

$$\tilde{\sigma}_i\left(t_j\right) = \sigma_{\left(i+v_{\text{drift}}t_j\right)} \mod 3. \tag{4.27}$$

We find that in the co-moving frame the numerically computed response function of $\chi_{f-1,-1}$ (red curve) agrees with $\dot{C}_{f-1,-1}$ (dashed black line) as seen in Fig. 4.7(b). The values of these two functions, as a matter of fact, are similar to those of the equilibrium system (Fig. 4.6). Due to the symmetry of the problem, we only show plots for the -1 state. For the other two states the reader is referred to Appendix 4.5.3.

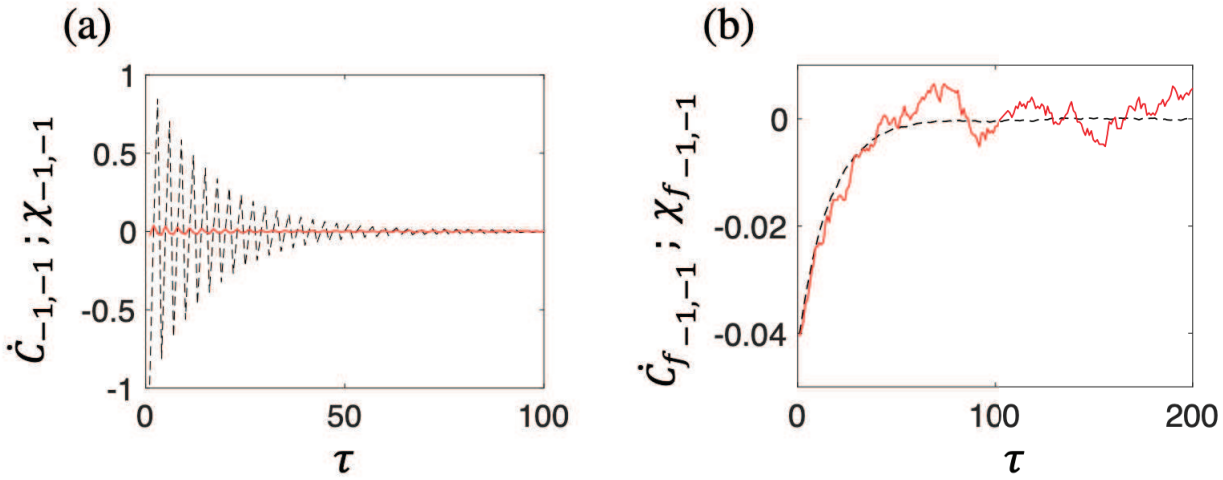

Figure 4.7: Driven system violates FDT

(a) In the presence of an internal drive, the system violates FDT, as can be seen in the comparison of its linear response function $\chi_{-1,-1}$ (red) and the time derivative of its auto-correlation function $\dot{C}_{-1,-1}$ (black dashed). (b) However, upon transforming to the co-moving reference frame, we show that the three-state model satisfies GFDT. The derivative $\dot{C}_{f-1,-1}$ (dashed black) and the response function $\chi_{f-1,-1}$ (red) are now in agreement with each other.

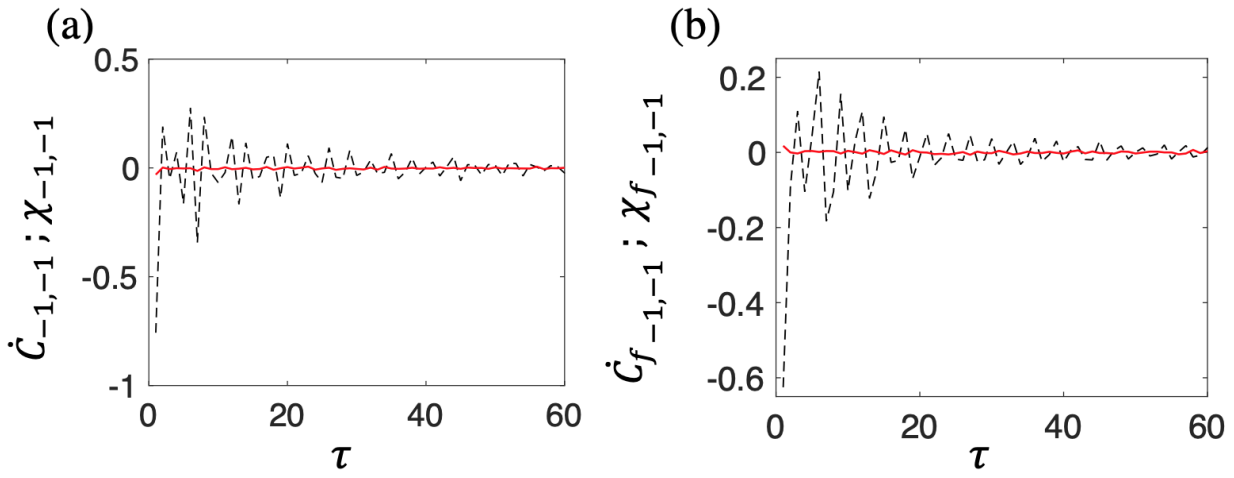

Figure 4.8: The three-state model with a computational drive

(a) We juxtapose the derivative $\dot{C}_{-1,-1}$ (dashed black) and the response function $\chi_{-1,-1}$ (red) to illustrate the breakdown of FDT. (b) Furthermore, unlike the one illustrated in Fig. 4.7, this system also violates GFDT, as is evident by comparing $\dot{C}_{f-1,-1}$ and $\chi_{f-1,-1}$, calculated in the associated co-moving frame.

Next, we study the computationally driven three-state model by choosing $r = 2$ and $\lambda = 0.1$. This non-Markovian system violates FDT as shown by the plots in Fig. 4.8(a). The time derivative of the auto-correlation $C_{-1,-1}$ (black dashed line) deviates appreciably from the response function $\chi_{-1,-1}$ (shown in red). Plots for the other two states are given in Appendix 4.5.5. Moreover, in the co-moving frame, the computational nature of the internal drive precludes restoration of the generalized theorem (Fig. 4.8(b)). In order to test the GFDT in the rotating frame we chose a reference frame co-moving with the average drift velocity, which in our simulations was 1. There exists no other reference frame that may restore the GFDT in the computationally driven system. The breakdown of both FDT and GFDT relations in this system is similar to the computationally-driven Hopf limit cycle with parameter b" > 0.

One may ask whether any time variation of the drive is sufficient to invalidate the FDT or the GFDT. To address this, we considered a randomly varying drive that has the same average drift velocity as the one examined above. We consider the three-state model with a

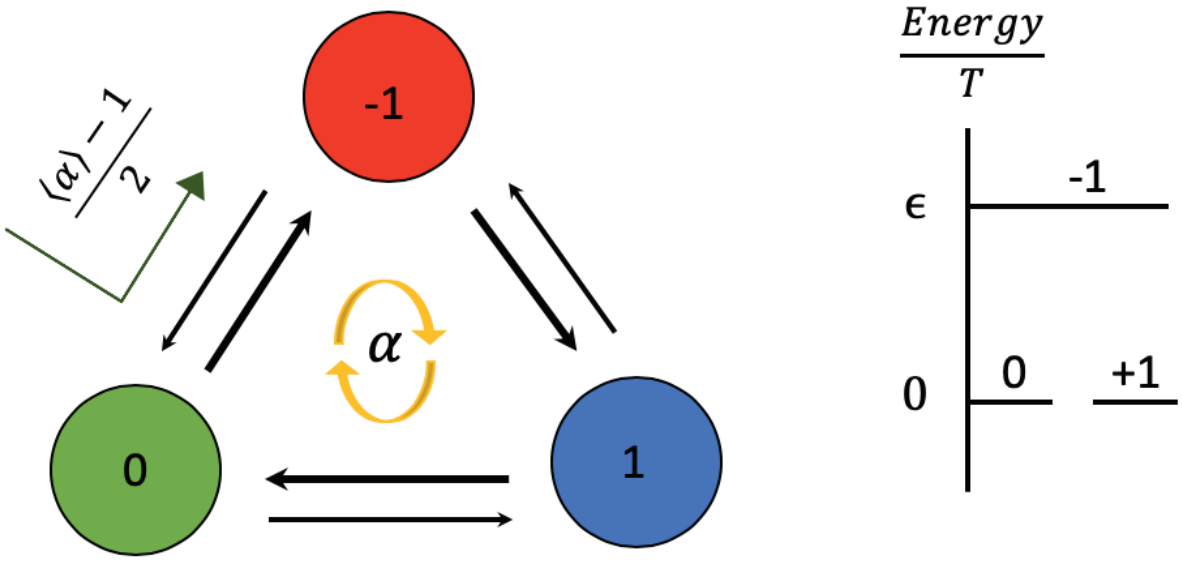

Figure 4.9: Schematic diagram of the three-state system

States $\{-1, 0, 1\}$ are denoted by red, green, and blue disks respectively. These states have energies $\{\epsilon, 0, 0\}$. In the nonequilibrium steady state, the clockwise transitions rates are enhanced over their detailed-balance values by $\alpha(t)$. The resulting steady state probability current may again be removed by working in a co-moving frame.

randomly varying drift velocity that has equal probabilities at each time step of being 0,1,or 2. There are no temporal correlations in the stochastic v_{drift}. It is easy to see that the mean drift velocity is unity. This system, unlike the computationally-driven three-state model, obeys the GFDT (data not shown). We conclude that the state-dependent mechanism of the drive is required to invalidate the GFDT.

4.3.2 Model II

We also examine the stochastic dynamics of a more general three-state model defined by the discrete-time master equation for the probability $p_n(t)$ of observing the system in state n = -1,0,1 at time t_i :

$$p_n\left(t_{i+1}\right) = \sum_{m \neq n} \left[p_m(t_i)\alpha_{mn}(t_i) - p_n(t_i)\alpha_{nm}(t_i)\right]. \tag{4.28}$$

See Fig. 4.9 for a schematic representation. The system evolves via six transition probabilities, *e.g.*, the transition rate from state n to m at time t_i: $\alpha_{nm}(t_i)$. These six transition probabilities are given by the following rules. We set

$$\alpha_{nm} = \alpha_{mn} e^{\epsilon_n - \epsilon_m} \alpha(t_i), \tag{4.29}$$

where n is to the right of m in the list of states $\{-1, 0, 1\}$ or its cyclic permutations. The factor $\alpha(t)$ allows us to drive the system into a nonequilibrium steady-state by breaking detailed balance. By choosing $\alpha(t)$ to be a constant greater than one, we generate a clockwise probability current – see Fig. 4.9 – in steady state. Such a choice is analogous to turning on a non-computational drive in the isochronous Hopf model ($\omega_0 \neq 0, b'' = 0$) of the hair cell oscillator. Later, to introduce a computational process, we will consider the case in which the drive depends upon the history of the system by setting

$$\alpha\left(t_i\right) = 1 + r \sum_{j=1}^{\infty} e^{\lambda(i-j)} \xi\left(t_{i-j}\right), \tag{4.30}$$

where $\xi(t_{i-j})$ has been defined in Eq. 5.6.

The strength of the computation is again controlled by r. λ controls the exponential decay rate of the memory kernel in Eq. 4.30. It is measured in inverse time units $\delta t = t_{i+1} - t_i$, which we always set to 0.01. The effect of the feedback is to increase the drive when the system has recently been in the $+1$ state and decrease it when the system has visited the -1 state. The simulations for this three-state model, as for the one before, were performed using 40 realizations over 4×10^4 time steps.

We first study the detailed-balance system, which can easily be shown to be equivalent to the non-driven case of the first three-state model. In Fig. 4.10, we illustrate the time derivatives $\dot{C}_{-1,-1}(\tau)$, $\dot{C}_{0,-1}(\tau)$ and $\dot{C}_{1,-1}(\tau)$ as the dashed black, solid black and dot-dashed black lines respectively. Also shown are the linear response functions of $\chi_{-1,-1}(\tau)$ (red), $\chi_{0,-1}(\tau)$(green) and $\chi_{1,-1}(\tau)$(blue), which, as anticipated, overlap with their corresponding correlation derivatives. The empirical temperature of this system is 0.11.

We now repeat this measurement in a non-equilibrium system by setting $\alpha(t) = 98$. This choice of a non-computational drive breaks detailed balance and is similar to the Hopf

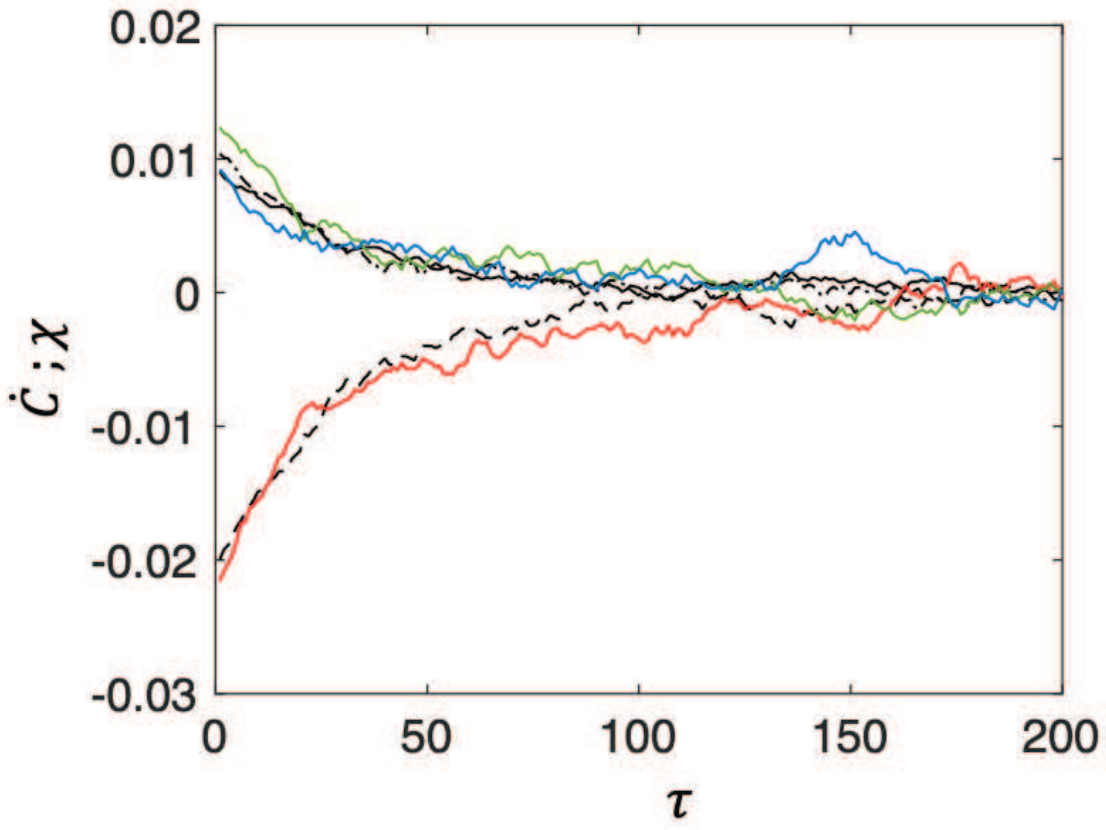

Figure 4.10: The FDT relation is satisfied by the detailed-balance system.

As in Fig. 4.6, we compare the response of the system to a change in the energy of state -1 with the corresponding correlation function derivatives. We show $\dot{C}_{-1,-,1}$ (dashed black), $\dot{C}_{0,-,1}$ (solid black), $\dot{C}_{1,-,1}$ (dot dashed black), $\chi_{-1,-,1}$ (red), $\chi_{0,-,1}$ (green) and $\chi_{1,-,1}$ (blue).

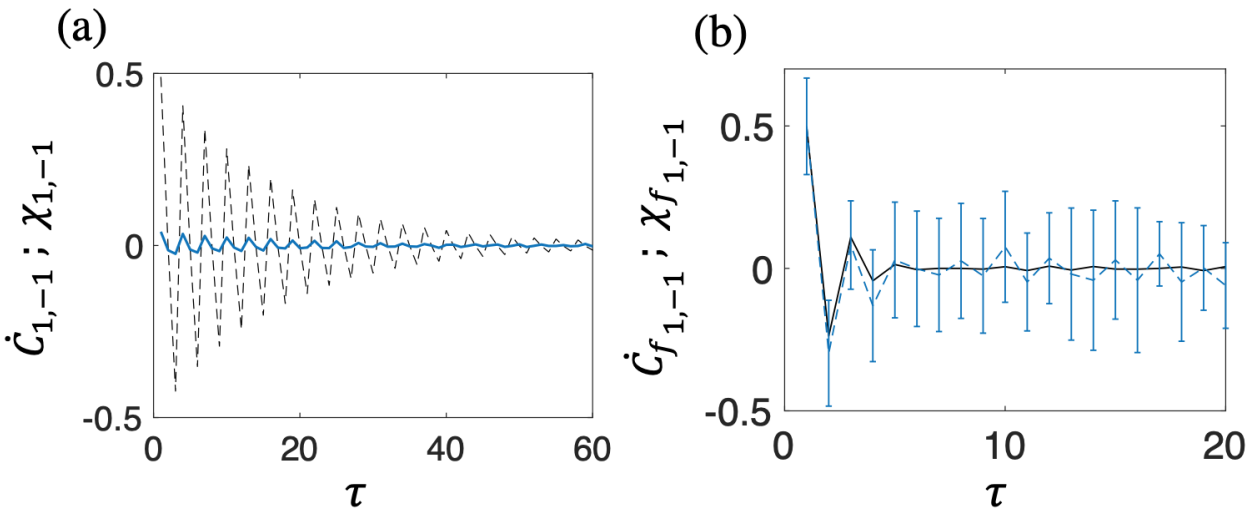

Figure 4.11: FDT violation in the broken detailed balance system at $\alpha(t) = 98$. (a)We compare the time derivative of the cross-correlation $\dot{C}_{1,-1}$ (black line) and the response function $\chi_{1,-1}$ (blue dashed line). (b) In the co-moving frame the GFDT holds as seen by comparing correlation $\dot{C}_{f_{1,-1}}$ (black line) and response function $\chi_{f_{1,-1}}$ (dashed blue line). Error bars denote the standard deviation of the mean.

model of hair cell oscillations with $b'' = 0$ but $\omega > 0$. In Fig. 4.11(a), we show the measured response function $\chi_{1,-1}(\tau)$. As in the equilibrium case, the applied force pushes the system out of the -1 state into the $0, 1$ states. But, unlike the equilibrium case, the change in probability oscillates in time due to the detailed-balance-breaking drive. For example, the occupation probability of $+1$ cycles the three-state system in the clockwise direction while slowly decaying over longer times (not shown), resulting in an oscillatory response function as in the dashed blue line in the figure. The correlation function $C_{1,-1}(\tau)$ also shows this oscillatory behavior, but its derivative (black line) *does not* match the corresponding response function. The standard FDT is violated.

We can, however, obtain a GFDT in the driven system by working in a "rotating" reference frame – one that moves with the clockwise probability current of the non-equilibrium steady state. Unlike the previous three-state model the Frenet frame state occupation variables are not well-defined. The frame's velocity is determined by the mean probability

current of the system. Moving at the speed of $\frac{\alpha-1}{2}$, we now find that the response function of the $+1$ state in this co-rotating frame to a force acting on the -1 state – the dashed blue line in Fig. 4.11(b) – agrees with the numerically measured time derivative of the correlation function (calculated using Eq. 4.25), shown as the black line in this figure. The error bars represent the standard deviation of the mean for the response data. We find a similar agreement between the other correlation and response functions in the co-rotating frame; these are shown in Appendix 4.5.3 (Figs. 4.18 and 4.19). While neither the time derivative of the correlation function nor the response function in the driven system agrees with predictions based on the equilibrium system, their agreement with each other shows that a generalized fluctuation dissipation theorem holds in the driven system, as expected based on the work of Seifert and collaborators [51]. The appearance of the GFDT in the co-rotating frame, which zeros out the steady-state probability current of the driven system, is analogous to our observation of a similar fluctuation theorem in the isochronous Hopf oscillator system.

We now introduce a computational drive in this more general three-state system via Eq. 4.30, taking $r = 0.095$ and $\lambda = 0.1$. This is analogous to the nonisochronous Hopf system. We obtain a steady-state system with non-equal occupation probabilities of the three states in steady state. In spite of the fact that the energies of all three states are equal, the computational drive breaks the permutation symmetry of these states, as shown in panel (a) of Fig. 4.12. As a result, the simple occupation probabilities of the states in this nonequilibrium steady state do not reflect their relative energies. Conversely, just by observing these occupation probabilities, one might conclude erroneously that this system was in equilibrium with a particular spectrum of energy levels. To test this conclusion, one must not only examine these probabilities but also compare the correlation and response functions of the system.

In the three remaining panels (b-d) of Fig. 4.12, we show a comparison of the time derivative of the correlation function $\dot{C}_{k,-1}(\tau)$ and the response function $\chi_{k,-1}(\tau)$ for $k = -1, 0, +1$ in panels (b), (c), and (d) respectively. The standard FDT fails vividly for one set of measurements: $\dot{C}_{1,-1}(\tau) \neq \chi_{1,-1}(\tau)$ – see Fig. 4.12(d).

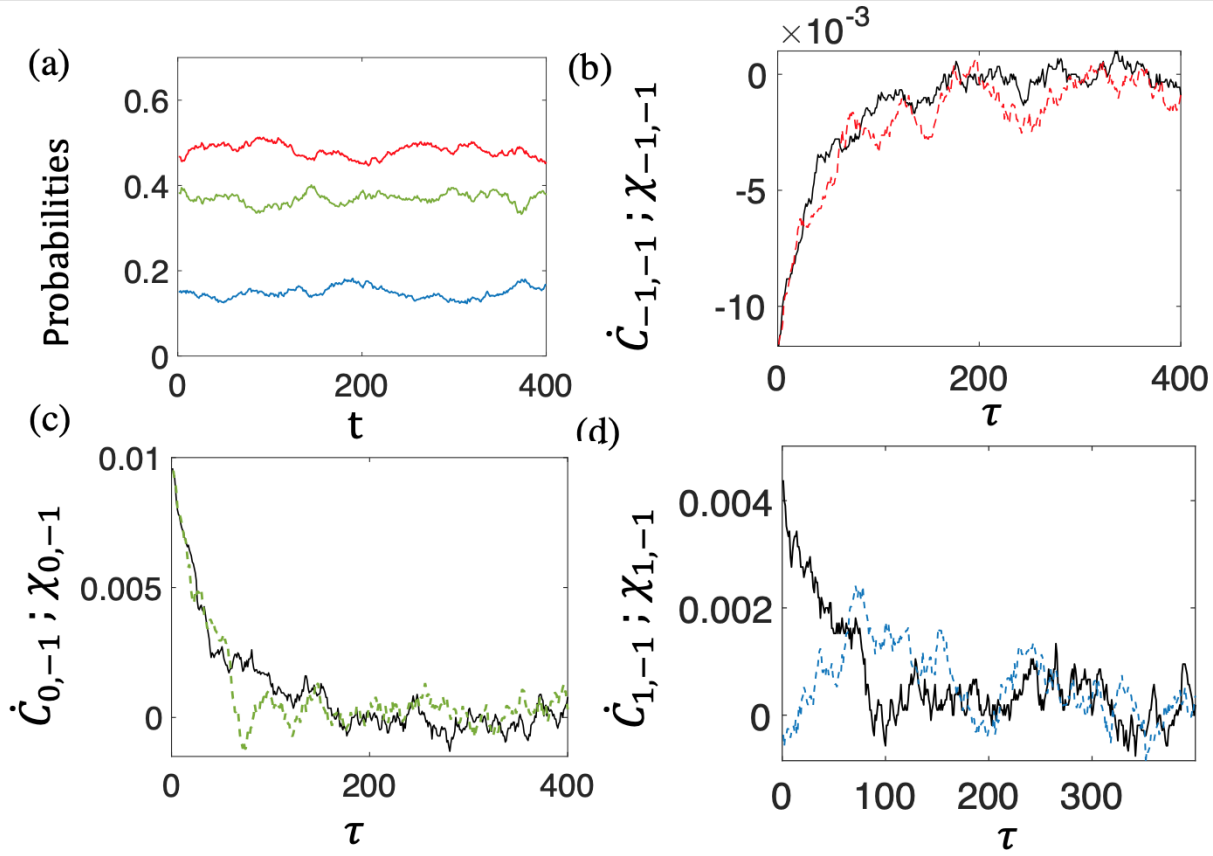

Figure 4.12: The three-state system with a computational drive, Eq. 4.30.

(a) With the drive parameters at r = 0.095 and $\lambda = 0.1$, the states are no longer occupied with equal probability even when their occupation energies are equal. In panels (b)-(d) we compare $\dot{C}$ (black solid) with the appropriate χ (color) in the ground frame. In (d) we observe significant deviations from the FDT.

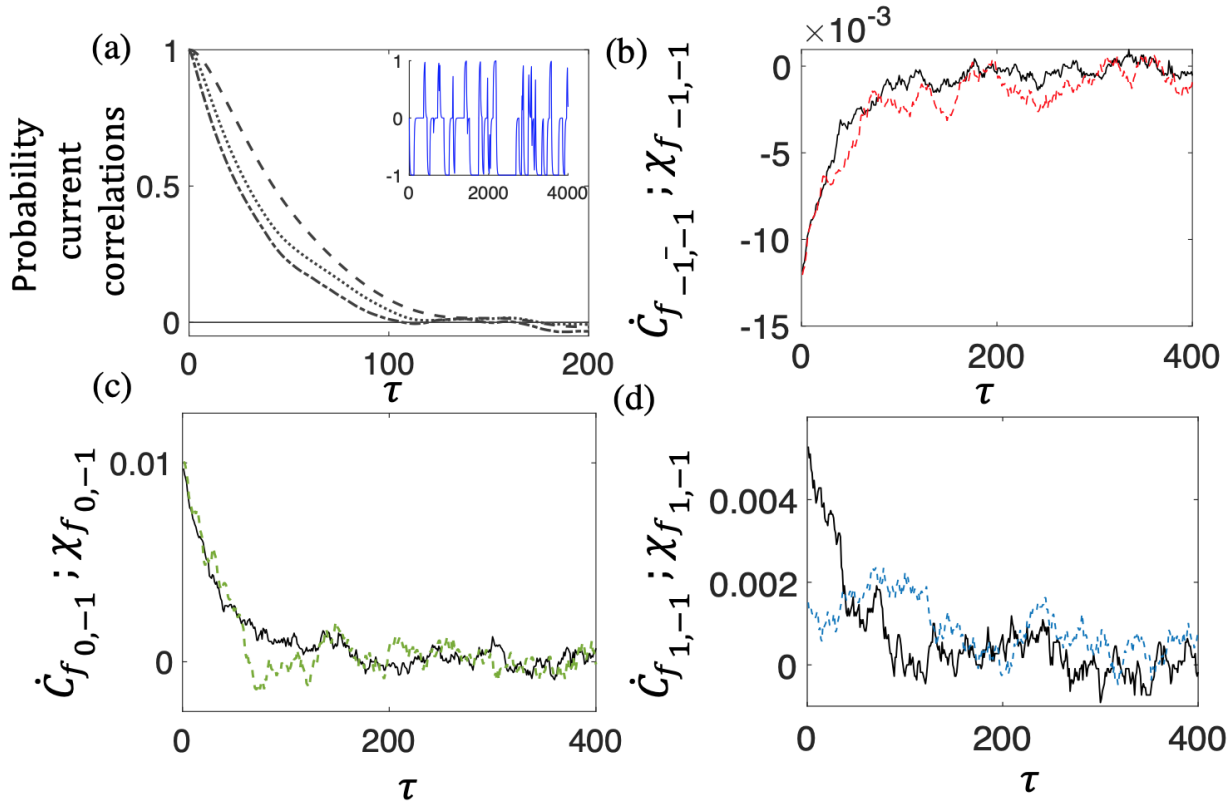

Figure 4.13: Violation of GFDT in the computationally-driven three state model (a) Correlation of the steady-state probability current $\alpha(t) - 1$ for different λ and r values: $r = 0.095, \lambda = 0.1$ (dashed line), $r = 0.095, \lambda = 0.25$ (dotted line), $r = 0.095, \lambda = 1$ (dot-dashed line) and $r = 0$ (solid). For $r = 0.095$ and $\lambda = 0.1$, we show the stochastic current from a representative trajectory (inset). In panels (b)-(d), we illustrate the violation of the GFDT when working in a co-moving frame that works to eliminate the mean probability current. Comparing with Fig. 4.12, we see that this frame partially, but rather imperfectly restores the fluctuation theorem.

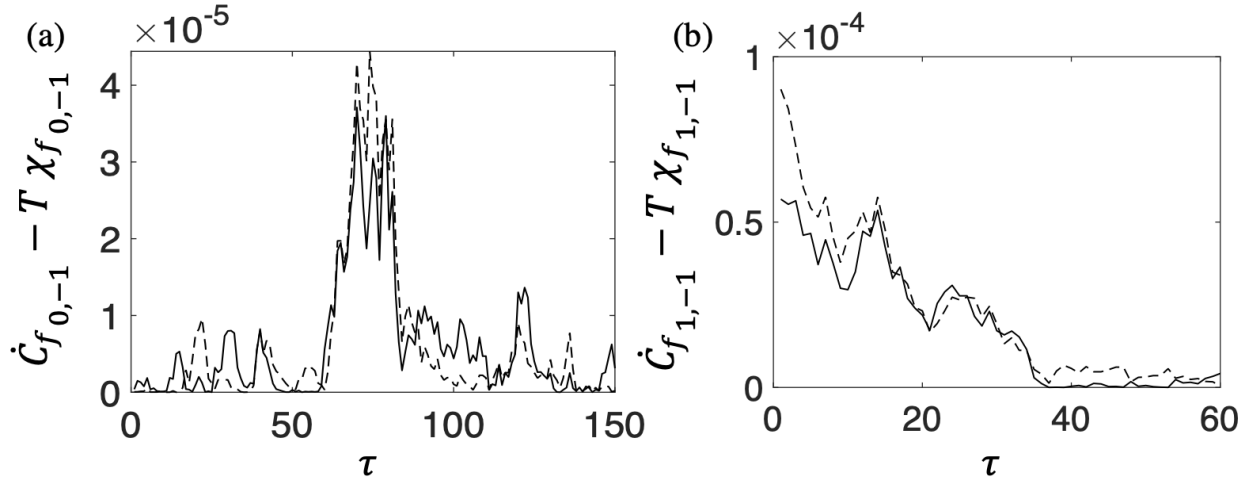

Figure 4.14: L2 norm illustrating partial restoration of GFDT

In panels (a) and (b) we compare the plots in Figs. 4.12 (c), (d) and 4.13 (c), (d) using the L2 norm of the difference between the time derivative of the correlation functions and the response functions. The dashed lines denote the differences in the lab frame (FDT) while the solid lines denote those in the frenet frame (GFDT).

We examine the probability current in this more general three-state model. We show the temporal correlation function of the current in the computationally driven system in Fig. 4.13 (a). In the inset of the same panel we show a representative part of the time series of the probability current from which the correlation functions were obtained. Clearly, as λ is decreased (drive memory time increased) the probability current's correlation time increases, so that the effect of the drive's computation is reduced. Its current value depends on a long time average of the system, which itself necessarily varies only slowly in time. As a result, we find that with sufficiently long memory times, the computationally driven system begins to resemble a non-computationally driven one, so long as r/λ remains fixed. As a result, the magnitude of the violations of the GFDT will decrease.

Given this intuition, it is interesting to examine the residual violation of the GFDT in a system driven by a weakly computing drive. Due to the current fluctuations that are still correlated with the state of the system, it is clear that no co-moving frame can precisely reestablish the GFDT. But we can find the best approximation to the GFDT

in this system by working in a co-moving reference frame selected to eliminate the mean probability current, *i.e.*, we chose a velocity $\frac{\langle\alpha\rangle-1}{2}$ to minimize GFDT discrepancies. In the remaining panels of Fig. 4.13 (b-d) we do this. The results shown in Figs. 4.13(c) and 4.13(d) demonstrate that the GFDT still fails due to feedback between the system and the drive. But a comparison between Fig. 4.13(c) and Fig. 4.13(d) measured in the co-moving frame with Fig. 4.12(c) and Fig. 4.12(d), showing the same quantities in the non-rotating lab frame, demonstrates the partial restoration of the GFDT. Fig. 4.14 shows the reduction in L2 norm of the difference between time derivative of the correlation function $\dot{C}_{k,-1}(\tau)$ and the response function $\chi_{k,-1}(\tau)$. The decrease in L2 norm metric is more pronounced for state 1 (panel (b)). The dashed black lines illustrate the L2 norms for differences calculated in the lab (ground) frame, those calculated in the frenet frame are shown by the solid black lines. With even weaker drive adaptation, this restoration of the GFDT further improves (data not shown).

4.4 Discussion

Systems that exhibit nonequilibrium steady states violate the fluctuation dissipation theorem. Failure to satisfy the conditions set by that theorem has therefore been used as a test of the nonequilibrium nature of various stochastic steady-states, indicating the presence of an energy consuming process. There are, however, multiple ways to violate the FDT. For example, in actomyosin gels, one observes enhanced strain fluctuations at low frequencies due to motor activity. This is a consequence of the fact that the motor dynamics introduce force autocorrelations with a colored noise spectrum. As a result, the strain fluctuations do not correspond to the (visco-) elastic system at any temperature. One outcome of this analysis and that of related systems is that one can use the breakdown of the FDT as a type of sensor tuned to the detection of nonequilibrium steady states. As complex biological systems frequently include active processes, such a tool is useful for experimentally probing the underlying mechanisms.

In this chapter, we consider a different class of nonequilibrium systems, which break

the FDT: those driven into stochastic steady states characterized by a stationary probability current and broken detailed balance. In this case, previous work has introduced a new class of generalized fluctuation theorems based on working in a co-moving reference frame that zeroes out the stationary probability current. When fluctuations are now viewed in that frame there is a familiar relation between them and the response function(s) of the system. The simplest hair cell model provides an example of such a stochastic driven system; our previous work on fluctuations in a Frenet frame co-moving with the mean probability current of the system reproduced the expected GFDT. This model, however, introduces a new complication – an adaptive drive: the external drive maintaining the nonequilibrium steady state in effect measures the state of the system and adapts its power input based on that measurement.

We first observed in the Hopf hair cell oscillator model with adaptive drive, the violation of GFDT. Moreover, the quantitative degree of that violation is proportional to single model parameter b'' controlling degree of adaptation of the drive, as shown by our analytic results. To isolate this feature of drive adaptation in an even simpler system, we introduced a three state system defined by a discrete time master equation. By introducing a violation of detailed balance, we produced states with a nonzero probability current. These violate the standard FDT, as expected. Moreover, by introducing a co-rotating frame to zero the probability current in the three-state system we obtain a GFDT, as is consistent with previous work. But when we introduce drive adaptation by allowing the probability current to adjust based on the history of the system's trajectory, we once again observe the breakdown of the GFDT.

Based on this work, we propose that just as the failure of the FDT has been used to test for nonequilibrium steady states, one should be able to look for the breakdown of the GFDT as a test of stochastic steady states driven out of equilibrium by an adaptive drive. Two emblematic features of living systems are long-lived nonequilibrium steady states and homeostasis. One method to maintain homeostatic control of driven states is through an adaptive drive, as seen in the non-isochronous hair cell model. Other example of a similar homeostatic control through an adaptive drive may not be as readily apparent in complex

biological systems. We propose that one may use the breakdown of the GFDT as a tool to look for them.

4.5 Appendix

4.5.1 Simulation details

Hopf oscillator The stochastic and externally perturbed Hopf oscillator of Eq. 4.1 was simulated using the 4^{th}- order Runge-Kutta method for a duration of 60s, with a time step of 10^{-4}s. We explore a large range in the amplitude of the noise variances $\langle \eta_x^2 \rangle$ and $\langle \eta_y^2 \rangle$ (where, $\langle \eta_x^2 \rangle = \langle \eta_y^2 \rangle$) covering 10^{-7} to 0.4, as well as a range of perturbative forces 10^{-3} to 10^{-1}. All throughout, the amplitude of mean limit cycle oscillators was held to be $O(1)$. While consistent results were obtained over the full span of these values, Figs. 4.3 and 4.4 employ the highest value of force and noise in their respective ranges.

Mean limit cycle of the Hopf oscillator The Hopf oscillator's phase space $\{-\pi, \pi\}$ is partitioned into nearly 200 bins. Trajectories in each bin are then averaged, resulting in the mean curve.

Three-state model Eq. 4.28 was numerically computed using a random number generator that outputs a value in the range [0 - 1]. Comparison of this value with the occupation probabilities of the three states determines the stochastic trajectory for each of the 40 realizations. Further, since we define Fig. 4.9 in terms of transition rates, these probabilities are the product of the respective rates and a time step duration of 10^{-2}. Data was always taken after running the system long enough so that its initial conditions were no longer relevant. All simulations were performed in MATLAB (R2019a, the MathWorks, Natick, MA).

4.5.2 Electrically-charged particle in a magnetic field

The motion of a damped, harmonically bound charged particle of mass m and charge e in the xy plane under the influence of magnetic field $H\hat{z}$ is given by,

$$\ddot{\hat{r}} + \gamma\dot{\hat{r}} + \omega_0^2\hat{r} = \frac{e}{mc}\dot{\hat{r}} \times H \tag{4.31}$$

where γ is the friction coefficient, ω_0 is the natural frequency of the oscillator ($\omega_0 = \sqrt{k/m}$ for a Hookean spring constant k), and c the speed of light. The equations of motion may be written in terms of x and y as

$$\ddot{x} + \gamma\dot{x} + \omega_0^2 x = \frac{eH}{mc}\dot{y}, \tag{4.32}$$

$$\ddot{y} + \gamma\dot{y} + \omega_0^2 y = -\frac{eH}{mc}\dot{x} \tag{4.33}$$

with introduction of the classical Larmor frequency $\omega_r = \frac{eH}{mc}$. Upon driving Eqs. 4.32 and 4.33 using either stochastic or deterministic (externally applied) forces, we obtain:

$$\begin{bmatrix} x \\ y \end{bmatrix} = \frac{1}{(-\omega^2 + \omega_0^2 - i\omega\gamma)^2 - \omega_r^2\omega^2} \times \begin{bmatrix} -\omega^2 + \omega_0^2 - i\omega\gamma & -i\omega_r\omega \\ i\omega_r\omega & -\omega^2 + \omega_0^2 - i\omega\gamma \end{bmatrix} \begin{bmatrix} \eta_x \\ \eta_y \end{bmatrix} \tag{4.34}$$

When considering these as Langevin equations, we assume rotationally symmetric thermal noise so that $\langle\eta_x^2\rangle = \langle\eta_y^2\rangle = \langle\eta^2\rangle$.

Since the dynamics in directions $\hat{x}$ and $\hat{y}$ are symmetric, we compute and compare one of each of the autocorrelation and cross-correlation functions. A lengthy but straightforward calculation yields the following response and correlation functions. In order to confirm the validity of the FDT, we present the response functions in combinations such that these combinations should be equivalent to the corresponding correlation functions. We find:

$$\frac{\tilde{\chi}_{xx}(\omega) - \tilde{\chi}_{xx}(-\omega)}{2i} = \frac{\gamma\omega((\omega_0^2 - \omega^2)^2 + \gamma^2\omega^2 + \omega_r^2\omega^2)}{(\omega^2\gamma^2 + (\omega_0^2 - \omega^2 - \omega\omega_r)^2)(\omega^2\gamma^2 + (\omega_0^2 - \omega^2 + \omega\omega_r)^2)} \tag{4.35}$$

$$C_{xx} = \frac{\langle\eta^2\rangle((\omega_0^2 - \omega^2)^2 + \gamma^2\omega^2 + \omega_r^2\omega^2)}{(\omega^2\gamma^2 + (\omega_0^2 - \omega^2 - \omega\omega_r)^2)(\omega^2\gamma^2 + (\omega_0^2 - \omega^2 + \omega\omega_r)^2)} \tag{4.36}$$

$$\frac{\tilde{\chi}_{xy}(\omega) - \tilde{\chi}_{yx}(-\omega)}{2i} = \frac{i\omega_r\omega(\omega_r^2\omega^2 - (-\omega^2 + \omega_0^2 + i\omega\gamma)^2 + (-\omega^2 + \omega_0^2 - i\omega\gamma)^2 - \omega_r^2\omega^2)}{2(\omega^2\gamma^2 + (\omega_0^2 - \omega^2 - \omega\omega_r)^2)(\omega^2\gamma^2 + (\omega_0^2 - \omega^2 + \omega\omega_r)^2)} \tag{4.37}$$

$$= \frac{\gamma\omega(2i\omega^3\omega_r - 2i\omega_0^2\omega\omega_r^2)}{(\omega^2\gamma^2 + (\omega_0^2 - \omega^2 - \omega\omega_r)^2)(\omega^2\gamma^2 + (\omega_0^2 - \omega^2 + \omega\omega_r)^2)} \tag{4.38}$$

$$C_{xy} = \frac{\langle\eta^2\rangle(2i\omega^3\omega_r - 2i\omega\omega_r\omega_0^2)}{(\omega^2\gamma^2 + (\omega_0^2 - \omega^2 - \omega\omega_r)^2)(\omega^2\gamma^2 + (\omega_0^2 - \omega^2 + \omega\omega_r)^2)} \tag{4.39}$$

By direct comparison of Eqs. 4.35, 4.36, as well as the cross correlations Eqs. 4.38 and 4.39, we verify that FDT is satisfied for a system responding to a magnetic field. Even though the force is generated from the curl of a vector potential (like our driving force in the Hopf system), the magnetic field does not invalidate the FDT since the magnetic forces cannot do work on the system.

4.5.3 Driven systems without computation

In the main text, we present three representative systems that incorporate a computational drive. For completeness, we show results obtained from the Hopf system with a non-computational drive, *i.e.*, one with $b'' = 0$. This system without a non-computational drive admits a GFDT. In Fig. 4.15 we show that the response (black lines) and fluctuations (colored dots) agree as expected from the GFDT, or the FDT in the Frenet frame that is co-moving with the mean probability current in the driven oscillator. The fluctuations in the normal (radial) direction (blue) are still well described by a simple Lorentzian (black), whose corner frequency is once again marked by a vertical line. However, the phase diffusion constant exhibits no frequency dependence (red) consistent with Eq. 4.16. Furthermore, the cross correlations $C_{r\phi}$ vanish, and the correlation data depicted in subplots (c and d) agree with those inferred from GFDT and the numerically computed response functions. When b" $= 0$, the hair cell model violates FDT but obeys GFDT.

For the stochastic three-state system with a constant v_{drift} (Fig. 4.5), we have shown in the main text for state -1 that the FDT breaks down, but the GFDT is satisfied. In Figs. 4.16 and 4.17 we illustrate the same for the other two states, where we obtain similar results.

When examining the second three-state system (Fig. 4.9) with broken detailed balance

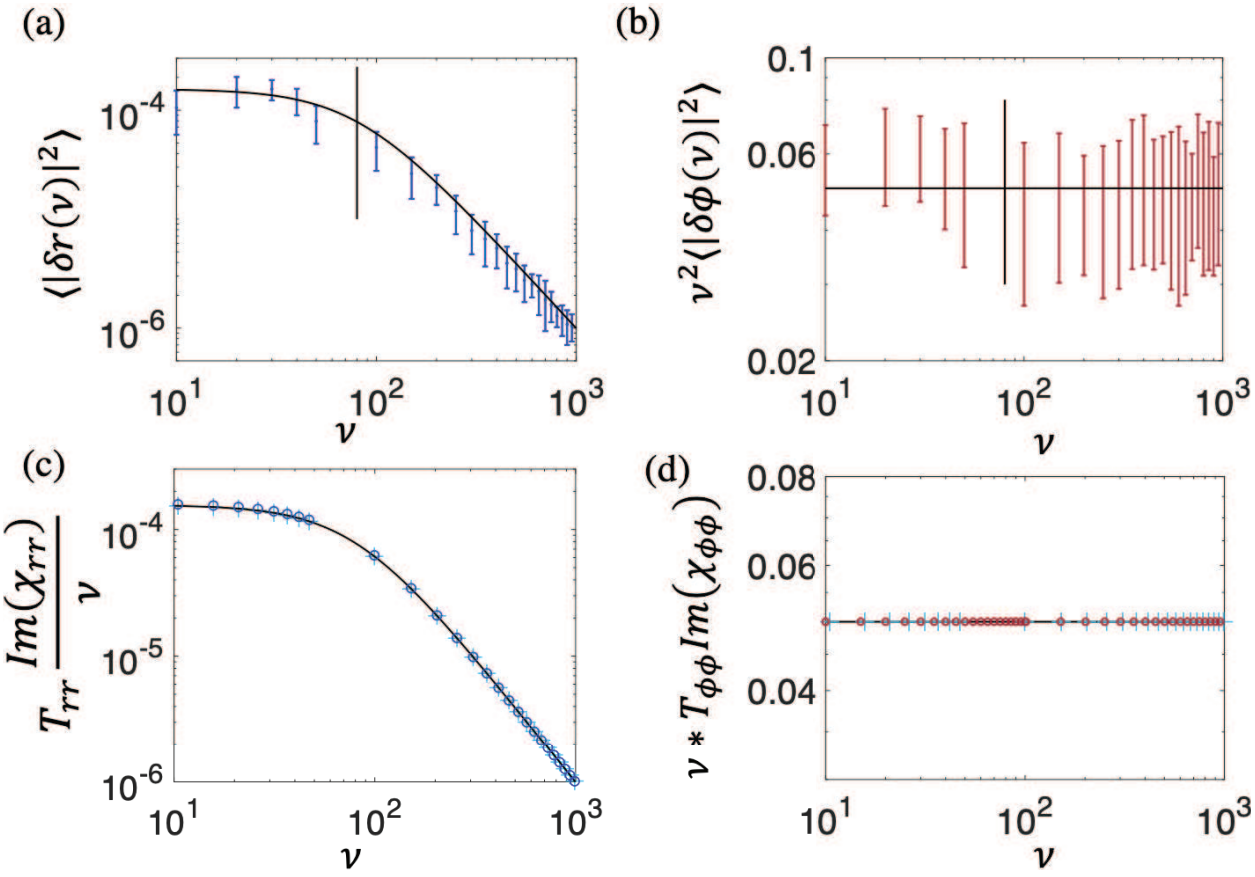

Figure 4.15: Correlation and response functions for the isochronous Hopf oscillator (a) Power spectral density of radial fluctuations as a function of frequency ν (blue dots). (b) Phase diffusion constant, obtained from the product of the phase fluctuation power spectral density and ν^2 (red dots). In both panels, the vertical (black) line indicates the corner frequency of 2μ. In panels (c) and (d) we compare the measured two-point auto correlation functions with those inferred via GFDT from the numerically obtained response function data of χ_{rr} and $\chi_{\phi\phi}$. The predicted correlation functions agree with those directly measured from the Hopf oscillator simulations for both the radial and phase fluctuations. Overlaid on all four plots are the respective theoretical calculations from Eqs. 4.16 and 4.18.

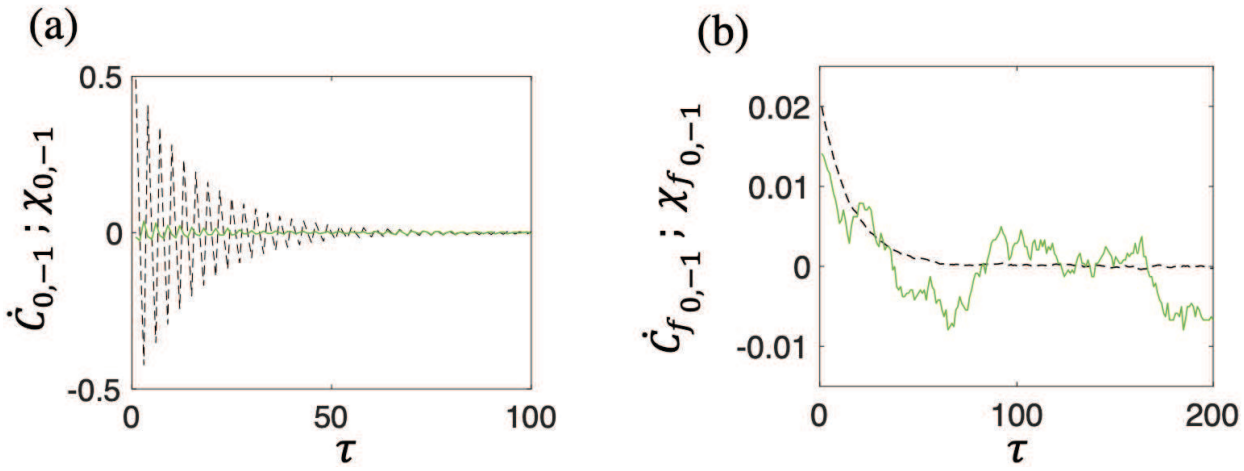

Figure 4.16: $\dot{C}_{0,-1}$ (black dashed) vs $\chi(\tau)_{0,-1}$ (green solid) for $v_{\text{drift}} = 1$

. (a) Time derivative of the numerically computed cross-correlation function $\dot{C}_{0,-1}$ and the linear response function of $\chi_{0,-1}$ disagree revealing the breakdown of FDT. (b) However the system satisfies GFDT as seen on comparing these functions calculated in the Frenet frame.

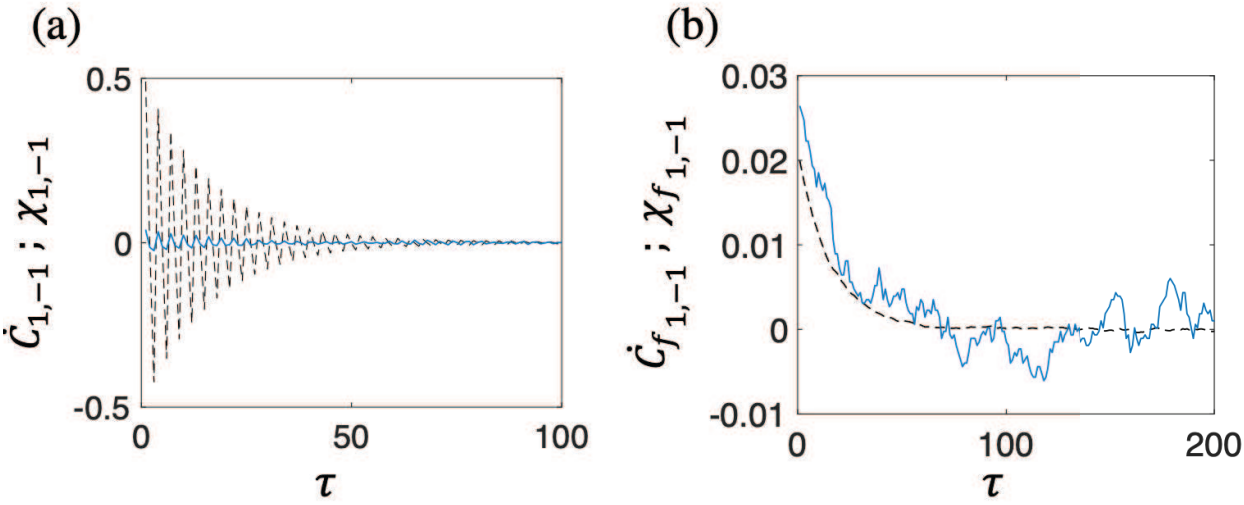

Figure 4.17: $\dot{C}_{1,-1}$ (black dashed) vs $\chi(\tau)_{1,-1}$ (blue solid) for $v_{\text{drift}} = 1$

. Comparing the time derivative of the cross-correlation $\dot{C}_{1,-1}$ and response function χ_{1-1} we observe significant deviations from FDT in (a) and the satisfaction of GFDT in (b).

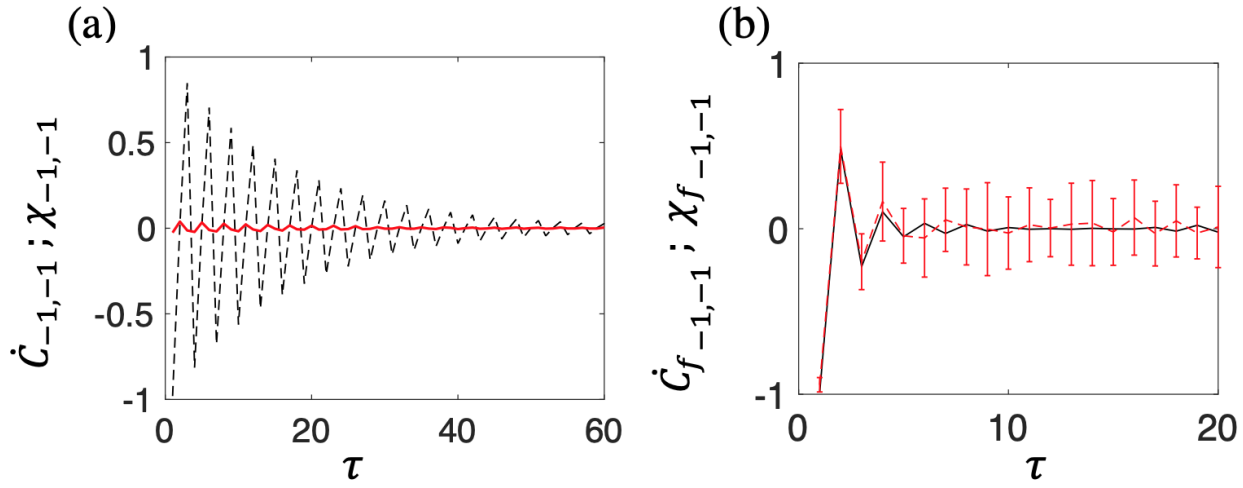

Figure 4.18: $\dot{C}$ (black solid) vs $\chi(\tau)$ (red dashed) for $\alpha = 98$ and state -1.
(a) Time derivative of the cross-correlation $\dot{C}_{-1-1}$ and the response functions χ_{-1-1} superimposed illustrate the breakdown of FDT. (b) The Frenet frame formalism allows for the obedience of GFDT.

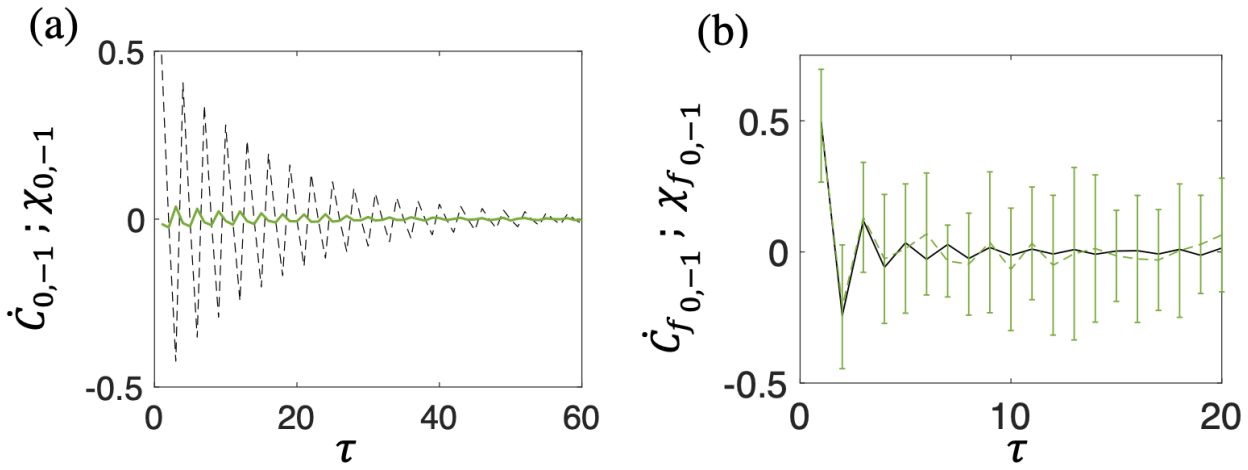

Figure 4.19: $\dot{C}$ (black solid) vs $\chi(\tau)$ (green dashed) for $\alpha = 98$ for state 0.
Time derivative of the cross-correlation $\dot{C}_{0-1}$ and response functions χ_{0-1} demonstrating violation of FDT in (a) and validity of GFDT in (b).

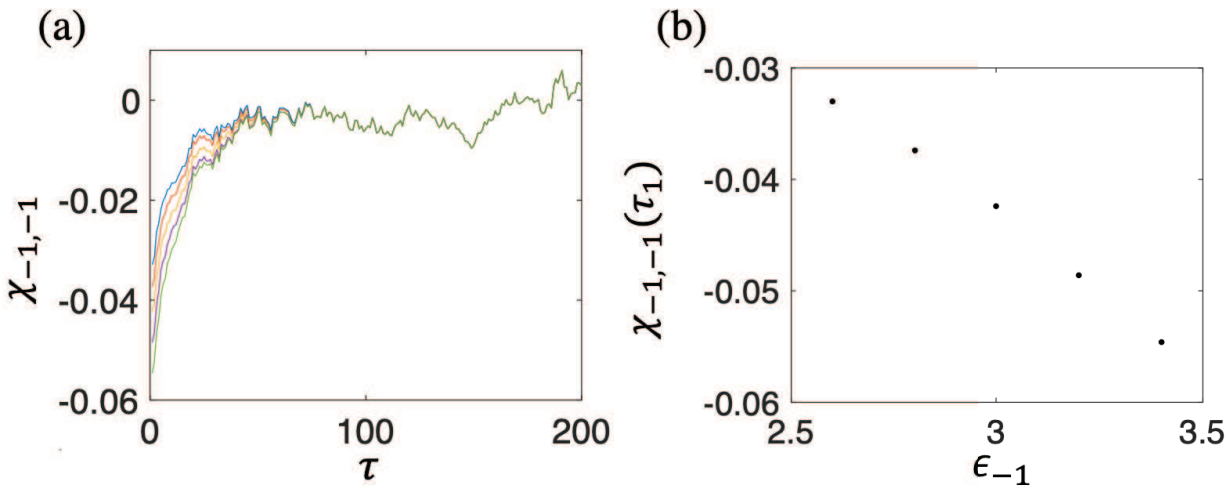

Figure 4.20: Variation of $\chi_{-1,-1}$ with ϵ_{-1}.

(a) With the three-state model obeying detailed balance, we obtain its $\chi_{-1,-1}$ response by setting the energy of state -1, $\epsilon_{-1} = [2.6, 2.8, 3, 3.2, 3.4]$ for one time step. These are respectively colored with blue, orange, yellow, purple and green. (b) The magnitude of the $\chi_{-1,-1}(\tau_1)$ values linearly increase with ϵ_{-1}.

but no computation, we found that the GFDT holds as expected. In the main text, we demonstrated the necessary correspondence for only one correlation function – see Fig. 4.11. For completeness, here we show the analogous results for states -1 and 0 in Figs. 4.18 and 4.19 respectively. In all of these examples, the standard FDT breaks down, but the GFDT relations are valid.

4.5.4 Linear regime of the equilibrium three-state model

In Fig. 4.10, we perturb the system using an ϵ_{-1} value of 3. To verify that the response of this forced oscillator is within its linear regime, in panel (a) of Fig. 4.20 we plot over a range of ϵ_{-1} values (2.6, 2.8, 3, 3.2, and 3.4) their respective $\chi_{-1,-1}$s. Additionally, in panel (b), we show that the magnitude of these response functions at time τ_1 varies with ϵ_{-1} in a linear fashion.

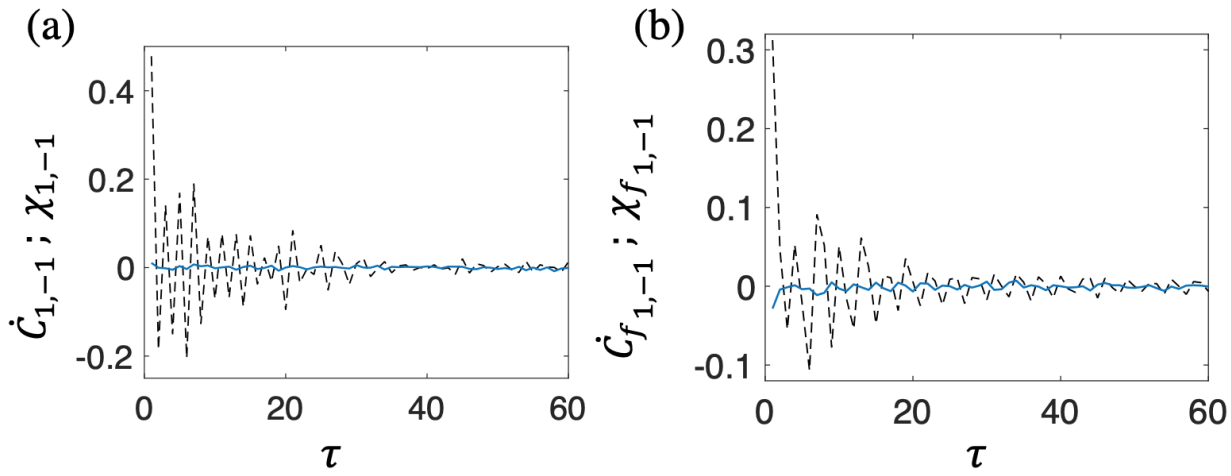

Figure 4.21: $\dot{C}_{0,-1}$ (black dashed) vs $\chi(\tau)_{0,-1}$ (green solid) for history-dependent v_{drift}. Time derivative of the cross-correlation function $\dot{C}_{0,-1}$ and the response function $\chi_{0,-1}$ juxtaposed to reveal the breakdown of FDT in (a) and GFDT in (b).

4.5.5 Three-state system with a computational drive

In Fig. 4.8, we depicted the effects of a computational drive only for the state -1, namely the violation of both FDT and GFDT. We obtain similar plots for both states 0 and 1 – see Figs. 4.21 and 4.22.

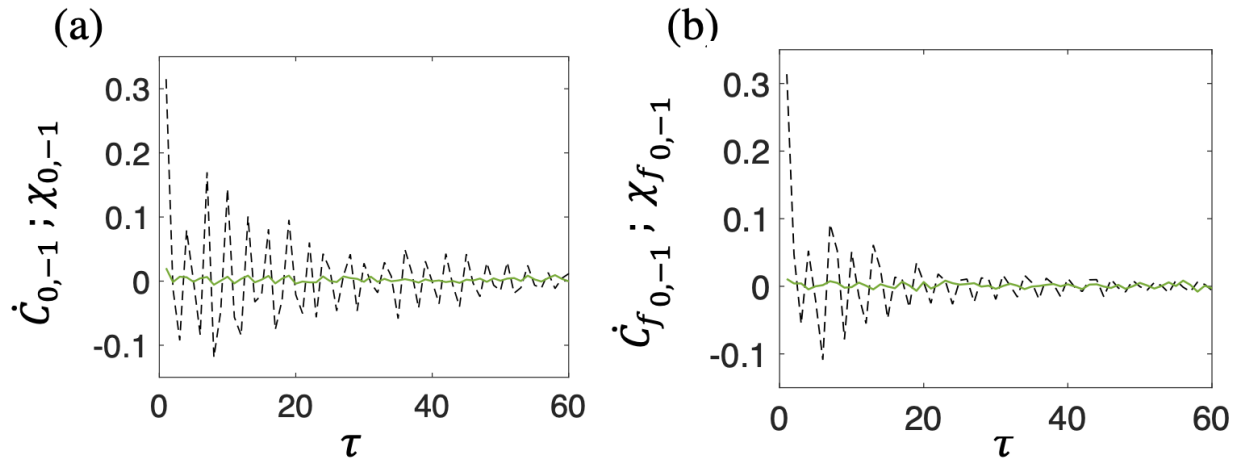

Figure 4.22: $\dot{C}_{1,-1}$ (black dashed) vs $\chi(\tau)_{1,-1}$ (blue solid) for $v_{\text{drift}} = 1$.

Comparison of the time derivative of the cross-correlation $\dot{C}_{1,-1}$ and response function χ_{1-1} exemplifies violation of both the equilibrium (in panel (a)) and generalized (panel (b)) fluctuation-dissipation relations.

CHAPTER 5

Future work

5.1 Introduction

To further study the non-equilibrium steady-state nature of the hair bundle oscillators, we look to several variants of GFDT which can be applied to systems that are characterized by internal driving, non-vanishing currents. In chapter 4, we specifically analyzed the super-critical Hopf hair bundle model and simpler three-state models using the theorem proposed by Speck and Seifert in [53]. In this chapter we shall elaborate upon two more theorems, the Agarwal formulation of GFDT and a different relation proposed by Seifert et al. [51] which we shall henceforth refer to as the Entropic GFDT. It has previously been shown that for a system with an underlying non-computational drive all of the three GFDTs, namely, the Seifert-ian GFDT of chapter 4, the Agarwal GFDT and the Entropic GFDT are equivalent.

Here, we verify that the three-state model defined in 4.3.1 with a non-computational drive indeed satisfies the above equivalence, however we also show that one with a computational drive does not. In brief, a computational drive measures the system's current state and responds predictably by modifying its power input accordingly. A biological argument for why such a drive might be interesting to study, rests in the continuously adapting myosin-motor based feedback mechanism integral to inner ear hair cells (see 1.2.1 and the introduction of chapter 4). In this chapter, we propose that a computationally-driven system violates the afore-mentioned generalized fluctuation-dissipation theorems due to its non-markovian nature. The information it retains about its trajectory can in fact be quantified using computational entropy. We hope to show that once we account for this additional entropy, one may obtain a new nonequilibrium GFDT which can be satisfied by both the computationally-

driven three-state toy model systems and more generally by biological systems such as the inner ear hair cells.

Please note that this work is currently in progress, and thus incomplete though to the best of my knowledge scientifically correct. We aim to finish and publish this work soon.

5.2 Generalized Fluctuation-Dissipation Theorems

Consider a discrete-time system with $\{n\}$ states, the transition rate from state m to state n is $\omega_{mn}(h)$ which may depend on an external perturbation parameter h. In our three-state system, the states are labeled by $n = \{-1, 0, 1\}$. While the energies of states 0 and 1 are equal to 0, h will henceforth be used to vary the energy of state -1, and is thus equivalent to the parameter ϵ_{-1} used in chapter 4. The system's dynamics as shown in Fig. 4.5 are entirely determined by its drift velocity v_{drift} and stochastic hopping. v_{drift} is the internal drive that introduces a non-zero probability current in the non-equilibrium steady-state thus explicitly breaking detailed balance. Meanwhile stochastic hopping regulated by the parameter p where, $0 \leq p \leq 0.5$, is unbiased and underlies diffusive dynamics amongst the three states.

We also introduce additional notation which is useful to describe the Agarwal and Entropic GFDTs - p_ns denote the state occupation probabilities and p_n^0s give the unperturbed system's stationary distribution. $\sigma_n(t_i)$ will be used to represent the indicator function which is 1 (0) when the system is (is not) in state $\{n\}$ at time t_i. Thus, $p_n = \langle \sigma_n \rangle$.

5.2.1 Agarwal GFDT

The Agarwal GFDT can then be expressed as,

$$\chi_{n,-1}(t_i - t_j) = \langle \sigma_n(t_i) B^a(t_j) \rangle \tag{5.1}$$

where χ is defined using,

$$\delta p_n(t_i) = -\Sigma_{j=-\infty}^{i} \chi_{n,-1}(t_i - t_j) h(t_j) \tag{5.2}$$

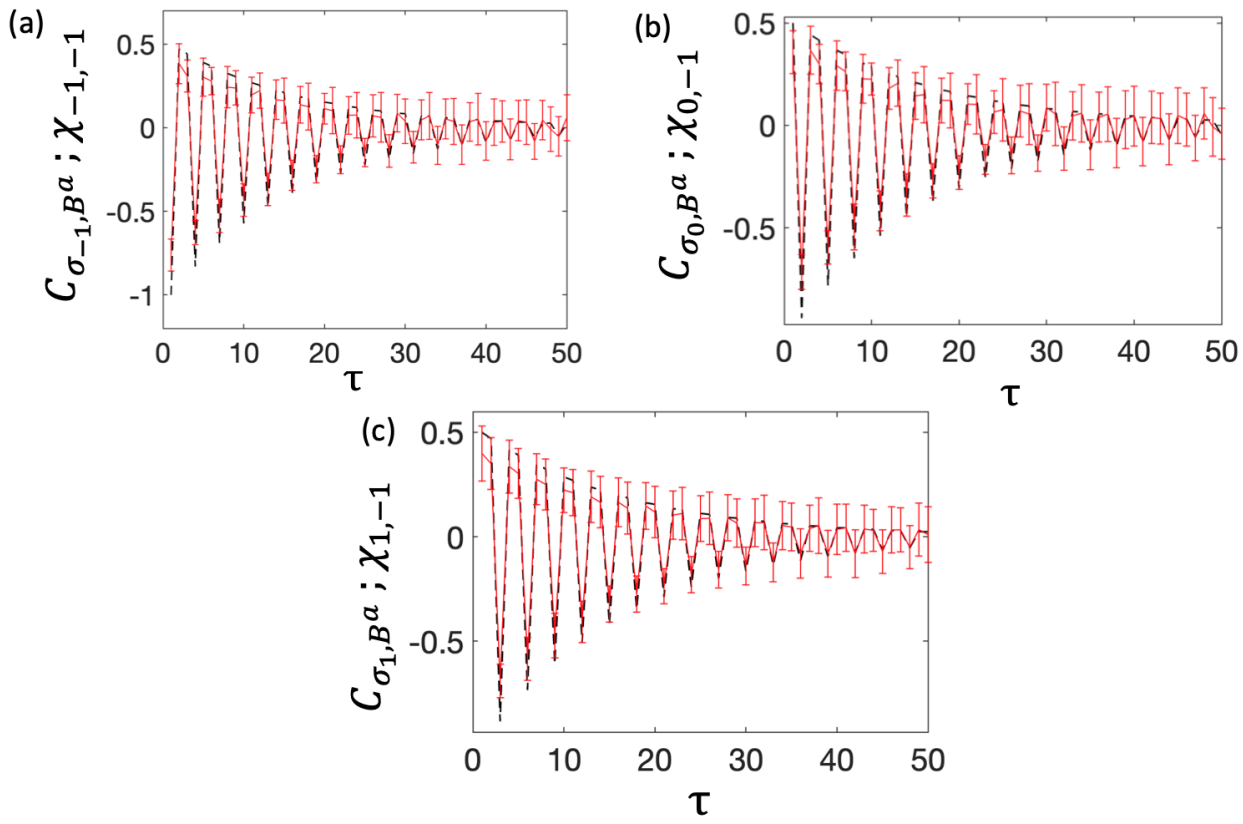

Figure 5.1: C_{σ_n,B^a} (black dashed) vs $\chi(\tau)_{n,-1}$ (red solid) for $v_{\text{drift}} = 1$.

The cross-correlation functions C_{σ_n,B^a} matches with the corresponding response function $\chi_{n,-1}$ obtained by driving the system out of its -1 state. Here, $n = \{-1, 0, 1\}$. Errors bars on the response function depict one standard deviation of the mean.

and B^a is a stochastic quantity whose value is given by,

$$B^a_m = \Sigma_n \frac{p^0_n}{p^0_m} \partial_h \omega_{nm} - \Sigma_n \partial_h \omega_{mn} \tag{5.3}$$

We first consider the case of a constant drive by setting $v_{\text{drift}} = 1$. When $v_{\text{drift}} = 1$ the occupation probability distribution traverses from state $\{m\}$ to state $\{n\}$ such that $\{n\}$ lies circularly to the right of $\{m\}$ in the set $\{-1, 0, 1\}$. In Fig. 5.1 we plot $\chi_{-1,-1}(\tau)$, $\chi_{0,-1}(\tau)$ and $\chi_{1,-1}(\tau)$ in red along with the corresponding Agarwal correlation functions C_{σ_{-1},B^a}, C_{σ_0,B^a} and C_{σ_1,B^a} (dashed black curves). As expected, the two are in agreement with each other within one standard deviation.

We will now introduce a computational drive by making the system non-markovian and dependent on the previous state. We do this in two ways. First we consider,

$$v_{\text{drift}}(t_i) = \lfloor \sum_{j=1}^{\infty} r|\xi\left(t_{i-j}\right)| \rfloor \mod 3. \tag{5.4}$$

Next, we simulate a system with

$$v_{\text{drift}}(t_i) = \lfloor \sum_{j=1}^{\infty} r(2 - |\xi\left(t_{i-j}\right)|) \rfloor \mod 3. \tag{5.5}$$

$\lfloor . \rfloor$ is the floor function which returns the integral part of its argument and r gives the strength of the drive. In our simulations, $r = 1$. We have also introduced a new function $\xi(t_{i-j})$ which takes values -1, 0, or 1 when the system is in state -1,0 or 1 at time t_{i-j}. It is defined using the indicator functions,

$$\xi\left(t_i\right) = (-1)^{\sigma_{-1}(t_i)}\left[1 - \sigma_0(t_i)\right]. \tag{5.6}$$

For each of these systems, we plot the Agarwal cross-correlations (black dashed) and response functions (red solid) in Figs. 5.2 and 5.3. We note that for both the systems, the two plots do not match.

5.2.2 Entropic GFDT

The entropic GFDT is based on the idea that the response of a non-equilibrium steady-state system to a small perturbation is given by a correlation function of the corresponding observable and another variable that is conjugate to the perturbation with respect to *stochastic entropy*, just as, in case of the equilibrium FDT the second variable is taken to be conjugate with respect to *energy*. In this scenario, the GFDT relation can be written as,

$$\chi_{n,-1}(t_i - t_j) = \langle \sigma_n(t_i) B^e(t_j) \rangle \tag{5.7}$$

and,

$$B^e = -\partial_h \dot{s}. \tag{5.8}$$

s is the stochastic entropy of the system:

$$s(t) = -\ln p_{n(t)} \tag{5.9}$$

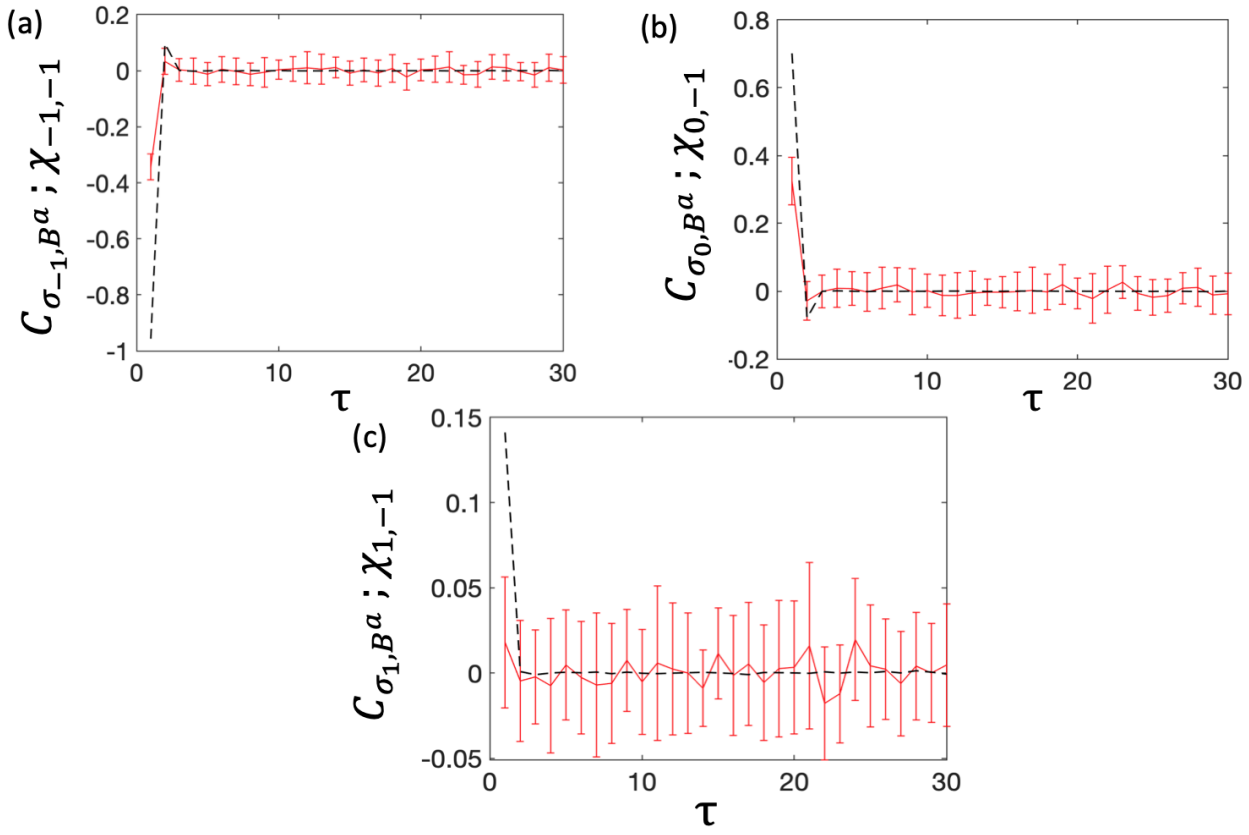

Figure 5.2: Three-state model with computational drive (Eq. 5.4).

This system has a drive of 1 when in state 1 or -1 and a drive of 0 otherwise. For all three states we superimpose the cross-correlation functions C_{σ_n,B^a} (black dashed lines) atop the corresponding response functions $\chi_{n,-1}$ to demonstrate breakdown of the Agarwal GFDT. Errors bars illustrate one standard deviation of the mean.

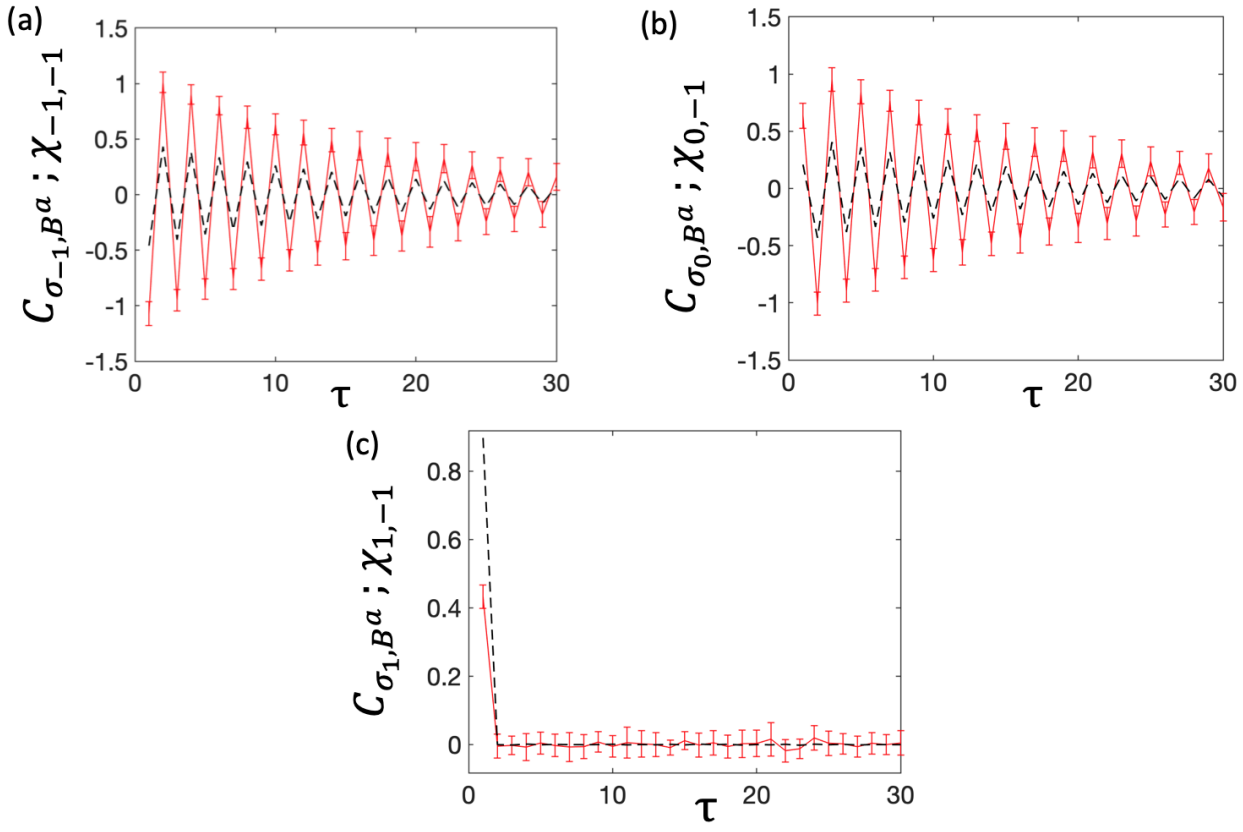

Figure 5.3: Computationally-driven thee-state system violates the Agarwal GFDT. Given by Eq. 5.5 the drive takes value 1 when the system in state 1 or -1 and 2 when it is in state 0. The breakdown of Agarwal GFDT is made evident by juxtaposing the cross-correlation functions C_{σ_n,B^a} (black dashed lines) and the corresponding response functions $\chi_{n,-1}$ for each of the three states n. Errors bars again illustrate one standard deviation of the mean.

with its derivative for discrete-time dynamics given by,

$$\dot{s}(t) = -\Sigma_i \delta(t - t_i) \ln \frac{p_{n_i^+}}{p_{n_i^-}}. \tag{5.10}$$

Here, the system's trajectory is discretized such that it is a sequence of hops at time t_i from state n_{i^-} to state n_{i^+}. This enables us to rewrite 5.7 as,

$$\chi_{n,-1}(t_i - t_j) = \frac{-\langle \sigma_n(t_i) \dot{s}_h \rangle + \langle \sigma_n(t_i) \dot{s}_0 \rangle}{h} \tag{5.11}$$

Using these equations to compute the entropic cross-correlation and response functions for the non-computationally driven model with $v_{\text{drift}} = 1$, we arrive at Fig. 5.4. As expected, the entropic cross-correlation functions C_{σ_n, B^e} agree with the responses of the occupation probability p_n to the perturbative force h. Moreover, these correlations are equivalent to the Agarwal correlation functions.

We now consider the case of the computationally-driven three-state systems. In Figs. 5.5 and 5.6 we demonstrate the violation of the Entropic GFDT by these systems. The red solid curves are the numerically computed response functions $\chi_{-1,-1}(\tau)$, $\chi_{0,-1}(\tau)$ and $\chi_{1,-1}(\tau)$ and the black dashed lines are the respective cross-correlation functions. The oscillatory nature of the response $\chi_{-1,-1}$ and $\chi_{0,-1}$ can be attributed to the fact that the two states -1 and 0 essentially have cyclical dynamics with the system occasionally in state 1. In addition we empirically observe that the entropic correlation functions differ from their Agarwal counterparts.

5.3 Entropy of different systems

Amongst the three cases we have analyzed, the differentiating factor is the value of v_{drift} when the system is in state 0. For the non-computationally driven system $v_{\text{drift}} = 1$, for that defined using Eq. 5.4, $v_{\text{drift}} = 0$, and lastly when the computational drive is given by Eq. 5.4, v_{drift} takes the value of 2. To quantify the system's memory of its previous state, we now numerical compute the entropy production rate in the medium ($\dot{s}_{med}$) and also introduce a new dynamical variable - computational entropy rate ($\dot{s}_{mem}$).

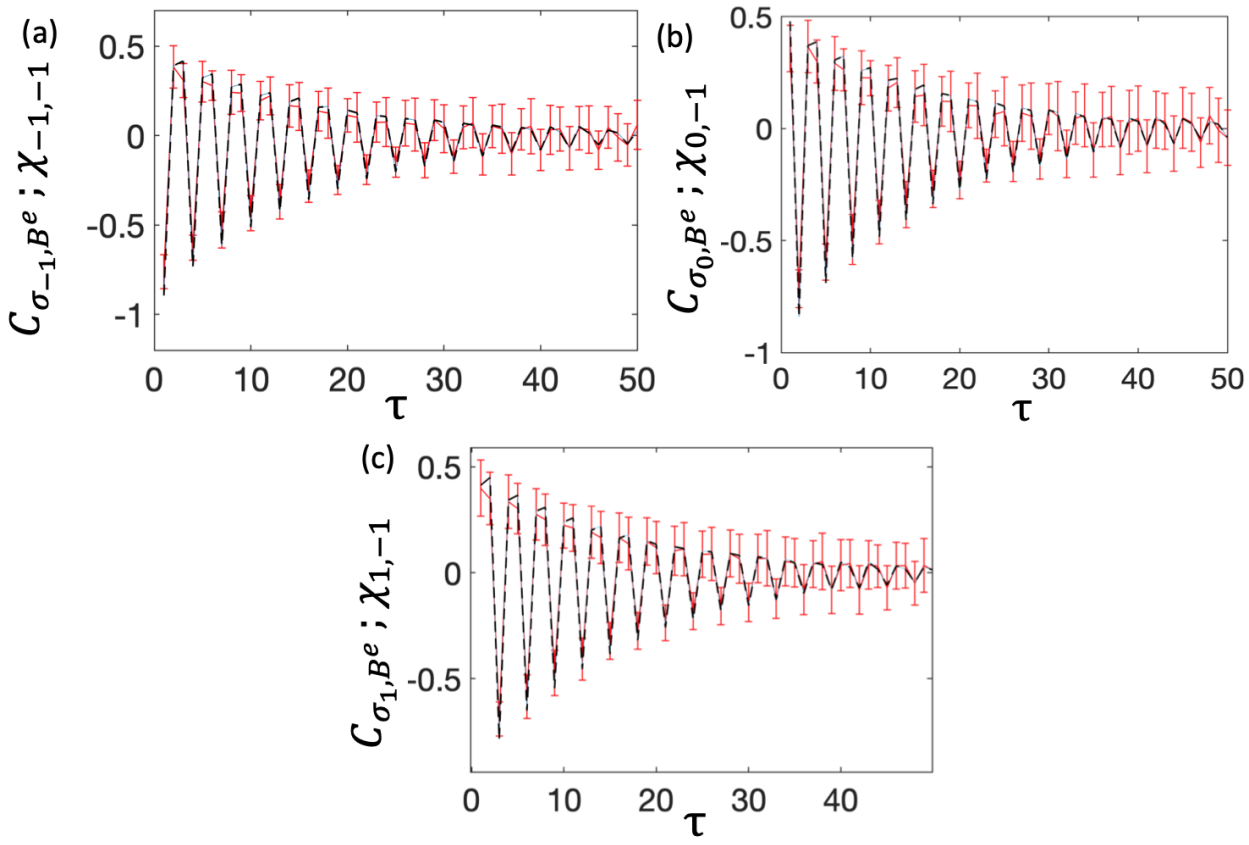

Figure 5.4: C_{σ_n,B^e} (black dashed) vs $\chi(\tau)_{n,-1}$ (red solid) for $v_{\text{drift}} = 1$.

The cross-correlation function C_{σ_n,B^e} for each of the three states equals the corresponding response function within one standard deviation of the mean.

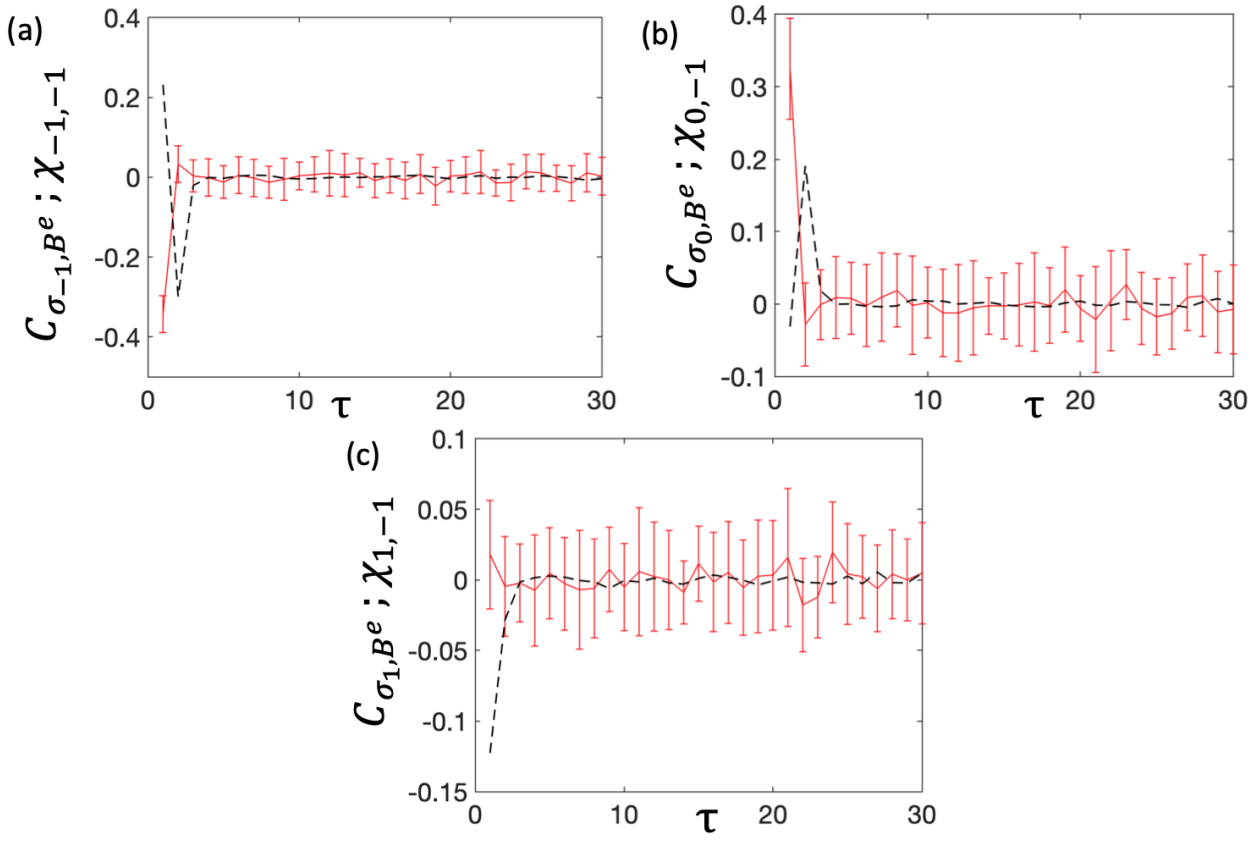

Figure 5.5: Correlation (black curve) vs response functions (red curve) for the computationally-driven system with the drive given by Eq.5.4

C_{σ_n,B^e} for each of the three states deviates from the corresponding response function. Error bars represent one standard deviation of the mean.

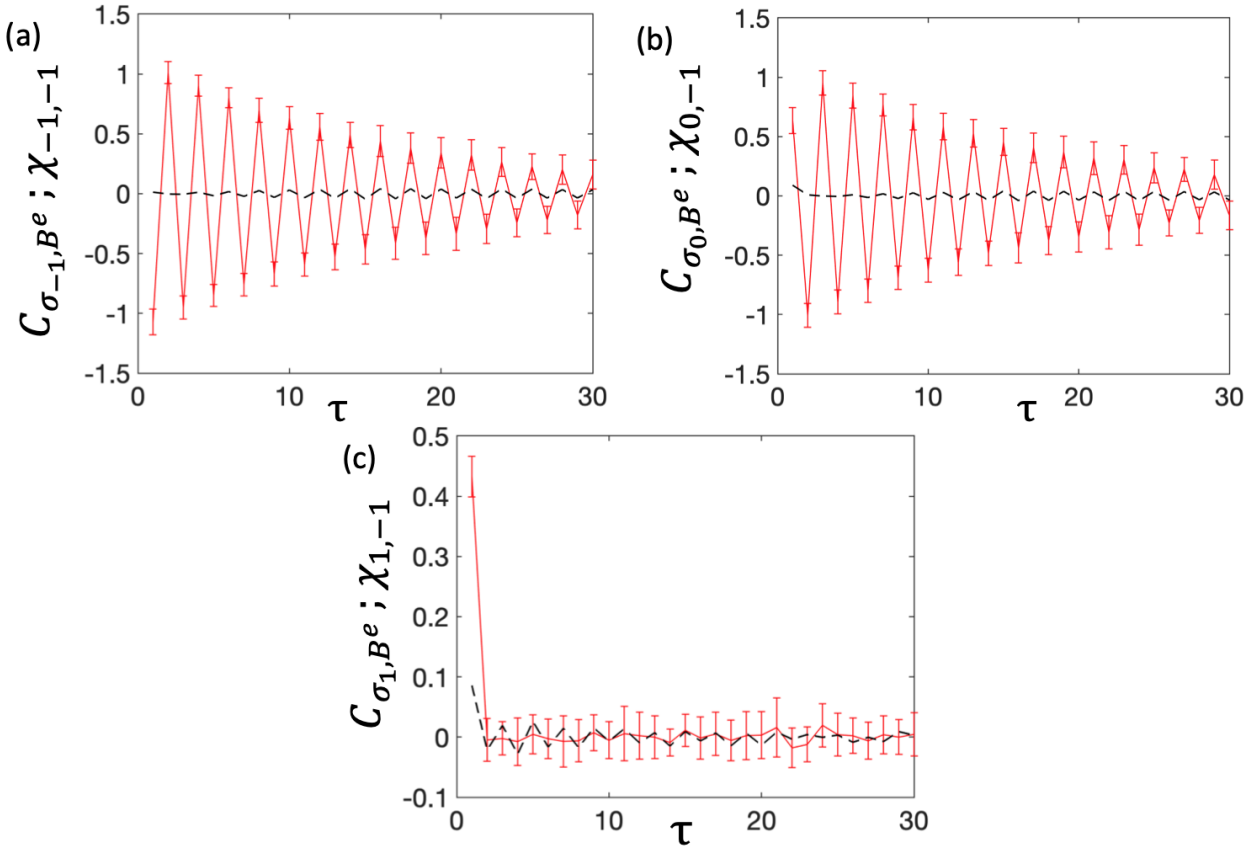

Figure 5.6: C_{σ_n,B^e} (black dashed) vs $\chi(\tau)_{n,-1}$ (red solid) for the computational v_{drift} of Eq.5.5 Superposition of the two curves clearly elucidates the breakdown of Entropic GFDT for each of the three states.

$\dot{s}_{med}$ is defined as,

$$\dot{s}_{med}(t) = -\Sigma_i \delta(t - t_i) \ln \frac{\omega_{n_j^- n_i^+}}{\omega_{n_j^+ n_i^-}} \tag{5.12}$$

where, $\omega_{n_j^- n_i^+}$ as defined earlier is the transition rate as the system hops from state n_i^- to state n_i^+ at time t_i. In Fig.5.7 we illustrate $\dot{s}_{med}$ for all three three-state systems. The entropy production rate for the non-computationally driven system has the mode value of $\dot{s}_{med} = \ln \frac{1-2p}{p}$ as expected from underlying constant v_{drif} value. However in contrast the modes of $\dot{s}_{med}$ for the non-computationally driven systems are 0.

The new dynamical variable of $\dot{s}_{mem}$ meanwhile can be given by,

$$\dot{s}_{mem}(t) = -\Sigma_i \delta(t - t_i) \ln \frac{p_{mem,n_i^+}}{p_{mem,n_i^-}} \tag{5.13}$$

where $p_{mem} = \langle \sigma_{mem,n} \rangle$. The observable $\langle \sigma_{mem,n} \rangle$ is in turn an indicator function which takes the value 1 when it is in state 0 and the value 0 otherwise. $\dot{s}_{mem}$ thus captures the system's knowledge of its previously occupied state. Again for all three systems of interest we plot $\dot{s}_{mem}$ in Fig 5.8. While the computational entropy rate fluctuates about 0 for all three systems, the fluctuations are revealing of the underlying dynamics of the system. When $v_{\text{drift}} = 1$, all the three states $\{-1, 0, 1\}$ are equally occupied and $\dot{s}_{mem}$ thus oscillates between $\ln 2$ and $-\ln 2$. However when $v_{\text{drift}} = 0$ the occupation probability is heavily biased towards state 0, while for $v_{\text{drift}} = 2$ the probability of occupying state 1 is negligible.

5.4 Next steps

Since this is currently work in progress we next would like to incorporate the computational entropy rate in Eq. 5.11 and devise a new GFDT which would also be satisfied by computationally-driven three-state systems. Just as violation of the equilibrium FDT is a hallmark of active systems, we hope that violating the Entropic GFDT but satisfying our newly proposed GFDT will be a quantitative measure of the presence of an underlying computational drive.

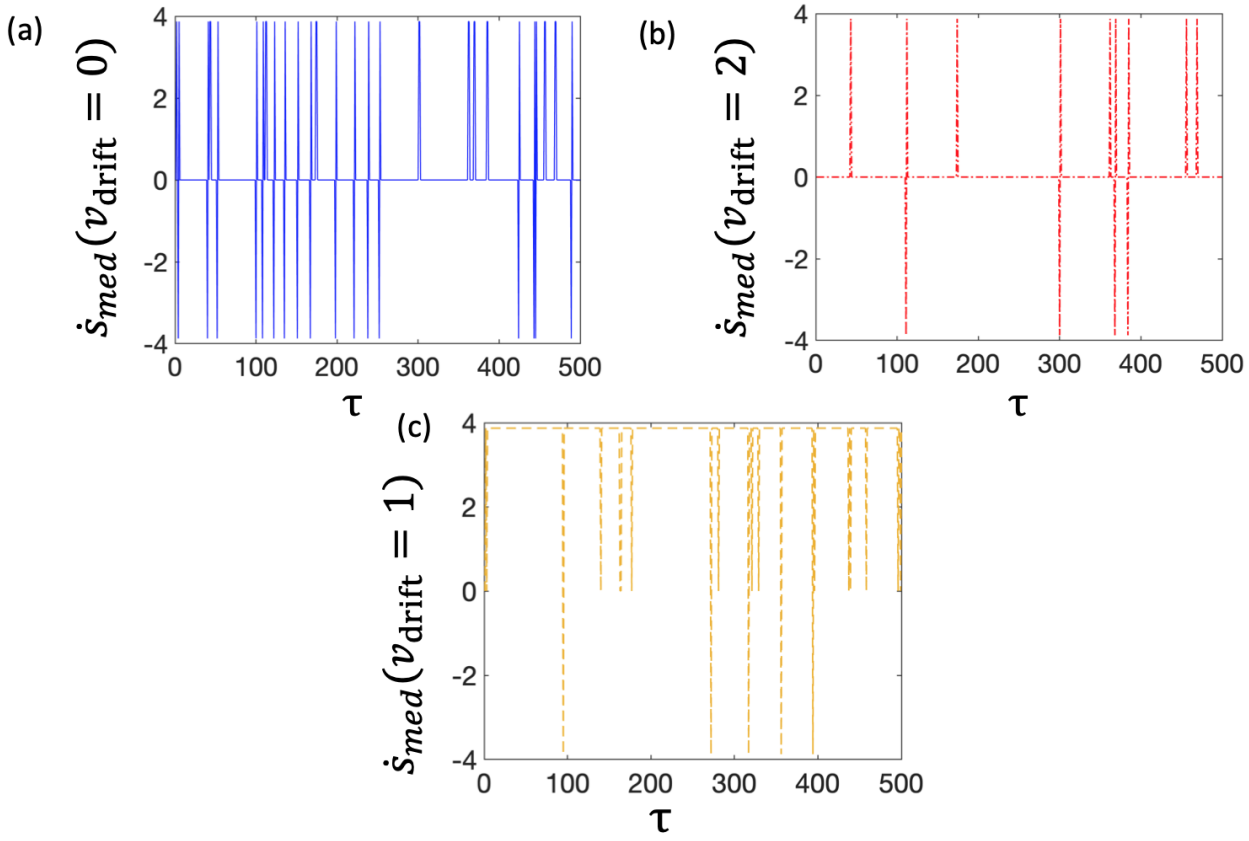

Figure 5.7: Comparison of $\dot{s}_{med}$ for the three driven systems

The entropy productions rates for the computationally driven systems are shown in sub-figures (a) and (b), while that for the computationally driven system is depicted in (c). Comparing the three, we note that (c) mostly exhibits a non-zero positive $\dot{s}_{med}$, which is a signature of broken detailed balance due to the presence of an underlying cyclical drive. Such a drive however is absent in the non-computationally driven systems.

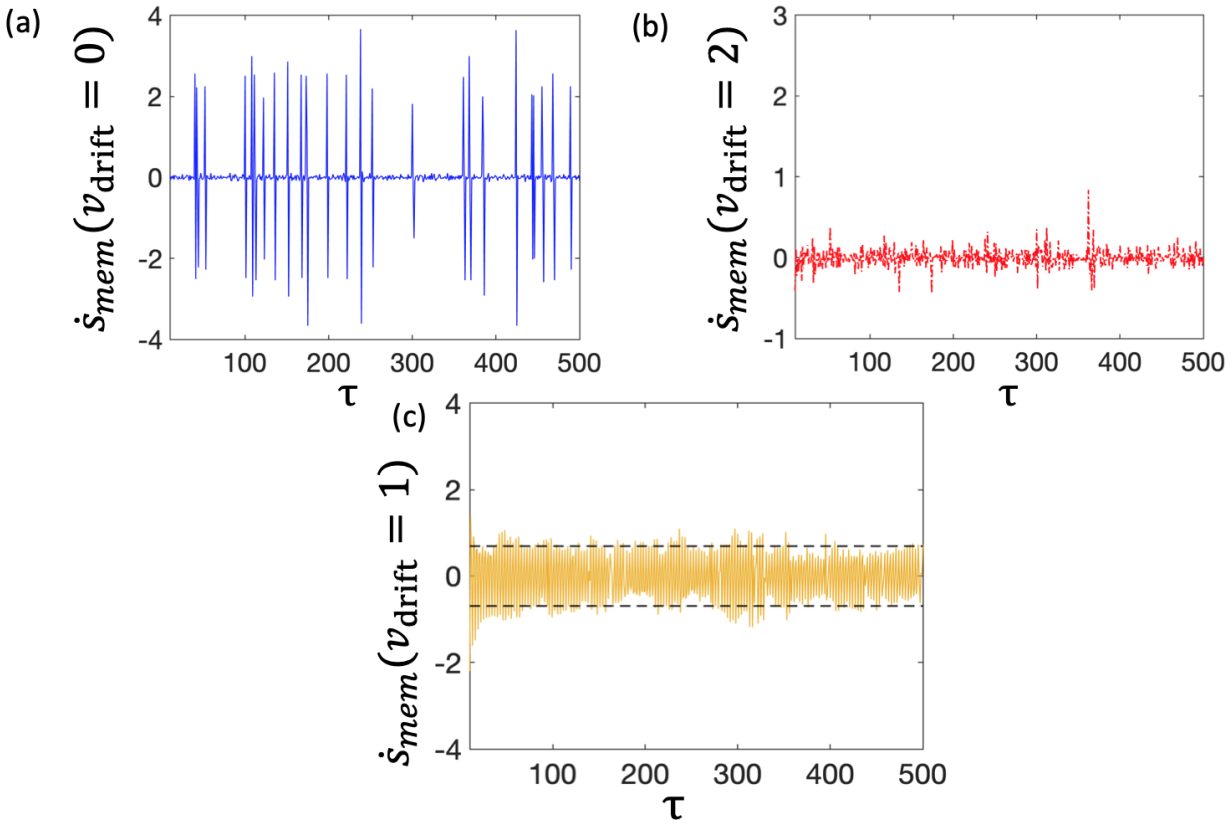

Figure 5.8: $\dot{s}_{mem}$ plots for all three driven systems

The computational entropy rates for the non-markovian driven systems are shown in (a) and (b). (c) illustrates the same for the non-computationally driven system. In this case, due to the presence of a constant non-zero cyclic probability current all the three states are equally occupied and the $\dot{s}_{mem}$ in (c) oscillates between the numerical values $\ln 2$ and $-\ln 2$ (shown using dashed black lines).

APPENDIX A

Source Codes

All numerical simulations in this thesis were performed in Matlab.

A.1 Hopf oscillator correlation function script

```
clear variables; close all;

%Constants
h = 0.0001; %time step
time = 0:h:h*250000; % duration length

mu = 40;
w = 10;
Kb = 1.38*10^-23;
T = 300;
b = 2;
b1 = 0;

%State variables
X = zeros (length(time),1);
Y = zeros(length(time),1);
X(1) = 1;
Y(1) = 1;
```

```
19
20 %Noise variables
21 noise_X = randn([length(time)-1,1]); %noise in X variable
22 noise_Y = randn([length(time)-1, 1]); %noise in Y variable
23 noise_X_amp = 1/2; %amplitude of noise in X
24 noise_Y_amp = 1/2; %amplitude of noise in Y
25
26 %Differential equations for $4^{th}$ order Runge-Kutta
27 Fn1 = @(X,Y) mu*X - w*Y - b*(X^2 + Y^2)*X - b1*(X^2 + Y^2)*Y;
28 Fn2 = @(X,Y) mu*Y + w*X - b*(X^2 + Y^2)*Y + b1*(X^2 + Y^2)*X;
29
30 for i = num:(length(time)-1)
31         ph = atan2(Y(i), X(i));
32         k1 = Fn1(X(i),Y(i));
33         m1 = Fn2(X(i), Y(i));
34         k2 = Fn1(X(i) + 0.5*h*k1 + 0.5*sqrt(noise_X_amp*h)*noise_X
               , ...
35         Y(i) + 0.5*h*m1 + 0.5*sqrt(noise_Y_amp*h)*noise_Y(i));
36         m2 = Fn2(X(i) + 0.5*h*k1 + 0.5*sqrt(noise_X_amp*h)*noise_X
               , ...
37         Y(i) + 0.5*h*m1 + 0.5*sqrt(noise_Y_amp*h)*noise_Y(i));
38         k3 = Fn1(X(i) + 0.5*h*k2 + 0.5*sqrt(noise_X_amp*h)*noise_X
               , ...
39         Y(i) + 0.5*h*m2 + 0.5*sqrt(noise_Y_amp*h)*noise_Y(i));
40         m3 = Fn2(X(i) + 0.5*h*k2 + 0.5*sqrt(noise_X_amp*h)*noise_X
               ,...
41         Y(i) + 0.5*h*m2 + 0.5*sqrt(noise_Y_amp*h)*noise_Y(i));
42         k4 = Fn1(X(i) + h*k3 + sqrt(noise_X_amp*h)*nnoise_X, ...
```

```
43          Y(i) + h*m3 + sqrt(noise_Y_amp*h)*noise_Y(i));
44          m4 = Fn2(X(i) + h*k3 + sqrt(noise_X_amp*h)*nnoise_X, ...
45          Y(i) + h*m3 + sqrt(noise_Y_amp*h)*noise_Y(i));
46          X(i+1) = X(i) + (1/6)*(k1+ 2*k2 + 2*k3 + k4)*h + ...
47          sqrt(noise_X_amp*h)*noise_X(i);
48          Y(i+1) = Y(i) + (1/6)*(m1 +2*m2 + 2*m3 + m4)*h + ...
49          sqrt(noise_Y_amp*h)*noise_Y(i);
50  end
51
52  %Calculating limit cycle of the oscillator} \\
53  phase_array = [X(num:end), Y(num:end)];
54  phase = atan2(phase_array(:,2), phase_array(:,1));
55
56  div = (-pi:2*pi/200:pi)'; %Number of points in the limit cycle
        (200)
57  sum_amp = zeros(length(div)-1,2); %Radial vectors at each phase
        angle
58  norm_amp = zeros(length(div)-1,1); %Radial norms at each phase
        angle
59  devi_amp = zeros(length(phase)-1,1); % Deviation from the limit
        cycle
60
61  for i = 1:length(div)-1
62    ind = find(phase >= div(i) & phase <  div(i+1));
63          for j = 1:length(ind)
64          sum_amp(i,:) = sum_amp(i,:) + ...
65               phase_array(ind(j),:)/length(ind);
66                    norm_amp(i) = norm_amp(i) + ...
```

```
67                 norm(phase_array(ind(j),:))/length(ind);
68             end
69             for ph = 1:length(phase)
70                     if(any(abs(ph-ind)<1e-10))
71                             devi_amp(ph) = norm(phase_array(ph,:)) -
                                   norm_amp(i);
72             end
73         end
74 end
75
76 % Power spectrum of radial fluctuations
77 baseline_amp_devi = smooth(devi_amp, 0.01, 'loess');
78 amp_devi = devi_amp - baseline_amp_devi;
79 [psd_filtdv, freqdv] = pwelch(devi_amp, [],[], ...
80     length(devi_amp)*4, 1/sampling_time);
81 freqdv = 2*pi*freqdv;
82 f = figure(); loglog(freqdv, psd_filtdv);
83
84 % Power spectrum of radial fluctuations
85 phase_un = unwrap(phase);
86 P = polyfit(time, phase_un - phase_un(1), 1);
87 yfit = P(1)*time + P(2);
88 phase_noise = phase_un - phase_un(1) - yfit;
89 baseline_ph_noise = smooth(phase_noise, 0.1, 'loess');
90 final_phase_noise = phase_noise - baseline_ph_noise;
91 [psd_filtph, freqph] = pwelch(final_phase_noise, [],[],...
92     length(final_phase_noise)*4, 1/sampling_time);
93 freqph = 2*pi*freqph;
```

```
94 f = figure(); loglog(freqph, psd_filtph);
```

A.2 Hopf oscillator response function script

```
1  clear variables; close all;
2
3  mu = 40;
4  w = 10;
5  Kb = 1.38*10^-23;
6  T = 300;
7  b = 2;
8  b1 = 0;
9
10 h = 0.0001; %time step
11 t_final = 300000; %duration length
12 num = 50000; % number of time steps to get to steady state
13
14 %State variables
15 X = zeros (length(time),1);
16 Y = zeros(length(time),1);
17 X(1) = 1;
18 Y(1) = 1;
19
20 %Noise variables
21 noise_X = randn([length(time)-1,1]); %noise in X variable
22 noise_Y = randn([length(time)-1, 1]); %noise in Y variable
23 noise_X_amp = 0; %amplitude of noise in X
24 noise_Y_amp = 0; %amplitude of noise in Y
25
```

```
26 %Differential equations for $4^{th}$ order Runge-Kutta
27 Fn1 = @(X,Y) mu*X - w*Y - b*(X^2 + Y^2)*X - b1*(X^2 + Y^2)*Y;
28 Fn2 = @(X,Y) mu*Y + w*X - b*(X^2 + Y^2)*Y + b1*(X^2 + Y^2)*X;
29
30 for i = 1:num
31         ph = atan2(Y(i), X(i));
32         k1 = Fn1(X(i),Y(i));
33         m1 = Fn2(X(i), Y(i));
34         k2 = Fn1(X(i) + 0.5*h*k1 + 0.5*sqrt(noise_X_amp*h)*noise_X
               , ...
35         Y(i) + 0.5*h*m1 + 0.5*sqrt(noise_Y_amp*h)*noise_Y(i));
36         m2 = Fn2(X(i) + 0.5*h*k1 + 0.5*sqrt(noise_X_amp*h)*noise_X
               , ...
37         Y(i) + 0.5*h*m1 + 0.5*sqrt(noise_Y_amp*h)*noise_Y(i));
38         k3 = Fn1(X(i) + 0.5*h*k2 + 0.5*sqrt(noise_X_amp*h)*noise_X
               , ...
39         Y(i) + 0.5*h*m2 + 0.5*sqrt(noise_Y_amp*h)*noise_Y(i));
40         m3 = Fn2(X(i) + 0.5*h*k2 + 0.5*sqrt(noise_X_amp*h)*noise_X
               ,...
41         Y(i) + 0.5*h*m2 + 0.5*sqrt(noise_Y_amp*h)*noise_Y(i));
42         k4 = Fn1(X(i) + h*k3 + sqrt(noise_X_amp*h)*nnoise_X, ...
43         Y(i) + h*m3 + sqrt(noise_Y_amp*h)*noise_Y(i));
44         m4 = Fn2(X(i) + h*k3 + sqrt(noise_X_amp*h)*nnoise_X, ...
45         Y(i) + h*m3 + sqrt(noise_Y_amp*h)*noise_Y(i));
46         X(i+1) = X(i) + (1/6)*(k1+ 2*k2 + 2*k3 + k4)*h + ...
47         sqrt(noise_X_amp*h)*noise_X(i);
48         Y(i+1) = Y(i) + (1/6)*(m1 +2*m2 + 2*m3 + m4)*h + ...
49         sqrt(noise_Y_amp*h)*noise_Y(i);
```

```
50 end
51
52 % Calculating natural frequency
53 [psd_X, freq_X] = pwelch(X(1000:num),[],[],length(X)*4,1/h);
54 [~, index] = max(psd_X);
55 natural_freq = freq_X(index);
56
57 % Since noise values are 0, we simplify limit cycle calculation...
58 %by just taking the simulated last complete cycle
59 limit_cycle = [X(num - floor(1/(h*natural_freq)+6) :num), ...
60     Y(num - floor(1/(h*natural_freq)+6):num)];
61 phase = atan2(limit_cycle(:,2), limit_cycle(:,1));
62 phase_limit_cycle = unwrap(phase);
63 P = polyfit(h*(1:length(limit_cycle))', phase_limit_cycle,1);
64
65 % Frenet frame
66 T = zeros(length(limit_cycle)-1,2);
67 N = zeros(length(limit_cycle)-1,2);
68 for t_id = 1:length(T)
69     T(t_id,:) =  limit_cycle(t_id+1,:) - limit_cycle(t_id,:);
70     T(t_id,:) = T(t_id,:)./norm(T(t_id,:));
71 end
72 for n_id = 2:length(N)
73     N(n_id,:) = T(n_id,:) - T(n_id-1,:);
74     N(n_id,:) = N(n_id,:)./norm(N(n_id,:));
75 end
76 N(1,:) = T(1,:) - T(end,:);
77 N(1,:) = N(1,:)./norm(N(1,:));
```

```
78
79 ping_num = 0;
80 devi_amp_array = [];
81 phase_dev_array = [];
82 ping = [];
83
84 % $4^{th}$-order Runge Kutta for the perturbed Hopf oscillator.
85 % The perturbation occurs when the current phase of the oscillator
86 % is 0, though this is not imperative to reproduce our results.
87
88 for i= num:(length(time)-1)
89     ph = atan2(Y(i), X(i));
90     if(mod(floor((i - num)*natural_freq*h), 6) == 0 && (0 < ph)...
91             && (ph < natural_freq*2*pi*h - 0) && ping_num==0)
92         [~, force_id] = min((X(i) - limit_cycle(:,1)).^2 ...
93             + (Y(i)-limit_cycle(:,2)).^2);
94
95         force = 1000; % Force along the radial direction}\\
96         % Deconvolving the radial force into x,y}\\
97         force_X = force*N(force_id,1);
98         force_Y = force*N(force_id,2);
99
100        k1 = Fn1(X(i),Y(i));
101        m1 = Fn2(X(i), Y(i));
102        k2 = Fn1(X(i) + 0.5*h*k1 + 0.5*sqrt(noise_X_amp*h)*noise_X
               , ...
103             Y(i) + 0.5*h*m1 + 0.5*sqrt(noise_Y_amp*h)*noise_Y(i));
104        m2 = Fn2(X(i) + 0.5*h*k1 + 0.5*sqrt(noise_X_amp*h)*noise_X
```

```
        , ...
105          Y(i) + 0.5*h*m1 + 0.5*sqrt(noise_Y_amp*h)*noise_Y(i));
106      k3 = Fn1(X(i) + 0.5*h*k2 + 0.5*sqrt(noise_X_amp*h)*noise_X
        , ...
107          Y(i) + 0.5*h*m2 + 0.5*sqrt(noise_Y_amp*h)*noise_Y(i));
108      m3 = Fn2(X(i) + 0.5*h*k2 + 0.5*sqrt(noise_X_amp*h)*noise_X
        ,...
109          Y(i) + 0.5*h*m2 + 0.5*sqrt(noise_Y_amp*h)*noise_Y(i));
110      k4 = Fn1(X(i) + h*k3 + sqrt(noise_X_amp*h)*nnoise_X, ...
111          Y(i) + h*m3 + sqrt(noise_Y_amp*h)*noise_Y(i));
112      m4 = Fn2(X(i) + h*k3 + sqrt(noise_X_amp*h)*nnoise_X, ...
113          Y(i) + h*m3 + sqrt(noise_Y_amp*h)*noise_Y(i));
114      X(i+1) = X(i) + (1/6)*(k1+ 2*k2 + 2*k3 + k4)*h + ...
115          sqrt(noise_X_amp*h)*noise_X(i);
116      Y(i+1) = Y(i) + (1/6)*(m1 +2*m2 + 2*m3 + m4)*h + ...
117          sqrt(noise_Y_amp*h)*noise_Y(i);
118      ping_num = i;
119      ping = [ping, ping_num]; % Time array of external
        perturbations
120      i = i+1;
121  end
122
123 % Differential equations for the oscillator post perturbation
124      k1 = Fn1(X(i),Y(i));
125      m1 = Fn2(X(i), Y(i));
126      k2 = Fn1(X(i) + 0.5*h*k1 + 0.5*sqrt(noise_X_amp*h)*noise_X
        , ...
127      Y(i) + 0.5*h*m1 + 0.5*sqrt(noise_Y_amp*h)*noise_Y(i));
```

```
128         m2 = Fn2(X(i) + 0.5*h*k1 + 0.5*sqrt(noise_X_amp*h)*noise_X
                , ...
129         Y(i) + 0.5*h*m1 + 0.5*sqrt(noise_Y_amp*h)*noise_Y(i));
130         k3 = Fn1(X(i) + 0.5*h*k2 + 0.5*sqrt(noise_X_amp*h)*noise_X
                , ...
131         Y(i) + 0.5*h*m2 + 0.5*sqrt(noise_Y_amp*h)*noise_Y(i));
132         m3 = Fn2(X(i) + 0.5*h*k2 + 0.5*sqrt(noise_X_amp*h)*noise_X
                ,...
133         Y(i) + 0.5*h*m2 + 0.5*sqrt(noise_Y_amp*h)*noise_Y(i));
134         k4 = Fn1(X(i) + h*k3 + sqrt(noise_X_amp*h)*nnoise_X, ...
135         Y(i) + h*m3 + sqrt(noise_Y_amp*h)*noise_Y(i));
136         m4 = Fn2(X(i) + h*k3 + sqrt(noise_X_amp*h)*nnoise_X, ...
137         Y(i) + h*m3 + sqrt(noise_Y_amp*h)*noise_Y(i));
138         X(i+1) = X(i) + (1/6)*(k1+ 2*k2 + 2*k3 + k4)*h + ...
139         sqrt(noise_X_amp*h)*noise_X(i);
140         Y(i+1) = Y(i) + (1/6)*(m1 +2*m2 + 2*m3 + m4)*h + ...
141         sqrt(noise_Y_amp*h)*noise_Y(i);
142
143     if (i == ping_num + 3000 && ping_num~=0)
144         nearest_id = zeros(3000,1);
145         devi_amp = zeros(3000,1);
146         for j = 1:3000
147             [~, nearest_id(j)] = ...
148                 min((X(ping_num+j) - limit_cycle(:,1)).^2 + ...
149                 (Y(ping_num+j)-limit_cycle(:,2)).^2);
150             if nearest_id(j) ~= length(limit_cycle)
151                 devi_amp(j) = dot({[X(ping_num+j),Y(ping_num+j)]}
                        - ...
```

```
152                     limit_cycle(nearest_id(j),:), N(nearest_id(j)
                            ,:));
153                 else
154                     devi_amp(j) = dot([X(ping_num+j),Y(ping_num+j)]
                        ...
155                         - limit_cycle(nearest_id(j),:), N(1,:));
156                 end
157             end
158             % Perturbations in the normal/radial direction
159             devi_amp_array = [devi_amp_array, devi_amp];
160             [psd_r, f_r] = pwelch(devi_amp,[],[], ...
161                 length(devi_amp)*4,1/sampling_time);
162             f = figure; loglog(f_r , psd_r);
163             rawdata =[X(ping_num:ping_num+j), Y(ping_num:ping_num+j)];
164             % Perturbations in the phase direction
165             phase = atan2(rawdata(:,2), rawdata(:,1));
166             phase_rawdata = unwrap(phase);
167             phase_diff = (phase_rawdata(1) +  h*P(1)*(0:length(rawdata
                )-1))...
168                 - phase_rawdata';
169             phase_dev = (phase_diff(3:end) - phase_diff(2:end-1))/h;
170             [psd_phdev, f_phdev] = pwelch(final_phase_noise,[],[],...
171                 length(final_phase_noise)*4, 1/sampling_time);
172             figure; loglog(f_phdev , psd_phdev.*(f_phdev.^2));
173             ping_num = 0;
174         end
175     end
```

A.3 3-state system oscillator model a script

```
%% Description
%This script is to for a three-state jump system with states {-1,0,1} and tests its
% behaviour for three scenarios : detailed balance observed, detailed balance broken
% but can be restored in the presence of a rotating frame and detailed
% balance broken but due to history dependence of the particle's transition
% rates cannot be restored.

%% Setting random number generator

rng(0);

%% numerical
time = 39999; h = 0.01; % # of time steps and scale
num_part = 40; % particle ensemble
p = 2; % particle's transition rate values
rate = 0;%2;
lambda = 0.1;
vel_array = zeros(num_part*time,1);
cnt = 1;
ping = 1;

%probabilities of being in one of the three states {1: -1, 2: 0, 3: 1}
```

```
23 energies_1_cum = zeros(time+1,3);
24 energies_2_cum = zeros(time+1,3);
25 energies_3_cum = zeros(time+1,3);
26
27 state = [ones(1,num_part)*-1;zeros(time,num_part)];
28
29 for i = 1:num_part
30       probs = rand(time,1);
31       vel = 1;
32       for j = 2:time+1
33           if (mod(j+1,3000) == 0 || mod(j+2,3000) == 0) %|| mod(j
                +3,3000) == 0 ) %force ping for response function
34               eta = 0;
35           else
36               eta = 0;
37           end
38           energies_1_cum(j,:) = [1 - 2*h*p*ping*exp(eta), 1 - h*p*
                ping*exp(eta), 1];
39           energies_2_cum(j,:) = [exp(-eta)*ping*h*p, 1 - h*p, 1];
40           energies_3_cum(j,:) = [exp(-eta)*ping*h*p, exp(-eta)*ping*
                h*p + h*p, 1];
41
42           %particle transition depends on its previous state in the
                broken detailed balance cases
43           if vel == 0
44               if state(j-1,i) == -1
45                   state(j,i) = find(probs(j-1)<energies_1_cum(j,:)
                        ,1)-2;
```

```
46              elseif state(j-1,i) == 0
47                  state(j,i) = find(probs(j-1)<energies_2_cum(j,:)
                        ,1)-2;
48              else
49                  state(j,i) = find(probs(j-1)<energies_3_cum(j,:)
                        ,1)-2;
50              end
51          else
52              if vel == 1
53                  if state(j-1,i) == -1
54                      interim = 0;
55                  elseif state(j-1,i) == 0
56                      interim = 1;
57                  else
58                      interim = -1;
59                  end
60              elseif vel == 2
61                  if state(j-1,i) == -1
62                      interim = 1;
63                  elseif state(j-1,i) == 0
64                      interim = -1;
65                  else
66                      interim = 0;
67                  end
68              end
69              if interim == -1
70                  state(j,i) = find(probs(j-1)<energies_1_cum(j,:)
                        ,1)-2;
```

```
71                elseif interim == 0
72                    state(j,i) = find(probs(j-1)<energies_2_cum(j,:)
                          ,1)-2;
73                else
74                    state(j,i) = find(probs(j-1)<energies_3_cum(j,:)
                          ,1)-2;
75                end
76            end
77            part_state = state(1:j,i);
78            vel_array(cnt) = vel;
79            if rate ~= 0
80                vel = mod(floor(sum(rate*exp((-j+1:0)*lambda)'.*(
                      part_state))),3);
81            end
82            cnt = cnt+1;
83        end
84    end
85
86    %Occupation probabilities
87    prob_particle = zeros(num_part,3);
88    for pp = 1:num_part
89        prob_particle(pp,1) = sum(state(:,pp) == -1)/(time+1);
90        prob_particle(pp,2) = sum(state(:,pp) == 0)/(time+1);
91        prob_particle(pp,3) = sum(state(:,pp) == 1)/(time+1);
92    end
93
94    prob_time = zeros(time+1,3);
95    for pt = 1:time+1
```

```
96      prob_time(pt,1) = sum(state(pt,:) == -1)/num_part;
97      prob_time(pt,2) = sum(state(pt,:) == 0)/num_part;
98      prob_time(pt,3) = sum(state(pt,:) == 1)/num_part;
99  end
100
101 %% probabilities numerical
102 figure; hold on;
103 plot(prob_time(1:time+1,:));
104 xlabel('Time');
105 ylabel('Probabilities');
106
107
108 %% Calculation of state response function by averaging over all
        the force pings
109
110 resp_avg = zeros(3000,13);
111 for t = 0:12
112     resp_avg(:,t+1) = prob_time(t*3000+700:(t+1)*3000+699,2);
113 end
114 figure; plot(resp_avg);
115
116 %% Tensor crosscorrelation functions of the three states
117 C_00 = zeros(time*2+1,num_part);
118 C_01 = zeros(time*2+1,num_part);
119 C_0neg1 = zeros(time*2+1,num_part);
120 C_10 = zeros(time*2+1,num_part);
121 C_11 = zeros(time*2+1,num_part);
122 C_1neg1 = zeros(time*2+1,num_part);
```

```
123 C_neg10 = zeros(time*2+1,num_part);
124 C_neg11 = zeros(time*2+1,num_part);
125 C_neg1neg1 = zeros(time*2+1,num_part);
126
127 for n = 1:num_part
128     sigma_0 = state(:,n) == 0;
129     sigma_1 = state(:,n) == 1;
130     sigma_neg1 = state(:,n) == -1;
131     C_00(:,n) = xcorr(sigma_0, sigma_0, 'coeff');
132     C_01(:,n) = xcorr(sigma_0, sigma_1, 'coeff');
133     C_0neg1(:,n) = xcorr(sigma_0, sigma_neg1, 'coeff');
134     C_10(:,n) = xcorr(sigma_1, sigma_0, 'coeff');
135     C_11(:,n) = xcorr(sigma_1, sigma_1, 'coeff');
136     C_1neg1(:,n) = xcorr(sigma_1, sigma_neg1, 'coeff');
137     C_neg10(:,n) = xcorr(sigma_neg1, sigma_0, 'coeff');
138     C_neg11(:,n) = xcorr(sigma_neg1, sigma_1, 'coeff');
139     C_neg1neg1(:,n) = xcorr(sigma_neg1, sigma_neg1, 'coeff');
140 end
141
142
143 %% Variable transform in the frenet frame
144 vel_avg = floor(mean(vel_array));
145 if vel_avg == 1
146     nu_neg1 = [repmat([-1;0;1], floor(time/3),1);-1];
147     nu_0 = [repmat([0;1;-1], floor(time/3),1);0];
148     nu_1 = [repmat([1;-1;0], floor(time/3),1);1];
149 elseif vel_avg == 2
150     nu_neg1 = [repmat([-1;1;0], floor(time/3),1);-1];
```

```
151     nu_0 = [repmat([0;-1;1], floor(time/3),1);0];
152     nu_1 = [repmat([1;0;-1], floor(time/3),1);1];
153 end
154
155 %% Response function in the frenet frame
156 probf_time = zeros(time+1,3);
157 statef = zeros(size(state));
158
159 for pp = 1:num_part
160     statef((state(:,pp) == nu_neg1),pp) = -1;
161     statef((state(:,pp) == nu_0),pp) = 0;
162     statef((state(:,pp) == nu_1),pp) = 1;
163 end
164
165 for pt = 1:time+1
166     probf_time(pt,1) = sum(statef(pt,:) == -1)/num_part;
167     probf_time(pt,2) = sum(statef(pt,:) == 0)/num_part;
168     probf_time(pt,3) = sum(statef(pt,:) == 1)/num_part;
169 end
170
171 %% probabilities numerical
172 figure; hold on;
173 plot(probf_time(1:time+1,:));
174 xlabel('Time');
175 ylabel('Probabilities');
176
177 %% Calculation of state response function by averaging over all
    the force pings
```

```
178
179 respf_avg = zeros(3000,13);
180 for t = 0:12
181     respf_avg(:,t+1) = probf_time(t*3000+700:(t+1)*3000+699,2);
182 end
183 figure; plot(respf_avg);
184
185 %% Tensor crosscorrelation functions of the three states in the
      frenet frame
186
187 Cf_00 = zeros(time*2+1,num_part);
188 Cf_01 = zeros(time*2+1,num_part);
189 Cf_0neg1 = zeros(time*2+1,num_part);
190 Cf_10 = zeros(time*2+1,num_part);
191 Cf_11 = zeros(time*2+1,num_part);
192 Cf_1neg1 = zeros(time*2+1,num_part);
193 Cf_neg10 = zeros(time*2+1,num_part);
194 Cf_neg11 = zeros(time*2+1,num_part);
195 Cf_neg1neg1 = zeros(time*2+1,num_part);
196
197 for n = 1:num_part
198     sigmaf_0 = statef(:,n) == 0;
199     sigmaf_1 = statef(:,n) == 1;
200     sigmaf_neg1 = statef(:,n) == -1;
201     Cf_00(:,n) = xcorr(sigmaf_0, sigmaf_0, 'coeff');
202     Cf_01(:,n) = xcorr(sigmaf_0, sigmaf_1, 'coeff');
203     Cf_0neg1(:,n) = xcorr(sigmaf_0, sigmaf_neg1, 'coeff');
204     Cf_10(:,n) = xcorr(sigmaf_1, sigmaf_0, 'coeff');
```

```
205     Cf_11(:,n) = xcorr(sigmaf_1, sigmaf_1, 'coeff');
206     Cf_1neg1(:,n) = xcorr(sigmaf_1, sigmaf_neg1, 'coeff');
207     Cf_neg10(:,n) = xcorr(sigmaf_neg1, sigmaf_0, 'coeff');
208     Cf_neg11(:,n) = xcorr(sigmaf_neg1, sigmaf_1, 'coeff');
209     Cf_neg1neg1(:,n) = xcorr(sigmaf_neg1, sigmaf_neg1, 'coeff');
210 end
```

A.4 3-state system oscillator model b script

```
1  % Setting random number generator
2  rng(0);
3
4  % Simulating the trajectories}}
5  epsi = 0; %energy scale for correlation functions
6  time = 29999; h = 0.01; % no. of time steps and scale
7  num_part = 50; % particle ensemble
8  alpha = zeros(time-1,num_part); % particles' transition rate
       values
9  alpha = [ones(1,num_part);alpha];
10 alpha_delta = 0; % comoving frame velocity
11 rate = 0.095; lambda = 0.1; %strength and period of history
       dependence
12
13 %probabilities of being in one of the three states {1: -1, 2: 0,
       3: 1}
14 energies_1_cum = zeros(time+1,3);
15 energies_2_cum = zeros(time+1,3);
16 energies_3_cum = zeros(time+1,3);
17
```

```
18 %states of 50 particles at all time points
19 state = [ones(1,num_part)*-1;zeros(time,num_part)];
20
21 for i = 1:num_part
22     probs = rand(time,1); %these determine the next state of a
          particle
23     for j = 2:time+1
24         if (mod(j+2,1000) == 0 || mod(j+1,1000) == 0)
25             eta = 3;
26         else
27             eta = 0;
28         end
29         energies_1_cum(j,:) = [1-h*(1 + alpha(j-1,i))*exp(eta)...
30             ,1-h*(alpha(j-1,i) - alpha_delta)*exp(eta),1];
31         energies_2_cum(j,:) = [exp(epsi-eta)*(alpha(j-1,i) -
             alpha_delta)*h...
32             ,1-exp(epsi)*(1 + alpha_delta)*h,1];
33         energies_3_cum(j,:) = [exp(epsi-eta)*(1 + alpha_delta)*h/
             exp(-epsi),...
34             exp(epsi-eta)*(1 - alpha_delta)*h/exp(-epsi) + ...
35             exp(epsi)*h*(alpha(j-1,i) - alpha_delta)/exp(-epsi)
                 ,1];
36
37         %Particle transition depends on its previous state
38         %in the broken detailed balance cases;
39         %subtracting 2 merely because find yields \{1,2 or 3\}
40         %and the states are defined as \{-1,0 or 1\}
41         if state(j-1,i) == -1
```

```
42              state(j,i) = find(probs(j-1) < energies_1_cum(j,:),1)
                    -2;
43          elseif state(j-1,i) == 0
44              state(j,i) = find(probs(j-1) < energies_2_cum(j,:),1)
                    -2;
45          else
46              state(j,i) = find(probs(j-1) < energies_3_cum(j,:),1)
                    -2;
47          end
48          part_state = state(1:j,i);
49          alpha(j,i) = alpha(1,i) + sum(rate*exp((-j+1:0)*lambda)
                '.*(part_state));
50      end
51  end
52
53  %Occupation probabilities
54  prob_particle = zeros(num_part,3);
55  for pp = 1:num_part
56      prob_particle(pp,1) = sum(state(:,pp) == -1)/(time+1);
57      prob_particle(pp,2) = sum(state(:,pp) == 0)/(time+1);
58      prob_particle(pp,3) = sum(state(:,pp) == 1)/(time+1);
59  end
60
61  prob_time = zeros(time+1,3);
62  for pt = 1:time+1
63      prob_time(pt,1) = sum(state(pt,:) == -1)/num_part;
64      prob_time(pt,2) = sum(state(pt,:) == 0)/num_part;
65      prob_time(pt,3) = sum(state(pt,:) == 1)/num_part;
```

```
66 end
67
68 f = figure; hold on;
69 plot(prob_time(1:time+1,:));
70 xlabel('Time');
71 ylabel('Probabilities');
72
73 % Calculation of -1 state response function
74 %by averaging over all the force pings
75 resp_avg = zeros(1000,18);
76 for t = 0:17
77     resp_avg(:,t+1) = prob_time(t*1000+700:(t+1)*1000+699,3);
78 end
79 figure; plot(mean(resp_avg,2) - mean(mean(resp_avg(800:end,:),2)))
      ;
80
81 % Tensor of cross-correlation functions of the three states
82 C_00 = zeros(time*2+1,num_part);
83 C_01 = zeros(time*2+1,num_part);
84 C_0neg1 = zeros(time*2+1,num_part);
85 C_10 = zeros(time*2+1,num_part);
86 C_11 = zeros(time*2+1,num_part);
87 C_1neg1 = zeros(time*2+1,num_part);
88 C_neg10 = zeros(time*2+1,num_part);
89 C_neg11 = zeros(time*2+1,num_part);
90 C_neg1neg1 = zeros(time*2+1,num_part);
91
92 for n = 1:num_part
```

```
93      sigma_0 = state(:,n) == 0;
94      sigma_1 = state(:,n) == 1;
95      sigma_neg1 = state(:,n) == -1;
96      C_00(:,n) = xcorr(sigma_0, sigma_0);
97      C_01(:,n) = xcorr(sigma_0, sigma_1);
98      C_0neg1(:,n) = xcorr(sigma_0, sigma_neg1);
99      C_10(:,n) = xcorr(sigma_1, sigma_0);
100     C_11(:,n) = xcorr(sigma_1, sigma_1);
101     C_1neg1(:,n) = xcorr(sigma_1, sigma_neg1);
102     C_neg10(:,n) = xcorr(sigma_neg1, sigma_0);
103     C_neg11(:,n) = xcorr(sigma_neg1, sigma_1);
104     C_neg1neg1(:,n) = xcorr(sigma_neg1, sigma_neg1);
105 end
```

A.5 Three-dimensional model function script

```
1  clear variables;
2  close all;
3
4  %time_start = datestr(now, 'yymmdd_HHMMSS');          %stores time
       of execution of program in a string
5  %save_directory = ['nudrowski_model_spontaneous_oscillations_',
       time_start]; % name of directory
6  %mkdir(save_directory); %makes directory
7
8  % variables
9  function [X_vec, natural_freq] = neimanmodel(f_max,P0,alpha,gt,
       t_final,dt,noise_amp,IC,viscosity_change)
10
```

```
11 L = 2.8 * 10^-6 * viscosity_change;
12 L_a = 10 * 10^-6;
13 Kgs = 750 * 10^-6;
14 Ksp = 600 * 10^-6;
15 gamma = 0.14;
16 D = 6.21 * 10^-8;
17 energy_of_temparound = noise_amp;
18 T_a = 1.5 ;
19
20 h = dt;
21
22 X = zeros(t_final +1,1);
23 Xa = zeros(t_final +1,1);
24 t = zeros(t_final +1,1);
25 Prob = zeros(t_final +1,1);
26 vss = zeros(t_final +1,1);
27 S = zeros(t_final +1,1);
28 Z = zeros(t_final+1,1);
29
30 %parameters
31 f_max = f_max * 10^-12;
32 gt = gt*10^-9;
33 A = 2.382 *10^7; %exp((delta_G + Kgs*D.^2 /(2*N))/(Kb*T));
34 delta = 4.444 * 10^-9;
35 diff_Xss_Xa_ss = -delta*log((1/P0 -1)/A);
36 S0 = (1 - Kgs*(diff_Xss_Xa_ss - D*P0)/(gamma * f_max))/P0;
37
38 Prob(1) = P0;
```

```
39
40 %constants for voltage equations
41 I0 = 10*10^-12;
42 wv = 2*pi*20;
43 Cm = 14*10^-12;
44 sigma = gt/(Cm*wv);
45 Qv = 30;
46 v0 = -0.055 + I0/(wv*Cm*(1 + sigma*0.5));
47 vm0 = -0.055;
48 vss(1) =  v0 + I0/(wv*Cm*(1 + sigma*P0));
49
50 noise_channelclatter = sqrt(2*energy_of_temparound/L)*randn(
       t_final,1); % noise for the displacement function
51 noise_activemotors = sqrt(2*energy_of_temparound*T_a/L_a)*randn(
       t_final,1);    %noise for active motors
52
53 X(1) = IC(1);
54 Xa(1) = IC(2);
55
56 for i = 1:(t_final)
57 % equations for probability
58
59 S(i) = S0*(1 + alpha*(vss(i)/vm0 - 1));
60
61 %equations for state variables (ignoring calcium noise terms and
       tau = 0)
62
63 X(i+1) = X(i) + h*(-Kgs*(-delta*log((1-Prob(i))/(Prob(i)*A)) - D*
```

```
    Prob(i)) - Ksp*X(i))/L  + sqrt(h)*noise_channelclatter(i) ;
Xa(i+1) = Xa(i)+ h*(Kgs*(-delta*log((1-Prob(i))/(Prob(i)*A)) - D*
    Prob(i)) - gamma * f_max * (1 - S(i)*Prob(i)))/L_a + sqrt(h)*
    noise_activemotors(i);

k_1 = Z(i);
j_1 = -wv*(1/Qv + sigma*Prob(i))*Z(i) - wv^2*(1 + sigma*Prob(i))*(
    vss(i) - v0) - I0*wv/Cm;
k_2 = Z(i) + 0.5*h*j_1;
j_2 = -wv*(1/Qv + sigma*Prob(i))*(Z(i) + 0.5*h*j_1) - wv^2*(1 +
    sigma*Prob(i))*(vss(i) + 0.5*h*k_1 - v0) - I0*wv/Cm;
k_3 = Z(i) + 0.5*h*j_2;
j_3 = -wv*(1/Qv + sigma*Prob(i))*(Z(i) + 0.5*h*j_2) - wv^2*(1 +
    sigma*Prob(i))*(vss(i) + 0.5*h*k_2 - v0) - I0*wv/Cm;
k_4 = Z(i) + h*j_3;
j_4 = -wv*(1/Qv + sigma*Prob(i))*(Z(i) + h*j_3) - wv^2*(1 + sigma*
    Prob(i))*(vss(i) + h*k_3 - v0) - I0*wv/Cm;

vss(i+1) = vss(i) + (1/6)*(k_1+ 2*k_2 + 2*k_3 + k_4)*h ;  % main
    equation
Z(i+1) = Z(i) + (1/6)*(j_1 +2*j_2 + 2*j_3 + j_4)*h ;
Prob(i+1) = 1/(1 + A*exp((Xa(i) - X(i))/delta));
t(i+1) = t(i)+h;

end


f = figure();
```

```
84 ax = axes(f);
85 plot (ax,t,X);
86 title('Displacement vector');
87 xlabel('Time (s)');
88 ylabel('Displacement (m)');
89 %savefig(f, [save_directory, filesep, 'Displacement vector of
      spontaneous oscillations.fig']);
90 %print(f, '-dpng', '-r300',[save_directory, filesep, 'Displacement
       vector of spontaneous oscillations.png']);
91
92 f = figure();
93 ax = axes(f);
94 plot (ax,t,Xa);
95 title('Motor activity');
96 xlabel('Time (s)');
97 ylabel('Displacement of motors (m)');
98 %savefig(f, [save_directory, filesep, 'Motor activity of
      spontaneous oscillations.fig']);
99 %print(f, '-dpng', '-r300',[save_directory, filesep, 'Motor
      activity of spontaneous oscillations.png']);
100
101 f = figure();
102 ax = axes(f);
103 plot (ax,t,vss);
104 title('voltage');
105 xlabel('Time (s)');
106 ylabel('voltage (mV)');
107
```

```
108 X = X(10000:end);
109 Xa = Xa(10000:end);
110 vss = vss(10000:end);
111
112 baseline_X = smooth(X, 0.02, 'loess');
113 baseline_Xa = smooth(Xa, 0.02, 'loess');
114 baseline_vss =  smooth(vss, 0.02, 'loess');
115
116 final_X = X - baseline_X;
117 final_Xa = Xa - baseline_Xa;
118 final_vss = vss - baseline_vss;
119
120 X_vec = [final_X*10^9, final_Xa*10^9, final_vss*10^3];
121
122 [psd_X, freq_X] = pwelch(final_X, [],[],length(X)*4,1/h);
123
124 %plotting psd and calculating natural frequencies
125 f = figure();
126 ax = axes(f);
127 [~, index] = max(psd_X);
128 natural_freq = freq_X(index);
129 plot(ax,freq_X, psd_X);
130 title('PSD of displacement of spontaneous oscillations');
131 xlabel('Frequencies (Hz)');
132 ylabel('Power spectral density (a.u.)');
133 zip([save_directory, filesep, 'code_snapshot.zip'] , {'*.m'}); %
      saves all the m files in working directory into a zip file
134
```

```
135 end
```

A.6 Neiman model correlation function using 3d frenet frames script

```
1  clear variables;
2  sampling_time = 0.0001;
3
4  [X_vec ,~] = neiman_model(500,0.63,0.8,1.5,200000,sampling_time
       ,0.1*4.14*10^-21,[0,0,0],0.5);
5
6  final_X = X_vec(:,1);
7  final_Xa = X_vec(:,2);
8  final_vss = X_vec(:,3);
9  figure;
10 plot3(final_X, final_Xa, final_vss,'blue :');
11
12 [X_vec_limitcycle, natural_freq_0] = neiman_model
       (500,0.63,0.8,1.5,200000,sampling_time,0,[0,0,0],0.5);
13 limit_cycle = X_vec_limitcycle(100000:100000 + floor(1/(
       natural_freq_0*sampling_time)),:);
14
15 dx = diff(limit_cycle(:,1));
16 dy = diff(limit_cycle(:,2));
17 dz = diff(limit_cycle(:,3));
18
19 T = zeros(length(limit_cycle),3);
20 T(1:length(limit_cycle)-1,:) = [dx,dy,dz];
21 T(length(limit_cycle),:) = [limit_cycle(1,1) - limit_cycle(end,1),
```

```
    limit_cycle(1,2)-limit_cycle(end,2),limit_cycle(1,3)-
    limit_cycle(end,3)];

for i = 1:length(limit_cycle)
    T(i,:) = T(i,:)./norm(T(i,:));
end

N_x = diff(T(:,1));
N_y = diff(T(:,2));
N_z = diff(T(:,3));
N(1,:) = [T(1,1)-T(end,1), T(1,2)-T(end,2),T(1,3)-T(end,3)];
N(2:length(limit_cycle),:) = [N_x,N_y,N_z];

for i = 1:length(limit_cycle)
    N(i,:) = N(i,:)./norm(N(i,:));
end

B = cross(T,N);

X_vec = [X_vec, zeros(length(X_vec),1)];
for ph = 1:size(X_vec,1)
    [min_val, index_S] = min((X_vec(ph,1) - limit_cycle(:,1)).^2 +
        (X_vec(ph,2) - limit_cycle(:,2)).^2 + (X_vec(ph,3) -
       limit_cycle(:,3)).^2);
    X_vec(ph,4) = index_S;
end

proj_T = zeros(size(X_vec,1),1);
```

```
for i = 1:size(proj_T,1)-1
    proj_T(i) = dot((X_vec(i+1,1:3) - X_vec(i,1:3)), T(X_vec(i,4),:));%/norm(X_vec(i,1:3));
end

S = zeros(length(X_vec),1);
for i = 1:size(X_vec,1)-1
    S(i+1) = S(i) + proj_T(i);
end

X_input_noiseless = zeros(length(X_vec_limitcycle),3);
for i = 1:ceil(length(X_vec_limitcycle)/length(limit_cycle))
    X_input_noiseless(((i-1)*length(limit_cycle) + 1):(i*length(limit_cycle)),:) = limit_cycle;
end
X_input_noiseless = X_input_noiseless(1:length(X_vec_limitcycle),:);

S_noiseless = zeros(length(X_input_noiseless),1);
for i = 1:size(X_vec_limitcycle,1)-1
    S_noiseless(i+1) = S_noiseless(i) + norm(X_input_noiseless(i+1,:) - X_input_noiseless(i,:));%/norm(X_input_noiseless(i,:));
end

figure;
circum_S = S - S_noiseless;
base_cir_S = smooth(circum_S, 0.02, 'loess');
```

```
final_cir_S = circum_S - base_cir_S;
[psd_filtcir_S, freqcir_S] = pwelch(final_cir_S, [],[],length(
    final_cir_S)*4, 1/sampling_time);
freqcir_S = 2*pi*freqcir_S;
loglog(freqcir_S, psd_filtcir_S.*freqcir_S.^2);

proj_N = zeros(size(X_vec,1),2);
proj_B = zeros(size(X_vec,1),2);

for i = 1:length(X_vec)
proj_B(i,1) = norm(X_vec(i,1:3) - limit_cycle(X_vec(i,4),:));
proj_B(i,2) = dot((X_vec(i,1:3) - limit_cycle(X_vec(i,4),:)), B(
    X_vec(i,4),:))/proj_B(i,1);
end

figure;
base_B = smooth(proj_B(:,2), 0.02, 'loess');
final_B = proj_B(:,2) - base_B;
[psd_filtdvB, freqdvB] = pwelch(proj_B(:,2), [], [], length(
    final_B)*4, 1/sampling_time);
freqdvB = 2*pi*freqdvB;
loglog(freqdvB, psd_filtdvB);

for i = 1:length(X_vec)
proj_N(i,1) = norm(X_vec(i,1:3) - limit_cycle(X_vec(i,4),:));
proj_N(i,2) = dot((X_vec(i,1:3) - limit_cycle(X_vec(i,4),:)), N(
    X_vec(i,4),:))/proj_N(i,1);
end
```

```
93
94 figure;
95 base_N = smooth(proj_N(:,2), 0.02, 'loess');
96 final_N = proj_N(:,2) - base_N;
97 [psd_filtdvN, freqdvN] = pwelch(proj_N(:,2), [], [], length(
       final_N)*4, 1/sampling_time);
98 freqdvN = 2*pi*freqdvN;
99 loglog(freqdvN, psd_filtdvN);
```

A.7 Neiman model response function script

```
1
2 viscosity_change = 0.3;
3 L = 2.8 * 10^-6 * viscosity_change;
4 L_a = 10*10^-6;
5 Kgs = 750 *10^-6;
6 Ksp = 600 * 10^-6;
7 gamma = 0.14;
8 D = 6.21 * 10^-8;
9 T_a = 1.5 ;
10 f_max = 500;
11 P0 = 0.63;
12 alpha = 0.8;
13 gt = 1.5;
14
15 t_final = 200000;
16 h = 0.0001;
17
18 X = zeros(t_final +1,1);
```

```
19 Xa = zeros(t_final +1,1);
20 t = zeros(t_final +1,1);
21 Prob = zeros(t_final +1,1);
22 vss = zeros(t_final +1,1);
23 S = zeros(t_final +1,1);
24 Z = zeros(t_final+1,1);
25
26 %parameters
27 f_max = f_max * 10^-12;
28 gt = gt*10^-9;
29 A = 2.382 *10^7; %exp((delta_G + Kgs*D.^2 /(2*N))/(Kb*T));
30 delta = 4.444 * 10^-9;
31 diff_Xss_Xa_ss = -delta*log((1/P0 -1)/A);
32 S0 = (1 - Kgs*(diff_Xss_Xa_ss - D*P0)/(gamma * f_max))/P0;
33
34 Prob(1) = P0;
35
36 %constants for voltage equations
37 I0 = 10*10^-12;
38 wv = 2*pi*20;
39 Cm = 14*10^-12;
40 sigma = gt/(Cm*wv);
41 Qv = 30;
42 v0 = -0.055 + I0/(wv*Cm*(1 + sigma*0.5));
43 vm0 = -0.055;
44 vss(1) = v0 + I0/(wv*Cm*(1 + sigma*P0));
45
46 energy_of_temparound = 0;
```

```
47 noise_channelclatter = sqrt(2*energy_of_temparound/L)*randn(
       t_final,1); % noise for the displacement function
48 noise_activemotors = sqrt(2*energy_of_temparound*T_a/L_a)*randn(
       t_final,1);    %noise for active motors
49
50 IC = [0,0];
51 X(1) = IC(1);
52 Xa(1) = IC(2);
53
54 num = 60000;
55
56 for i = 1:num
57 % equations for probability
58
59 S(i) = S0*(1 + alpha*(vss(i)/vm0 - 1));
60
61 %equations for state variables (ignoring calcium noise terms and
       tau = 0)
62
63 X(i+1) = X(i) + h*(-Kgs*(-delta*log((1-Prob(i))/(Prob(i)*A)) - D*
       Prob(i)) - Ksp*X(i))/L  + sqrt(h)*noise_channelclatter(i) ;
64 Xa(i+1) = Xa(i)+ h*(Kgs*(-delta*log((1-Prob(i))/(Prob(i)*A)) - D*
       Prob(i)) - gamma * f_max * (1 - S(i)*Prob(i)))/L_a + sqrt(h)*
       noise_activemotors(i);
65
66 k_1 = Z(i);
67 j_1 = -wv*(1/Qv + sigma*Prob(i))*Z(i) - wv^2*(1 + sigma*Prob(i))*(
       vss(i) - v0) - I0*wv/Cm;
```

```
68 k_2 = Z(i) + 0.5*h*j_1;
69 j_2 = -wv*(1/Qv + sigma*Prob(i))*(Z(i) + 0.5*h*j_1) - wv^2*(1 +
       sigma*Prob(i))*(vss(i) + 0.5*h*k_1 - v0) - I0*wv/Cm;
70 k_3 = Z(i) + 0.5*h*j_2;
71 j_3 = -wv*(1/Qv + sigma*Prob(i))*(Z(i) + 0.5*h*j_2) - wv^2*(1 +
       sigma*Prob(i))*(vss(i) + 0.5*h*k_2 - v0) - I0*wv/Cm;
72 k_4 = Z(i) + h*j_3;
73 j_4 = -wv*(1/Qv + sigma*Prob(i))*(Z(i) + h*j_3) - wv^2*(1 + sigma*
       Prob(i))*(vss(i) + h*k_3 - v0) - I0*wv/Cm;
74
75 vss(i+1) = vss(i) + (1/6)*(k_1+ 2*k_2 + 2*k_3 + k_4)*h ;  % main
       equation
76 Z(i+1) = Z(i) + (1/6)*(j_1 +2*j_2 + 2*j_3 + j_4)*h ;
77 Prob(i+1) = 1/(1 + A*exp((Xa(i) - X(i))/delta));
78 t(i+1) = t(i)+h;
79
80 end
81
82 baseline_X = smooth(X(2:num), 0.02, 'loess');
83 final_X = (X(2:num) - baseline_X)*10^9;
84 baseline_Xa = smooth(Xa(2:num), 0.02, 'loess');
85 final_Xa = (Xa(2:num) - baseline_Xa)*10^9;
86 baseline_vss = smooth(vss(2:num), 0.02, 'loess');
87 final_vss = (vss(2:num) - baseline_vss)*10^3;
88
89 [psd_X, freq_X] = pwelch(final_X, [],[],length(final_X)*4,1/h);
90
91 %plotting psd and calculating natural frequencies
```

```
92 [~, index] = max(psd_X);
93 natural_freq = freq_X(index);
94
95 limit_cycle = [X(num - floor(1/(h*natural_freq)+4):num-1), Xa(num
       - floor(1/(h*natural_freq)+4):num-1), vss(num - floor(1/(h*
       natural_freq)+4):num-1)];
96 limit_cycle_frenet = [limit_cycle(:,1:2)*10^9,limit_cycle(:,3)
       *10^3];
97 T = zeros(length(limit_cycle_frenet)-1,3);
98 N = zeros(length(limit_cycle_frenet)-1,3);
99 B = zeros(length(limit_cycle_frenet)-1,3);
100
101 dx = diff(limit_cycle_frenet(:,1));
102 dy = diff(limit_cycle_frenet(:,2));
103 dz = diff(limit_cycle_frenet(:,3));
104 T(1:length(limit_cycle_frenet)-1,:) = [dx,dy,dz];
105 T(length(limit_cycle_frenet),:) = limit_cycle_frenet(1,:) -
       limit_cycle_frenet(end,:);
106
107 for i = 1:length(limit_cycle_frenet)
108     T(i,:) = T(i,:)./norm(T(i,:));
109 end
110
111 N_x = diff(T(:,1));
112 N_y = diff(T(:,2));
113 N_z = diff(T(:,3));
114 N(1,:) = [T(1,1)-T(end,1), T(1,2)-T(end,2),T(1,3)-T(end,3)];
115 N(2:length(limit_cycle_frenet),:) = [N_x,N_y,N_z];
```

```
116
117 for i = 1:length(limit_cycle_frenet)
118     N(i,:) = N(i,:)./norm(N(i,:));
119 end
120
121 B = cross(T,N);
122 for i = 1:length(limit_cycle_frenet)
123     B(i,:) = B(i,:)./norm(B(i,:));
124 end
125
126 cnt = 0;
127 ping_num = 0;
128
129 devi_amp_array = [];
130 phase_dev_array = [];
131 fft_S_array = [];
132 ping = [];
133
134 for i= num:(t_final-1)
135
136     if(mod(floor((i - num)*natural_freq*h), 6) == 0 && ping_num
        ==0)
137
138         [~, force_id] = min((X(i) - limit_cycle(:,1)).^2 + (Xa(i)-
            limit_cycle(:,2)).^2 + (vss(i)-limit_cycle(:,3)).^2);
139         force_Xa = 0;  force_vss = 0;  force_X = 70*10^-7;
140         force_proj = [abs(N(force_id,1)), abs(B(force_id,1)), abs(
            T(force_id,1))];
```

```
141         force_proj = force_proj/norm(force_proj);
142         force_N = force_Xa * force_proj(1);
143         force_B = force_Xa * force_proj(2);
144         force_T = force_Xa * force_proj(3);
145
146         S(i) = S0*(1 + alpha*(vss(i)/vm0 - 1));
147
148         X(i+1) = X(i) + h*(-Kgs*(-delta*log((1-Prob(i))/(Prob(i)*A
                )) - D*Prob(i)) - Ksp*X(i))/L  + force_X*h;
149         Xa(i+1) = Xa(i)+ h*(Kgs*(-delta*log((1-Prob(i))/(Prob(i)*A
                )) - D*Prob(i)) - gamma * f_max * (1 - S(i)*Prob(i)))/
                L_a + force_Xa*h;
150
151         k_1 = Z(i);
152         j_1 = -wv*(1/Qv + sigma*Prob(i))*Z(i) - wv^2*(1 + sigma*
                Prob(i))*(vss(i) - v0) - I0*wv/Cm + force_vss*h;
153         k_2 = Z(i) + 0.5*h*j_1;
154         j_2 = -wv*(1/Qv + sigma*Prob(i))*(Z(i) + 0.5*h*j_1) - wv
                ^2*(1 + sigma*Prob(i))*(vss(i) + 0.5*h*k_1 - v0) - I0*
                wv/Cm + force_vss*h;
155         k_3 = Z(i) + 0.5*h*j_2;
156         j_3 = -wv*(1/Qv + sigma*Prob(i))*(Z(i) + 0.5*h*j_2) - wv
                ^2*(1 + sigma*Prob(i))*(vss(i) + 0.5*h*k_2 - v0) - I0*
                wv/Cm + force_vss*h;
157         k_4 = Z(i) + h*j_3;
158         j_4 = -wv*(1/Qv + sigma*Prob(i))*(Z(i) + h*j_3) - wv^2*(1
                + sigma*Prob(i))*(vss(i) + h*k_3 - v0) - I0*wv/Cm +
                force_vss*h;
```

```
159
160         vss(i+1) = vss(i) + (1/6)*(k_1+ 2*k_2 + 2*k_3 + k_4)*h ;
                % main equation
161         Z(i+1) = Z(i) + (1/6)*(j_1 +2*j_2 + 2*j_3 + j_4)*h ;
162         Prob(i+1) = 1/(1 + A*exp((Xa(i) - X(i))/delta));
163         t(i+1) = t(i)+h;
164
165         ping_num = i;
166         ping = [ping,ping_num];
167         i = i+1;
168         cnt = cnt+1;
169
170     end
171
172     S(i) = S0*(1 + alpha*(vss(i)/vm0 - 1));
173
174     X(i+1) = X(i) + h*(-Kgs*(-delta*log((1-Prob(i))/(Prob(i)*A)) -
            D*Prob(i)) - Ksp*X(i))/L  + sqrt(h)*noise_channelclatter(i
            ) ;
175     Xa(i+1) = Xa(i)+ h*(Kgs*(-delta*log((1-Prob(i))/(Prob(i)*A)) -
            D*Prob(i)) - gamma * f_max * (1 - S(i)*Prob(i)))/L_a +
            sqrt(h)*noise_activemotors(i);
176
177     k_1 = Z(i);
178     j_1 = -wv*(1/Qv + sigma*Prob(i))*Z(i) - wv^2*(1 + sigma*Prob(i
            ))*(vss(i) - v0) - I0*wv/Cm;
179     k_2 = Z(i) + 0.5*h*j_1;
180     j_2 = -wv*(1/Qv + sigma*Prob(i))*(Z(i) + 0.5*h*j_1) - wv^2*(1
```

```
    + sigma*Prob(i))*(vss(i) + 0.5*h*k_1 - v0) - I0*wv/Cm;
181 k_3 = Z(i) + 0.5*h*j_2;
182 j_3 = -wv*(1/Qv + sigma*Prob(i))*(Z(i) + 0.5*h*j_2) - wv^2*(1
    + sigma*Prob(i))*(vss(i) + 0.5*h*k_2 - v0) - I0*wv/Cm;
183 k_4 = Z(i) + h*j_3;
184 j_4 = -wv*(1/Qv + sigma*Prob(i))*(Z(i) + h*j_3) - wv^2*(1 +
    sigma*Prob(i))*(vss(i) + h*k_3 - v0) - I0*wv/Cm;
185
186 vss(i+1) = vss(i) + (1/6)*(k_1+ 2*k_2 + 2*k_3 + k_4)*h +
    force_vss*h;  % main equation
187 Z(i+1) = Z(i) + (1/6)*(j_1 +2*j_2 + 2*j_3 + j_4)*h ;
188 Prob(i+1) = 1/(1 + A*exp((Xa(i) - X(i))/delta));
189 t(i+1) = t(i)+h;
190
191 if (i == ping_num + 8000 && ping_num~=0)
192     nearest_id = zeros(8000,1);
193     devi_N = zeros(length(nearest_id),1);
194     for j = 1:length(nearest_id)
195         [~, nearest_id(j)] = min((X(ping_num+j) - limit_cycle
                (:,1)).^2*10^18 + (Xa(ping_num+j)-limit_cycle(:,2))
                .^2*10^18 + (vss(ping_num+j)-limit_cycle(:,3))
                .^2*10^6);
196         if nearest_id(j) ~= length(limit_cycle)
197             devi_N(j) = dot([X(ping_num+j)*10^9 - limit_cycle(
                    nearest_id(j),1)*10^9, ...
198                 Xa(ping_num+j)*10^9 - limit_cycle(nearest_id(j
                        ),2)*10^9, ...
199                 vss(ping_num+j)*10^3 - limit_cycle(nearest_id(
```

```
                    j),3)*10^3], N(nearest_id(j),:));
200             else
201                 devi_N(j) = dot([X(ping_num+j)*10^9 - limit_cycle(
                        nearest_id(j),1)*10^9, ...
202                     Xa(ping_num+j)*10^9 - limit_cycle(nearest_id(j
                        ),2)*10^9, ...
203                     vss(ping_num+j)*10^3 - limit_cycle(nearest_id(
                        j),3)*10^3], N(1,:));
204             end
205         end
206         devi_amp_array = [devi_amp_array, devi_N];
207         base_N = smooth(devi_N, 0.2, 'loess');
208         final_N = devi_N - base_N;
209         fft_N = fft(final_N,4*length(final_N));
210         f = (2*pi/h)*(1:(4*length(devi_N)))/(4*length(devi_N));
211         figure; loglog(f, abs(imag(fft_N))./f');
212
213         devi_B = zeros(length(nearest_id),1);
214         for j = 1:length(nearest_id)
215             [~, nearest_id(j)] = min((X(ping_num+j) - limit_cycle
                    (:,1)).^2*10^18 + (Xa(ping_num+j)-limit_cycle(:,2))
                    .^2*10^18 + (vss(ping_num+j)-limit_cycle(:,3))
                    .^2*10^6);
216             if nearest_id(j) ~= length(limit_cycle)
217                 devi_B(j) = dot([X(ping_num+j)*10^9 - limit_cycle(
                        nearest_id(j),1)*10^9, ...
218                     Xa(ping_num+j)*10^9 - limit_cycle(nearest_id(j
                        ),2)*10^9, ...
```

```
219                     vss(ping_num+j)*10^3 - limit_cycle(nearest_id(
                            j),3)*10^3], B(nearest_id(j),:));
220             else
221                 devi_B(j) = dot([X(ping_num+j)*10^9 - limit_cycle(
                        nearest_id(j),1)*10^9, ...
222                     Xa(ping_num+j)*10^9 - limit_cycle(nearest_id(j
                            ),2)*10^9, ...
223                     vss(ping_num+j)*10^3 - limit_cycle(nearest_id(
                            j),3)*10^3], B(1,:));
224             end
225         end
226         devi_amp_array = [devi_amp_array, devi_B];
227         base_B = smooth(devi_B, 0.2, 'loess');
228         final_B = devi_B - base_B;
229         fft_B = fft(final_B,4*length(final_B));
230         figure; loglog(f, abs(imag(fft_B))./f');
231
232         devi_T = zeros(length(nearest_id),1);
233         for j = 1:length(nearest_id)
234             [~, nearest_id(j)] = min((X(ping_num+j) - limit_cycle
                    (:,1)).^2*10^18 + (Xa(ping_num+j)-limit_cycle(:,2))
                    .^2*10^18 + (vss(ping_num+j)-limit_cycle(:,3))
                    .^2*10^6);
235             if nearest_id(j) ~= length(limit_cycle)
236                 devi_T(j) = dot([X(ping_num+j)*10^9 - X(ping_num+j
                        -1)*10^9, ...
237                     Xa(ping_num+j)*10^9 - Xa(ping_num+j-1)*10^9,
                            ...
```

```
238                     vss(ping_num+j)*10^3 - vss(ping_num+j-1)
                            *10^3], T(nearest_id(j),:));
239             else
240                 devi_T(j) = dot([X(ping_num+j)*10^9 - X(ping_num+j
                        -1)*10^9, ...
241                     Xa(ping_num+j)*10^9 - Xa(ping_num+j-1)*10^9,
                            ...
242                     vss(ping_num+j)*10^3 - vss(ping_num+j-1)
                            *10^3], T(1,:));
243             end
244         end
245
246         S = zeros(length(devi_T),1);
247         for k = 1:length(S) - 1
248             S(k+1) = S(k) + devi_T(k);
249         end
250
251         X_input_noiseless = zeros(length(devi_T),3);
252         for k = 1:ceil(length(devi_T)/length(limit_cycle))
253             X_input_noiseless(((k-1)*length(limit_cycle) + 1):(k*
                    length(limit_cycle)),:) = limit_cycle;
254         end
255         X_input_noiseless = X_input_noiseless(1:length(devi_T),:);
256
257         S_noiseless = zeros(length(X_input_noiseless),1);
258         for k = 1:length(S_noiseless)-1
259             S_noiseless(k+1) = S_noiseless(k) + 10^(18)*norm(
                    X_input_noiseless(k+1,1) - X_input_noiseless(k,1))
```

```
                .^2 +...
260                 10^(18)*norm(X_input_noiseless(k+1,2) -
                        X_input_noiseless(k,2)).^2 + ...
261                 10^(6)*norm(X_input_noiseless(k+1,3) -
                        X_input_noiseless(k,3)).^2;
262         end
263
264         circum_S = S - S_noiseless;
265         base_cir_S = smooth(circum_S, 0.2, 'loess');
266         final_cir_S = circum_S - base_cir_S;
267         fft_S = fft(final_cir_S,4*length(final_cir_S));
268         figure; loglog(f, abs(imag(fft_S)).*f');
269         fft_S_array = [fft_S_array,fft_S];
270
271         ping_num = 0;
272     end
273 end
```

A.8 Script to plot final figures for psd plots with errorbars

```
1 [~,indxi] = min(abs(freqdv - 2));
2 [~,indxend] = min(abs(freqdv -10^3));
3 freq_bin = [2:1:9,10:25:10^3];
4
5 freqN = freqdv(indxi:indxend);
6 psdN = psd_filtdv(indxi:indxend)/(noise_X_amp+noise_Y_amp);
7 mean_psdN = zeros(length(freq_bin),1);
8 min_psdN = zeros(length(freq_bin),1);
9 max_psdN = zeros(length(freq_bin),1);
```

```
10 std_psdN = zeros(length(freq_bin),1);
11
12 for i = 1:length(freq_bin)-1
13     ind = find(freqN > freq_bin(i) & freqN <= freq_bin(i+1));
14     mean_psdN(i) = mean(psdN(min(ind):max(ind)));
15     min_psdN(i) = min(psdN(ind));
16     max_psdN(i) = max(psdN(ind));
17     std_psdN(i) = std(psdN(min(ind):max(ind)));
18 end
19
20 freqB = freq_corr(indxi:indxend);
21 psdB = abs(imag(psd_corr(indxi:indxend)));
22 mean_psdB = zeros(length(freq_bin),1);
23 min_psdB = zeros(length(freq_bin),1);
24 max_psdB = zeros(length(freq_bin),1);
25 std_psdB = zeros(length(freq_bin),1);
26
27 for i = 1:length(freq_bin)-1
28     ind = find(freqB > freq_bin(i) & freqB <= freq_bin(i+1));
29     mean_psdB(i) = mean(psdB(min(ind):max(ind)));
30     min_psdB(i) = min(psdB(ind));
31     max_psdB(i) = max(psdB(ind));
32     std_psdB(i) = std(psdB(min(ind):max(ind)));
33 end
34 %}
35 freqphi = freqph(indxi:indxend);
36 psdphi = psd_filtph(indxi:indxend).*freqph(indxi:indxend).^2/(
       noise_X_amp+noise_Y_amp);
```

```
37 mean_psdphi = zeros(length(freq_bin),1);
38 min_psdphi = zeros(length(freq_bin),1);
39 max_psdphi = zeros(length(freq_bin),1);
40 std_psdphi = zeros(length(freq_bin),1);
41
42 for i = 1:length(freq_bin)-1
43     ind = find(freqphi > freq_bin(i) & freqphi <= freq_bin(i+1));
44     mean_psdphi(i) = mean(psdphi(min(ind):max(ind)));
45     min_psdphi(i) = min(psdphi(ind));
46     max_psdphi(i) = max(psdphi(ind));
47     std_psdphi(i) = std(psdphi(min(ind):max(ind)));
48 end
49
50 [~,indxi] = min(abs(freqcir_S - 2));
51 [~,indxend] = min(abs(freqcir_S -2000));
52 freq_bin = [10:1:99, 100:10:2000];
53
54 freqT = freqcir_S(indxi:indxend);
55 psdT = smooth(psd_filtcir_S(indxi:indxend).*freqcir_S(indxi:
    indxend).^2,100);
56 mean_psdT = zeros(length(freq_bin),1);
57 min_psdT = zeros(length(freq_bin),1);
58 max_psdT = zeros(length(freq_bin),1);
59 std_psdT = zeros(length(freq_bin),1);
60
61 for i = 1:length(freq_bin)-1
62     ind = find(freqT > freq_bin(i) & freqT <= freq_bin(i+1));
63     mean_psdT(i) = mean(psdT(min(ind):max(ind)));
```

```
64      min_psdT(i) = min(psdT(ind));
65      max_psdT(i) = max(psdT(ind));
66      std_psdT(i) = std(psdT(min(ind):max(ind)));
67  end
```

A.9 Script for the corner cutting project of chapter 3

```
1  % This code is not well commented, so the reader is advised to
       follow
2  % through the whole code to address parts of interest.
3  % The broad idea of the code is to figure out the limit cycles of
       the
4  % underlying oscillator and study how they are distorted in the
       presence of
5  % noise. The corner cutting trajectories are counted to be those
       that
6  % deviate from the noiseless path with their potential energies
       greater
7  % than 3kT from the minima.
8
9  %%
10 [psd_X, freq_X] = pwelch(X(10^5:5000000),[],[],length(X
       (10^5:5000000))*4, 1/h);
11 [max_psd, index] = max(psd_X);
12 natural_freq = freq_X(index);
13 samp_period = 1/(natural_freq*h);
14
15 %%
16 phase = atan2(Y,X);
```

```
17 phase_space = [X,Y];
18
19 Pot_fn = @(X,Y) -mu*(X.^2 + Y.^2)*0.5 + b*0.25*(X.^2 + Y.^2).^2
       ...
20     +alpha.*cos(4*atan2(Y,X)).*exp(-(sqrt(X.^2+Y.^2) - sqrt(mu/b)
           +0.000001).^2);
21 Pot = -mu*(X.^2 + Y.^2)*0.5 + b*0.25*(X.^2 + Y.^2).^2  ...
22     +alpha.*cos(4*atan2(Y,X)).*exp(-(sqrt(X.^2+Y.^2) - sqrt(mu/b)
           +0.000001).^2);
23
24 div = (-pi:2*pi/400:pi)';
25 div_Pot_cnt = zeros(size(div));
26 div_R = zeros(length(div),2);
27 limit_cycle_in = zeros(length(div),2);
28 limit_cycle_out = zeros(length(div),2);
29
30 for i = 1:length(div)-1
31     ind = (phase >= div(i) & phase < div(i+1));
32     X_ph = X(ind);
33     Y_ph = Y(ind);
34     R_ph = sqrt(X_ph.^2 + Y_ph.^2);
35     [N, edges] = histcounts(R_ph,50);
36     [~,id] = max(N);
37     if sqrt(mu/b) - 0.2 < [edges(id),edges(id+1)] & [edges(id),
          edges(id+1)]< sqrt(mu/b) + 0.2
38         R = (edges(id) + edges(id+1))/2;
39         limit_cycle_in(i,:) = [R*cos(div(i)),R*sin(div(i))];
40         limit_cycle_out(i,:) = [R*cos(div(i)),R*sin(div(i))];
```

```
41          div_R(i,:) = [R,R];
42      end
43      if sqrt(mu/b) - 0.2 > [edges(id),edges(id+1)]
44          [~,id_R] = min(abs(edges - sqrt(mu/b)));
45          [~,id_oth] = max(N(id_R:length(N)));
46          id_oth = id_oth + id_R -1;
47          R_in = (edges(id) + edges(id+1))/2;
48          if id_R == id_oth
49              R_out = R_in;
50          else
51              R_out = (edges(id_oth) + edges(id_oth+1))/2;
52          end
53          limit_cycle_in(i,:) = [R_in*cos(div(i)),R_in*sin(div(i))];
54          limit_cycle_out(i,:) = [R_out*cos(div(i)),R_out*sin(div(i)
                )];
55          div_R(i,:) = [R_in, R_out];
56      end
57      if sqrt(mu/b) + 0.2 < [edges(id),edges(id+1)]
58          [~,id_R] = min(abs(edges - sqrt(mu/b)));
59          [~,id_oth] = max(N(1:id_R));
60          R_out = (edges(id) + edges(id+1))/2;
61          if id_R == id_oth
62              R_in = R_out;
63          else
64              R_in = (edges(id_oth) + edges(id_oth+1))/2;
65          end
66          limit_cycle_in(i,:) = [R_in*cos(div(i)),R_in*sin(div(i))];
67          limit_cycle_out(i,:) = [R_out*cos(div(i)),R_out*sin(div(i)
```

```
            )];
68          div_R(i,:) = [R_in, R_out];
69      end
70      div_Pot_cnt(i) = sum(Pot_fn(X_ph,Y_ph)< (min(Pot) + 3*
            noise_X_amp));
71      %figure; plot(edges(1:end-1),N);
72  end
73
74  for i = 1:length(div_R)-1
75      if (div_R(i,:) == [0,0])
76          low = find(div_R(1:i-1)~=0, 1,'last');
77          high = find(div_R(i+1:end)~=0, 1);
78          div_R(i,:) = (div_R(low,:)*high + div_R(i+high,:)*(i-low))
                /(i-low+high);
79          limit_cycle_in(i,:) = [div_R(i,1)*cos(div(i)),div_R(i,1)*
                sin(div(i))];
80          limit_cycle_out(i,:) = [div_R(i,2)*cos(div(i)),div_R(i,2)*
                sin(div(i))];
81      end
82  end
83  %%
84
85  Pot_min_id = find(div_Pot_cnt);
86
87  figure;
88  plot(X,Y);
89  hold on;
90  plot(limit_cycle_in(1:end-1,1), limit_cycle_in(1:end-1,2),'Color',
```

```
    'black','Linewidth',1);
plot(limit_cycle_out(1:end-1,1), limit_cycle_out(1:end-1,2),'Color
    ','black','Linewidth',1);
%%
outliers = [];
for i = 1: length(Pot_min_id)
    ind_Pot_min = (phase > div(Pot_min_id(i)) & phase < div(
        Pot_min_id(i)+1));
    X_Pot_min = X(ind_Pot_min);
    Y_Pot_min = Y(ind_Pot_min);
    R_Pot_min = sqrt(X_Pot_min.^2 + Y_Pot_min.^2);
    Pot_min = Pot_fn(X_Pot_min, Y_Pot_min);
    outlier_id = find(R_Pot_min > (sqrt(mu/b) + 0.5) | R_Pot_min <
        (sqrt(mu/b) - 0.5));
    outliers = [outliers;[X_Pot_min(outlier_id), Y_Pot_min(
        outlier_id)]];
end
%%
outliers_rem = zeros(size(outliers));
i = 1;
while ~isempty(outliers)
    outlier_id = find((phase_space(:,1) == outliers(1,1))& (
        phase_space(:,2) == outliers(1,2)));
    ps_chop = phase_space(max(outlier_id - floor(samp_period/8),1)
        : min(outlier_id + ceil(samp_period/8), length(phase_space
        )),:);
    [Com,id_out,id_chop] = intersect(outliers, ps_chop, 'rows');
    outliers_rem(i,:) = outliers(1,:);
```

```
111         outliers(id_out,:) = [];
112         i = i+1;
113     end
114     outliers_rem = outliers_rem(1:i-1,:);
115
116     %%
117     nrst_R_exit = zeros(size(outliers_rem));
118     nrst_R_entry = zeros(size(outliers_rem));
119
120     cnt = 0;
121     for i = [1:length(outliers_rem)]
122         outlier_rem_id = intersect(find(phase_space(:,1) ==
                outliers_rem(i,1)), find(phase_space(:,2) == outliers_rem(i
                ,2)));
123         ps_chop = phase_space(max(outlier_rem_id - floor(1.5*
                samp_period/8),1) : min(outlier_rem_id + ceil(1.5*
                samp_period/8),length(phase_space)),:);
124         %plot(ps_chop(:,1), ps_chop(:,2),'black');
125         R_chop = sqrt(ps_chop(:,1).^2 + ps_chop(:,2).^2);
126         R_chop(:,2:4) = zeros(length(R_chop),3);
127         for r = 1:length(R_chop)
128             phase_chop = atan2(ps_chop(r,2), ps_chop(r,1));
129             ph_bin_id = find(phase_chop - div > 0, 1,'last');
130             [min_val,min_id] = min(abs(div_R(ph_bin_id,:) - R_chop(r
                    ,1)));
131             R_chop(r,2) = min_val;
132             R_chop(r,3) = min_id;
133             R_chop(r,4) = ph_bin_id;
```

```
134     end
135
136     i_ex = find(R_chop(1:ceil(length(R_chop)/2),2)<0.1,1,'last');
137     i_ent = find(R_chop(ceil(length(R_chop)/2):end,2)<0.1,1);
138     if (~isempty(i_ex) && ~isempty(i_ent))
139         nrst_R_exit(i,3) = i_ex;
140         nrst_R_entry(i,3) = ceil(length(R_chop)/2)+i_ent -1;
141        % plot(ps_chop(nrst_R_exit(i,3):nrst_R_entry(i,3),1),
            ps_chop(nrst_R_exit(i,3):nrst_R_entry(i,3),2),'black');
142         nrst_R_exit(i,1) = R_chop(i_ex,3);
143         nrst_R_exit(i,2) = R_chop(i_ex,4);
144         nrst_R_entry(i,1) = R_chop(ceil(length(R_chop)/2)+i_ent
              -1,3);
145         nrst_R_entry(i,2) = R_chop(ceil(length(R_chop)/2)+i_ent
              -1,4);
146         cnt = cnt+1;
147     end
148 end
149
150 nrst_R_entry((nrst_R_exit(:,1) == 2),1) = 2;
151
152 S_in = zeros(length(div)-1,3);
153 S_out = zeros(length(div)-1,3);
154 for i = 2:length(div)-1
155     S_in(i,1) = S_in(i-1,1) + norm(limit_cycle_in(i,:) -
          limit_cycle_in(i-1,:));
156     S_out(i,1) = S_out(i-1,1) + norm(limit_cycle_out(i,:) -
          limit_cycle_out(i-1,:));
```

```
157 end
158
159 for i = 1:length(div)
160     S_in(i,2) = sum(nrst_R_exit(:,2) == i & nrst_R_exit(:,1) == 1)
        ;
161     S_in(i,3) = sum(nrst_R_entry(:,2) == i & nrst_R_entry(:,1) ==
        1);
162     S_out(i,2) = sum(nrst_R_exit(:,2) == i & nrst_R_exit(:,1) ==
        2);
163     S_out(i,3) = sum(nrst_R_entry(:,2) == i & nrst_R_entry(:,1) ==
         2);
164 end
165 %%
166 figure;
167 plot(limit_cycle_in(1:end-1,1), limit_cycle_in(1:end-1,2),'Color'
    ,[212/255,208/255,200/255],'Linewidth',1);
168 hold on;
169 plot(limit_cycle_out(1:end-1,1), limit_cycle_out(1:end-1,2),'Color
    ',[212/255,208/255,200/255],'Linewidth',1);
170
171 prob_array = linspace(min([min(S_in(:,2:3)),min(S_out(:,2:3))]),
    max([max(S_in(:,2:3)),max(S_out(:,2:3))]),41);
172 hold on;
173 for j =1:length(div)-1
174     if (0 < S_in(j,2)) && (S_in(j,2) <= prob_array(10)) || (0 <
        S_in(j,3)) && (S_in(j,3) <= prob_array(10))
175         plot(limit_cycle_in(j:j+1,1),limit_cycle_in(j:j+1,2),'blue
            ', 'Linewidth',1);
```

```
176     end
177     if (prob_array(10) < S_in(j,2)) && (S_in(j,2) <= prob_array
        (20)) || (prob_array(10) < S_in(j,3)) && (S_in(j,3) <=
        prob_array(20))
178         plot(limit_cycle_in(j:j+1,1),limit_cycle_in(j:j+1,2),'cyan
            ', 'Linewidth',1);
179     end
180     if (prob_array(20) < S_in(j,2)) && (S_in(j,2) <= prob_array
        (30)) || (prob_array(20) < S_in(j,3)) && (S_in(j,3) <=
        prob_array(30))
181         plot(limit_cycle_in(j:j+1,1),limit_cycle_in(j:j+1,2),'
            Color',[222/255,125/255,0], 'Linewidth',1);
182     end
183     if (prob_array(30) < S_in(j,2)) && (S_in(j,2) <= prob_array(
        end)) || (prob_array(30) < S_in(j,3)) && (S_in(j,3) <=
        prob_array(end))
184         plot(limit_cycle_in(j:j+1,1),limit_cycle_in(j:j+1,2),'
            Color',[1,0,0], 'Linewidth',1);
185     end
186
187     if (0 < S_out(j,2)) && (S_out(j,2) <= prob_array(10)) || (0 <
        S_out(j,3)) && (S_out(j,3) <= prob_array(10))
188         plot(limit_cycle_out(j:j+1,1),limit_cycle_out(j:j+1,2),'
            blue', 'Linewidth',1);
189     end
190     if (prob_array(10) < S_out(j,2)) && (S_out(j,2) <= prob_array
        (20)) || (prob_array(10) < S_out(j,3)) && (S_out(j,3) <=
        prob_array(20))
```

```
191             plot(limit_cycle_out(j:j+1,1),limit_cycle_out(j:j+1,2),'
                    cyan', 'Linewidth',1);
192         end
193         if (prob_array(20) < S_out(j,2)) && (S_out(j,2) <= prob_array
                (30)) || (prob_array(20) < S_out(j,3)) && (S_out(j,3) <=
                prob_array(30))
194             plot(limit_cycle_out(j:j+1,1),limit_cycle_out(j:j+1,2),'
                    Color',[222/255,125/255,0], 'Linewidth',1);
195         end
196         if (prob_array(30) < S_out(j,2)) && (S_out(j,2) <= prob_array(
                end)) || (prob_array(30) < S_out(j,3)) && (S_out(j,3) <=
                prob_array(end))
197             plot(limit_cycle_out(j:j+1,1),limit_cycle_out(j:j+1,2),'
                    Color',[1,0,0], 'Linewidth',1);
198         end
199
200 end
201
202 figure;
203 plot(S_in(1:end-1,1), S_in(1:end-1,2))
204 hold on;
205 plot(S_in(1:end-1,1), S_in(1:end-1,3))
206
207 figure;
208 plot(S_out(:,1), S_out(:,2))
209 hold on;
210 plot(S_out(:,1), S_out(:,3))
211 %}
```

```
212 R_ex_ent = zeros(length(div), length(div));
213
214 for i = 1:length(div)
215     for j = 1:length(div)
216         R_ex_ent(i,j) = length(intersect(find((nrst_R_exit(:,2) ==
                i) & (nrst_R_exit(:,1) == 1)),...
217             find((nrst_R_entry(:,2) == j) & (nrst_R_entry(:,1) ==
                1))));
218     end
219 end
220
221 mat_cut = R_ex_ent(1:100,1:100);
222 [~, max_idx] = max(mat_cut(:));
223 [max_id_100(2), max_id_100(1)] = ind2sub(size(mat_cut),max_idx);
224 mat_cut = R_ex_ent(101:200,101:200);
225 [~, max_idx] = max(mat_cut(:));
226 [max_id_200(2), max_id_200(1)] = ind2sub(size(mat_cut),max_idx);
227 mat_cut = R_ex_ent(201:300,201:300);
228 [~, max_idx] = max(mat_cut(:));
229 [max_id_300(2), max_id_300(1)] = ind2sub(size(mat_cut),max_idx);
230 mat_cut = R_ex_ent(301:400,301:400);
231 [~, max_idx] = max(mat_cut(:));
232 [max_id_400(2), max_id_400(1)] = ind2sub(size(mat_cut),max_idx);
233 %}
234 ex_id = find(nrst_R_exit(:,2) == max_id_400(:,2)+300);
235 en_id = find(nrst_R_entry(:,2) == max_id_400(:,1)+300);
236 max_crn_cut = intersect(ex_id, en_id);
237 max_crn_cut = max_crn_cut(nrst_R_exit([max_crn_cut],1)==1);
```

```
238
239 %f1 = figure; ax1 = axes(f1); hold on;
240 %f2 = figure; ax2 = axes(f2); hold on;
241
242 for max_id = 1:length(max_crn_cut)
243     i = max_crn_cut(max_id);
244     outlier_rem_id = intersect(find(phase_space(:,1) ==
        outliers_rem(i,1)), find(phase_space(:,2) == outliers_rem(i
        ,2)));
245     ps_chop = phase_space(max(outlier_rem_id - floor(1.5*
        samp_period/8),1) : min(outlier_rem_id + ceil(1.5*
        samp_period/8),length(phase_space)),:);
246     ccut = ps_chop(nrst_R_exit(i,3):nrst_R_entry(i,3),:);
247     S_crn_cut = zeros(length(ccut),1);
248     for lc = 2:length(ccut)
249         S_crn_cut(lc,1) = S_crn_cut(lc-1,1) + norm(ccut(lc,:) -
            ccut(lc-1,:));
250     end
251     Pot_crn_cut = Pot_fn(ccut(:,1), ccut(:,2));
252     %plot(ccut(:,1), ccut(:,2));
253     R_ccut = sqrt(ccut(:,1).^2 + ccut(:,2).^2);
254     force_ccut = w0*R_ccut;
255     work_ccut = zeros(length(ccut),1);
256     for wa = 2:length(work_ccut)
257         ph_ccut = atan2(ccut(wa-1,2),ccut(wa-1,1));
258         tangent = R_ccut(wa-1)*[cos(ph_ccut+pi/400), sin(ph_ccut+
            pi/400)] - R_ccut(wa-1)*[cos(ph_ccut), sin(ph_ccut)];
259         %quiver(ccut(wa-1,1), ccut(wa-1,2), tangent(1),tangent(2)
```

```
                ,0.2);
260             work_ccut(wa) = work_ccut(wa-1) + force_ccut(wa-1)*dot(
                    tangent/norm(tangent), (ccut(wa,:)-ccut(wa-1,:)));
261         end
262         plot(ax1, S_crn_cut/S_crn_cut(end), Pot_crn_cut,'green');
263         plot(ax2, S_crn_cut/S_crn_cut(end), work_ccut,'green');
264     end
265
266     ccut_b = limit_cycle_in(max_id_400(2)+300:max_id_400(1)+300,:);
267     Pot_ccut_b = Pot_fn(ccut_b(:,1),ccut_b(:,2));
268
269     R_ccut_b = sqrt(ccut_b(:,1).^2 + ccut_b(:,2).^2);
270     force_ccut_b = w0*R_ccut_b;
271     work_ccut_b = zeros(length(ccut_b),1);
272
273     for wa = 2:length(work_ccut_b)
274         ph_ccutb = atan2(ccut_b(wa-1,2),ccut_b(wa-1,1));
275         tangent = R_ccut_b(wa-1)*[cos(ph_ccutb+pi/400), sin(ph_ccutb+
                pi/400)] - R_ccut_b(wa-1)*[cos(ph_ccutb), sin(ph_ccutb)];
276         %quiver(ccut_b(wa-1,1), ccut_b(wa-1,2), tangent(1),tangent(2)
                ,0.5);
277         work_ccut_b(wa) = work_ccut_b(wa-1) + force_ccut_b(wa-1)*dot(
                tangent/norm(tangent), (ccut_b(wa,:)-ccut_b(wa-1,:)));
278     end
279     S_temp = S_in(max_id_400(2)+300:max_id_400(1)+300) - S_in(
            max_id_400(2)+300);
280     plot(ax1, S_temp/S_temp(end), Pot_ccut_b,'black','Linewidth',1);
281     plot(ax2, S_temp/S_temp(end), work_ccut_b,'black','linewidth',1);
```

A.10 Script for plotting the potential maps in chapters 3 and 4

```
1
2  %time_start = datestr(now, 'yymmdd_HHMMSS');
3  %save_directory = ['mesh_potential_hopf_', time_start];
4  %mkdir(save_directory);
5
6  dr = 0.02;
7  dphi = 0.1;
8  R_mesh = dr/2:0.5:15-dr/2;
9  Phi_mesh = -pi:dphi*pi/180:pi;
10 R_pot = (R_mesh(1:end-2)+R_mesh(2:end-1))/2;
11 Phi_pot = (Phi_mesh(1:end-2)+Phi_mesh(2:end-1))/2;
12
13 Pot = zeros(length(R_pot), length(Phi_pot));
14 X_pot = zeros(size(Pot));
15 Y_pot = zeros(size(Pot));
16
17 %Code to add perturbations to the basic mexican hat potential
18 %Fn_charge = @(Y,X) alpha*exp(-(sqrt(X^2+Y^2) - sqrt(mu/b)
       +0.000001)^2)*cos(2*atan2(Y,X))*...
19      %(4 - 4*(sqrt(X^2+Y^2) - sqrt(mu/b)+0.000001)^2 - 2*sqrt(mu/(b
           *(X^2+Y^2))) + 2*0.000001/sqrt(X^2+Y^2) + 4/(X^2+Y^2));   %
           remember to change to scalar or vector potential while
           saving the figure
20 Fn_charge = @(R,Phi) alpha*exp(-(R - sqrt(mu/b))^2)*cos(4*Phi)*(4
       - 4*(R - sqrt(mu/b)+0.000001)^2 - 2*sqrt(mu/(b*R^2)) +
       2*0.000001/R + 16/(R^2));
21
```

```
for i_p = 1:length(R_pot)
    for j_p = 1:length(Phi_pot)
        for i_m = 1:length(R_mesh)
            for j_m = 1:length(Phi_mesh)-1
                Pot(i_p, j_p) = Pot(i_p, j_p) + Fn_charge(R_mesh(
                    i_m), Phi_mesh(j_m))*log((R_mesh(i_m)*cos(
                    Phi_mesh(j_m)) - R_pot(i_p)*cos(Phi_pot(j_p)))
                    .^2 + (R_mesh(i_m)*sin(Phi_mesh(j_m)) - R_pot(
                    i_p)*sin(Phi_pot(j_p))).^2)*R_mesh(i_m)*dr*dphi
                    /(4*180);
            end
        end
    end
end

%{
for i_p = 1:length(X_pot)
    for j_p = 1:length(Y_pot)
        for i_m = 1:length(X_mesh)
            for j_m = 1:length(Y_mesh)
                Pot(i_p, j_p) = Pot(i_p, j_p) + Fn_charge( Y_mesh(
                    j_m), X_mesh(i_m))*log((X_mesh(i_m) - X_pot(i_p
                    )).^2 + (Y_mesh(j_m) - Y_pot(j_p)).^2)*dx*dy
                    /(4*pi);
            end
        end
    end
end
```

```
%}
%Pot_alt = Pot - mean(Pot(1,:));

% converting polar to cartesian coordinates
for i_Xrow = 1:length(R_pot)
for i_Xcol = 1:length(Phi_pot)
X_pot(i_Xrow, i_Xcol) = R_pot(i_Xrow)*cos(Phi_pot(i_Xcol));
Y_pot(i_Xrow, i_Xcol) = R_pot(i_Xrow)*sin(Phi_pot(i_Xcol));
end
end


Pot_add = zeros(size(Pot,1),size(Pot,2));
for i = 1:length(R_pot)
for j = 1:length(Phi_pot)
Pot_add(i,j) = mu*(R_pot(i)^2)/2 - b*(R_pot(i)^4)/4;
end
end
Pot_tot = Pot + Pot_add;

f = figure;
colormap (f,winter);
surf(X_pot(:,1:1790), Y_pot(:,1:1790), -Pot_tot(:,1:1790),'
    FaceColor','interp','EdgeColor','none');
xlabel('X (a.u)');
ylabel('Y (a.u)');
set(gca, 'fontsize',16);
savefig(f, [save_directory, filesep, 'Scalar potential contourmap.
```

```
    fig']);
print(f, '-dpng', '-r300',[save_directory, filesep, 'Scalar potential contourmap.png']);

%save([save_directory, filesep, 'data.mat']); %saves workspace
%zip([save_directory, filesep, 'code_snapshot.zip'] , {'*.m'}); % saves all the m files in working directory into a zip file
```

A.11 Experimental data analysis

Note: This code assumes that the bundle follows the Hopf model. Can we easily tweaked for the X-V plots in Sheth (PRE, 2018).

```
close all; clear variables;

% Extracting data stored in a figure
open('/Users/janaki/Dropbox/MATLAB/smoothening data and fdt analysis/raw\_data/probes\_control/probe7x(t).fig');
h = gcf;
axesObjs = get(h, 'Children');  %axes handles
dataObjs = get(axesObjs, 'Children'); % handles to low-level graphics objects in axes
objTypes = get(dataObjs, 'Type'); %  type of low-level graphics object
ydata = get(dataObjs, 'YData');
xdata = get(dataObjs, 'XData');

%  Extracting data from a mat file
rawdata_matrix = load('/Users/janaki/Dropbox/MATLAB/smoothening data and fdt analysis/raw\_data/justin\_spikes/quiescent.mat');
```

```
14 rawdata = rawdata_matrix.W.Cam(10000:50000);
15 rawdata = -quiescent;
16 sampling_time = 0.001;
17 time = (sampling_time:sampling_time:length(rawdata)*sampling_time)
       ';
18 data = [time,rawdata(1:end)];
19
20 %  Preprocessing
21 figure; plot(time,data(:,2));
22 baseline = smooth(rawdata,0.5, 'loess');
23 final_data = data(:,2) - baseline;
24 f1 = figure(); ax = axes(f1);
25 plot (ax, time, final_data);
26 title('Raw data');
27 xlabel('Time(s)');
28 ylabel('Position(nm)');
29
30 %  Calculating natural frequency
31 [psd_filtdt,freqdt] = pwelch(final_data,[],[],length(final_data)
      *4,1/sampling_time);
32 freqdt = 2*pi*freqdt;
33 [max_psd, index] = max(psd_filtdt);
34 natural_freq = freqdt(index);
35 f2 = figure(); ax = axes(f2);
36 plot(ax,freqdt, psd_filtdt);
37 title('PSD in linear axes');
38 xlabel('$\omega$(Hz)');
39 ylabel('PSD(nm^{2}/Hz)');
```

```
40 f3 = figure(); ax = axes(f3);
41 plot(ax, log10(freqdt), log10(psd_filtdt));
42 title('PSD in linear axes');
43 xlabel('log\_{10}($\omega$)(Hz)');
44 ylabel('log\_{10}PSD(nm\^{}{2}/Hz)');
45
46 % Calculation of phase angle
47 y_rect = final_data;
48 hilt = hilbert(y_rect, 2.^ceil(log2(length(rawdata))));
49 phase_array = [y_rect, imag(hilt(1:length(rawdata)))];
50 phase_array = phase_array(floor(0.2*length(rawdata)):floor(0.8*
      length(rawdata)),:);
51 phase = atan2(phase_array(:,2), phase_array(:,1));
52 time = time(floor(0.2*length(rawdata)):floor(0.8*length(rawdata)))
      - time(floor(0.2*length(rawdata)));
53 f = figure(); ax = axes(f);
54 plot (ax, time, phase);
55 title('Phase of the limit cycle using atan');
56 xlabel('Time(s)');
57 ylabel('Phase(rad)');
58
59 %fitting a straight line to derive stochasticity in the phase
      angle
60 phase_un = unwrap(phase);
61 P = polyfit(time, phase_un - phase_un(1), 1);
62 yfit = P(1)*time + P(2);
63 f = figure(); ax = axes(f);
64 plot (ax,time, phase_un - phase_un(1));
```

```
65 hold on;
66 plot(ax, time, yfit);
67 title('Unwrapped phase using acos and adding angles');
68 xlabel('Time(s)');
69 ylabel('Phase(rad)');
70
71 %Fluctuations in tangential direction
72 baseline_ph_noise = smooth(phase_noise, 0.5, 'loess');
73 final_phase_noise = phase_noise - baseline_ph_noise;
74 [psd_filtph, freqph] = pwelch(final_phase_noise,[],[],length(
      final_phase_noise)*4, 1/sampling_time);
75 freqph = 2*pi*freqph;
76 f = figure(); ax = axes(f);
77 loglog (ax,freqph, psd_filtph);
78 title('PSD of differential phase');
79 xlabel('Log(Frequency)');
80 ylabel('Log(PSD)');
81
82 %Calculating limit cycle and radial deviation from it
83 div = (-pi:2*pi/200:pi)';
84 sum_amp = zeros(length(div)-1,2);
85 norm_amp = zeros(length(div)-1,1);
86 devi_amp = zeros(length(phase)-1,1);
87 cnt = 0;
88 for i = 1:length(div)-1
89     ind = find(phase >= div(i) & phase < div(i+1));
90     for j = 1:length(ind)
```

```
91          sum_amp(i,:) = sum_amp(i,:) + phase_array(ind(j),:)/length
                (ind);
92          norm_amp(i) = norm_amp(i) + norm(phase_array(ind(j),:))/
                length(ind);
93      end
94      for ph = 1:length(phase)
95          if(any(abs(ph-ind)<1e-10))
96              devi_amp(ph) = norm(phase_array(ph,:)) - norm_amp(i);
97          end
98      end
99  end
100
101 f = figure(); ax = axes(f);
102 plot (ax,phase_array(:,1), phase_array(:,2));
103 hold on;
104 plot(ax,sum_amp(:,1), sum_amp(:,2));
105 title('Noisy and approximated limit cycle ');
106 xlabel('x($\phi$)');
107 ylabel('x($\phi + \pi/2$)');
108
109 baseline_amp_devi = smooth(devi_amp, 0.02, 'loess');
110 amp_devi = devi_amp - baseline_amp_devi;
111 [psd_filtdv, freqdv] = pwelch(devi_amp,[],[],length(final_data)*4,
        1/sampling_time);
112 freqdv = 2*pi*freqdv;
113 f = figure(); ax = axes(f);
114 loglog(ax,freqdv, psd_filtdv);
115 title('PSD of differential amplitude');
```

```
116 xlabel('Log(frequency)');
117 ylabel('Log(PSD)');
```

Bibliography

[1] A.J.Hudspeth. How the ear's works work. *Nature*, 341:397–404, 1989.

[2] A.J.Hudspeth. Making an Effort to Listen: Mechanical Amplification in the Ear. *Neuron*, 59:530–545, 2008.

[3] R. Amro and A.B. Neiman. Effect of bidirectional mechanoelectrical coupling on spontaneous oscillations and sensitivity in a model of hair cells. *PRE*, 90:052704, 2014.

[4] M. Baiesi, C. Maes, and B. Wynants. Nonequilibrium Linear Response for Markov Dynamics, I: Jump processes and overdamped diffusions. *Journal of Stat. Phys.*, 137:1094, 2009.

[5] M. Benser, R. Marquis, and A. Hudspeth. Rapid, Active Hair Bundle Movements in Hair Cells from the Bullfrogs Sacculus. *J. Neurosci.*, 16:5629 – 5643, 1996.

[6] D. Bozovic and A. Hudspeth. Hair-bundle movements elicited by transepithelial electrical stimulation of hair cells in the bullfrog's sacculus. *PNAS*, 100:958–963, 2003.

[7] H. Callen and T. Welton. Irreversibility and Generalized Noise. *PR*, 83:34, 1951.

[8] S. Camalet, T. Duke, F.Jlicher, and J. Prost. Auditory sensitivity provided by self-tuned critical oscillations of hair cells. *PNAS*, 97:3183–88, 2000.

[9] L. Catacuzzeno, B. Fioretti, P. Perin, and F. Franciolini. Spontaneous lowfrequency voltage oscillations in frog saccular hair cells. *J. Physiol.*, 561:685 – 701, 2004.

[10] E. Cheung and D. Corey. Ca2+ changes the force sensitivity of the hair-cell transduction channel. *Biophys. J.*, 90:124–139, 2006.

[11] C.J.Lin and D. Bozovic. Effects of Efferent Activity on Hair Bundle Mechanics. *J. Neuroscience*, 40:2390–2402, 2020.

[12] C.F.Schmidt D. Mizuno, C. Tardin and F.C. MacKintosh. Nonequilibrium mechanics of active cytoskeletal networks. *Science*, 315:370–3, 2007.

[13] L. Dinis, P. Martin, J. Barral, J. Prost, and J.F. Joanny. Fluctuation-response theorem for the active noisy oscillator of the hair-cell bundle. *PRL*, 109:160602, 2012.

[14] R. A. Eatock. Adaptation in Hair Cells. *Annual Review of Neuroscience*, 23:285–314, 2000.

[15] A. Flock, B. Flock, and E. Murray. Studies on the sensory hairs of receptor cells in the inner ear. *Acta Otolaryngol.*, 83:85–91, 1977.

[16] F. S. Gnesotto, F. Mura, J. Gladrow, and C. P. Broedersz. Broken detailed balance and non-equilibrium dynamics in living systems: a review. *Rep. Prog. Phys.*, 81:066601, 2018.

[17] L. Le Goff, D. Bozovic, and A. J. Hudspeth. Adaptive shift in the domain of negative stiffness during spontaneous oscillatfion by hair bundles from the internal ear. *PNAS*, 102:16996 – 17001, 2005.

[18] T. Gold. Hearing II. The physical basis of action in the cochlea. *Proc. R. Soc. Lond. B. Biol. Sci.*, 135:492–498, 1948.

[19] L. Han and A.B. Neiman. Spontaneous oscillations, signal amplification, and synchronization in a model of active hair bundle mechanics. *PRE*, 81:041913, 2010.

[20] J. Howard and A. Hudspeth. Mechanical relaxation of the hair bundle mediates adaptation in mechanoelectrical transduction by the bullfrogs saccular hair cell. *PNAS*, 84:3064–8, 1987.

[21] A. J. Hudspeth and R. Lewis. A model for electrical resonanceand frequency tuning in saccular hair cells of the bull-frog *Rana catesbeiana*. *J. Physiol.*, 400:275–97, 1988.

[22] A. J. Hudspeth and R. Lewis. Kinetic analysis of voltage- and ion-dependent conductances in saccular hair cells of the bull-frog *Rana catesbeiana*. *J. Physiol.*, 400:237–74, 1988.

[23] A.J. Hudspeth. Integrating the active process of hair cells with cochlear function. *Nat. Rev. Neurosci.*, 15:600–14, 2014.

[24] J. Hudspeth, Y. Choe, A. Mehta, and P. Martin. Putting ion channels to work: Mechanoelectrical transduction, adaptation, and amplification by hair cells. *PNAS*, 97:11765–72, 2000.

[25] F. Jorgensen and A. B. A. Kroese. Ion channel regulation of the dynamical instability of the resting membrane potential in saccular hair cells of the green frog Rana esculenta. *Acta Physiol. Scand.*, 185:271, 2005.

[26] E. R. Kandel, J. H. Schwartz, T. M. Jessell, S. A. Siegelbaum, and A. J. Hudspeth. *Principles of Neural Science*. The McGraw-Hill Companies, Inc., 2013.

[27] R. Kubo. Statistical-Mechanical Theory of Irreversible Processes. I: General Theory and Simple applications to Magnetic and Conduction Problems. *J. Phys. Soc. Jpn.*, 12:570–586, 1957.

[28] G. Lan, P. Sartori, S. Neumann, V. Sourjik, and Y. Tu. The energy-speed-accuracy tradeoff in sensory adaptation. *Nature Physics*, 8:422–428, 2012.

[29] M. LeMasurier and P. Gillespie. Hair-Cell Mechanotransduction and Cochlear Amplification. *Neuron*, 48:403–415, 2005.

[30] P. Martin, D. Bozovic, Y. Choe, and A.J. Hudspeth. Spontaneous Oscillation by Hair Bundles of the Bullfrog's Sacculus. *J. Neurosci.*, 23:4533–48, 2003.

[31] P. Martin and A.J. Hudspeth. Active hair-bundle movements can amplify a hair cells response to oscillatory mechanical stimuli. *PNAS*, 96:14306–11, 1999.

[32] P. Martin, A.J. Hudspeth, and F. Julicher. Comparison of a hair bundle's spontaneous oscillations with its response to mechanical stimulation reveals the underlying active process. *PNAS*, 98:14380–85, 2001.

[33] P. Martin, A. Mehta, and A. Hudspeth. Negative hair-bundle stiffness betrays a mechanism for mechanical amplification by the hair cell. *PNAS*, 97:12026 – 31, 2000.

[34] S.W.F. Meenderink, P. Quinones, and D. Bozovic. Voltage-Mediated Control of Spontaneous Bundle Oscillations in Saccular Hair Cells. *J. Neurosci.*, 35:14457–66, 2015.

[35] K.A. Montgomery, M. Silber, and S.A. Solla. Amplification in the auditory periphery: The effect of coupling tuning mechanisms. *PRE*, 75:051924, 2007.

[36] B. Nadrowksi, P. Martin, and F.Julicher. Active hair-bundle motility harnesses noise to operate near an optimum of mechanosensitivity. *PNAS*, 101:12195–12200, 2004.

[37] A.B. Neiman, K. Dierkes, B. Lindner, L. Han, and A.L. Shilnikov. Spontaneous voltage oscillations and response dynamics of a Hodgkin-Huxley type model of sensory hair cells. *The Journal of Mathematical Neuroscience*, 1:041913, 11.

[38] J. Newby and M. Schwemmer. Effects of Moderate Noise on a Limit Cycle Oscillator: Counterrotation and Bistability. *PRL*, 112:114101, 2014.

[39] L.K. Nguyen. Regulation of oscillation dynamics in biochemical systems with dual negative feedback loops. *J.R. Soc. Interface*, 9:1998–2010, 2012.

[40] M. Ospeck, V.M. Eguiliz, and M.O. Magnasco. Evidence of a Hopf Bifurcation in Frog Hair Cells. *Biophys. J.*, 80:2597–2607, 2001.

[41] J. Pickles, S. Comis, and M. Osbourne. Cross-links between stereocilia in the guinea pig organ of Corti, and their possible relation to sensory transduction. *Hear. Res.*, 15:103–12, 1984.

[42] J. Prost, J.F. Joanny, and J.M.R. Parrondo. Generalized Fluctuation-Dissipation Theorem for Steady-State Systems. *PRL*, 103:090601, 2009.

[43] D. Ramunno-Johnson, C.E. Strimbu, L. Fredrickson, K. Arisaka, and D. Bozovic. Distribution of Frequencies of Spontaneous Oscillations in Hair Cells of the Bullfrog Sacculus. *Biophys. J.*, 96:1159–68, 2009.

[44] T. Reichenbach and A.J.Hudspeth. The physics of hearing: fluid mechanics and the active process of the inner ear. *Rep. Prog. Phys.*, 77:076601, 2017.

[45] L. Robles and M. Ruggero. Mechanics of the Mammalian Cochlea. *Physiol. Rev.*, 81:1305–1352, 2001.

[46] Y. Roongthumskul, L. Fredrickson-Hemsing, A. Kao, and D. Bozovic. Multiple-timescale dynamics underlying spontaneous oscillations of saccular hair bundles. *Biophys. J.*, 101:603–10, 2011.

[47] M.A. Ruggero, N.C. Rich, A. Recio, S.S. Narayan, and L. Robles. Basilar-membrane responses to tones at the base of the chinchilla cochlea. *J. Acoust. Soc. Am.*, 101:2151–63, 1997.

[48] M.. Rutherford and W. Roberts. Spikes and Membrane Potential Oscillations in Hair Cells Generate Periodic Afferent Activity in the Frog Sacculus. *J. Neurosci.*, 29:10025–37, 2009.

[49] J. Salvi, D. Maoilidigh, and A.J. Hudspeth. Identification of Bifurcations from Observations of Noisy Biological Oscillators. *Biophys. J.*, 111:798–812, 2016.

[50] U. Seifert. Stochastic thermodynamics, fluctuation theorems and molecular machines. *Rep. Prog. Phys.*, 75:126001, 2012.

[51] U. Seifert and T. Speck. Fluctuation-dissipation theorem in nonequilibrium steady states. *Euro. Phys. Lett.*, 89:10007, 2010.

[52] J. Sheth, S.W.F. Meenderink, P.M. Quiones, D. Bozovic, and A.J. Levine. Nonequilibrium limit-cycle oscillators: Fluctuations in hair bundle dynamics. *PRE*, 97:062411, 2018.

[53] T. Speck and U. Seifert. Restoring a fluctuation-dissipation theorem in a nonequilibrium steady state. *Europhys. Lett.*, 74:391–396, 2006.

[54] R. Stoop, A. Kern, M. C. Gpfert, D. A. Smirnov, T. V. Dikanev, and B. P. Bezrucko. A generalization of the van-der-Pol oscillator underlies active signal amplification in Drosophila hearing. *Euro. Biophys. J.*, 35:511–16, 2006.

[55] C. E. Strimbu, A. Kao, J. Tokuda, D. Ramunno-Johnson, and D. Bozovic. Dynamic state and evoked motility in coupled hair bundles of the bullfrog sacculus. *Hear. Res.*, 265:38–45, 2010.

[56] Strogatz. *Nonlinear Dynamics And Chaos: With Applications To Physics, Biology, Chemistry And Engineering.* Westview Press, 1994.

[57] G. Verley, K. Mallick, and D. Lacoste. Modified fluctuation-dissipation theorem for nonequilibrium steady states and application to molecular motors. *Euro. Phys. Lett.*, 93:1, 2011.

[58] M. Vollrath, K.Y. Kwan, and D. Corey. The Micromachinery of Mechanotransduction in Hair Cells. *Annu. Rev. Neurosci.*, 30:339–365, 2007.